

**Computational modelling studies of titanium Ti_N ($N = 2-32$)
nanoclusters**

by

PHAAHLA TSHEGOFATSO MICHAEL

THESIS

Submitted in fulfilment of the requirements for the degree of

DOCTOR OF PHILOSOPHY

in

PHYSICS

in the

FACULTY OF SCIENCE AND AGRICULTURE

(School of Physical and Mineral Sciences)

at the

UNIVERSITY OF LIMPOPO

SUPERVISOR: Prof H.R Chauke

CO-SUPERVISOR: Prof P.E Ngoepe

: Prof C.A.R Catlow

2022

Abstract

Transition metal nanoclusters have attracted a significant attention in both theoretical and experimental studies due to their unique properties such as structural, electronic and magnetic. These properties are distinct, size dependent and ranges between those of bulk and single-particle species. Some of the systems sizes have been experimentally synthesized, which enables direct theory-experiment comparison. Other clusters that have been examined theoretically are of interest as models of larger systems. Often, the size dependence of their HOMO-LUMO (H-L) gap, optical properties, magnetic properties, etc., is of interest.

In this study, we have performed a genetic algorithm search on the tight-binding interatomic potential energy surface (PES) for small Ti_N ($N = 2-32$) clusters. Lowest energy candidate clusters were further refined using density functional theory (DFT) calculations with the PBEsol exchange-correlation functional and evaluated with the PBEsol0 hybrid functional. The resulting clusters were analysed in terms of their structural features, growth mechanism and surface area. The results suggest a growth mechanism that is based on forming coordination centres by interpenetrating icosahedra, icositetrahedra and Frank–Kasper polyhedra. We identified centres of coordination, which act as centres of bulk nucleation in medium-sized clusters and determine the morphological features of the cluster.

Molecular dynamics simulations were performed in order to investigate the impact of thermal agitation on the Ti_N ($N = 7, 13, 17, 32, 57, 80$ and 89). The calculations were carried out at 300 – 2400 K. The interatomic interactions for vacuum and inert gas environment were modelled using Gupta and Leonard-Jones potentials as implemented within the classical molecular dynamics simulation software DL_POLY.

The total potential energy, radial distribution functions (RDF), diffusion coefficient, mean square displacement and density profiles were examined to study the structural changes as a function of temperature. The Ti_N ($N = 7, 17, 32, 57, 80$ and 89) nanoclusters exhibit lower temperature structural transitions, whereas Ti_{13} nanocluster displayed melting-like structural transitions above the Ti bulk melting point. These transitions are dependent on the composition of the nanocluster. The icosahedron, two interpenetrating icosahedron and pentagonal bi-pyramid were found to be the most dominant building block geometries. The phase transitions from solid to liquid have been identified by a simple jump in the total potential energy curve, with the predicted melting temperature near that observed. As expected, the RDF's and density profile peaks decrease with increasing temperature. The inert gas environment was found to exhibit features that are associated with the melting of nanoclusters below bulk Ti melting point.

We further explored the reactivity and electronic properties of the Ti nanoclusters when they are modified by different impurity elements. Structures and electronic properties of $Ti_{N-1}M$ ($N = 2 - 16$) nanoclusters have been investigated using the density functional theory method with the PBEsol exchange-correlation functional. In order to locate the stable $Ti_{N-1}M$ ($M = Pt, Ir, Pd$ and Ni) bimetallic clusters, the Pt atom was doped in all the coordinated atoms of Ti_N ($N = 2-16$) clusters. Then, the same position with the lowest energy was used to investigate the stability and electronic properties for other impurities. The results suggested Iridium as the most energetically favoured dopant as revealed by the lowest binding energy. However, the relative stability and dissociation energy revealed $Ti_{12}Pt$ as the most stable isomer. Furthermore, H-L gaps revealed the reduction of the quantum confinement, reactive and non-reactive isomers as the cluster size N increases. The H-L and density of state revealed no correlation with the stability measure quantities (relative stability and dissociation energy).

Declaration

I declare that the thesis hereby submitted to the University of Limpopo (Turfloop Campus) for the degree of Doctor of Philosophy (PhD) has not previously been submitted by me for a degree at this or any other university, that it is my work both in design and execution, and that all material contained herein has been duly acknowledged.

Signature:



Mr T.M Phaahla

Date: 31/03/2022

Acknowledgements

I would like to thank:

- My Supervisors; Professor Hasani R Chauke, Professor Phuti E Ngoepe, and Professor Sir C. Richard. A Catlow for formulating the research study and affording me an incredible opportunity to visit the University College London (UCL) group. If it was not for you, I would not be able to handle everything that research studies and life throws at me. This research would not have been possible without the exceptional support from my supervisor Prof Hasani R Chauke.
- The UCL group: Doctor Alexey A Sokol, Doctor Tomas Lazauskas, Professor Scott M Woodley for their useful comments in the course of the study and provided expertise required in the study.
- The Material Modelling Centre (MMC) members, who kept life interesting by providing numerous occasions to chat about science and life in general.
- My parents, who have always encouraged me to pursue my studies through difficult times of losing my baby girl, sister and brothers.
- The Material Modelling Centre administrator Dr Sentshuhlang Jacob Mothapo for the encouraging words that inspired me to work hard.
- The Materials modelling Centre systems administrators Dr Kenneth Kgwane and Dr Katlego Phoshoko for their undivided assistance concerning computer systems.
- Sponsors of this project: University of Limpopo (UL), University College London (UCL), the Royal Society Newton's Grant (NA140447) and the National Research Foundation; and Titanium Centre of Competence (TiCoC) is highly acknowledged.

Dedications

This work is dedicated to:

My wonderful kids

Seetsša Talane, Lesedi and Thekgo Sedibane

My wonderful siblings

Lindah, Jimmy, Justice, and the late Julius

My wonderful elder brothers and sisters

George, Jacob, Sophia, and the late Daniel and Paulinah

My wonderful parents

Cordrey and Alinah

Kea leboga!!

Table of Contents

CHAPTER 1	1
1. General introduction	1
1.1. Background	2
1.2. Rationale and problem statement	4
1.3. Research hypothesis	6
1.4 Aims of the study	7
1.4.1. Objectives	8
1.4.2. Research questions	9
1.5 Summary	10
1.6. Outline of the study	10
CHAPTER 2	12
2. Literature review	12
2.1. The structural properties	13
2.2. Metal clusters of various transition metals	15
2.2.1. Ti clusters	16
2.2.2. Pd clusters	19
2.2.3. Al clusters	20
2.2.4. Fe clusters	21
2.2.5. Pt clusters	22
2.2.6. Si clusters	23
2.2.7. Ag clusters	24
2.2.8. Ni clusters	25
2.2.9. Cu clusters	26
2.3. The molecular dynamics of metal clusters	27

2.4. Background on methodology and properties to be investigated.....	29
2.4.1. Binding energy, relative stability, bond length, coordination, potential energy, diffusivity, radial distribution function and density profiles.....	29
CHAPTER 3	33
Methodology	33
3.1. First-principles method.....	34
3.2. Density functional theory.....	35
3.3. Approximation methods	41
3.4. Plane-wave pseudopotential method	44
3.4.1. Plane-wave basis sets	44
3.5. Pseudopotential method.....	47
3.6. Projector augmented-wave.....	49
3.7. Molecular Dynamics	50
3.7.1. Energy.....	52
3.7.2. Temperature.....	52
3.7.3. Pressure	53
3.7.4. Ensembles	54
3.8. Interatomic potentials	57
3.8.1. Embedded atom method	58
3.8.2. Buckingham potentials.....	59
3.8.3. GUPTA potentials.....	60
3.9. Simulation codes.....	61
3.9.1. GULP	61
3.9.2. The knowledge led master code.....	62
3.9.3. Genetic algorithm	63

3.9.4. CASTEP	64
3.9.5. Dmol3	65
3.9.6. DL_POLY	66
3.9.10 FHI-aims code	67
3.10 Computational details	67
CHAPTER 4	71
Results and Discussion: Structures and energies	71
4.1. Optimisation of Ti structures	71
4.1.1. FCC, HCP titanium and validation of its potentials	71
4.2. Optimisation of Ti clusters and growth	73
4.3. Stability of clusters	79
4.3.1. Binding Energy	79
4.3.2. Second-order energy difference	79
4.3.3. Bond length and average coordinations	80
4.3.4. Electronics: HOMO-LUMO	80
4.4. Structural properties	81
4.4.1. Ti_N clusters growth pattern	81
4.4.2 Spin polarization	89
4.4.3 Stability of the Ti_N (N = 2-32) clusters.	92
4.4.4 Energetic distribution and surface area.	99
4.4.5. Refinement and electronic properties.	103
CHAPTER 5	109
Effect of Temperature on Ti_N nanoclusters	109
5.1 Molecular dynamics study of the stable titanium nanoclusters	109
5.2 DL_POLY parameter and settings	110

5.3 The search for the most effective ensemble on Ti₁₃ nanocluster in a vacuum.....	111
5.3.1. The thermal agitated phase transition of Ti₁₃ employing Hoover thermostat...	111
5.3.2. The thermal agitated phase transition of Ti₁₃ employing Andersen thermostat	114
5.3.3. The thermal agitated phase transition of Ti₁₃ employing Berendsen thermostat	116
5.3.4. The potential energy (heating and cooling) on Ti₁₃ nanocluster	117
5.3.5. Mean square displacement (MSD) for Ti₁₃ nanocluster at various temperatures	121
5.3.6. The radial distribution function for Ti₁₃ nanocluster	123
5.3.7. Density profiles for Ti₁₃ nanoclusters at various temperatures	125
5.4 The search for the most effective ensemble on Ti₁₃ nanoclusters in an Argon gas environment.....	127
5.4.1. The thermal agitated phase transition of Ti₁₃ employing Hoover thermostat in an inert gas	128
5.4.2. The thermal agitated phase transition of Ti₁₃ employing Andersen thermostat in an inert gas	129
5.4.3. The thermal agitated phase transition of Ti₁₃ employing Berendsen thermostat in an inert gas	131
5.4.4. The potential energy of the Ti₁₃ nanocluster in an inert gas	132
5.4.5. Mean square displacement (MSD) for the Ti₁₃ nanocluster inserted in the inert gas at various temperatures	134
5.4.6. The radial distribution functions (RDFs) for Ti₁₃ nanocluster in an inert gas ..	135
5.4.7. The density profiles for Ti₁₃ nanoclusters in an inert gas at various temperatures	137
5.5 The thermal agitated phase transition on the Ti_N (N = 7 & 17) nanocluster in a vacuum	140
5.5.1. The thermal agitated phase transition of Ti₇ nanocluster	140

5.5.2. The thermal agitated phase transition of Ti_{17} nanocluster	141
5.5.3. The potential energy (heating and cooling) for Ti_N ($N = 7$ & 17) nanoclusters .	144
5.5.4. The mean square displacement (MSD) for Ti_N ($N = 7$ & 17) nanoclusters at various temperatures	146
5.5.5. The radial distribution function (RDFs) for Ti_N ($N = 7$ & 17) nanoclusters	148
5.5.6. The density profiles for Ti_N ($N = 7$ & 17) nanoclusters at various temperatures	150
5.6. The thermal agitated phase transition on the Ti_N ($N = 7$ & 17) nanocluster inert gas insertion.....	151
5.6.1. The thermal agitated phase transition of Ti_7 in an inert gas	151
5.6.2. The thermal agitated phase transition of Ti_{17} in an inert gas.....	153
5.6.3. The potential energy of the Ti_N ($N = 7$ & 17) nanocluster in an inert gas	154
5.6.4. The mean square displacement (MSD) for Ti_N ($N = 7$ & 17) nanoclusters in an inert gas at various temperatures.....	156
5.6.5. The radial distribution function (RDFs) for Ti_N ($N = 7$ & 17) nanoclusters in an inert gas	157
5.6.6. The density profiles for Ti_N ($N = 7$ & 17) nanoclusters in an inert gas at various temperatures	159
CHAPTER 6	161
The effect of the thermal agitation on Ti_N ($N = 32, 57, 80$ & 89) using molecular dynamics simulation.....	161
6.1. The thermal agitated phase transition on the Ti_{32} nanocluster	161
6.1.1. The potential energy (heating and cooling) on Ti_{32} nanocluster	165
6.1.2. Configuration energy of the thermal agitated Ti_{32} nanocluster	167
6.1.3. Diffusion coefficient for thermal agitated Ti_{32} nanocluster	168
6.1.4. Mean square displacement (MSD) for Ti_{32} nanocluster	170
6.1.5. Radial distribution function for Ti_{32} nanocluster.....	171

6.1.6. Density profiles for Ti_{32} nanocluster	172
6.2. The thermal agitated phase transition on the argon gas inserted Ti_{32} nanocluster .	174
6.2.1. The potential energy for Ti_{32} nanocluster in an argon gas environment.....	175
6.2.2. Diffusion coefficient for thermal agitated Ti_{32} nanocluster in an inert gas environment	176
6.2.3. Mean square displacement (MSD) for Ti_{32} nanocluster	177
6.2.4. Radial distribution function for Ti_{32} nanocluster.....	178
6.2.5. Density profiles for Ti_{32} nanocluster.....	179
6.3. Structural evolution and thermal transitions on Ti_N ($N = 57, 80 \& 89$).....	181
6.3.1. The thermal agitated phase transition of Ti_{57}	181
6.3.2. The thermal agitated phase transition of Ti_{80}	185
6.3.3. The thermal agitated phase transition of Ti_{89}	189
6.3.4. The dominant configurations for Ti_N ($N = 32, 57, 80, 89$) nanoclusters	193
6.3.5. The potential energy for Ti_N ($N = 32, 57, 80, 89$) nanoclusters.....	195
6.3.6. The configuration energy of the thermal agitated Ti_N ($N = 57, 80, 89$) nanoclusters	197
6.3.7. Mean square displacement (MSD) for Ti_N ($N = 57, 80 \& 89$) nanoclusters	198
6.3.8. Radial distribution function for Ti_N ($N = 32, 57, 80, 89$) nanocluster.....	200
6.3.9. Density profiles for Ti_N ($N = 32, 57, 80, 89$) clusters at various temperatures...	202
CHAPTER 7	205
Structural characterization of Ti-doped $Ti_{N-1}M$ ($M = Pt, Ni, Ir, Pd$) nanoclusters	205
7.1. Background knowledge on bimetallic transition metal nanoclusters.....	205
7.2. Structure and characterization for $Ti_{N-1}Pt$	206
7.3. Electronic and structural properties of $Ti_{N-1}Pt$	208
7.4. Structure and stability of $Ti_{13-N}Pt_N$ nanoclusters	215
7.5. Stability effect of $Ti_{N-1}M$ ($M = Pd, Ir, Ni$) nanoclusters.....	218

7.6. HOMO – LUMO (H-L) energy gabs of $Ti_{N-1}M$ (M = Pd, Pt, Ir and Ni)	225
7.7 Density of states of selected Ti_N clusters doped with Ni, Pt, Ir, Pd	231
7.8. The charge density difference of $Ti_{12}M$ (M = Ir, Pt, Pd, Ni)	234
7.9. HOMO-HOMO orbital analysis for $Ti_{12}M$ (M = Pt, Ni, Pd, Ir)	237
CHAPTER 8	239
Summary and conclusion	239
Future work	245
References	249

Table of figures

FIGURE 2.1: CRYSTAL STRUCTURE OF TITANIUM ALLOY SHOWING (A) B-STRUCTURE (BODY CENTRED) AND (B) A-STRUCTURE (HEXAGONAL CLODED PAKED) [56].	15
FIGURE 3.1 COMPARISON OF A WAVE FUNCTION IN THE COULOMB POTENTIAL OF THE NUCLEUS (BLUE) TO THE ONE IN THE PSEUDOPOTENTIAL (RED). THE REAL AND THE PSEUDO-WAVE FUNCTION AND POTENTIALS MATCH ABOVE A CERTAIN CUT-OFF [179].	48
FIGURE 3.2: THE SCHEMATIC REPRESENTATION OF THE MULTI-STAGES OF TECHNICAL METHODOLOGIES USED IN THIS STUDY.	70
FIGURE 4.1 ENERGY (E) “EVOLUTION” OF THE 20 LOWEST ENERGY STRUCTURES OF Ti_{21} DURING A GA SIMULATION CARRIED OUT FOR 2000 ITERATIONS. THE RED LINE SHOWS THE AVERAGE ENERGY OF THE 20 LOWEST ENERGY STRUCTURES.	74
FIGURE 4.2: MAP OF ENERGY RANKING OF Ti_{32} BETWEEN DIFFERENT ENERGY LANDSCAPES: IP, PBEsol WITH LIGHT AND PBEsol WITH TIGHT BASIS SETS. THE LINES BETWEEN THE VALUES DEPICT THE CLUSTER ENERGY EVOLUTION ON ENERGY REFINEMENT FROM LEFT TO RIGHT.	77
FIGURE 4.3: TENTATIVE GLOBAL MINIMA OF Ti_N, $N = 3-20$ CLUSTERS. AS DISCUSSED IN THE MAIN TEXT, FOR STRUCTURAL ANALYSIS OF THE BIGGEST CLUSTERS $N = 18-20$, THE FOLLOWING COLOURING WAS USED: ATOMS FROM ICOSAHEDRA ARE COLOURED YELLOW AND CAPPING ATOMS ARE COLOURED PINK.	82
FIGURE 4.4: TENTATIVE GLOBAL MINIMA OF Ti_N, $N = 21-32$ CLUSTERS THE FOLLOWING COLOURING WAS USED: ATOMS FROM ICOSAHEDRA ARE COLOURED YELLOW (OR KHAKI OR PINK), FROM SIXFOLD ICOSITETRAHEDRA – BLUE (OR LIGHT BLUE) AND FROM THE Z15 FRANK–KASPER POLYHEDRA – ORANGE. ATOMS SHARED BY NEIGHBOURING FRAGMENTS ARE COLOURED RED.	83
FIGURE 4.5: RELATIVE ENERGIES OF LM WITHIN A RANGE OF 0.2 eV ENERGY RANGE FROM THE TENTATIVE GM, $\Delta E = E(GM) - E(LM)$, FOR ALL THE CLUSTER SIZES CONSIDERED. THE DATA POINTS ARE COLOURED ACCORDING TO THE CLUSTER SPIN MOMENT; THE DATA	

LABEL SHOWS THE ENERGY RANK IN THE INITIAL SPIN UNPOLARISED CALCULATION. “?” MARKS NEW CONFIGURATIONS. 90

FIGURE 4.6: SPIN POLARIZATION ENERGIES OF TENTATIVE GM STRUCTURES ($\Delta E = E(S) - E(0)$). 91

FIGURE 4.7: BINDING ENERGY OF THE TENTATIVE GM PBESOL PES. THE HORIZONTAL BOLD LINE AT THE BOTTOM REPRESENTS THE CALCULATED BINDING ENERGY OF THE BULK HCP (HEXAGONAL CLOSE-PACKED) Ti METAL. THE BACKGROUND BANDS INDICATE THE NUMBER OF COORDINATION CENTRES (C.C.) IN THE TENTATIVE GM. BALL AND STICK MODELS ARE ALSO SHOWN FOR 4 MAGIC SIZED TENTATIVE GM. 94

FIGURE 4.8: FIRST AND SECOND-ORDER ENERGY DIFFERENCES OF THE TENTATIVE GM (RED TRIANGLES, LEFT VERTICAL AXIS AND BLUE CIRCLES, RIGHT VERTICAL AXIS, RESPECTIVELY). THE BACKGROUND BANDS INDICATE THE NUMBER OF COORDINATION CENTRES (C.C.) IN THE TENTATIVE GM. 95

FIGURE 4.9: AVERAGE BONDING DISTANCE VARIES WITH THE CLUSTER SIZE. 96

FIGURE 4.10: AVERAGE COORDINATION NUMBER OF THE TENTATIVE GM. THE BLUE LINE SHOWS THE AVERAGE COORDINATION NUMBER WITH 1σ ERROR BARS. THE RED AND GREEN LINES SHOW THE MINIMUM AND MAXIMUM COORDINATION NUMBERS, RESPECTIVELY. THE BACKGROUND BANDS INDICATE THE NUMBER OF COORDINATION CENTRES (C.C.) IN THE TENTATIVE GM. 97

FIGURE 4.11: RELATIVE LM ENERGIES PER ATOM WITH RESPECT TO THE TENTATIVE GM STRUCTURE. THE RED BARS REPRESENT THE RELATIVE ENERGIES OF THE LM AND THE BLUE BARS REPRESENT $[E_{REL} = E_{GM}(N - 1)/(N - 1) - E_{GM}(N)/N]$ FOR THE N - 1 TENTATIVE GM. 99

FIGURE 4.12: SURFACE AREA PER ATOM FOR THE FIVE LOWEST ENERGY LM STRUCTURES. THE BLUE LINE CONNECTING THE GM IS A GUIDE FOR THE EYE. THE BACKGROUND BANDS INDICATE THE NUMBER OF COORDINATION CENTRES (C.C.) IN THE TENTATIVE GM. 101

FIGURE 4.13: BINDING ENERGY OF THE TENTATIVE GM ON THE PBESOL0 PES (DARK BLUE LINES AND TRIANGLES). THE GREEN (ORANGE) ELIPSES HIGHLIGHT KEY SIZES WHERE GREATER STABILITY IS PREDICTED (NOT) TO BE THE SAME USING BOTH LEVELS OF THEORY. TWO BALL AND STICK MODELS OF KEY GM CONFIGURATIONS ON THE PBESOL0 PES ARE MARKED WITH ARROWS. BOUNDS ON THE DATA SHOWN ARE PROVIDED BY THE BINDING

ENERGIES FOR THE SMALLEST ($N = 2$) AND LARGEST (BULK) ARE SHOWN WITH HORIZONTAL LINES: THE EXPERIMENTAL DISSOCIATION ENERGY OF Ti_2 IS SHOWN IN GREEN; [30] PBESOL0 FOR BULK IN BLUE; PBESOL FOR BULK IN CYAN; AND THE EXPERIMENTAL VALUE OF COHESIVE ENERGY IS INDICATED IN RED. [248] THE BACKGROUND BANDS INDICATE THE NUMBER OF COORDINATION CENTRES (C.C.) IN THE TENTATIVE GM.....	104
FIGURE 4.14: FIRST AND SECOND-ORDER ENERGY DIFFERENCES OF THE TENTATIVE GM (RED LINE, PRIMARY Y-AXIS AND BLUE LINES, SECONDARY Y-AXIS, RESPECTIVELY) ON THE PBESOL0 PES. THE BACKGROUND BANDS INDICATE THE NUMBER OF COORDINATION CENTRES (C.C.) IN THE TENTATIVE GM.	105
FIGURE 4.15: ELECTRONIC PROPERTIES OF TENTATIVE GM Ti_N CLUSTERS AT TWO LEVELS OF THEORY: PBESOL AND PBESOL0. THE BACKGROUND BANDS INDICATE THE NUMBER OF COORDINATION CENTRES (C.C.) IN THE TENTATIVE GM. THE HOMO AND LUMO STATES.	106
FIGURE 4.16: THE ENERGY DIFFERENCE BETWEEN HOMO-LUMO	107
FIGURE 5.1: Ti_{13} NANOCUSTER IN THE VACUUM AT VARIOUS TEMPERATURES.....	113
FIGURE 5.2: SNAPSHOTS Ti_{13} NANOCUSTER IN VACUUM SHOWING CHANGES IN THE GEOMETRY AT ELEVATED TEMPERATURES.	114
FIGURE 5.3: SNAPSHOTS FOR Ti_{13} NANOCUSTERS SHOWING CONFIGURATIONAL CHANGES AS A FUNCTION OF TEMPERATURE.....	116
FIGURE 5.4: THE POTENTIAL ENERGY (E_p) FOR THE HEATING AND COOLING USING (A) HOOVER, (B) ANDERSEN AND (C) BERENDSEN THERMOSTATS.	119
FIGURE 5.5: MEAN SQUARE DISPLACEMENT (MSD) FOR Ti_{13} NANOCUSTERS AT VARIOUS TEMPERATURES FOR (A) HOOVER, (B) ANDERSEN AND (C) BERENDSEN ENSEMBLES.	122
FIGURE 5.6: THE RADIAL DISTRIBUTION FUNCTIONS (RDFs) OF THE Ti_{13} AT VARIOUS TEMPERATURES FOR (A) HOOVER AND (B) BERENDSEN THERMOSTATS.....	124
FIGURE 5.7: COMPARISON OF Ti_{13} NANOCUSTER ATOMIC DISTRIBUTION FOR (A) HOOVER AND (B) BERENDSEN ENSEMBLES ALONG A CARTESIAN COORDINATE (z) AT DIFFERENT TEMPERATURES.....	126
FIGURE 5.8: THE Ti_{13} NANOCUSTER INSERTED IN AN INERT GAS AT VARIOUS, WHERE THE GREEN CIRCLES REPRESENTS AR ATOMS TEMPERATURES.....	128

FIGURE 5.9: THE Ti_{13} NANOCUSTER INSERTED IN AN INERT GAS AT VARIOUS TEMPERATURES, WHERE THE GREEN CIRCLES REPRESENTS AR ATOMS.....	130
FIGURE 5.10: THE Ti_{13} NANOCUSTER INSERTED IN AN INERT GAS AT VARIOUS TEMPERATURES, WHERE THE GREEN CIRCLES REPRESENTS AR ATOMS	131
FIGURE 5.11: THE POTENTIAL ENERGY VS TEMPERATURE FOR Ti_{13} NANOCUSTERS INSERTED IN THE INERT GAS AT VARIOUS TEMPERATURES FOR (A) HOOVER, (B) ANDERSEN AND (C) BERENDSEN ENSEMBLES.	133
FIGURE 5.12: MEAN SQUARE DISPLACEMENT (MSD) OF Ti_{13} NANOCUSTERS INSERTED IN THE INERT GAS AT VARIOUS TEMPERATURES FOR (A) HOOVER, (B) ANDERSEN AND (C) BERENDSEN ENSEMBLES.	136
FIGURE 5.13: THE RADIAL DISTRIBUTION FUNCTIONS (RDFs) OF THE Ti_{13} AT VARIOUS TEMPERATURES FOR (A) HOOVER AND (B) BERENDSEN THERMOSTATS.	138
FIGURE 5.14: COMPARISON OF Ti_{13} ATOMIC DISTRIBUTION ALONG A CARTESIAN COORDINATE (Z) AT DIFFERENT TEMPERATURES IN AN ARGON ENVIRONMENT FOR (A) HOOVER AND (B) BERENDSEN THERMOSTATS.	139
FIGURE 5.15: THE Ti_7 NANOCUSTER IN THE VACUUM AT VARIOUS TEMPERATURES.	141
FIGURE 5.16: SNAPSHOT OF Ti_{17} NANOCUSTERS IN THE VACUUM AT VARIOUS TEMPERATURES.	142
FIGURE 5.17: VARIATION OF POTENTIAL ENERGY WITH TEMPERATURE FOR Ti_N (N= 7 & 17) NANOCUSTER.	144
FIGURE 5.18: THE MSD FOR THE Ti_N (N = 7 & 17) NANOCUSTER AT VARIOUS TEMPERATURES.	147
FIGURE 5.19: THE RADIAL DISTRIBUTION FUNCTION OF THE Ti_N (7 & 17) AT VARIOUS TEMPERATURES.	149
FIGURE 5.20: THE COMPARISON OF Ti_N (N = 7 & 17) ATOMIC DISTRIBUTION ALONG A CARTESIAN COORDINATE (Z) AT DIFFERENT TEMPERATURES.	150
FIGURE 5.21: SNAPSHOTS OF Ti_7 NANOCUSTERS INSERTED IN AN INERT GAS ENVIRONMENT AT VARIOUS TEMPERATURES, WHERE THE GREEN CIRCLES REPRESENTS AR ATOMS	152
FIGURE 5.22: THE Ti_{17} NANOCUSTER INSERTED IN AN INERT GAS AT VARIOUS TEMPERATURES.	154

FIGURE 5.23: THE POTENTIAL ENERGY VS TEMPERATURE FOR Ti_N ($N = 7$ & 17) NANOCUSTER INSERTED IN INERT GAS ENVIRONMENT.	155
FIGURE 5.24: THE MSD OF Ti_N ($N = 7$ & 17) NANOCUSTER INSERTED IN INERT GAS AT VARIOUS TEMPERATURES.	156
FIGURE 5.25: THE RADIAL DISTRIBUTION FUNCTION FOR Ti_N ($N = 7$ & 17) AT VARIOUS TEMPERATURES.	158
FIGURE 5.26: THE COMPARISON OF Ti_N ($N = 7$ & 17) ATOMIC DISTRIBUTION ALONG A CARTESIAN COORDINATE (z) AT DIFFERENT TEMPERATURES IN AN INERT GAS.	159
FIGURE 6.1 Ti_{32} NANOCUSTERS IN THE VACUUM AT VARIOUS TEMPERATURES.	162
FIGURE 6.2: THE POTENTIAL ENERGY AT VARIOUS TEMPERATURE COOLING FOR Ti_{32} NANOCUSTER.	166
FIGURE 6.3: CONFIGURATION ENERGY AGAINST TEMPERATURE FOR Ti_{32} NANOCUSTER.	168
FIGURE 6.4: DIFFUSION COEFFICIENT AS A FUNCTION OF TEMPERATURE FOR Ti_{32} NANOCUSTER.	170
FIGURE 6.5: MSD FOR Ti_{32} NANOCUSTER AT VARIOUS TEMPERATURES.	171
FIGURE 6.6: THE RADIAL DISTRIBUTION FUNCTION FOR Ti_{32} NANOCUSTER AT VARIOUS TEMPERATURES.	172
FIGURE 6.7: COMPARISON OF Ti_{32} NANOCUSTER ATOMIC DISTRIBUTION ALONG A CARTESIAN COORDINATE (z) AT DIFFERENT TEMPERATURES.	173
FIGURE 6.8: Ti_{32} NANOCUSTERS IN AN INERT GAS ENVIRONMENT AT VARIOUS TEMPERATURES, WHERE THE GREEN CIRCLES REPRESENTS Ar ATOMS.	174
FIGURE 6.9: VARIATION OF THE POTENTIAL ENERGY WITH TEMPERATURE FOR Ti_{32} NANOCUSTER IN AN ARGON ENVIRONMENT.	176
FIGURE 6.10: DIFFUSION COEFFICIENT AS A FUNCTION OF TEMPERATURE FOR Ti_{32} NANOCUSTER IN AN INERT GAS ENVIRONMENT.	177
FIGURE 6.11: THE MSD OF Ti_{32} NANOCUSTER IN AN INERT GAS ENVIRONMENT.	178
FIGURE 6.12: THE RADIAL DISTRIBUTION FUNCTION OF THE Ti_{32} IN AN INERT GAS ENVIRONMENT AT VARIOUS TEMPERATURES.	179
FIGURE 6.13: COMPARISON OF Ti_{32} ATOMIC DISTRIBUTION ALONG A CARTESIAN COORDINATE (z) AT DIFFERENT TEMPERATURES IN INERT GAS.	180
FIGURE 6.14: THE Ti_{57} NANOCUSTERS IN THE VACUUM AT VARIOUS TEMPERATURES.	182

FIGURE 6.15: THE Ti_{80} NANOCCLUSERS IN THE VACUUM AT VARIOUS TEMPERATURES.....	186
FIGURE 6.16: THE Ti_{89} NANOCCLUSERS IN THE VACUUM AT VARIOUS TEMPERATURES.....	190
FIGURE 6.17: THE MOST DOMINANT GEOMETRIES FORMING PART OF THE BUILDING BLOCK FRAGMENTATIONS FOR Ti_N ($N = 32, 57, 80 \& 89$).....	194
FIGURE 6.18: THE POTENTIAL ENERGY OF THE Ti_N ($N = 32, 57, 80, 89$) SHOWING SMOOTH VARIATION AS THE TEMPERATURE INCREASE. THE Ti_{32} IS INSERTED FOR COMPARISON.	196
FIGURE 6.19: THE CONFIGURATION ENERGY OF THE Ti_N ($N = 57, 80, 89$) AT VARIOUS TEMPERATURES.....	197
FIGURE 6.20: DYNAMICS PROPERTIES FOR Ti_N ($N = 57, 80 \& 89$). TEMPERATURE EFFECT ON THESE NANOCCLUSERS MEAN SQUARE DISPLACEMENT.....	200
FIGURE 6.21: THE RADIAL DISTRIBUTION FUNCTIONS FROM THE INTEGRAL-EQUATION THEORY, SHOWING THE INCREASE OF SHORT-RANGED ORDER AS A FUNCTION OF TEMPERATURE.	201
FIGURE 6.22: ATOMIC DENSITY PROFILE $N(Z)$ AS A FUNCTION OF TEMPERATURE, IN THE DIRECTION PERPENDICULAR OF THE SUBSTRATE LOCATED AT $Z = 0$, IN Ti_N ($N = 32, 57, 80,$ 89).....	203
FIGURE 7.1: THE $Ti_{N-1}Pt$ ($N = 2-16$) CONFIGURATIONS SHOWING THE LOWEST ENERGY POSITIONS WHERE GREY ATOMS REPRESENTS Ti AND WHITE ATOMS REPRESENTS Pt...	207
FIGURE 7.2: THE BINDING ENERGIES OF $Ti_{N-1}Pt$ NANOCCLUSERS.	210
FIGURE 7.3 : RELATIVE STABILITY (D_2E) OF THE MOST STABLE $Ti_{N-1}Pt$ SITE AS A FUNCTION OF N.....	212
FIGURE 7.4: THE DISSOCIATION ENERGY OF THE MOST STABLE $Ti_{N-1}Pt$ SITES AS A FUNCTION OF N.....	213
FIGURE 7.5: THE HOMO AND LUMO ENERGY GAP FOR $Ti_{N-1}Pt$ CLUSTERS, WHERE N IS THE NUMBER OF SUBSTITUTED Pt ATOMS.	214
FIGURE 7.6: THE AVERAGE ENERGY FOR $Ti_{13-N}Pt_N$ COMPOSITION REPLACED WITH Pt AT ALMOST ALL Ti POSITIONS OF Ti_{13}, WHERE N REPRESENTS THE NUMBER OF ATOMS.....	216
FIGURE 7.7: THE ELECTRONIC PROPERTIES (HOMO-LUMO) OF $Ti_{13-N}Pt_N$ NANOCCLUSERS.	217
FIGURE 7.8: THE BINDING ENERGY OF $Ti_{N-1}M$ ($M = Ni, Ir, Pd$) AGAINST THE CLUSTER SIZE.	220
FIGURE 7.9: THE RELATIVE STABILITY (D_2E) AS A FUNCTION OF CLUSTER SIZE FOR $Ti_{N-1}M$ (M $= Ni, Ir, Pd$).....	221

FIGURE 7.10: THE DISSOCIATION ENERGY OF THE MOST STABLE $Ti_{N-1}M$ ($M = Ni, Ir, Pd$) SITES AS A FUNCTION OF N.	223
FIGURE 7.11: THE ELECTRONIC PROPERTIES (HOMO-LUMO) OF $Ti_{N-1}Ni$ NANOCCLUSERS.	226
FIGURE 7.12: THE ELECTRONIC PROPERTIES (HOMO-LUMO) OF $Ti_{N-1}Ir$ NANOCCLUSERS.	228
FIGURE 7.13: THE ELECTRONIC PROPERTIES (HOMO - LUMO) OF $Ti_{N-1}Pd$ NANOCCLUSERS.	229
FIGURE 7.14: COMPARISON OF THE TOTAL DENSITY OF STATES FOR Pt, Ni, Ir, Ni DOPANTS ON Ti_{13} AND Ti_{15}.	232
FIGURE 7.15: COMPARISON OF THE TOTAL DENSITY OF STATES FOR Ni, Pt, Ir, Pd DOPANTS ON Ti_8, Ti_7 AND Ti_6 CLUSTERS.	233
FIGURE 7.16: CHARGE DENSITY DIFFERENCE FOR (A) $Ti_{12}Ir$, (B) $Ti_{12}Pt$, (C) $Ti_{12}Pd$ AND (D) $Ti_{12}Ni$. THE BLUE REGION REPRESENTS ACCUMULATION WHILE THE YELLOW REGION REPRESENTS ELECTRON DEPLETION.	235

List of tables

TABLE 2.1: LATTICE PARAMETERS AND CELL VOLUME FOR HCP-A, BCC-B AND FCC	14
TABLE 3.1: EMBEDDED ATOM METHOD (EAM) POTENTIALS PARAMETERS FOR TI	59
TABLE 3.2: BUCKINGHAM POTENTIALS PARAMETERS FOR TI.....	60
TABLE 4.1: MEAM POTENTIAL TEST ON BULK AND FCC TITANIUM	72
TABLE 4.2: EAM AND BUCKINGHAM POTENTIALS PARAMETERS FOR TI.....	72
TABLE 4.3: GULP TEST OF THE NEW REFINED POTENTIALS ON THE TITANIUM CLUSTERS, N=1-6	73
TABLE 4.4: MAIN COMPUTATIONAL SETTINGS USED WITHIN THE FHI-AIMS PACKAGE	78
TABLE 4.5: THE BINDING ENERGY PER ATOM E_B (eV), THE AVERAGE COORDINATION NUMBER N_0, THE AVERAGE BOND LENGTHS R_0 (Å) FOR Ti_N (N= 2-32), AND REPORTED LOWEST ENERGY STRUCTURES A_0, SECOND-LOWEST ENERGY A_1 OF OTHER TRANSITION METAL CLUSTERS.	87
TABLE 5.1 THE GUPTA AND LENNARD – JONES POTENTIAL PARAMETERS.....	110
TABLE 6.1: DOMINANT GEOMETRIES FOR Ti_N (N = 57, 80, 89 AS A FUNCTION OF TEMPERATURE	193
TABLE 7.1: THE CLUSTER NUMBER, ISOMER IDENTIFICATION AND SUBSTITUTED PT STABLE SITES ON $Ti_{N-1}M$ NANOCCLUSERS.	208
TABLE 7.2: THE BINDING ENERGY (E_B) FOR $Ti_{N-1}M$ (M = Pt, Ni, Ir, Pd) AND PURE TI.....	211
TABLE 7.3: THE CALCULATED HOMO AND LUMO GABS) FOR $Ti_{N-1}M$ (M = Pt, Ni, Ir AND Pd).	215
TABLE 7.4: THE TOTAL RELATIVE ENERGIES (D_2E) FOR $Ti_{N-1}M$ (M = Pt, Ni, Ir, Pd) AND PURE TI.	222
TABLE 7.5: THE TOTAL DISSOCIATION ENERGY (E_D) FOR $Ti_{N-1}M$ (M = Pt, Ni, Ir AND Pd) AND PURE TI.....	224
TABLE 7.6: AVERAGE HOMO – LUMO (H-L) ENERGY GAPS OF $Ti_{N-1}M$ (M = Pd, Pt, Ir AND Ni)	230
TABLE 7.7 THE COMPUTED ISO-SURFACES OF THE HOMO-LUMO FOR $Ti_{12}M$ (M = Pt, Pd, Ir, Ni).....	238

CHAPTER 1

In this chapter, we give a brief review on the nanoclusters, production of titanium metal and titanium nanoclusters. The rationale and problem statement, research hypothesis, aim of the study, objectives, summary, research questions and outline of the study are given.

1. General introduction

In previous years, we have seen explosive development of a new field, commonly known as nanoscience [1]. This field gained extensive research interest in physics, chemistry, and engineering. It addresses a huge number of significant issues such as basic science to a variety of technological applications. Nanoscience and technology intend to understand, control and manipulate objects of few nanometers in size (1 – 100 nm). These objects are intermediate between single atoms and molecules and matter [2]. In particular, nano-systems can present properties that vary with size. This behaviour opened research interest in controlling these properties by controlling precisely their formation process.

Nanoclusters are aggregates of atoms or molecules of nanometric size, containing several constituents particles ranging from ~ 10 to 10^6 [3, 4]. Nanoparticles containing no more than a few hundred atoms (1 – 3 nm) are expected to have strong size-dependent properties such as geometric, electronic structure, binding energy and melting temperature. However, larger nanoparticles with many thousands of atoms have smoothly varying behaviour which tends to bulk limit as the particle size increases [2]. The understanding of whether crystalline or noncrystalline systems prevail for

a given size and composition is of significant importance in cluster science. Small nanoparticles have a higher surface/volume ratio. Thus, the surface energy contribution is not negligible and have a strong size-dependent behaviour [5].

1.1. Background

Transition metals (TMs), both metal oxide metal alloys and pure metal clusters are of significant importance worldwide due to their physical and chemical properties. Their applications are in many industries and not limited to alloy development and design, energy storage devices, catalysis, medical and aeronautic. Research in both experiment and theoretical aspects has been conducted by a desire to understand the fundamental properties involved in the transition from the discrete energy levels of free atoms to the continuous, k-dependent energy bands, strength and response to corrosion as well as behaviour under pressure and temperature [6].

There is an increasing demand for titanium in the world, and its production does not sustain the current market. This is due to continuous demand to find a role in various fields such as in jet engine materials fan blades, low pressure and high-pressure compressor components, as well as in medical for Dental Implants, Surgical Instruments, bone and joint replacement and its excellent physical properties such as high strength and excellent corrosion resistance. The Council for Scientific and Industrial Research (CSIR) developed a suite of complementary technology (titanium pilot plant) that is a step towards a commercial-scale plant that will be able to produce titanium powder at a much lower cost than present imports, making this light metal an economically viable option from which many industries can be created and sustained [7].

South Africa has large reserves of titanium-bearing minerals and is currently the second-largest producer of mineral concentrate. There are various ways of producing or growing Ti, one

significant approach will be to grow titanium from metal particles or powder. The growth of Ti from powder is being examined at the CSIR titanium plant. The product morphology (the form of the particles) can be varied and this gives it an added advantage in some downstream applications. Boeing Research & Technology will oversee this technology implementation activity in collaboration with the Titanium Centre of Competence (TiCoC) at the CSIR. The company is focused on developing future aerospace solutions and improving the cycle time, cost, quality and performance of current aerospace systems [7].

Thus, the production of titanium metal with an average size of several microns requires the development of modelling methodologies that may estimate the rate of titanium crystal formation and growth. Recently, investigations of the structural, electronic, energetic and magnetic properties and evolution of metal clusters as a function of cluster size have attracted significant interest. In particular, studies of the transition metals clusters have received significant attention due to their excellent physical and chemical properties and great technological application in many fields [8]. Previous studies have investigated titanium nanoclusters from smallest ($N = 2$) to larger clusters up to 130 using both experimental and theoretical approaches. Different studies revealed different Ti magic clusters. For example, titanium nanoclusters have been reported to have magic numbers $N = 7, 13, 15, 25,$ and 55 [9, 10].

The evolution of structural, electronic and bonding properties of titanium clusters Ti_N ($N = 2-20$) were studied using DFT and reported nanoclusters with $N = 7, 13, 15$ atoms as the most stable Sun [11]. It was also found that smaller titanium clusters with different spin states generally present close energies due to the complicated 3d electrons, and may result in unrealistic ground states energy clusters [12].

The recent theoretical studies showed that the electronic properties of titanium clusters always possess complicated signatures due to the 4s and 3d electrons [13]. It was reported that the small titanium clusters do not provide well-defined free energies, and information on the relative energies and stabilities of the clusters is uncertain. Furthermore, the titanium clusters are reported to give different magic numbers or high stability clusters based on prediction techniques used. As such inconsistency and lack of compatible techniques used for generating and optimising nanoclusters may lead to incorrect stable clusters.

1.2. Rationale and problem statement

In recent years, the structures and properties of transition metal clusters have been studied extensively [14, 15], mainly due to the inherent size dependence, as cluster and bulk structures often exhibit substantially different properties [16, 17]. Titanium, in particular, has, as noted, many uses in a wide range of fields, from medical applications to aerospace, to catalysis. Efficient fabrication of commercially useful products is, however, hampered by the high mechanical strength of pure Ti metal, and, therefore, production routes of Ti powders are extremely important and of high interest [18, 19, 20]. One of the viable processes is via chlorination of Ti slag, containing ilmenite and rutile minerals, which can be either formed by direct enrichment of Ti containing ores or present as a by-product in pigment production.

This process has for example been developed by the Council for Scientific and Industrial Research in South Africa (CSIR) [20] which should enable novel technologies including the use of Ti powder in 3D printing of metal components for several industries. Various processes are being tested starting from Ti powder, mainly the lithiothermic process, a step-wise processes from TiCl_4 , TiF_4 , TiBr_4 , and TiI_4 precursors to Ti. However, the process is very fast and produce Ti particles

that are clustered and are very difficult to separate and observe the energetic ranking, particularly the small clusters. Studies on transition metal clusters, including Ni, [21] Si, [22] Al [23] and V [24, 25], have been carried out to investigate their structural evolution and electronic properties. It was found that the properties of small metal clusters may differ significantly from those of the bulk, but they can in part reproduce the behaviour either of the crystal defects or metal particle in supported crystals by Estiu [26]. Ti_N clusters, however, have drawn less scientific attention compared to other transition metals. There are a small number of experimental studies reported on titanium clusters.

Notably, Sakurai *et al.* [10] reported magic number Ti_N clusters in time-of-flight (TOF) mass spectra at $N= 7, 13, 15, 19,$ and $25,$ as they observed higher TOF intensities around these sizes [10]. Lian *et al.* studied dissociation pathways and bond energies of titanium cluster ions [27] and suggested that small titanium clusters prefer icosahedral structures. Using photoelectron spectroscopy Liu *et al.* [28] confirmed the findings by Lian and Armentrout [27] by observing abrupt photoelectron spectral narrowing for highly symmetric icosahedral structures at $N= 13$ and $55.$

The later study also showed that the electron affinities of the titanium clusters did not extrapolate to the bulk work function and that the clusters may not possess the bulk packing. Previous theoretical studies on Ti clusters mainly focused on small or selected sizes [29, 30, 12, 31, 32]. Only one recent work by Sun *et al.* [33] provided a systematic study of $Ti_N,$ for sizes $N= 2-20,$ with an analysis of the evolution of structural, electronic and bonding properties with cluster size. To the authors' knowledge, there has not been a systematic study of Ti clusters for larger sizes ($N > 20$) and there is not as yet a complete understanding of their structure and thermodynamic properties. Hence, we have performed atomistic and spin polarised electronic structure calculations

on Ti_N nanoclusters of up to 32 atoms, and explored their electronic, geometric and bonding properties with the focus on finding new particularly stable (abundant) cluster sizes, known as magic numbers, within this range. Thereafter, we have evaluated the thermodynamic evolution and diffusion behaviour of the stable clusters ($N = 7, 13, 17$) and bigger clusters ($N = 32, 57, 80, 89$) using molecular dynamics calculations. The melting process is traced from the change of the clusters, the atomic distribution (MSD, RDFs and density profiles) and the atomic energy (potential energy) as a function of temperature. Lastly, to understand the interplay between the structural and electronic effects in Ti-doped clusters, the FHI-aims technique based on density functional theory is used to study the structural and electronic properties of $Ti_{N-1}M$ ($M = Ni, Pt, Ir, Pd$). The M atoms ($M = Ni, Pt, Ir, Pd$) were taken as the impurities to probe into their influence on the structural and electronic properties of Ti_N clusters. The average binding energy, relative stability and dissociation energy for every cluster size were computed. The HOMO-LUMO, density of states and charge density were also evaluated to study the bonding mechanism.

1.3. Research hypothesis

There is a relationship between the size of the nanocluster and energy. The metal nanoclusters have different properties from the bulk metals. The evolution of the nanoclusters depends on the lower nanoclusters as the building block fragmentations. Nanocluster transitions into different isomers as the temperature increases. Stable nanoclusters have their melting point higher than unstable nanoclusters. Argon gas is capable of reducing metal clusters melting point. The substitution of Pt, Pd, Ir and Ni enhances the binding energy of Ti nanoclusters. Platinum and Iridium stabilizes the system more than the other impurities.

1.4 Aims of the study

A central issue in cluster physics is the need to identify particularly stable sizes. The binding energy gives a detailed structural picture and the nonmonotonic variation in the properties of clusters which are obtained by locating the global minimum as a function of size. This can then give information about the abundance of particularly stable clusters. The first and second-order energy differences allow us to identify the more stable structures. Higher stability clusters are classified as magic numbers or magic clusters. The dissociation energy also gives information about the bonding strength of the clusters.

The (H-L) gap between the highest occupied molecular orbital (HOMO) and the lowest unoccupied molecular orbital (LUMO) are generally considered as a useful quantity to estimate the stability and the movement of electrons from the HOMO to the LUMO of one system. The density of states describes the number of states that are available in the system of the cluster. The density of states (DOS) can determine the carrier concentration and energy distribution within a system. The KLMC [34], FHI-aims [8] and DL_POLY [35] software are employed to evaluate the evolution, growth and stability of the Ti nanoclusters. Firstly, the local minimisation calculation will be carried out using the KLMC code to generate the titanium clusters.

Secondly, the calculated locally minimised clusters will then be minimised globally using FHI-aims to locate the equilibrium stable clusters. Most importantly, the growth pattern, spin polarisation, energy distribution, binding energy, first-order energy (dissociation energy), second-order energy (relative stability) and H-L of the equilibrium stable clusters will be evaluated.

Thirdly, the effect of temperature on the Ti_N ($N = 7, 13, 17, 32$) clusters in both vacuum and Argon environment will be evaluated using DL_POLY [35] employing different ensembles (Hoover [36], Andersen [37] and Berendsen [38] thermostat). Nanoclusters are frequently said to have melting behaviour above the bulk melting temperature. However, inert gas is capable of reducing the arc melting temperature of metals. The analysis is compared with the bulk Ti melting point as a benchmark. Moreover, the effect of temperature on the Ti_N ($N = 57, 80, 89$) clusters will be evaluated in a vacuum. The structural evolution, potential energy, mean square displacement, radial distribution function and density profiles will be used to evaluate the phase changes as the nanoclusters are thermally agitated.

Lastly, the effect of metal doping Ti_N ($N = 2 - 16$) clusters with Ir, Ni, Pt and Pd atoms will be evaluated using FHI-aims code. This calculation is undertaken to investigate the effect of the dopants on the structural and electronic properties of $N = 2 - 16$ clusters. The properties which will be evaluated are; binding energy, relative stability, HOMO-LUMO, the density of states and charge density. The stability of the electronic density of states (DOS), in particular, will be deduced by observing the electronic states behaviour near the Fermi level ($E-E_f = 0$) for the possible pseudo gaps.

1.4.1. Objectives

In this thesis, we investigate the structural evolution of titanium nanoclusters Ti_N ($N = 2-32$), the effect of temperature on the Ti_N ($N = 7, 13, 32, 57, 80, 89$) clusters and investigate the Ni, Ir, Pt and Pd atoms that are taken as impurities to probe into their influence on the structural and electronic properties of Ti_N ($N = 2 - 16$) clusters using the first-principles DFT Kohn and Sham [39] and molecular dynamics (MD) approach [40]. The KLMC-GA and plane-wave

pseudopotential code FHI-aims have been employed in the current study. Thus, by determining the binding energy, relative stability, energy distribution, surface area, coordination number and bond length of Ti clusters and their electronic structure, the clusters will be ranked according to their energies. The MD calculations are carried out using DL_POLY computational code.

The following specific objectives will be explored:

- i. generate titanium clusters using KLMC-GA and re-optimize the clusters using FHI-aims code.
- ii. study the growth pattern of the Ti_N clusters
- iii. investigate the spin polarisation, stability, energetic distribution and surface area
- iv. investigate the coordination and bond length of various Ti_N clusters
- v. determine the HOMO-LUMO gap of Ti_N clusters
- vi. determine temperature effect on the structural properties of Ti_N ($N = 7, 13, 17, 32$) clusters in a vacuum and Argon gas environment
- vii. determine temperature effect on the structural properties of Ti_N ($N = 57, 80, 89$) in a vacuum
- viii. investigate (Pt, Pd, Ni, Ir) doping effect on the structural and stability of Ti_N clusters
- ix. determine the density of states, charge density and HOMO-LUMO of doped Ti_N clusters

1.4.2. Research questions

The research questions to be addressed in this study are:

- i. Which geometries forms part of the building block as the Ti cluster evolves to higher clusters?

- ii. Which clusters will be considered as the magic clusters?
- iii. How will the thermal agitation affect the shape of the Ti clusters in a vacuum and inert gas?
- iv. Will doping with the metal impurities enhance the properties of Ti clusters?

1.5 Summary

The study aims to investigate the nucleation, growth and stability of pure Ti_N ($N = 2-32$), the melting and diffusion behaviour of Ti_N ($N = 7, 13, 17, 32, 57, 80, 89$) clusters and doped Ti_N ($N = 2 - 16$) clusters with Pt, Pd, Ir, Ni atoms.

1.6. Outline of the study

This thesis is divided into eight chapters.

Chapter 1 gives briefly a summary of the importance and the uses of titanium clusters, and also what has been achieved previously in both computational and experimental techniques. The rationale, intention of the study, aim, research hypothesis, objectives, research questions and lastly, the outline of the thesis.

Chapter 2 deals with a literature review on commercial titanium metal, structural properties of titanium, metal clusters of various transition metals, the molecular dynamics on metal clusters, background on methodology and properties to be investigated.

Chapter 3 provides an introduction to the method used and various software programs such as density functional theory, approximation methods i.e. local density approximation (LDA) and generalized gradient approximation (GGA), genetic algorithm (GA), General Utility Lattice

Program (GULP) plane-wave pseudopotential method and simulation codes such as KLMC, FHI-aims, DL_POLY, CASTEP and DMol3.

Chapter 4 presents the evolution of Ti_N ($N = 2 - 32$) clusters, binding energy, relative stability, second-order energy, HOMO-LUMO gaps, coordination and bonding of titanium clusters. Lastly, spin polarisation, energetic distribution, refinement and electronic properties are discussed.

Chapter 5 focuses on the temperature dependence of Ti_N ($N = 7, 13, 17$) using the DL_POLY technique and three ensembles (Hoover, Andersen and Berendsen).

Chapter 6 focuses on the temperature dependence of Ti_N ($N = 32, 57, 80, 89$) using the DL_POLY technique and Hoover thermostat.

Chapter 7 provide results on Ni, Ir, Pt and Pd atoms that are taken as impurities to probe into their influence on the structural and electronic properties of Ti_N ($N = 2 - 16$) clusters.

Chapter 8 gives the summary and conclusion of the study. The recommendation and future work is also highlighted. Finally, the references are listed.

CHAPTER 2

In this chapter, we give a detailed literature review on titanium metal, its structural properties, metal clusters of various transition metals, molecular dynamics on metal clusters and lastly background on methodology and properties to be investigated.

2. Literature review

Titanium is one of the most studied transition metals due to its high tensile strength to density ratio, high corrosion resistance, fatigue resistance, high crack resistance, and ability to withstand moderately high temperatures without creeping. It can form bonds using electrons from more than one of its shells, or energy levels. It shares this feature with other transition metals, including gold, copper and mercury. Titanium has no known biological role, but it is non-toxic. It is almost always present in igneous rocks and the sediment derived from them. It occurs in the minerals ilmenite, rutile, and sphene and is present in titanates and many iron ores [41].

Titanium plays a role as an alloying element with many metals including aluminium, molybdenum and iron. It is pretty unreactive and forms a thin protective layer of the oxide, and thus a good corrosion resistance material. Titanium's relatively low density, which is 56% that of steel and half that of nickel and copper alloys. That is twice as much metal volume per weight and a much more attractive mill cost when compared to other metals. Its higher strength translates into extreme lighter and smaller components and lower stresses for lighter rotating and reciprocating components. Titanium metals are mainly used in aircraft, spacecraft and missiles because of their low density and ability to withstand extremes of temperatures. They are also used in golf clubs,

laptops, bicycles and crutches. Power plant condensers use titanium pipes because of their resistance to corrosion. Molecular dynamics (MD) have greatly been used to investigate the microstructural, dynamics, and thermal effects in a variety of systems at the atomistic level. This technique can simulate millions of atoms and also can investigate collective phenomena, such as melting and phase transitions of these systems. In addition, the molecular dynamics (MD) method is a powerful and effective tool to study the physical characteristics of nanostructures/nanoparticles/clusters [42].

The thermodynamics properties of the transition metals at nano-scales have been of great interest in both theoretical [43, 44] and experimental [45, 46] studies due to their enormous different behaviour from bulk materials [47]. In most cases, these differences are related to their large fraction of surface atoms. It is widely known that the melting temperature decreases with decreasing diameter of the nanoclusters [48]. These clusters, more especially the transition, noble metals [49, 50] or alloy clusters [51, 52] and nanowires have lately been studied mainly because of their extensive applications in optoelectronic nano-devices, catalysis and electronics. Therefore, the theoretical investigation of the dependency of the shape and structural changes of the nanoclusters to the temperature could give more insights for a better understanding of their application activities.

2.1. The structural properties

In Fig. 2.1 we show the crystal structure of titanium with α -, β - phases. Lattice crystal parameters inclusive of fcc crystal structure are summarized in table1.

Table 2.1: Lattice parameters and cell volume for hcp- α , bcc- β and fcc

Structures	α-hcp (Å)	β-bcc (Å)	Fcc (Å)
a	2.9508	3.3200	3.8072
b	2.9508	3.3200	3.8072
c	4.6855	3.3200	3.8072
Lattice parameters	α : 90 β : 90 γ : 120	α : 90 β : 90 γ : 90	α : 90 β : 90 γ : 90
Space group	P63/MMC(194) [53]	IM-3M(229) [54]	Fm-3m(225)

Pure titanium, as well as the majority of titanium alloys, crystallizes at low temperature in a modified ideally hcp structure, (called α titanium). At high temperature, however, the bcc (β titanium.) structure is stable. The β -transus temperature for pure titanium is 1155 ± 275 K. The existence of the two different crystal structures and the corresponding allotropic transformation temperature is of central importance since they are the basis for the large variety of properties achieved by titanium alloys. Both plastic deformation and diffusion rate are closely connected with the respective crystal structure. Moreover, the hexagonal crystal lattice causes a distinctive anisotropy of mechanical behaviour for the α -titanium.

The crystal packing of titanium helps to predict how titanium will give into stretching or other deforming forces, as deformations will tend to occur along crystal planes that align and dictate the direction of the weakest planes in the material. The elastic anisotropy is particularly pronounced. The young modulus of titanium single-crystal consistently varies between 145 GPa for a load vertical to the basal plane and only 100 GPa parallel to this plane [55].

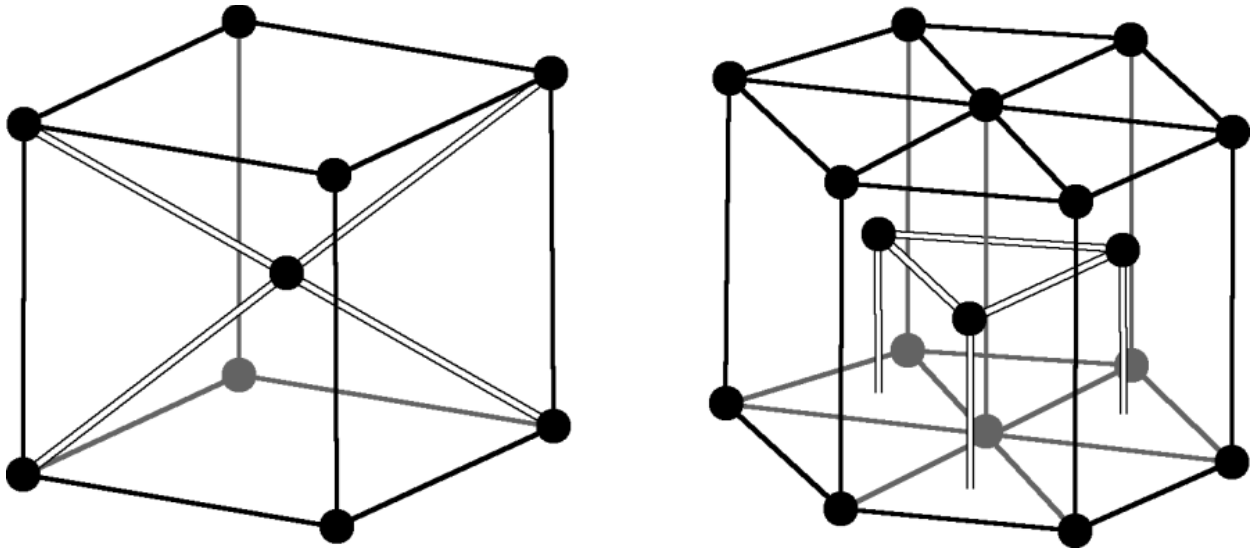


Figure 2.1: Crystal structure of titanium alloy showing (a) β -structure (body centred) and (b) α -structure (hexagonal closed packed) [56].

2.2. Metal clusters of various transition metals

In this section, we review studies carried on various metal clusters including titanium clusters. Several studies on transition metal clusters, such as Fe, Ni, V, Pd, Si and Cu have been carried out to investigate their structural evolution and electronic properties. It was found that the properties of small metal clusters changes may differ significantly from those of the bulk, but they can in part reproduce the behaviour either of the crystal defects or metal particle in supported crystals Estiú. [57]. Their characteristic represents an important step in understanding fundamental mechanism in various fields such as aerospace, military, health, etc. However, the increase of clusters size causes a gradual evolution of the properties towards the bulk phase and open new possibilities for tunable materials which are excellent for applications in many areas [57].

2.2.1. Ti clusters

Investigations of the structural, electronic, energetic, magnetic properties and evolution of metal clusters as a function of cluster size are currently wide. In particular, studies of the transition metals clusters have received significant attention due to their excellent physical and chemical properties and great technological application in many fields [12, 29, 33, 58].

Recently, several studies investigated the geometry and electronic structures of Ti clusters [32, 33]. Titanium clusters are reported to have geometries similar to the bulk and the atomic distribution favours hexagons and decahedra [59, 60]. However, the elastic properties of titanium nanoclusters, in particular, the bulk modulus is nearly three times as large as that of the bulk, which is important for processes of nanoparticle agglomeration for producing compact titanium-based nanomaterials [60]. This follows that the titanium clusters becomes metallic at relatively small sizes [61].

Previous experimental and theoretical approaches were used investigated titanium nanoclusters, from smallest $N = 2$ to larger clusters up to 130 atoms. However, both approaches focus on selected few clusters. It was reported that titanium nanoclusters have magic numbers $N = 7, 13, 15, 25,$ and 55 [10, 12, 62]. Most recently, a DFT study on the evolution of structural, electronic and bonding properties of titanium clusters Ti_N ($N = 2-20$) found nanoclusters with $N = 7, 13, 15$ atoms as the most stable than their neighbours [33]. For smaller titanium clusters, Du *et al.* [58] reported that different spin states generally present close energies due to the effects of 3d electrons, and may result in unrealistic ground states.

The study on Ti_2 clusters revealed that the binding energy varies from 1.05 to 2.1 eV [63, 64, 30, 65], and is considered as the lowest limit by Haslett *et al.* [64]. Other theoretical studies by Wei *et*

al. [12] employed the local spin density approximation (LSDA) to study Ti clusters up to 10, and found the cluster with $N = 7$ as the only magic number. Furthermore, the electronic structure of the titanium clusters is observed to develop bulk-like features at a rather small size.

Zhao *et al.* [31] investigated the evolution of selected structures of Ti_N clusters ($N = 2-14, 19, 55$) using the plane wave ultrasoft pseudo-potential method with generalized gradient approximation (GGA), and found that Ti clusters favour a pentagonal growth pattern. Photoelectronic spectroscopy of anion Ti_N clusters ($N = 1-130$) by Liu *et al.* [66] revealed that symmetric structure for anion Ti_{17} is more likely observed. Rodriguez-Kessler and Rodríguez-Domínguez [32] reported that the binding energy for titanium clusters ($N = 1-16$) increases gradually with the size of the cluster, much more rapidly up to $N \geq 7$, and the size dependence becomes smooth at $N > 7$.

The bond length of the Ti_2 (dimer) cluster ranges between 1.89 Å and 1.96 Å, and depend entirely on the functional [30, 32, 58, 67, 68]. It was also found that the PW91 gave better agreement with the experimental value of 1.943 Å for both projector-augmented wave (PAW) and the all-electron method predicting 1.92 Å and 1.958 Å, respectively. Furthermore, it was reported that compact Tm clusters tend to make the structure stable by forming maximum coordination energy (CN) with short bond lengths. An increase in the average nearest distance with cluster size would lead to a decrease in binding energy [33].

The structural stability of neutral and singly charged icosahedral Ti_{13} clusters was studied by performing BPW/DNP calculations [69] and it was reported that due to Jahn-Teller distortions the Ti_{13} , Ti_{13}^{-1} , and Ti_{13}^{+1} cluster favour D_{3d} symmetry, and these small distortions form the icosahedral geometry in agreement with the experimental observations. Furthermore, they also studied the icosahedral Ti_N ($N = 13, 19, 43, 55$) clusters analysing the binding energies, bond lengths, HOMO-LUMO, DOS, and magnetism [70]. It was found that the icosahedral geometry

displays the lowest energy in most cases except for Ti_{43} , which favours the fcc closed packed structure. The icosahedral Ti_{55} DOS was reported to be very close to that of bulk Ti, including those of the weak magnetism in icosahedral Ti_{13} , Ti_{19} , and fcc Ti_{43} . It was also revealed that the quenched magnetic moments in icosahedral Ti_{55} are attributed to strong s, p-d hybridization.

A comparative study of Ti_N ($N = 13 - 19$) clusters were carried out using the PBE level of theory with PAW [71]. The distorted icosahedral Ti_{13} was found to be the lowest structure of Ti_{13} . It was also reported that the distortions evolve with the increasing cluster size, where atoms are added onto the cluster surface. The shell effect of 3d electrons has been found to play a key role in the formation of directional bonds. Medina *et al.* [72] studied the structural, energetic and magnetic properties of small Ti clusters have been carried out using DFT, applying two different exchange-correlation functionals (PBE and BLYP). The calculated binding energies and bond lengths have shown that the properties of titanium up to 13 atoms are significantly different from the bulk properties. It was also found that the distorted icosahedral Ti_{13} is the lowest energy isomer.

The geometric, electronic, and magnetic properties of phosphorous – doped Ti clusters, Ti_NP ($N = 1-12$) was carried out using the PW91 level of theory. It was found that $Ti_{10}P$, $Ti_{11}P$ and $Ti_{12}P$ have P-encapsulated Ti cages [73]. P-doping increased the stability of Ti clusters while imposing special stability to $Ti_{12}P$ cluster. The magnetic moments of Ti_NP clusters displayed an odd-even staggering pattern, whereas these clusters did not show the quenching of the magnetic moments. It has been reported that the magnetic moments are predominantly due to the Ti 3d electrons.

Some reports from previous experimental studies [61] revealed sharp spectra that are only observed to about Ti_8 . For Ti_9 and above, the spectral features appear to congest to a broad feature near the Fermi level and width increases with clusters size, which indicates that the electronics of the titanium clusters appear to behave bulk-like at rather smaller sizes.

2.2.2. Pd clusters

One of the most studied Pd cluster is the 13-atom cluster. Reddy and Khanna [74] used the linear combination of atomic orbitals methods within the DFT. The Pd₁₃ icosahedral geometry was found to be the most stable than the fcc octahedron. It was revealed that Pd₁₃ have nonzero magnetic moments unlike the bulk, which is nonmagnetic. Furthermore, they calculated binding energy per atom of the Pd₁₃ cluster (1.56 eV) and compared the results to the bulk cohesive energy (3.89 eV). Reddy et al also reported that the icosahedral geometry is the most stable for Pd₁₃ [26]. However, their final structure was found to be a distorted icosahedron structure with D_{5d} symmetry with a zero magnetic moment.

Studies of palladium clusters ground states by Nava *et al.* [75] showed that the small Pd clusters appear to be very floppy with various isomeric structures that are very close in energy. Larger clusters with $N > 100$, showed that the fcc structures have consistently higher cohesive energies than icosahedra and decahedra, although differences in cohesive energies are small. Thus, suggests an early preference for the packing in the bulk. However, decahedral packings were found to be competitive in energy with the other structures of the same nuclearity for $N \leq 85$ and become slightly less stable for larger clusters. Furthermore, all clusters with high spin states are preferred, usually with small HOMO-LUMO gaps below 0.1 eV.

Kumar and Kawazoe performed DFT calculations within spin-polarized general gradient approximation (GGA) to study the evolution of the atomic and electronic structure and magnetism of Pd clusters $N = 2-23, 55, \text{ and } 147$ atoms [76]. The study focused on the changes in the magnetic behaviour of clusters due to H and O adsorption. It was found that the icosahedral growth pattern where the atomically closed shell 13, 55, and 147 atom clusters have higher magnetic moments

that gradually decrease with the increasing cluster size. Moreover, it was observed that the binding energy increases monotonically towards the bulk value with the increase in cluster size. The relative stability showed that 10, 13, 15, 18, 21, and 22 atom clusters are magic and also the reactants and impurities on the cluster were found to have a significant effect on their magnetic behaviour.

2.2.3. Al clusters

Genetic Algorithm search together with a tight-binding interatomic potential to locate the lowest energy structures of Al_n , $2 \leq N \leq 23$ was performed by Chuang *et al.* [77]. It was observed that the size-dependent growth behaviour of aluminum clusters forms an icosahedral-like motif from $N = 11$ to 13. Furthermore, the capping of extra atoms on the icosahedron of Al_{13} is observed for $N = 14$ to 18, and undergo an additional structural transformation for $N \geq 19$. The relative stability revealed magic clusters with $N = 13, 20,$ and 22 . The HOMO-LUMO gaps revealed that clusters with even numbers of atoms tend to have relatively larger gaps than two adjacent clusters with an odd number of atoms except for $N < 6$ where the spin effect is important.

The correlation between energetic stability and HOMO-LUMO gaps was not possible except for Al_{20} where the HOMO-LUMO gap is large. A large energy difference between the lowest energy isomers was noted for $N = 13, 16,$ and 17 , suggesting that the energy difference may be attributed to the fact that the first isomer has much higher symmetry than that of the second isomer. On the other hand, the energy difference between first and second lowest energy isomers in other clusters are small, indicating that at finite temperature, multi-isomers of the same size may coexist.

Zhang *et al.* [23] showed that Al_{27} - Al_{30} clusters favour a double icosahedron motif as well as the Al_{28} and Al_{30} which were found to have higher stability than Al_{27} and Al_{29} . The configurations of

Al_N ($N = 27-30$) are almost the same, suggesting that the larger cluster size with the stronger degree of metallic bonding is weakly affected by the extra electron [23].

2.2.4. Fe clusters

Previous studies on iron clusters Fe_N ($N = 2-7$) [78] focus on the six distinct configuration $N = 2-7$. It was found that Fe–Fe distances (2.10 and 2.33 Å) calculated for the Fe_3 isosceles triangle structure are relatively shorter than the bcc iron structure (2.86 Å). This suggests that the participation of 3d electrons is essential to form the Fe–Fe bond. In the case clusters Fe_4 , Fe_5 , Fe_6 , and Fe_7 , the resulted geometries were distorted tetrahedral, trigonal bipyramidal, octahedral and pentagonal bipyramidal, respectively. Their bond lengths were around 2.30–2.47 Å for all the clusters. Furthermore, it was reported that the resulting electron density ranges from -0.2910 to +0.1180 electrons. The positive charge densities indicate that the clusters possess an electron-deficient character and can be electrophilic in chemical reactions. It was also reported that for the Fe_3 cluster, atom Fe_2 (+0.037) and Fe_3 (+0.036) show a positive charge accounting for their electrophilic character.

The all-electron linear-combination of Gaussian-type-orbital (LCGTO) method with the PZ local density functional study by Dunlap [79], was used to investigate isomers of the pure Fe_{13} cluster. The study revealed the ground state structure with icosahedral configuration. The highest magnetic moment was also found for the icosahedral geometry, which was attributed to the enhanced symmetry-required orbital degeneracy for electrons of different spin [79]. Diequez *et al.* [80] used DFT to study structures, binding energies and magnetic moments of Fe_n cluster up to 17 atoms. The LSDA, a triple basis with double polarization functions were used. The growth pattern of these clusters favoured the icosahedral growth for $N = 11, 12$, and 13 clusters, whereas non-icosahedral C_{2v} and D_{6h} symmetries were predicted for Fe_{14} and Fe_{15} , respectively. A growth pattern based on

the geometry of Fe_{15} was found for Fe_{16} and Fe_{17} . The clusters with $N = 10, 13,$ and 15 were found to be the most stable clusters compared to their neighbours. Duan and Zheng [81] performed LSDA calculations on 13 and 55 atom Fe clusters and reported that the magnetic moments depends not only on the cluster symmetry but also on the size of the clusters. It was also found that contrary to Fe_{13} , the total magnetic moment of the Fe_{55} cluster with icosahedral symmetry is lower than that with octahedral symmetry.

2.2.5. Pt clusters

Previous studies on platinum clusters by Kumar and Kawazoe [82], reported that the binding energy of the lowest energy isomer is significantly higher compared to the icosahedron isomers. That is with increasing size, the binding energy of the icosahedron isomers becomes closer to the value for the octahedron isomers. The various magic clusters ranked by their binding energy were reported with $N = 6, 10, 14, 18, 22,$ and 27 . There were atomically closed shells and symmetric structures, such as a triangle, tetrahedron, square pyramid, layered triangular prism, empty centre decahedron and a cube, respectively. The binding energy revealed a significant rise going from 38 to 44 and 79 to 85. It was observed that the binding energy approaches the calculated bulk cohesive energy of 5.57 eV/atom as the limit $n \rightarrow \infty$. Furthermore, in the case of the magic clusters, it was reported that the HOMO lies in a region of a low density of states, indicating that there is a more significant HOMO-LUMO gap compared to the other clusters. Kumar and Kawazoe [82] concluded that platinum clusters have high dispersion with 10, 14, 18, and 22 atoms magic clusters and 27 atoms cluster has only one atom inside, which reduces the electronic kinetic energy.

The size-dependent electronic structures of Pt_N clusters up to $N = 12$ and their bond properties were carried out by Goepel *et al.* [83] using the ab initio method. It was reported that the Pt atoms

at the unsaturated coordination site has lower Pt_{6s} electrons occupancy and is also energetically unstable. The occupancy Pt_{6s} increases with cluster size and the reactivity decreases. Watari and Ohnishi [84] performed calculations to study the electronic structures of icosahedral and cuboctahedral Pt_{13} clusters. It was also found that cuboctahedral configuration is the most stable cluster than the icosahedral geometry in contrast to the oblate, multiply capped trigonal prism reported by Sun *et al.* [85].

The investigation, on the equilibrium clusters size, the total energy and the HOMO-LUMO orbitals of the 13 atom Pt cluster were performed [86]. It was found that the Fermi level of the Pt cluster is located in the d-band, unlike Au_{13} .

2.2.6. Si clusters

Silicon clusters have received great interest in the research field due to their quantum size effects and intense photoluminescence at room moderate temperature. Particularly, the size at which the stable clusters exhibits the bulk-like diamond structure. The laser vapourisation source was used to measure the binding energy in samples having size $N = 65 - 890$ atoms [87]. Bachels and Schafer [87] reported that the binding energy per atom in the size range $N^{1/3}$ is due to the characteristic exhibited by the spherical isomers. For $N > 10$ the binding energy was found to rapidly increase with cluster size and the compact elementary facets are build up. Bachels and Schafer also reported the metastable prolate geometries at size $N = 64 - 170$ atoms.

The quantum Monte Carlo, density functional theory, and tight-binding calculations were used to theoretically investigate the energetics of small silicon clusters. It was found that small clusters are planar only up to $N = 4$ [88] and $N = 10$ is the magic cluster that has the potential to act as a subunit of larger clusters [89]. Yu *et al.* [90] and Mitas *et al.* [91], reported that the stable clusters

at $N = 20$ are formed by two interpenetrating Si_{10} . These results explained the observations of prolate clusters that are built by stacked subunits, whose configuration is still under debate. Jackson and Kaxiras [92, 93] reported that the Si_{20} cluster subunits are sixfold rings, whereas, other researchers [89] were in favour of a tricapped trigonal prism of nine atoms. However, Rata *et al.* [22], found that $N = 20$ silicon clusters are made of six and eight subunits.

It was also found that the dissociation energies and inverse mobilities were in excellent agreement with the experiments [94]. The prolate clusters of few tens of atoms which are having 6 – 10 atoms as their building blocks were found to be consistent with the fragmentation experiment of clusters of about 150 atoms reported by Ehbrecht and Huisken [95], which yielded $\text{Si}_6^+ - \text{Si}_{11}^+$ products. Hudgins *et al.* [94] reported quasishpherical silicon clusters for about $N > 25$, however, they do not form crystalline structures at these sizes. Furthermore, Ho *et al.* [96] and Mitas *et al.* [91] reported that quasispherical noncrystalline clusters which are not built up by stacking smaller subunits become stable at $N \geq 20$. It was also found that the atom clustering of this magnitude is enough to allow the formation of cages containing at least one silicon inside.

2.2.7. Ag clusters

The energetics of Ag clusters have been the subject of intensive study in size ranges. The search for the lowest energy clusters ($N \leq 9$) reported by Bonacic-Koutecky and Cespiva *et al.* [97, 98] employing self-consistent Hartree-Fock was contacted. The search was able to produce clusters that are in good agreement with experiments [99, 100]. It was found that the most stable configurations are planar up to the pentamer as confirmed by Matulis *et al.* [101] and Santamaria *et al.* [102]. However, other studies considered $N \leq 12$ and $N = 13$ clusters [103, 104]. They suggested that the stable cluster of 13 atoms is low symmetry and the cuboctahedron is more stable

than icosahedron. By contrast, Jennison *et al.* [105], reported that at $N = 55$, the icosahedron is stable than the cuboctahedron cluster.

Doye *et al.* [106] and Yilmaz *et al.* [107], studied larger clusters using semi-empirical interatomic potentials. This technique allowed global minimisation for $N > 99$ atoms and the particularly more negative clusters belonging to the icosahedron, decahedral and truncated octahedral motifs were found. The Sutton and Chen potentials [108] were used by Doye *et al.* [106] to optimise Ag clusters at $N \leq 80$ and reported the same stable clusters as Cespiva *et al.* [98] for $N = 7, 8, 9, 13$ and 55.

They also reported structures that have icosahedral characteristics, however, several decahedron isomers and fcc clusters were found, with the lowest energy clusters at $N = 38$ as a truncated octahedron and decahedron ($N = 71, 75$). Mottet *et al.* [109] found that clusters of high stability can be obtained by removing a central atom in a perfect icosahedron. Particularly, a central vacancy allows the neighbouring atoms to relax and expands their intrashell distance.

2.2.8. Ni clusters

Small nickel clusters have been investigated by Reuse and Khanna [110] and Reuse *et al.* [111] using the density functional theory approach. They found that the stable clusters are nonplanar for $N \geq 4$. These observations were also reported by Nygren *et al.* [112]. At $N = 7$, Reuse *et al.* found two isomers, the pentagonal bipyramid and capped octahedron in close competition. The latter observations were reported experimentally by Parks *et al.* [113]. Nayak *et al.* [114] used the Ab initio approach and found that these clusters are almost degenerate in energy, then they performed molecular dynamics simulations using Finnis and Sinclair semiempirical potentials [115] and found that the capped octahedron has a wider catchment basin, becoming more favourable at elevated temperatures.

Parks *et al.* [116, 117] experimentally identified $N = 13$ (icosahedron) as the magic cluster. Reuse *et al.* [111] reported that the icosahedron is more favoured than the cuboctahedron, however, the lowest energy favoured cluster is obtained by distorting the icosahedron to obtain a cluster with a D_{3d} symmetry group. They also reported a truncated octahedron cluster at $N = 38$, a capped decahedron cluster at $N = 39$ and an icosahedral cluster at $N = 55$. However, Doye and Wales [106] and Lathiotakis *et al.* [118] predicted fcc and icosahedral clusters at $N = 38$ and 55. Furthermore, Andriotis and Menon [119] found capped decahedral clusters just above size $N = 38$. Mottel *et al.* [120] found the crossovers icosahedral \rightarrow decahedral and decahedral \rightarrow fcc take place at larger clusters.

2.2.9. Cu clusters

The energetics of small and larger copper clusters have been extensively studied in recent years. Ab Initio approach was used to perform calculations for $N \leq 10$. Calaminici *et al.* [121, 122] found the lowest energy planar clusters up to $N = 6$. The density functional theory study by Fujima and Yamaguchi [123] indicated that the icosahedron is more favoured than the cuboctahedron cluster. The global minimisation studies for larger clusters up to $N \sim 100$ using semiempirical potentials were conducted by Doye and Wales [106] using Sutton and Chen potentials [108] and Darby *et al.* [124] using Gupta potentials [125]. They found the lowest energy structure at $N = 13$ as the icosahedron and also found no indication in favour of disordered clusters as the magic clusters. Baletto *et al.* did a comparison study on the energetics of icosahedron, decahedron and truncated octahedron for larger clusters and found that the structural evolution from icosahedron to decahedral isomer is around 1000 atoms and decahedron and truncated octahedron are in close competition up to 30000 atoms at least. The same observations were reported experimentally by Berthoud *et al.* [126]. They found a prevalence of small icosahedron, intermediate-size decahedra

and large fcc clusters with wide size interval in which decahedra and fcc clusters coexisted. The structural evolution between the icosahedron and decahedron clusters were also reported to agree with the theoretical calculations.

2.3. The molecular dynamics of metal clusters

Investigations of the effect of raising the temperature on clusters structures have widely attracted researchers both in experimental and theoretical fields of study [127, 128, 37, 48, 129]. These clusters have been studied by a variety of theoretical tools (DL_POLY, Monte Carlo, analytical methods [130, 35, 131]. The most successful technique that was proven to provide a detailed understanding of structural evolution and diffusion of the metal clusters was found to be molecular dynamics [132, 133, 134]. This technique permits the realistic simulation of the melting and freezing process, which takes place at a finite time scale [2].

The use of this technique revealed that at low temperature, the atoms of clusters spend most of the time making small-amplitude vibrations [2]. Shvartburg *et al.* [135], studied the melting of Sn clusters. They reported that small clusters have elongated structures which change to nearly spherical upon melting. However, there was no signature observed and it was concluded that Sn cluster ions which contain 10 – 30 atoms have melting point (50 K) above the bulk melting point. Furthermore, Joshi *et al.* [136], confirmed this behaviour by performing molecular dynamics using ab initio on the melting of Sn₁₀. It was found that the binding of atoms in such a small cluster is covalent and higher temperatures distort the core atoms and break them up. Sn₂₀ was found to have a lower melting point than Sn₁₀, however, still higher than the bulk melting point [137].

Chuang *et al.* [138], employed ab initio Langevin molecular dynamics on tin small clusters and found that Sn₆, Sn₇ and Sn₁₃ melt at higher T than bulk Sn. A systematic study of the different morphologies on sodium clusters was reported by Liu *et al.* [139]. The Na clusters were revealed to have melting point for all sizes at T = 200 – 300 K and they showed a liquid-gas transition at T = 1000 K. Calvo and Spiegelman [140] reported a detailed study on $8 \leq N \leq 147$ atoms using Monte Carlo thermodynamic analysis and found that up to 147 atoms, the thermal agitation displays a direct relationship with lowest energy clusters and melting by steps is favoured by the presents of surface defects.

The icosahedra (13-atom) of Pd cluster was reported by Westergren *et al.* [141] to undergo a structural transition from a rigid, solid-like icosahedron to a non-rigid, liquid-like one through an intermediate temperature range in which both forms exist. Cleveland *et al.* [142] Lee *et al.* [143] and Li *et al.* [144] reported that solid-solid transition is essential without diffusive motion, occurring quickly and involving many cooperative displacements of the atoms. However, this was further clarified by Luo *et al.* [145]. They found that the structural transformation is driven by vibrational and configurational entropy at elevated temperature. Furthermore, Liu *et al.* [28] reported that the melting process occurs in three stages: a relatively long time of surface disordering and reordering, a relatively short time of surface melting and finally a rapid overall melting.

The canonical Monte Carlo simulation reported by Wang *et al.* [146], revealed that the melting point of Si clusters changes dramatically when the cluster changes from prolate and cagelike to an atom-centred and nearly spherical morphology. It was also found out that the nearly spherical clusters present a much-broadened melting region, extending from 750 – 1300 K. Furthermore, the melting of cagelike structures were found to often accompany the overall deformation and

fragmentation of the cage framework. Thus, an elevated temperature is needed to distort the cage. The metastable icosahedra gold cluster produced in an inert gas was reported to be thermally agitated up to $T = 1273$ by Koga *et al.* [147]. They found that an upward displacement of the crossover size with increasing temperature.

2.4. Background on methodology and properties to be investigated

The use of computational simulation techniques is becoming more important in the understanding of the physical properties of materials. Steadily growing computer power and improvements in numerical algorithms are making more materials problems approachable by computer simulations. A recently developed knowledge led master code (KLMC) with the genetic algorithm (GA) method capable to grow large Ti nanoclusters will be employed. These techniques are important for investigating the growth, symmetry group, electronic and thermodynamic properties of Ti nanoclusters Farrow *et al.* [8]. Furthermore, larger cluster sizes from 2 – 32 atoms and beyond will be studied systematically and predict relative energy stabilities. Additionally, molecular dynamics calculations will be performed using DL_POLY software to investigate the effect of temperature on seven stable nanoclusters, i.e. Ti₇, Ti₁₃, Ti₁₇, Ti₃₂, Ti₅₇, Ti₈₀ and Ti₁₈₉.

2.4.1. Binding energy, relative stability, bond length, coordination, potential energy, diffusivity, radial distribution function and density profiles

2.4.1.1. Binding energy

Binding energy is the amount of energy required to separate a particle from a system of particle or disperse all the particles of the system. This energy is particularly applicable to subatomic particles in atomic nuclei, to electrons bound to nuclei atoms, and ions bound together in crystals. The system that is bounded typically has lower potential energy than the sum of its component parts

and it keeps the system organised. This often means that energy is released upon the formation of a bound state. At large, it signifies the mechanical effort that must be done against the forces which hold the particle together, disassembling the particle into parts separated by satisfactory distance.

2.4.1.2. Relative stability and dissociation energy

The relative stability is evaluated to determine the most stable isomers amongst the other clusters and the dissociation energy to measure the strength of bond energy. The stability of clusters can be discussed based on the average binding energies, second-order difference energy and dissociation energy. It has been derived for electronic structure calculations that would yield the total energy of solid materials. This offers a prospect of approximating the stabilities of structures that are very difficult to achieve experimentally. The binding energy, relative stability and dissociation energy from DFT calculations have been successfully used to predict the structural stability of metals, metal-alloys and solid solutions.

2.4.1.3. Bond length and coordination

Bond length is the distance between the nuclei in a bond or the distance where the system energy is a minimum, knowing the bond length in a molecule can sometimes give clues as to the type of bonding present. The total number of points of attachment to the central element is termed the coordination number and this can vary from 2 to as many as 16, but it is usually 6. In simple terms, the coordination number of a complex is influenced by the relative sizes of the metal ion and the ligands and by electronic factors, such as charge which is dependent on the electronic configuration of the metal ion.

2.4.1.4. Potential energy

Potential energy is the energy that exists by the character of the relative position of the objects (structures), within a physical system. This energy has the potential to change the state of the structures or systems around it, for instance, the structural transitions or motion of the atoms in the structure. It is also used as an indicator for solid-liquid (melting) transitions of the structures. Particularly, the melting transition of the structure from the rigid or solid form in which atoms merely oscillate about the equilibrium isomer to a liquid or fluid form characterized by uncorrelated motion of atoms which is spread over a range of temperatures.

2.4.1.5. Mean square displacement and diffusion coefficient

Diffusion coefficients is an important quantitative descriptor of molecular dynamics that can provide information about the association of small molecules with macromolecules at varying temperatures. It also measures the proportionality between flux, and concentration gradient, which is expressed by Fick's first law. This is because the diffusion coefficient of a molecule in solution depends upon several factors, for instance, temperature, pressure, viscosity, etc. This makes it one of the most important parameters for the proper characterization of solvent-based recovery processes. The means square displacement (MSD) is a combination of how far the atoms inside the nanocluster moved. The melting temperature of metal nanoclusters can be obtained by monitoring the variation of the MSD as a function of temperature during diffusion.

2.4.1.6. Radial distribution function and density profiles

The radial distribution function (RDF) helps to understand the binding process of the structures. It is also used to understand the interactions of the atoms present in molecular systems. Particularly, it describes how, on average, the atoms in a system are radially packed around each other which

is an effective way of describing the average structure of disordered molecular systems such as the solid-liquid transitions. Additionally, it can deal with the average structure in systems like liquids, where there is continual movement shows only the instantaneous disorder. The density profiles give a useful qualitative guide to the chemical reactivity of the metals and help us to understand how distributed atoms are during thermal agitation. The higher the density of atoms and lower melting point are associated with lower reactivity, conversely, the lower density of atoms and lower melting point are associated with higher reactivity.

CHAPTER 3

Methodology

In this chapter, a brief overview of the theoretical background on methodologies used in this study is presented. The work was based on both quantum and classical calculations, being the first-principle density functional theory and molecular dynamics. These methods have been used widely to study the structure, chemical, electrical, optical, magnetic properties of a material and temperature dependence properties.

We employed various codes such as the Knowledge Led Master Code (KLMC) [34, 8], Fritz Haber Institute ab initio molecular simulations (FHI-aims) [148], Cambridge sequential total energy package (CASTEP) [149, 150], DMol3 [151, 152] and DL_POLY [130, 35]. The KLMC code was employed to search for the global and local minima clusters of Ti_N ($N = 2 - 32, 57, 80, 89$). The plane-wave pseudopotential code FHI-aims is capable of simulating electronic relaxation to ground states properties of metals, insulators or semiconductors. This code was used to re-optimize the clusters obtained from KLMC on a DFT level of theory.

The molecular dynamics simulation code, DL_POLY was employed to gain an understanding of the structural evolution, diffusivity and melting behaviour of stable Ti_N ($N = 7, 13, 17, 32, 57, 80, 89$). This approach can facilitate simulations of macromolecules, polymers, ionic systems, solutions and other molecular systems. It is suitable for simulations of up to 30,000 atoms. The CASTEP code was employed to calculate the charge density difference for $Ti_{12}M$ ($M = Pt, Pd, Ir, Ni$), whereas DMol3 was used to calculate the iso-surfaces of the HOMO-LUMO for $Ti_{12}M$ ($M = Pt, Pd, Ir, Ni$).

3.1. First-principles method

First-principles modelling refers to the application of quantum mechanics to determine the structure and properties of materials, this by considering the interactions of electrons and nuclei of a system. After the Schrödinger equation (SE) was formulated in 1929, Dirac studied the quantum mechanics of many-electron systems [153]. According to Dirac, the fundamental physical laws required for the mathematical theory of a large part of physics and the entire chemistry are known, however, the difficulty is only that the exact application of these laws leads to equations much too complicated to be solvable. As such, it is difficult to solve SE analytically. Thus, numerical approaches to obtaining approximate solutions for the electronic structure have become difficult to evaluate in the field of chemistry and materials science. These computational efforts received significant attention in 1964 and 1965 when Hohenberg and Kohn [39], and Kohn and Sham [40], reformulated the SE, which includes all the $3N$ spatial coordinates of N interacting electrons, into DFT, a theory based on the electron density, a function of only three spatial coordinates. The Kohn–Sham (KS) equations altered the intractable complexity of the detailed many-body interactions into a single-particle effective potential that is computationally controllable through the exchange-correlation functional. Although the ‘divine functional’ [154] that would make this reformulation exact has not been discovered and likely might not be found, the approximate functionals have proven to be extremely successful for describing many properties of materials. Materials science have therefore become dependent on DFT methods. Thus, DFT calculations have become a common, imperative constituent of many materials research studies.

3.2. Density functional theory

This section presents only a brief account of DFT due to the very brief application of it in this work. DFT is a quantum mechanical method used to investigate the ground state energies of many-body systems [155, 156, 157]. The method was first formulated by Hohenberg and Kohn [39] who provided the groundwork for accurate calculations. The DFT calculations add an additional step to each major phase unlike the Hartree-Fock (H-F) method [158], which was developed and applied to small molecular systems. This step is a numerical integration of various derivatives of the functional. The first Hohenberg-Kohn (H-K) [39] theorem illustrate that the ground state properties of a many-body system are uniquely determined by an electron density that depends on three spartial coordinates which write as,

$$E = E[\rho], \quad (3-1)$$

which is created from one-electron wave functions. The second H-K theorem states the energy functional for the system and proves that the ground state electron density minimises this energy functional within the framework of the Kohn-Sham DFT [40].

The idea of electron density as the essential entity of a quantum mechanical theory of matter was initiated in the era of quantum mechanics in the 1920s, specifically by Thomas [159] and Fermi [160]. In 1951, Slater [158] used ideas from the electron gas with the purpose to abridge Hartree-

Fock theory to a point where electronic structure calculations on solid became achievable. However, the work has contributed enormously to the advance of electronic structure calculations. In solid state structures, molecules and atoms, the electron density is a scalar function defined at each point r in real space,

$$\rho = \rho(\mathbf{r}). \quad (3-2)$$

The total energy and electron density depend on the nature and arrangements of the atomic nuclei, consequently, one can write

$$E = E[\rho(r), \{R_\alpha\}], \quad (3-3)$$

where the set $\{R_\alpha\}$ signifies the positions of all atoms, α , in the system under consideration. Thus, the above equation is the key to the atomic-scale knowledge and understanding of the electronic, structural and dynamic properties of the material. For evaluating expressions using the equation (3-3), one can calculate the equilibrium structure of solid, the reconstruction of surfaces and the equilibrium geometry of molecules adsorbed on surfaces. Additionally, the derivative of the total energy (3-3) with respect to the nuclear position of an atom provides the force acting on that atom.

In this method (DFT) [39], the total energy (3-1) is disintegrated into three contributions, coulomb energy and kinetic energy due to classical electrostatic interactions among all charged particles in the system and a term called the exchange-correlation energy that captures all many-body interactions written as,

$$E = T_0 + U + E_{xc}, \quad (3-4)$$

where U is the Coulomb energy and it is purely classical consisting of electrostatic energy arising from the Coulomb attraction between electrons and nuclei, the repulsion between all electronic charges and the repulsion between nuclei in which we write,

$$U = U_{en} + U_{ee} + U_{nn} , \quad (3-5)$$

with

$$U_{en} = -e^2 \sum_{\alpha} Z_{\alpha} \int \frac{\rho(r)}{|r - R_{\alpha}|} dr , \quad (3-6)$$

$$U_{en} = -e^2 \sum_{\alpha} Z_{\alpha} \int \frac{\rho(r)}{|r - R_{\alpha}|} dr , \quad (3-7)$$

$$U_{ee} = e^2 \iint \frac{\rho(r)\rho(r')}{|r - r'|} dr dr' , \quad (3-8)$$

$$U_{nn} = e^2 \sum_{\alpha\alpha'} \frac{Z_{\alpha}Z_{\alpha'}}{|R_{\alpha} - R_{\alpha'}|} , \quad (3-9)$$

where e is the elementary charge of a proton and Z_{α} is the atomic number of an atom α . The summations extend over all atoms and integrations over all space. After the atomic number and electron density and positions of all atoms are known, the above expressions (3-7) to (3-8) can be assessed by using the technique of classical electrostatics.

In DFT, the "real" electrons of a system are replaced by "effective" electrons with the same charge, mass and density distribution. However, effective electrons move as independent particles in an effective potential, whereas the motion of a "real" electron is correlated with those of all other electrons. The kinetic energy term T_0 is the sum of the kinetic energies of all effective electrons

with independent motion as particles. Frequently, one does not openly make difference between real and effective electrons.

If each effective electron is defined by a single-particle wave function, ψ_i , then the kinetic energy of all effective electrons in the system is specified as

$$T_0 = \sum n_i \int \psi_i^*(r) \left[-\frac{\hbar^2}{2m} \nabla^2 \right] \psi_i(r) dr , \quad (3-10)$$

where the above expression is the sum of the expectation values of one-particle kinetic energies; n_i signifies the number of electrons in state i . By construction, dynamical correlations between the electrons are excluded from T_0 .

The exchange-correlation energy [39], E_{xc} , the term in Eq (3-4) includes all remaining complicated electron contributions to the total energy. The Hohenberg-Kohn-Sham theorem [39], which is a central part of density functional theory, states that the total energy is at its minimum value for the ground state density and that the total energy is stationary with respect to first-order variations of the electron density, i.e.

$$\left. \frac{\partial E[\rho]}{\partial \rho} \right|_{\rho=\rho_0} = 0. \quad (3-11)$$

In conjunction with the kinetic energy, we have introduced one-particle wave-functions $\psi_i(r)$, which generate the electron density

$$\rho(r) = \sum_i n_i |\psi_i(r)|^2 , \quad (3-12)$$

where n_i signifies the occupation number of the eigenstate i , which is signified by the one-particle wave function ψ_i . By construction, $\rho(r)$ in the above equation is the exact many-body electron density.

The objective of the following step is the derivation of equations that can be used for practical density functional predictions. The variation condition (3-11) can be used to derive the condition for the one-particle wave function that lead to the ground state density. The substitution of Eq (3-12) in expression (3-11) and varies the total energy with respect to each wave function. This method results in the following equations:

$$\left[-\frac{\hbar^2}{2m} \nabla^2 + V_{eff}(r) \right] \psi_i(r) = \varepsilon_i \psi_i(r), \quad (3-13)$$

with

$$V_{eff}(r) = V_C(r) + \mu_{xc}[\rho(r)], \quad (3-14)$$

which are the Kohn-Sham equations. The electron density corresponding to this wave-function is the ground state density which minimizes the total energy. As a consequence of the separation of the total energy (3-5), the Hamiltonian operator in the Kohn-Sham equations (3-13 and 3-14) has three terms, one for kinetic energy, the second for Coulomb potential operator, and the third for the exchange-correlation potential. The kinetic energy term is the standard second-order differential operator of one-particle Schrödinger equations and its construction does not entail detailed knowledge of a system. In contrast, the exchange-correlation potential operator, μ_{xc} and the Coulomb potential operator, $V_C(r)$ relies on the specific electron distribution in the system under consideration.

The electrostatic potential $V_C(r)$ at point r is created from the electric charges of all nuclei and electrons in the system, and it can be assessed directly in the space, in which we write,

$$V_C(r) = -e^2 \sum_{\alpha} \frac{Z_{\alpha}}{|r - R_{\alpha}|} + e^2 \int \frac{\rho(r')}{|r - r'|} dr', \quad (3-15)$$

whereas in the condensed system it is more suitable to use Poisson's equation which writes as,

$$\nabla^2 V_C(r) = -4\pi e^2 q(r), \quad (3-16)$$

which is used to calculate the electrostatic potential. Moreover, $q(r)$ signifies both the electronic charge distribution $\rho(r)$ and the positive point charges of the nuclei at the position R_{α} . The relation of the exchange-correlation potential to the exchange-correlation energy writes as,

$$\mu_{xc}(r) = \frac{\partial E_{xc}[\rho(r)]}{\partial \rho(r)}, \quad (3-17)$$

and is formally exact because it does not contain any approximations to the complete many-body interactions.

Consequently, from the above discussions, the Kohn-Sham total energy functional can be written as,

$$E = \frac{1}{2} \sum_{occ} \varepsilon_i + U_{nn} - \frac{e^2}{2} \iint \frac{\rho(r)\rho(r')}{|r - r'|} dr dr' + E_{xc}[\rho(r)] - \int \rho(r) \mu_{xc} dr. \quad (3-18)$$

In practice, the exchange-correlation energy or the exchange-correlation potential is unknown and requires the use of approximations, which will be discussed in the next section.

3.3. Approximation methods

In this section, we give an overview of the exchange-correlation functionals and their applications. The DFT method is improved upon Hartree-Fock by counting an approximate treatment of the correlated movement of electrons. Electron correlation treatment is much cheaper than in correlated wavefunction methods.

3.3.1. Local density approximation

Local density approximations (LDA) [161] are a class of approximations to the exchange-correlation (XC) energy functional in the DFT that is determined by the electronic density at each point in space. It is the simplest approximation that one can make to envisage that at every point in space we can use the value of the density that the uniform electron gas would have at that point, and allow it to vary from point to point. The functional depends only on the density at a given point. In more detail, the LDA is written as:

$$E_{xc}^{LDA}[\rho] = \int \rho(r) \varepsilon_{xc}(\rho(r)) dr, \quad (3-19)$$

where

$$\varepsilon_{xc}(\rho(r)) = \varepsilon_x(\rho(r)) + \varepsilon_c(\rho(r)), \quad (3-$$

20)

and

$$\varepsilon_x(\rho(r)) = -\frac{3}{4} \left(\frac{3\rho(r)}{\pi} \right)^{1/3}, \quad (3-21)$$

is the Dirac-Slater Exchange Energy of the electron gas. The Coulomb correlation piece is attained from interpolations of Monte Carlo data by Ceperly and Alder (1980) [162]. The typical LDA approximation is the SWVN implementation that suggests Slater Exchange plus Coulomb Correlation found by Vosko *et al.* [161]. Perdew and Wang [163] made a more accurate implementation. This approximation was found to reproduce the ground state properties of many systems with astonishing great accuracy. Particularly, the bulk properties of d-shell transition metals and others are well defined within LDA.

LDA is useful in the construction of a more sophisticated approximation to the exchange-correlation energy, such as generalized gradient approximation. As such, comparison with the experiment shows that the LDA predicts densities, which are mostly too high (bond distances are too short) while the GGA improves the agreement with the experiment.

3.3.2. Generalized gradient approximation

Generalised gradient approximation (GGA) functional [164] evolved in two different forms. The first one is parameter-free, where the new parameters are determined from known expansion coefficients and other exact theoretical conditions. The second is empirical with parameters determined from fits to experimental data or accurately calculated atomic and molecular properties. The GGA is known to be semi-local approximations which does not use the local density $\rho(r)$ value but its gradient $\nabla(r)$. This approximation tend to improve the total energies [165], atomisation energies [166], energy barriers and also the difference in structural energies [167] in comparison with LSD. GGA's expand and soften bonds [168], an effect that sometimes corrects [169] and sometimes overcorrects [170] the LSD prediction. Typically, GGA's favour density inhomogeneity more than LSD does. GGA takes the form:

$$E_{xc}^{GGA} = \int (\rho(r), \nabla \rho(r)) dr, \quad (3-22)$$

The spin-independent form is considered in GGA but practically functional is more generally formulated in terms of spin densities ($\rho_{\uparrow}, \rho_{\downarrow}$) and their corresponding gradients of ($\nabla \rho_{\uparrow}, \nabla \rho_{\downarrow}$). There are several GGA based functionals that is the PBE [164], PBEsol [171], RPBE [172], BLYP [173] and AM05 [174]. The PBE functional is designed to have a smoother effective potential than PW91, which is prone to numerical instabilities [175]. PBEsol functional is a solution to PBE which has been designed specifically to improve the description of exchange in solids, resulting in better structures and energetics for bulk solids and their surfaces. The RPBE functional is a revised form of the PBE functional designed to improve the description of metallic surfaces.

The AM05 functional gives the best performance for applications of catalysis and give similar results with PBEsol for solids. Most GGA functional used in chemistry applications is Becke, Lee, Parr and Yang (BLYP), Becke three-parameter hybrid functional combined with LYP functional (B3LYP) and there are empirical [176]. The BLYP correlation employs the density's Laplacian (second derivative) and thus formally belongs to the third rung of Jacob's ladder, but it is commonly classified as a GGA. Other known GGA-based functionals are meta-GGA [177], hyper-GGA and generalized random phase approximation. Meta-GGA is the third Laplacian derivative of the density and kinetic energy and the degree of freedom added. Furthermore, hyper-GGA is normally known to belong to the fourth rung of Jacobs ladder. This functional involves the contribution of exact exchange with the GGA functional. The hyper-GGA functional is mostly employed in the B3LYP functional. However, it does not meet the uniform density limit and the three parameters are chosen to empirically optimise the performance of the functional for large molecule properties such as bond length, formation energy etc.

3.4. Plane-wave pseudopotential method

In the study of solids, the Kohn-Sham [40] equations are easily dealt with in reciprocal space, where the differential eigenvalue problem is mapped onto an algebraic linear system. The complicated many-body problem of strongly correlated electrons and nuclei has been mapped within the framework of the Born –Oppenheimer approximation [178] and the density functional theory to a single particle problem moving in an effective external potential for a set of fixed nuclei. The plane-wave pseudopotential method for the DFT is a technique used to calculate the variation self-consistent solution with accuracy. This technique has been advanced and perfected to reliably predict the static and dynamic properties of molecules and crystalline solids [179].

The practical numerical scheme to solve the resulting single-particle Kohn-Sham equation for extended systems like crystalline solids or liquids is developed. And most common approach for solving this problem is to expand the wave function of the single-particle eigenstates of the Kohn-Sham equations into a set of basis functions. Then, the Schrodinger equation transforms into an algebraic equation for the expansion coefficient solved by the numerical perfected method.

The plane-wave pseudopotential method deals with weak pseudopotentials and performs complete geometry optimization, more especially the relaxation of internal parameters. The Plane-wave pseudopotential method is also able to simulate the electronic ground states for metals, insulators and semiconductors.

3.4.1. Plane-wave basis sets

Plane-wave basis sets are usually coupled with an “effective core potential” or pseudopotential in practical performance so that they (plane-wave) are only used for valence charge density. The

basis sets are abundantly used in the calculations involving boundary conditions. In addition to the localized basis sets, plane-wave basis sets are also used in quantum-chemical calculations and are more efficient than the Gaussian-type basis because is guaranteed to converge to the target wavefunction, while there is no such in the Gaussian-type.

Since there is an infinite number of electrons, a wave function is needed for each electron. However, the basis set required for the expansion of each wave function is also infinite. Bloch's theorem [180], which starts with a periodicity of the crystal lattice, can handle this problem. Bloch's theorem defines the crystal momentum k as a good quantum number and also gives the boundary condition for the single-particle wave function, φ_k . Bloch's theorem is often stated in an alternative form: the equation

$$\varphi_k(r + R_L) = e^{ik \cdot R_L} \varphi_k(r), \quad (3-23)$$

is equivalent to the statement that all eigenfunctions φ_{k_i} of a single-particle Schrodinger equation with periodic potential can be written as a periodic function u_{k_i} modulated by a plane wave vector k [181]. R_L is a direct lattice vector.

$$\varphi_{k_j}(r) = e^{ikr} u_{k_j}(r). \quad (3-24)$$

Due to its periodicity can be expanded as a set of plane wave basis

$$u_{k_j}(r) = \sum_G C_{j,G} e^{iG \cdot r}, \quad (3-25)$$

where G and j are reciprocal lattice vectors. The functions are periodic and can be expanded in a set of plane waves. Thus the electronic wavefunction with the exponential prefactor is

$$\varphi_{kj}(\mathbf{r}) = \sum_G C_{j,k+G} e^{i(\mathbf{K}+\mathbf{G})\mathbf{r}}, \quad (3-26)$$

where $C_{j,K+G}$ the coefficient of the periodic plane waves. As it is the case with an infinite number of basis functions is needed to accurately recreate the real wave function. The number of wavefunctions used is controlled by the largest wave vector in the expansion in (3-36). This is equivalent to imposing a cut-off on the kinetic energy as the kinetic energy of an electron with wavevector \mathbf{k} is given by

$$E_K = \frac{\hbar^2 |\mathbf{K} + \mathbf{G}|^2}{2m}. \quad (3-27)$$

Thus only plane wave that obeys

$$E_K = \frac{\hbar^2 |\mathbf{K} + \mathbf{G}|^2}{2m} < E_{cut}, \quad (3-28)$$

are included in the basis. The plane wave set at finite cutoff energy will lead to an error in the computed total energy; hence the energy must be increased until the calculated energy has converged. It is highly advisable and wise to use much denser \mathbf{k} points to reduce errors and ensure convergence. Before making use of the plane wave expansion of the wavefunction we write the Kohn-Sham equation of density functional theory in the following way [179]:

$$\sum \left[\frac{\hbar^2}{2m} |\mathbf{K} + \mathbf{G}|^2 \delta_{GG} + V_{eff}(\mathbf{r}) \right] C_{j,K+G} = \varepsilon_j C_{j,K+G}, \quad (3-29)$$

where,

$$V_{eff}(\mathbf{r}) = V_{ext}(\mathbf{r}) + V_H[n(\mathbf{r})] + V_{XC}[n(\mathbf{r})] \quad (3-30)$$

and $V_{ext}(r)$, $V_H[n(r)]$, and $V_{XC}[n(r)]$ are Fourier transforms of the external potential of the nuclei, Hartree and exchange-correlation potentials respectively.

3.5. Pseudopotential method

The introduction of pseudopotential approximation is an attempt to eradicate the unsolvable complicated effects of the core electrons in motion and their nuclear with an effective potential, or pseudopotential [182]. Thus the Schrodinger equation now contains a modified effective potential term instead of the coulombic potential term for core electrons. In the pseudopotential approach, only valence electrons are dealt with explicitly [183]. The schematic Fig. 3.1 above illustrates the ionic potential (Z/r), the valence wave function (φ_v), the corresponding pseudopotential (V_{pseudo}), and pseudo-wave function (φ_{pseudo}) [179]. Due to strong ionic potential in the core region, the valence wavefunctions oscillate rapidly in the region occupied by the core electrons.

Hence, the orthogonality between the core electrons and valence electrons is maintained. The pseudopotential is constructed such that the pseudo wave function has no radial nodes within the core region and that the pseudo wave functions and potential agree with the *true* wave function and potential outside some cut-off radius(r_{cut}). The pseudopotential also must preserve the atomic properties of the element, including phase shifts on scattering across the core.

In general, the pseudopotential must be non-local, i.e. it must have projectors for the different angular momentum states. The general form of the pseudopotential is

$$V_{ion} = \sum |lm\rangle V_i \langle lm| \quad , \quad (3-31)$$

where $|lm\rangle$ are spherical harmonics, and V_i is the pseudopotential for angular momentum (l) [181]. The majority of the pseudopotentials used in the electronic structure are generated from all-electron atomic calculations.

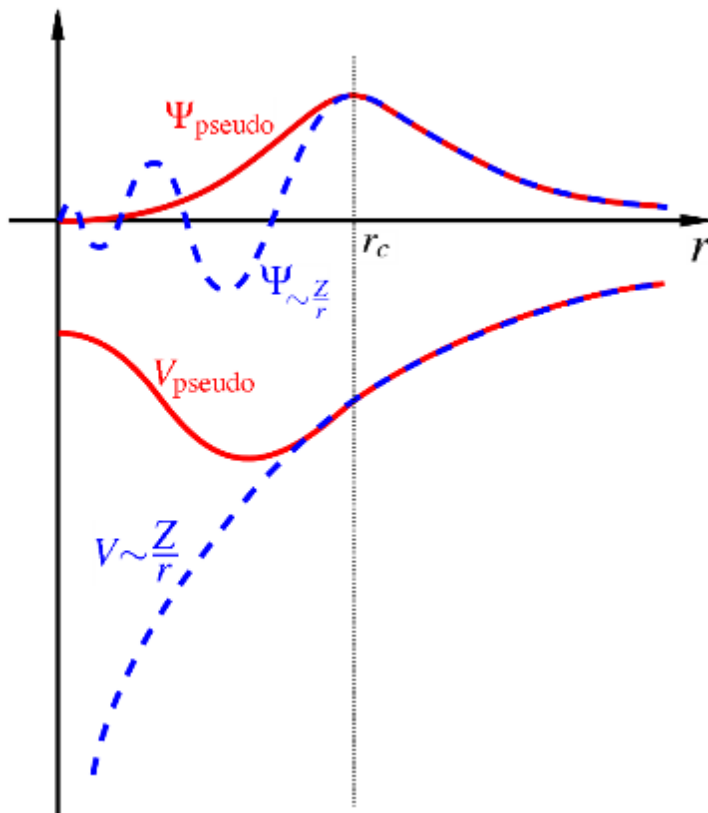


Figure 3.1 Comparison of a wave function in the Coulomb potential of the nucleus (blue) to the one in the pseudopotential (red). The real and the pseudo-wave function and potentials match above a certain Cut-off [179].

Norm conserving pseudopotential [184] is the example of non-local pseudopotential and uses a different potential for each angular momentum components of the wave function. However, pseudopotential that uses the same potentials for all angular momentum components of the wave function is called local pseudopotential. Between the two pseudo-potential, local pseudopotential is computationally efficient than non-local pseudopotential.

3.6. Projector augmented-wave

The projector augmented wave (PAW) [185] technique was firstly introduced in 1994 by Blöchl [180] and it is used in ab initio electronic structure calculations which allows DFT [39] calculations to be conducted with greater computational efficiency. This method is dependent on the transformation between the all-electron (AE), Kohn-Sham wave functions (φ_n^{PS}), (n signifies the band index) and the smooth pseudo-wave (PS) functions with frozen core states of the atoms:

$$|\varphi_n^{AE}\rangle = |\varphi_n^{PS}\rangle + \sum_i |\varphi_n^{PS}\rangle - |\varphi_i^{AE}\rangle \langle P_i^{PS} | \varphi_n^{PS}\rangle, \quad (3-32)$$

φ_n^{PS} (AE) is the variation quantities and are expanded in plane wave and AE-partial wave φ_i^{AE} are a solution of the spherical relativistic equation for non-spin polarized atoms.

In the regions between the PAW spheres surrounding the atoms, the φ_n^{PS} are the same as the AE wave functions φ_n^{AE} . However, inside the spheres the φ_n^{PS} are only a bad approximation to the exact wave functions, they are employed only as a computational instrument. The projector functions $P_i P_i^{PS}$ are constrained to be dual to the partial waves and constructed by a two-step procedure: First, intermediate functions χ_i are computed through,

$$|\chi_i\rangle = \langle \chi_i + \frac{1}{2}\nabla - V_{eff}^{PS} | \varphi_i^{PS}\rangle, \quad (3-33)$$

where, V_{eff}^{PS} is the spherical component of the effective pseudopotential, which can be selected arbitrarily inside the radius r_c , however, must match V_{eff}^{PS} for $r \geq r_c$. The projector functions are linear combinations of the χ_i [186].

$$\langle P_i^{PS}\rangle = \sum_j B_{ji}^{-1} |\chi_j\rangle, \quad (3-34)$$

where,

$$B_{ji} = \langle \phi_i^{PS} | \chi_i \rangle \quad (3-35)$$

such that the ϕ_i^{PS} and P_i^{PS} are dual $\langle P_i^{PS} | \phi_i^{PS} \rangle = \delta_{ij}$, and $\langle r | P_i^{PS} \rangle = 0$ for $r > r_c$.

The PAW method has been described for all-electron (AE) methods, this is constructed to correctly describe the model features of the valence orbital which are orthogonalised to the core wave functions. The exact all-electron wave function and charge density exhibiting the full nodal character are reassembled by subtraction of the pseudo-on-site term and the addition of the exact on-site term. However, both methods are expanded on a radial support grid. An analogous decomposition with no cross-terms between on-site and plane wave terms holds for all expectation values of quantum mechanical operators and particular for the total energy of the electrons i.e.,

$$E = E^{PS} + E^{PS,1} + E^{AE,1} \quad (3-36)$$

where each of the three terms consists of a kinetic, Hartree and exchange-correlation contribution.

3.7. Molecular Dynamics

Molecular dynamics (MD) is a computer simulation of the physical movements of atoms and molecules. It is the most natural method of performing equilibrium statistical-mechanical calculations via simulation [187]. The atoms and molecules are allowed to interact for a period of time, giving a view of the motion of the atoms. The trajectories of molecules and atoms are determined by numerically solving Newton's equations of motion for a system of interacting particles, where forces between the particles and potential energy are defined by molecular mechanics force fields. In MD, the position, velocities and accelerations of N particles at time t in the system is given by three-dimensional vectors $\mathbf{r}_i(t)$, $\mathbf{v}_i(t)$, and $\mathbf{a}_i(t)$ respectively. Since $v =$

dr/dt and $a = dv/dt$, Newton's equation can be written as a system of $6N$ first-order ordinary differential equations,

$$\dot{\mathbf{r}}_i \equiv \frac{d}{dt} \mathbf{r}_i = \mathbf{v}_i \quad (3-37)$$

$$\dot{\mathbf{v}}_i \equiv \frac{d}{dt} \mathbf{v}_i = \mathbf{a}_i = \frac{\mathbf{F}_i}{m_i}, \quad (3-38)$$

where, m_i signifies the mass of the particle i , F_i is the force acting on the particle i , and a_i can be a function of all particle positions and velocities, and it may be explicitly time-dependent which can be written as;

$$a_i = \frac{d^2 r_i}{dt^2}. \quad (3-39)$$

Amongst the variety of numerical algorithms for solving systems of first-order ordinary differential equations [188, 189, 190], the velocity verlet algorithm is one of the most popular for MD simulations. To improve the positions, velocities and accelerations that describe the dynamical behaviour of the particle, Newton's equation can be integrated using velocity verlet algorithm [191] such that,

$$\mathbf{r}(t + \Delta t) = \mathbf{r}(t) + \Delta t \mathbf{v}(t) + \frac{1}{2} (\Delta t)^2 \mathbf{a}(t) + O((\Delta t)^3), \quad (3-40)$$

$$\mathbf{a}(t + \Delta t) = \mathbf{a}(\mathbf{r}_1(t + \Delta t), \dots, \mathbf{r}_N(t + \Delta t); \mathbf{v}_1(t + \Delta t), \dots, \mathbf{v}_N(t + \Delta t); t + \Delta t), \quad (3-41)$$

$$\mathbf{v}(t + \Delta t) = \mathbf{v}(t) + \frac{1}{2} \Delta t [\mathbf{a}(t) + \mathbf{a}(t + \Delta t)] + O((\Delta t)^3). \quad (3-42)$$

Therefore, MD is a deterministic technique given an initial set of positions and velocities, the subsequent time evolution is in principle [192] completely determined. Some work on the new molecular dynamics method was studied in the canonical ensemble [193].

3.7.1. Energy

The internal energy is easily obtained from a simulation as the ensemble average of the energies of the states that are examined during the simulation:

$$U = \langle E \rangle = \frac{1}{M} \sum_{i=1}^M E_i. \quad (3-43)$$

The average potential energy V is obtained by averaging its instantaneous value, which is obtained at the same time as the force computation is made. Thus, the potential energy is given by:

$$V(t) = \sum_i \sum_{j \geq 1} \Phi(|r_i(t) - r_j(t)|). \quad (3-44)$$

The kinetic energy is given by:

$$K(t) = \frac{1}{2} \sum_i m_i [\bar{v}_i(t)]^2, \quad (3-45)$$

where m_i is the mass of atom i and \bar{v}_i is the velocity of atom i . The total energy of the system can be represented as the sum of the kinetic energy and the potential energy and the total energy of the system with a given set of positions and velocities is represented by:

$$E_{tot} = K(t) + V(t). \quad (3-46)$$

3.7.2. Temperature

The temperature depends on a certain kind of ensemble for a particular simulation. In a canonical ensemble, the total temperature is constant whereas in the microcanonical ensemble the temperature is fluctuating [194]. The temperature is directly related to the kinetic energy of the system as follows:

$$K = \sum_i^N \frac{|\dot{P}_i|^2}{2m_i} = \frac{K_B T}{2} (3N - N_c), \quad (3-47)$$

where, P_i is the total of particle i , m_i is its mass and N_c is the number of constraints on the system. Each degree of freedom contributes $k_B T/2$ this is according to the equipartition of energy. If there are N particles, each with three degrees of freedom, then the kinetic energy should be equal to $3Nk_B T/2$. Total linear momentum of the system is often constrained to a value of zero in a molecular dynamics simulation, which has the effect of removing three degrees of freedom from the system and N_c would be equal to 3.

3.7.3. Pressure

Calculation of pressure is usually in a computer simulation via the virial theorem of Clausius [195]. The virial is defined as the expectation value of the sum of the products of the coordinates of the particles and the forces acting on them. Usually, this is written as

$$W = \sum x_i \dot{p}_{x_i}, \quad (3-48)$$

where x_i is a coordinate (e.g. the x or y coordinate of an atom) and \dot{p}_{x_i} is the first derivative of the momentum along that coordinate (\dot{p}_i is the force, by Newton's second law). The virial theorem states that the virial is equal to $-3Nk_B T$ [194]. In an ideal gas, the only forces are those due to interactions between the gas and the container and it can be shown that the virial in this case is equal to $-3PV$. This result can be obtained directly from

$$PV = Nk_B T. \quad (3-49)$$

Forces between the particles in a real gas or liquid affect the virial, and thence the pressure. The total virial for a real system equals the sum of an ideal gas part ($-3PV$) and a contribution due to interactions between the particles. The result obtained is:

$$W = -3PV + \sum_{i=1}^N \sum_{j=i+1}^N r_{ij} \frac{dv(r_{ij})}{dr_{ij}} = -3Nk_B T. \quad (3-50)$$

If $d(\mathbf{r}_{ij})/d\mathbf{r}_{ij}$ is written as f_{ij} the force acting between i and j then pressure can be written as follows:

$$P = \frac{1}{V} \left[Nk_B T - \frac{1}{3k_B T} \sum_{j=i+1}^N r_{ij} f_{ij} \right]. \quad (3-51)$$

The forces are calculated as part of a molecular dynamics simulation, and so little additional effort is required to calculate the virial and thus the pressure. In the NPT ensemble, the total pressure of the system is constant while in the NVT ensemble the pressure is fluctuating throughout the simulation.

3.7.4. Ensembles

Integrating Newton's equations [196] of motion allows you to explore the constant energy surface of a system. However, most natural phenomena occur under conditions where the system is exposed to external pressure and/or exchanges heat with the environment. Under these conditions, the total energy of the system is no longer conserved and extended forms of MD are required. Several methods are available for controlling temperature. Depending on which state variables - the energy, E , enthalpy, H (i.e., $E + PV$), number of particles, N , pressure, P , stress, S , temperature, T , and volume, V - are kept fixed, different statistical ensembles can be generated. A variety of structural, energetic, and dynamic properties can then be calculated from the averages or the fluctuations of these quantities over the ensemble generated.

The three most common ensembles that are often used in MD simulations are NVT, NVE [197] and NPT ensembles [198]. NVT ensemble is also known as a canonical ensemble where temperature and volume are kept constant. NVT ensemble in statistical mechanics is a statistical ensemble representing a probability distribution of microscopic states of the system. For a system taking only discrete values of energy, the probability distribution is characterized by the probability of finding

the system in a particular microscopic state with energy level, conditioned on the prior knowledge that the total energy of the system and reservoir combined remains constant.

NVE ensemble is also known as a microcanonical ensemble where energy and volume are kept constant. NVE ensemble is obtained by solving the standard Newton equation without any temperature and pressure control. Energy is conserved when this (adiabatic) ensemble is generated. However, because of rounding and truncation errors during the integration process, there is always a slight fluctuation, or drift, in energy [197].

NPT ensemble is also known as an isothermal-isobaric ensemble. This ensemble plays an important role in chemistry as chemical reactions are usually carried out under constant pressure conditions. In the NPT ensemble, pressure and temperature are kept constant. The NPT ensemble is used for the comparison of MD simulations with experiments. The temperature in the NPT ensemble is controlled using the Langevin method [199]. The partition function can be written as the weighted sum of the partition function of the canonical ensemble, $Z(N, V, T)$.

$$\rho(N, P, T) = \int Z(N, V, T) e^{(-\beta p V) C dV}, \quad (3-52)$$

where,

$$\beta = \frac{1}{k_B T}, \quad (3-53)$$

k_B is the Boltzmann constant and V is the volume of the system.

3.7.4.1. Microcanonical ensemble

In the microcanonical ensemble [194] or NVE, the system is isolated from changes in moles (N), volume (V) and energy (E). It corresponds to an adiabatic process with no heat exchange. A

microcanonical molecular dynamics trajectory may be seen as an exchange of potential and kinetic energy, with total energy being conserved. For a system of N particles with coordinates X and velocities V , the following pair of first-order differential equations may be written in Newton's notation as [200];

$$F(X) = -\nabla U(X) = M(V)\dot{V}, \quad (3-54)$$

$$\dot{X}(t) = V(t), \quad (3-55)$$

where, the potential energy function $U(X)$ of the system is a function of the particle coordinates X .

3.7.4.2. Grand canonical ensemble

The isothermal-isobaric ensemble is a statistical mechanical ensemble that maintains constant temperature T and constant pressure P applied. It is also called the NPT-ensemble, where the number of particles is also kept as a constant [201, 202]. Notice that into the grand canonical (μVT) ensemble, the probability distribution function must also include N as its variable, because the number of particles can (in principle) be any non-negative integer at thermal equilibrium. The NPT ensemble is also useful for measuring the equation of state of model systems whose virial expansion for pressure cannot be evaluated, or systems near first-order phase transitions. Following the same approach as in the (NPT) ensemble, we obtain the equilibrium distribution of the grand canonical (μVT) [201] ensemble as the following:

$$\rho(\{q_i\}\{p_i\}N) = \frac{1}{Z} e^{-\beta(H(\{q_i\}\{p_i\}) - \mu N)}, \quad (3-56)$$

where,

$$Z = \sum_{N=0}^{\infty} \int \prod_{i=1}^{3N} dq_i dp_i e^{-\beta(H(\{q_i\}\{p_i\}) - \mu N)} \quad (3-57)$$

$$= \sum_{N=0}^{\infty} e^{\beta\mu N} Z(N, V, T), \quad (3-58)$$

ρ is grand canonical distribution and $Z(N, V, T)$ is the normalization factor in the canonical ensemble for N particles.

3.6.7.3. Canonical ensemble

In statistical mechanics, a canonical ensemble [194] or NVT, the system is isolated from changes in moles (N), volume (V) and temperature (T). It is a statistical ensemble that is used to represent the possible states of a mechanical system that is in thermal equilibrium with a heat bath. The system is said to be closed in the sense that the system can exchange energy with a heat bath so that various possible states of the system can differ in total energy. The system's composition, volume, and shape are kept the same in all possible states of the system [200]. In simple terms, the canonical ensemble assigns a probability P to each distinct microstate given by the following exponential:

$$P = e^{-\frac{A-E}{kT}}, \quad (3-59)$$

where, P = probability, A = free energy (Helmholtz free energy), E = total energy of the microstate, k = Boltzmann's constant and T = temperature.

3.8. Interatomic potentials

Interatomic potentials are used for calculating the potential energy of a system of atoms with given positions in space [203]. Interatomic potentials are widely used as the physical basis of molecular dynamics and molecular mechanics simulations in materials physics or science, chemistry and molecular physics, sometimes in connection with such effects as thermal expansion, cohesion and

elastic properties of materials [181]. There are various types of potentials, namely: pair potentials, many-body potentials, Buckingham potential, embedded atom method potentials and repulsive potentials for short-range interactions.

3.8.1. Embedded atom method

The first attempt to describe the metallic bond starting from the quantum mechanical considerations was the embedded atom method (EAM) [204, 205] later extended to account for directional bonding in the modified embedded atom method (MEAM). This method defines the energy E_i of an atom i in a lattice as the sum of the energy due to electrostatic interactions with its neighbours and the energy needed to embed this atom in the local electron density as generated by the other atoms in the system. This embedding energy depends only on the nature of atom i and can hence be derived from material constants of pure i . The energy of an atomic configuration x is then calculated as the sum of the energies of atoms i within x

$$E_x = \sum_i E_i = \sum_i \left[F_i(\rho_{h,i}) + \frac{1}{2} \sum_j \phi_{ij}(R_{ij}) \right], \quad (3-60)$$

where F_i is the embedding energy function atom i , $\rho_{h,i}$ is the host electron density around atom i due to the other atoms, and ϕ_{ij} is the electrostatic interaction energy between atoms i and j separated by the distance R_{ij} . This separation into pairwise interaction energy and ion-linear embedding energy can be derived starting from the expression for the cohesive energy of a solid in the density functional theory [206, 207] and by introducing two basic assumptions. The assumption is that the embedded energy can be written as a function of the local electron density and its lower derivatives. Secondly, the electron density is approximated as a linear superposition

of the density of the individual atoms. The first assumption is justified by the studies of the response theory of the nearly uniform electron gas, while the second is reasonable provided that covalent bonding effects in the metal are negligible. This naturally limits the range of applicability to simple metals and late early transition metals. The host electron density $\rho_{h,i}$ is obtained by summing the contributions of all neighbours j of atom i

$$\rho_{h,i} = \sum_j \rho_j^a(R_{ij}). \quad (3-61)$$

Only the distance between atom i and the other atoms are taken into account and angular characteristics of directional bonds are thus neglect.

Table 3.1: Embedded atom method (EAM) potentials parameters for Ti

	Ref [208]	EAM
r_0 (Å)	2.8791	1.7621
β	1.4163	3.2860
A (eV/Å)	1.6430	2.0059

3.8.2. Buckingham potentials

The Buckingham potential is the formula proposed by Buckingham. [209] which describe the Pauli repulsion energy and van der Waals energy $\phi_{ij}(r)$ for the interaction of two atoms that are not directly bonded as a function of the interatomic distance r . It is used to model two body non-bonded interactions in ionic solids. The general form of Buckingham potential is given by

$$\phi_{ij}(r) = A_{ij} \exp\left(\frac{-r_{ij}}{\rho_{ij}}\right) - \frac{C_{ij}}{r_{ij}^6}, \quad (3-62)$$

where A_{ij} is the size of the ions, ρ_{ij} is the hardness and C_{ij} is the dispersion parameter. The repulsive interaction between the ions is represented by the first term while the second term is the van der Waals attractive interaction of the ions.

Table 3.2: Buckingham potentials parameters for Ti

A (eV/Å)	ρ	r_0 (Å)	C (eV)
13477.9114	0.1723	1.7621	0.0000

3.8.3. GUPTA potentials

The empirical methods have attracted considerable attention in the past decades due to their ability to deal with long time and large scale systems. The difficulties of the first principle methods to deal with large scale containing more than thousands atoms resulted in the development of the empirical methods [210]. The development of the reliable potential parameters which can describe the atomistic interactions simply and correctly is key. Although the pair-wise potentials (Lennard-Jones and Morse potentials) own the simplest form, however, they fail to describe the many-body effects in metals. The successfully developed many-body potentials for metals and hcp metals [211, 212, 213] are tight-binding potential [214, 125], embedded atom method potential [204], Finnis-Sinclair potential [115], Glue potential [215]. However, with a concise form and almost fewest parameters, Gupta potential (or TB potential) [125] has drawn considerable attention among the current many-body empirical potentials. It was first proposed by Gupta [125] to calculate surface relaxation. This potential form was used by Tomanek *et al.* [216] for the electronic contribution and applied the potential to impurity segregation at metal surfaces. The tight-binding potentials developed by Cleri and Rosato [214] for transition metal within second-moment approximation reproduced the fundamental properties of some fcc (Ni, Cu, Pd, Rh, Ag, Ir, Pt, Au, Pb) and hcp (Ti, Zr, Co, Cd, Zn, Mg) metals. Since then, Gupta potential has been widely used in

atomistic simulations of different elementary metals and binary alloys [217, 218, 219]. Based on the second-moment approximation of tight-binding theory, the Gupta potential is presented and the ion-ion interaction is described by an electronic band term and a repulsive term. The general form is given below and the detailed meanings of each term can be found in the original papers [214, 204]:

$$E_c = \frac{U}{2} \sum_i \left(\sum_{j \neq i} A \exp \left(-p \left(\frac{r_{ij}}{r_0} - 1 \right) \right) - \left(\sum_{j(\neq i)} \exp \left(-2q \left(\frac{r_{ij}}{r_0} - 1 \right) \right) \right)^{\frac{1}{2}} \right), \quad (3-63)$$

where, U , q , A , p are empirical parameters; r_0 is the equilibrium first neighbour distance in hcp solid; r_{ij} represents the distance between atom i and atom j .

3.9. Simulation codes

In this section, we give an overview of the simulation codes and their applications. The usual extension of the availability of an analytical code is the ability to perform parameter optimisation.

3.9.1. GULP

The General Utility Lattice Program (GULP) [220] is developed to perform a variety of tasks based on the force field method (e.g., calculation at the interatomic level of theory). The code was written to facilitate the fitting of interatomic potentials to both energy surfaces and empirical data [221]. GULP supports molecular dynamics and geometry optimization of molecules, clusters, 0D, 2D, and 3D systems using a wide range of potential models that span both organic and inorganic fields with fully flexible molecules. The potentials include shell model, embedded atoms (for metals), and bond order reactive forcefields. The potentials describing the interatomic interactions between two ions with formal charge Z separated by the distance r are presented as:

$$U_{ij} = \frac{Z_i Z_j e^2}{r} + A \exp\left(-\frac{r}{\rho}\right) - \frac{C}{r^6}, \quad (3-64)$$

where, the first term is the long-range Coulomb term and the second term is the short-range described by the two-body Buckingham form, which is composed of the short-range Pauli repulsion and the last term is the dispersion energy. The parameters A , ρ , and C are related to the size of the ion and the hardness, while the C parameter represents the attractive van der Waals interaction.

3.9.2. The knowledge led master code

The knowledge led master code (KLMC) [222] is the code that was created in the interest to automate many tasks traditionally to enable a multistage approach where this code learns on the fly and refines input files that are submitted for a new calculation. This technique can update a simple database of structures, perform post-analysis (e.g., computing radial distribution functions, ensemble average-Boltzmann weighted properties); generate and read inputs and output files for GULP, FHI-AIMS. Therefore, KLMC can be seen as the tool to link optimization iteration together at the differing level of theory. Moreover, this code has been developed to enable the flexibility of searching either on the interatomic potential energy ground state, on DFT ground state, or DFT ground state energy after initial refinement at interatomic potential ground state energy. The first application to chain two energy functions within the Monte Carlo basin hopping routines of KLMC, enable the successful predictions of low energy structures of LiF_3 nanoclusters [34].

3.9.3. Genetic algorithm

In this study, genetic algorithms (GAs) [223] techniques are used to generate and study the properties of Ti_N ($N = 2-32, 57, 80, 89$) nanoclusters. In 1975, Holland introduced a genetic algorithm as a computational analogue of adaptations for natural systems. This method has been successfully applied in a variety of fields (e.g., Optimization, program induction, machine learning, etc.) [223], [224]. Moreover, genetic algorithms implement optimization strategies by simulating the evolution of species through natural selection. The continuing improvements of computational systems have made it useful for some type of optimization. Specifically, the genetic algorithm works very well on continuous, discrete, and combinatorial problems.

The fundamental idea behind the employment of genetic algorithm as a tool for optimizations is that, it has been proved capable of yielding approximately optimal solutions given complex, multimodal, non-differential, and discontinuous search spaces, and also it performs a process that simulates natural selection through survival of the fittest. The genetic algorithm then generates a population solution and applies genetic operators such as mutation and crossover to evolve the solutions to discover the best one(s). The three most significant features of using genetic algorithm are (1) definition of the objective function, definition and implementation of the genetic representation, and (3) definition and implementation of the genetic operators. After these have been well defined, the genetic algorithm should work fairly well.

In this study, GA will make use of the local optimization routines within the GULP program [220] to relax all newly generated structures. Whereas, for global optimization routine, better clusters within the final population, as measured by their energy landscape, will be selected for further

refinement using a bespoke library version of the numeric basis set computer program FHI-aims [148].

In this study, interatomic potentials are employed for Ti_N ($N = 2-32$) during calculations at the interatomic level of theory before evaluating the DFT energy. The chosen interatomic potential include several superimposed terms: The Buckingham potential

$$U^{Buck}(r_{ij}) = A_{ij} \exp\left(-\frac{r_{ij}}{\rho_{ij}}\right) - \frac{C_{ij}}{r_{ij}^6}, \quad (3-65)$$

where, A , and ρ parameters are related to the size of the ion and the hardness, r_{ij} which is the separation of the ions i and j , while the C parameter represents the attractive van der Waals interaction. The Buckingham potential is commonly employed in simple ionic solids.

3.9.4. CASTEP

The success of the total energy method applications largely depends on a good understanding of the underlying technology, its strong points and its limitations. CASTEP is a pseudo-potential total-energy code [149, 150] that employs special point integration over the Brillouin zone and a plane-wave basis for the expansion of the wavefunction. It is also referred to as a first-principles code and consists of many capabilities to calculate any physical property of the system. In this code, the total energy of the system is used to derive many other quantities, especially periodic systems. The periodic system is governed by periodic boundary conditions according to Blöch's theorem [180], which states that in a periodic system each electronic wavefunction can be written as a product of a cell-periodic part and a wavelike part. The cell periodic part, ψ , can then be

expanded using a basis set consisting of a discrete set of plane waves whose wave vectors are reciprocal lattice vectors of the crystal. Therefore, each electronic function can be written as a sum of plane waves $[(K+G).R]$. This is applicable in the simplified form of the Kohn-Sham equations where the kinetic energy is diagonal, and the various potentials (electron-ion, Hartree, exchange-correlation) are described in terms of their Fourier transforms. The CASTEP code was used to calculate the charge density difference for $Ti_{12}M$ ($M = Pt, Pd, Ir, Ni$).

3.9.5. Dmol3

DMol3 [152, 151] is a technique that combines computational speed with the accuracy of quantum mechanical methods to predict materials properties reliably and quickly. It is used to model the electronic structure and properties of organic and inorganic molecules such as molecular crystals, covalent solids, metallic solids, crystalline solid materials and infinite surfaces using DFT [176, 225]. This mechanism is responsible for optimizing the unit cells of periodic systems and can also be used to calculate the mechanical properties (for example, the elastic constants) of various materials. The energy is minimized using a standard geometry optimization procedure. The elastic constant tensor is then calculated from the energies corresponding to each finite displacement. The Dmol3 code was used to calculate the iso-surfaces of the HOMO-LUMO for $Ti_{12}M$ ($M = Pt, Pd, Ir, Ni$).

3.9.5.1. DMol3 advanced

The DMol3 advanced course offers a detailed introduction to accurate prediction of electronic properties, chemical reactions, IR and Raman spectra, optical properties, and electron transport properties such as band structure, the density of states (DOS), electron densities, electrostatics, molecular orbitals, and atomic populations.

3.9.6. DL_POLY

The molecular dynamics package DL_POLY [35, 130] has at its heart a number of versatile and efficient dynamics algorithms that can readily be adapted to extend the application of this code well beyond the time and length scales typically associated with atomistic simulations. In order to achieve this, it is necessary to substitute the appropriate interparticle potentials and forces in place of the default functional forms in DL_POLY, which are mainly suitable for molecular systems. To facilitate this, it may be required to incorporate additional variables into the simulation, such as velocity-dependent dissipation effects (friction), rotational degrees of freedom and non-spherosymmetric forces.

The classical molecular mechanics approach [226], which regards atomistic systems as being composed of discrete atomic particles interacting via a set of parameterised potential energy functions known as the ‘force field’, is now widely used in the field of materials science [227]. As a result of its popularity, there are now many freely available software packages, as well as commercial codes, which can carry out energy minimisation or exploration of phase space via molecular dynamics using the atomistic force fields. One such package, available under license from Daresbury Laboratory, is DL_POLY [35]

The package contains several efficient parallelised algorithms for carrying out molecular dynamics of free or partially constrained atomic particles and rigid bodies in various thermodynamic ensembles. It has also been well-validated over a wide range of applications by a worldwide community of scientists and engineers. Perhaps the most important benefit is the availability of source code for the package, which enables substantial changes to the types of systems that can be simulated. It is our intention in this paper to describe the modifications made to DL_POLY in our

research group to study mesoscopic particulate systems, in which the particles are many orders of magnitude larger than atoms, but where the fundamental classical equations of motion to be solved remain essentially the same (i.e. those based on Newton's second law, which can be formulated via an extended Lagrangian). This code was used to investigate the structural transition, solid-solid and solid-liquid transition for Ti_N ($N = 7, 13, 17, 32, 57, 80, 89$) nanoclusters.

3.9.10 FHI-aims code

The FHI-aims [148] is a computer program package for computational materials science based only on quantum-mechanical first principles. The main production method is density functional theory (DFT) [39] to compute the total energy and derived quantities of molecular or solid condensed matter in its electronic ground state. FHI-aims allows to describe wave-function based molecular total energy calculation based on Hartree-Fock and many-body perturbation theory (e.g., SOSEX, RPA, MP2) and electronic single-quasiparticle excitations in molecules using different self-energy formalisms (e.g., MP2 and GW). The FHI-aims code was used to search the lowest ground state or electronically stable Ti_N nanoclusters.

3.10 Computational details

The genetic algorithm implemented within the Knowledge Led Master Code (KLMC) [34, 228] was employed to search the local and global minima nanoclusters of Ti_N ($N = 2 - 32, 57, 80, 89$). The interaction between Ti-Ti was described by EAM and the Born-Mayer interatomic potentials [228]. The top 20 lowest minima nanoclusters from KLMC were further optimised using FHI-aims [17, 148] which is a DFT code to search electronically stable titanium nanoclusters. The

generalised gradient approximation (GGA) of Perdew-Burke-Ernzerhof (PBE), PBEsol [229] and PBEsol0 [171] approach functionals were applied for exchange-correlation energy calculations. All nanoclusters were fully optimised and electronic properties such as HOMO-LUMO energy; atomic coordination, bonding distance, spin polarisation, and energy distribution were studied to investigate stability, the contribution of coordination centres and surface energies. The binding and dissociation energies were calculated to determine the stability with respect to cluster size.

Molecular dynamics calculations were carried out in the canonical ensemble (NVT) using Berendsen [38], Hoover [36] and Andersen [37] thermostats. The equilibration time was set at 300 ps and the production time was set at 600 ps. Periodic boundary conditions were applied in the x, y and z directions. The equation of motion is the Verlet leapfrog algorithm [230] with a time step of 0.001 ps. Simulations are performed on nanoclusters with 7, 13, 17, 32, 57, 80 and 89 atoms of Ti and also supported by 100 atoms of argon gas. All simulations are made by the DL_POLY 2.20 [130] and DL_POLY 4.07 [35] packages. The structural transitions of the nanoclusters were monitored for each thermostat. The solid-solid and solid-liquid transitions were evaluated from total energy, configuration energy, diffusion coefficient, mean square displacement, radial distribution and density profiles.

Furthermore, the generalised gradient approximation GGA-PBEsol approach functional was applied for exchange-correlation energy calculations for $Ti_{N-1}M$ ($N = 1 - 16$, $M = Pt, Pd, Ir, Ni$). The stable proffered position of the dopant was investigated. The binding and dissociation energies were calculated to determine the stability with respect to cluster size. Moreover, the electron-charge transfer and iso-surfaces of the HOMO-LUMO were calculated to determine which metal atom withdraw electrons during the Ti_NM ($N = 2 - 16$, $M = Pt, Pd, Ir, Ni$). These properties were calculated using the DMol3 [152] and CASTEP [150] programs as embedded on Materials Studio

with a double numerical basis set and polarisation function (DNP). The density of states (DOS) curves was plotted to describe and investigate the electronic stability and hybridisation of orbitals.

Figure 3.2 shows the schematic representation of the multi-stage molecular modelling methods that were adopted in the current study. The two main approaches were considered i.e. the density functional theory and the classical molecular dynamics. These approaches can be explained in four stages as follows:

Stage 1: Classical molecular dynamics code i.e., KMLC software embedded within GULP code was used to simulate and generate local minima structures. The structures were further minimised to achieve global minimisation and energy ranking.

Stage 2: Density functional theory based code, FHI-aims was employed to minimise the KMLC generated local minima structures to locate the global minima nanoclusters ($N = 2 - 32, 57, 80$ and 89). The structural evolution, stability and electronic properties were evaluated for $N = 2-32$ clusters, and larger clusters as well as the doped nanoclusters.

Stage 3: DL_POLY code was used to evaluate the temperature dependence of the stable structures ($N = 7, 13, 17, 32, 57, 80$ and 89). The structural transitions were investigated to check which clusters are dominant below and beyond the melting temperature of bulk Ti. The potential energy, RDFs, diffusivity and density profiles will be monitored to observe the structural transitions (solid-liquid) at a varying temperature.

Stage 4: Density functional theory code FHI-aims was employed to optimise the doped $Ti_{N-1}M$, where represents the Ti clusters ($N = 2 - 16$) and M represents metal impurities ($M = Ir, Pt, Pd$ and Ni). The metal-doped nanoclusters were evaluated with regard to stability and electronic properties.

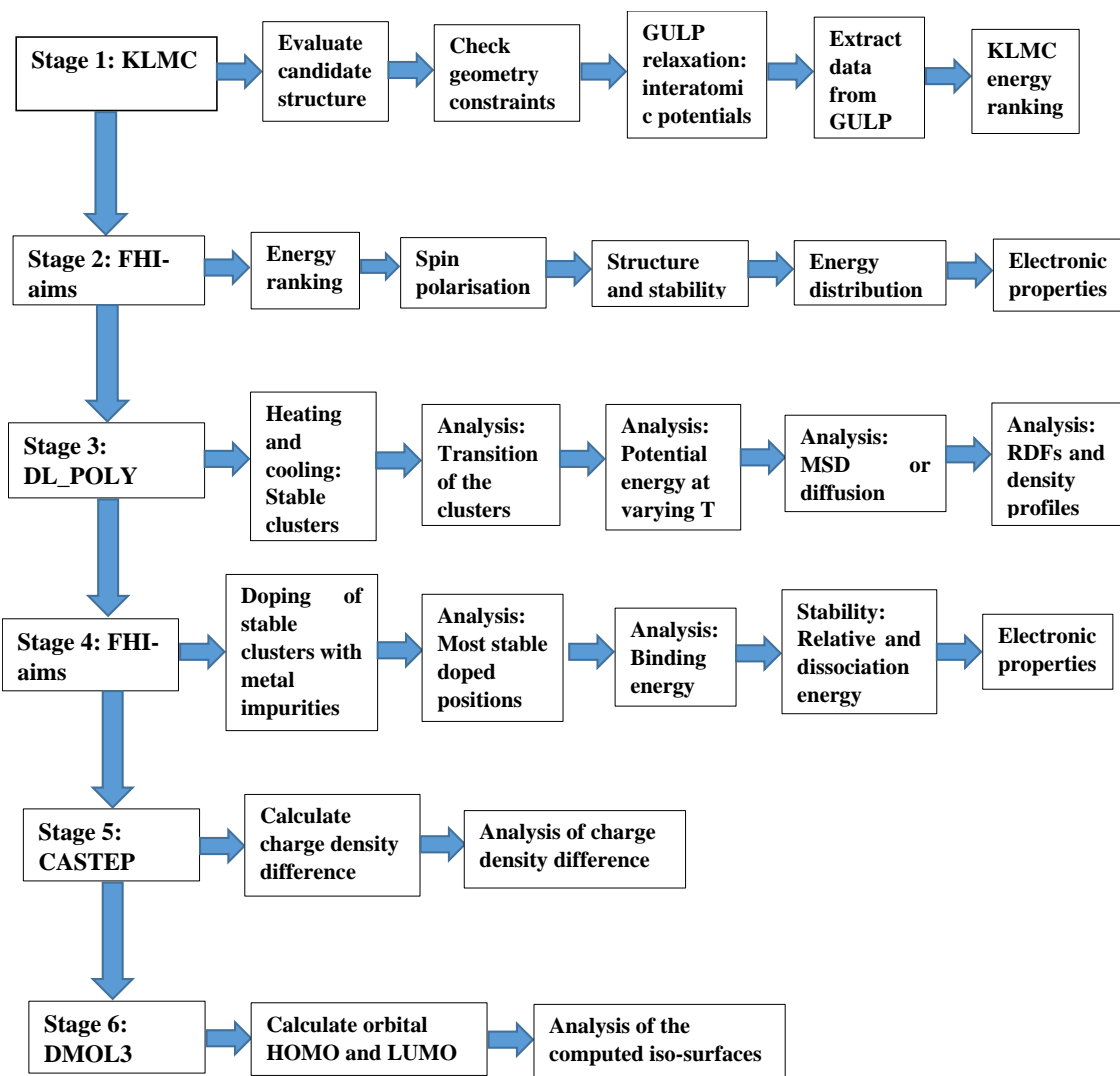


Figure 3.2: The schematic representation of the multi-stages of technical methodologies used in this study.

Stage 5: The CASTEP code was employed to calculate the charge density difference for $Ti_{12}M$ ($M = Pd, Ir, Ni, Pt$).

Stage 6: The density functional theory code DMOL3 was used to calculate the HOMO and LUMO orbital density for $Ti_{12}M$ ($M = Pd, Ir, Ni, Pt$).

CHAPTER 4

Results and Discussion: Structures and energies

In this chapter, we present the DFT results performed on titanium Ti_N ($N = 2-32$) clusters. The ground state geometrical structures and structural properties binding energy, bond length, coordination, and spin polarisation, stability, energetic distribution and surface area will be discussed in detail. The relative stability will be discussed based on the average binding energies and the second difference in energies. These are determined from performing geometry optimized clusters. Geometry optimisation for local minima and global minima is performed using KLMC and FHI-aims code which is discussed in detail in chapter 3. Furthermore, the electronic structures will be discussed, such as HOMO-LUMO.

4.1. Optimisation of Ti structures

4.1.1. FCC, HCP titanium and validation of its potentials

To evaluate the validity of the potentials to be used, we did a Modified Embedded Atom Method (MEAM) potential test for both hcp and fcc titanium obtained from Fabrizio and Rosato [208] and compared the lattice parameters in their initial state with their optimization state. It was observed that meam potentials in Gulp were refined from fcc bulk titanium, and it is also noticed that the lattice parameters for Ti fcc are better reproduced than the Ti hcp bulk structure, a big volume change is noticed, however, the energies are more favourable.

Table 4.1: Meam potential test on bulk and fcc titanium

GULP: Meam potentials test calculation on Bulk Fcc and Hcp					
Ti	Symmetry	Lattice (Å)	Lattice (Å)	Lattice (Å)	Energy (eV)
		Initial	optimization	chance	
Hcp	P63/mmc (194)	2.9398	3.0903	0.1505	-9.19376
	Vol	4.6511	5.3258	0.6741	
		34.8114	44.0472	9.2357	
Fcc	Fm-3M (225)	4.0610	4.1330	0.0720	-4.82445
		66.9728	70.5987	3.6258	
Gulp: New refined potentials calculations on Bulk Fcc and Hcp					
Hcp	P63/mmc (194)	2.9398	2.9471	0.0073	-8.0809
	vol	4.6511	4.8125	0.1614	
		34.8114	36.1977	1.386	
Fcc	Fm-3M (225)	4.0610	4.1677	0.1067	-4.04045
		66.9728	72.3955	5.422	

The new titanium potentials give a good account for both hcp and fcc titanium with minimal change in lattice parameters and volume but gives high energies compared to those predicted using meam. Table 4.2 below summarizes the total lattice energies of the clusters, and show an increase in lattice energy with the increase in the number of clusters

Table 4.2: EAM and Buckingham potentials parameters for Ti

EAM		Buckingham	
A (eV/Å)	2.0059	A (eV/Å)	13477.9114
β	3.2860	ρ	0.1723
r_0 (Å)	1.7621	C (eV)	0.0000

Table 4.3: GULP test of the new refined potentials on the titanium clusters, N=1-6

N	2	3	4	5	6
E total	-2.8745 eV	-5.7527 eV	-8.3682 eV	-12.13038 eV	-15.9393 eV

4.2. Optimisation of Ti clusters and growth

Simulations in this work were carried out using the Knowledge-Led Master Code (KLMC) software suite [34, 8] and its recently improved genetic algorithm (GA) module, [231] which has proved to locate efficiently local (LM) and global (GM) minima [232, 233, 234] on PES. Alternative global optimisation techniques, typically based on either a GA or a Monte Carlo Basin Hopping scheme, have been applied to predicting the structure of metallic clusters or their alloys or generic atomistic energy landscapes [235, 236, 237]. First, the GA module was employed to perform a search on the semi-classical interatomic PES, using the GULP code [220, 221] for energy and force evaluations, and local geometry optimisations.

Geometry optimisations were performed using the BFGS minimizer followed by the Rational Function Optimisation method to ensure that the system converges to a stable stationary point. The use of high-quality interatomic potentials (IP) to filter low energy candidates for a DFT analysis, or to compare regions of energy landscapes, is a strategy that has been exploited successfully in previous studies (e.g. ref. [8], [233], [234], [238] and [239]). In this work, the PES of Ti_N nanoclusters is evaluated using a many-body embedded atom method (EAM), which includes a combination of a many-body attractive term, E_a , and a repulsive two-body Born–Mayer IP, E_r .

Parameters for the EAM IP were obtained from a mathematically equivalent parameterisation of the tight-binding potentials [214, 115, 125], and are given in table 4.2. The forms of the potentials are given by where r_{ij} is the interatomic distance between atoms i and j , and A , β , r_0 , ρ , are potential

parameters. During GA simulations, the size of the cubic container, in which atoms are initially randomly placed, was adjusted to the cluster size (N), taking the values between 5 and 12 Å.

Other GA parameters, such as the population size and graph radius of the geometrical pre-screener (described in ref. [231]) were kept fixed at 200 and 3.34 Å for all the GA simulations, respectively.

To maintain diversity and ensure a healthy population, 80% of the structures obtained from the crossover operation were mutated using the same

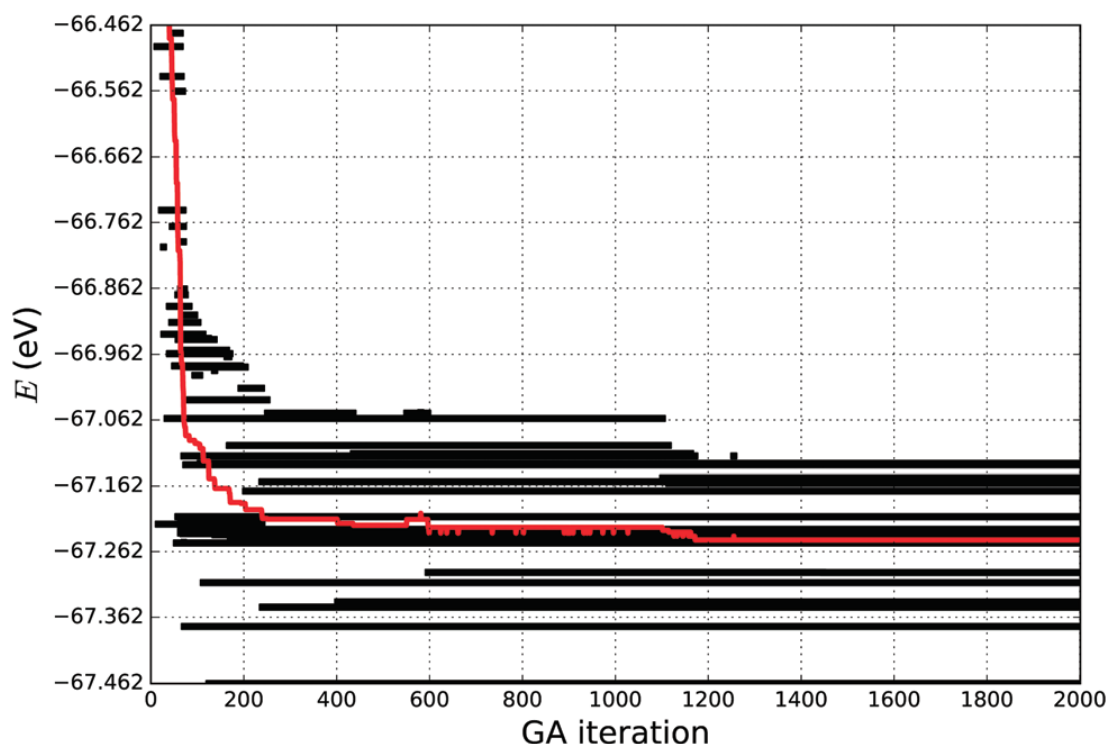


Figure 4.1 Energy (E) “evolution” of the 20 lowest energy structures of Ti_{21} during a GA simulation carried out for 2000 iterations. The red line shows the average energy of the 20 lowest energy structures.

probability weights as were established in the previous work [231]: 0.2 – self-crossover, 0.1 – atom exchange, 0.1 – expansion, 0.1 – contraction, and 0.5 – random displacement. Moreover, as the number of degrees of freedom increased with N , a greater number of GA iterations per simulation was performed, varying from 10 to 3000. If a simulation stopped too early, the tentative GM found might be a metastable LM, in which the simulation is trapped, and therefore a higher number of

GA iterations would be necessary for the simulation to escape from this particular LM. The “evolution” of energy as the measure of simulation convergence was used and we observed the twenty lowest energies, as it is shown in Fig. 4.1.

We stop our simulations when the average energy of the 20 lowest energy structures becomes stable for about 100–200 GA iterations, giving high confidence in having a good representative set of LMs and the desired GM. After completing the search on the IP PES, we have selected for refinement a subset of the lowest energy LM within approximately 1.0 eV energy range above the corresponding tentative GM. Using this criterion, for example, the Ti₃₂ subset included 250 LM. The selected clusters were re-optimised at the quantum mechanical, DFT level using the all-electron, full potential electronic structure code FHI-aims [8].

To reduce the computational time required for geometry relaxation (refinement), we use the PBEsol exchange-correlation functional [8] without spin polarization and a multi-step optimization procedure. The structures from the GA subsets were initially refined using the light basis sets (variationally equivalent to split valence double-zeta Gaussian plus polarisation basis sets) with “loose” convergence criteria. Then the resultant structures were further refined using the tight basis sets (equivalent to triplezeta plus polarisation) and “tight” convergence criteria. [240] The convergence criteria used for the light and tight basis sets are given in table 4.4 below.

The latter structures were used for a subsequent (PBEsol and tight basis set) refinement employing a spin-polarized approach with different overall spin moments S : 0, 1, 2, 3 \hbar . The lowest energy structures for each size were selected as the tentative GM. Finally, the tentative GM structures were evaluated using the hybrid functional PBEsol0, [229, 171] which includes 25% Hartree–Fock-like electron exchange, by performing single point energy calculations with the tight basis sets. If not stated otherwise, the results are given after the PBEsol tight refinement.

To calculate binding energies (or enthalpies of formation) and provide a reference for the asymptotic behaviour of structural and electronic properties of Ti_N clusters at the thermodynamic limit, we have evaluated bulk Ti at the same level of theory with a 20 sampling grid over the first Brillouin. The thermodynamic stability of the lower energy clusters has been analysed with the usual procedure, including binding and first and second difference energies [241]. Moreover, to help understand the structural stability of GM and lower energy metastable LM, in this study we investigate the surface area of each cluster by employing Delaunay's triangulation (DT) method [242, 243] from the Python Visualisation Tool-Kit library in the following manner: (i) atoms of the cluster are treated as points and triangulated, (ii) triangles from the surface triangulation are extracted, (iii) the sum of the extracted triangles is defined as the surface area of the cluster – *cf.* some alternative approaches to the definition and the calculation of the surface area [244, 245].

For the largest ($N = 32$) clusters investigated in this work, the number of LM decreases with the level theory. In the given case, the 250 lowest energy LM obtained on the IP PES using GA were refined using the PBEsol functional with the light basis set. On refinement, the number of LM decreased from 250 on the IP PES to 185 on the PBEsol light PES. This significant reduction is observed as some groups of metastable LM on the IP PES converge to a single LM on the PBEsol light PES. The graphical representation of how the energy ranking changes between the different levels of theory applied in this study is given in Fig. 4.2. Here we have shown relative (with respect to the tentative GM) energies of the Ti_{32} structures on the PES described by IP, PBEsol with the light and PBEsol with tight basis sets. For the largest ($N = 32$) clusters investigated in this work, the number of LM decreases with the level theory.

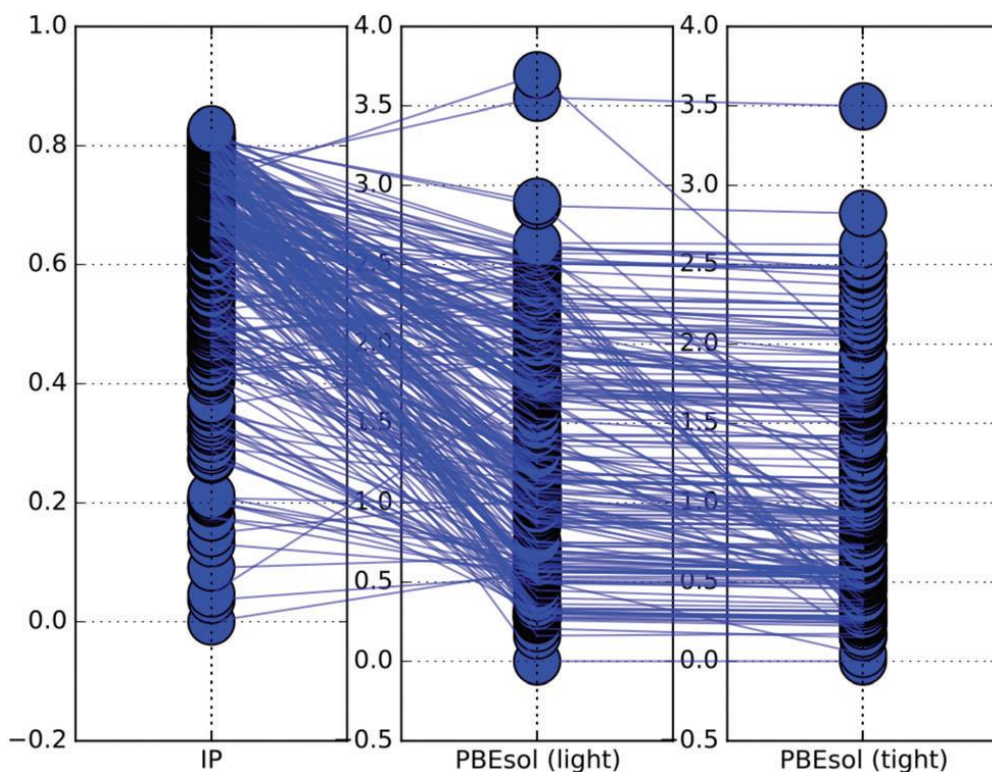


Figure 4.2: Map of energy ranking of Ti_{32} between different energy landscapes: IP, PBEsol with light and PBEsol with tight basis sets. The lines between the values depict the cluster energy evolution on energy refinement from left to right.

In the given case, the 250 lowest energy LM obtained on the IP PES using GA were refined using the PBEsol functional with the light basis set. On refinement, the number of LM decreased from 250 on the IP PES to 185 on the PBEsol light PES. This significant reduction is observed as some groups of metastable LM on the IP PES converge to a single LM on the PBEsol light PES.

Fig. 4.2 illustrates the change in the LM ranking, based on energy, when switching from one level of theory to another. The lowest energy structure on the IP PES is not necessarily the lowest energy structure on the PBEsol light PES. In fact, in most of the cases when $N \geq 10$, the lowest energy structure on the PBEsol energy landscape is different from the IP PES lowest energy structure.

Thus, it is necessary to choose a sufficiently large energy range for each cluster size that would ensure that at least one of the LM on the PES for the lower level would relax to the GM of the higher level. For our simulations, the chosen ≈ 1.0 eV energy range has proved to be sufficient. After the results on the PBEsol light PES were obtained, the new structures were re-optimised on the PBEsol tight PES. Similarly to the previous refinement, the number of unique LM decreased (185 to 132) and the energy ranking has changed, but at a much lower extent to that seen between IP and PBEsol light. The resultant configurations were then analysed using spin polarised calculations to investigate whether small Ti_N clusters have magnetic moments that also effect a change in energy ranking.

In order to save computational time, we chose a two-step refinement approach, where at first we refine the structures using the light basis set with fairly loose convergence criteria and then the resultant structures are refined using the tight basis set and tighter convergence criteria as given in table 4.4.

Table 4.4: Main computational settings used within the FHI-aims package

Basis	Convergence criterion based on				Structure optimization
	Charge density	Eigenvalues	Total energy	Forces	
	(electrons)	(eV)	(eV)	(eV/Å)	(eV/Å)
Light	10^{-2}	10^{-1}	10^{-2}	10^{-1}	10^{-1}
Tight	10^{-4}	10^{-3}	10^{-5}	10^{-3}	10^{-3}

For comparison, we also performed calculations for bulk titanium using the same computational parameters at both levels of theory.

4.3. Stability of clusters

4.3.1. Binding Energy

In order to determine the binding energy, geometry optimization calculations were performed. Firstly, optimizations were performed using KLMC with genetic algorithm (GA), where calculations at the interatomic level of theory were performed by the General Utility Lattice Program (GULP) to find the local minima, where the Embedded Atom (EAM) Method [204], and the Buckingham potentials Buckingham. [209] were used for the description of the interatomic interactions and secondly, we performed optimizations at the DFT level of theory using FHI-aims to find the global minima of each system with PBEsol. Total energies of the DFT / Hartree-Fock s.c.f. calculations were used to calculate the binding energy using the formulae discussed in section 4.4.2. All the binding energy values are reported in table 4.5 and the binding energy plot is discussed in Fig. 4.7 and 4.13. It was found that the binding energy decreases with increasing cluster size.

4.3.2. Second-order energy difference

For the stability of clusters, we calculated the second-order energy i.e. relative stability using the values from the binding energies of the clusters. The formulae used is discussed in section 4.4.3 and the values are reported in Table 4.5. The second-order energy $\Delta^2(N)$ of the most stable Ti clusters as a function of cluster size plot is discussed in Fig. 4-8 and 4-14. It was found that the Ti₅ and Ti₇ are the most stable clusters.

4.3.3. Bond length and average coordinations

The bond length and coordination counterbalance ultimately determine the equilibrium of each cluster. The values were obtained using python and report in table 4.5. Thus, the curve is evaluated in Fig. 4.9 as the number of clusters increases. The bond distance and coordination number were found to have a similar resemblance.

4.3.4. Electronics: HOMO-LUMO

HOMO-LUMO gaps are of great concern in organic reactivity. The HOMO of the nucleophile reacts with the LUMO of the electrophile and the closer in energy they are the stronger the interaction. This idea has been widely studied in what is called the Frontier Molecular Orbital theory (FMO). HOMO/LUMO gap may be most important for single electron transfer. This is useful for a number of reactions, and has huge implications in organic semiconductors, the field where this gap is most important. For materials that do not conduct electricity, the HOMO-LUMO gap is big, and those that can conduct electricity have lower gap between the two states.

Electrons are constantly shuttling between the two energy levels (considering one of them is the highest occupied and the other is the lowest unoccupied), and the energy gap usually reflects what kind of photons it absorbs in order to make this jump. Small HOMO-LUMO gaps are precisely why long conjugated molecules usually have colour. This is because they can be modelled as a particle in a box that has energy levels according to

$$E_n = \frac{\hbar^2 \pi^2}{2mL^2} n^2, \quad (4-1)$$

where L is the length of the box. Notice as L increases the energy gap between the two consecutive energy levels decreases.

For total energy calculations providing structural, electronic and bonding properties with respect to cluster size investigated systematically, there are two computational techniques used, namely the KLMC for interatomic potential and FHI-aims, a DFT level of theory technique. The HOMO-LUMO were successfully calculated using FHI-aims DFT level of theory. It was found that there is no simple correlation between the ΔE and the stability. Particularly, the highest maxima for $\Delta^2(N)$ are found at $N = 7$, and 13 , whereas the ΔE shows steep for $N = 5, 12, 18$, and 28 (PBEsol) and $N = 5, 13, 17$ (PBEsol).

4.4. Structural properties

The geometry optimizations parameter corresponding to these fully optimized geometries are shown in table 4.4 and 4.5. The results from previous studies are quoted for comparison.

4.4.1. Ti_N clusters growth pattern

We start by comparing our predictions with results from the most recent systematic study of Ti_N clusters, [33] in which clusters of up to twenty atoms were investigated. There is still little known about the configurations and properties of the structures with a greater number of atoms, where the phase space for such sizes is much larger. Even though a large number of isomers have been considered in this study, especially for larger sizes, for simplicity, we provide an image and description for just the ground state of each size.

The whole set of structures, which were considered, are uploaded into the WASP@N database [246] and can be found using the DOI (Digital Object Identifier) of the published paper from this

report [228]. The ground state geometrical structures of Ti_N ($N = 2-32$) clusters are shown in Fig 4.3 and 4.4. Some of these configurations have been reported in previous work Sun *et al.* 2015 [11]; Sun *et al.* 2005 [247], in particular clusters with $N = 3-15$. Several of these clusters display similar ground-state structures in comparison with the above literature, but have a different symmetry group; however, some of the most stable clusters have significantly different structures. The binding energies, bond length, coordination number and symmetry are listed in table 4.5.

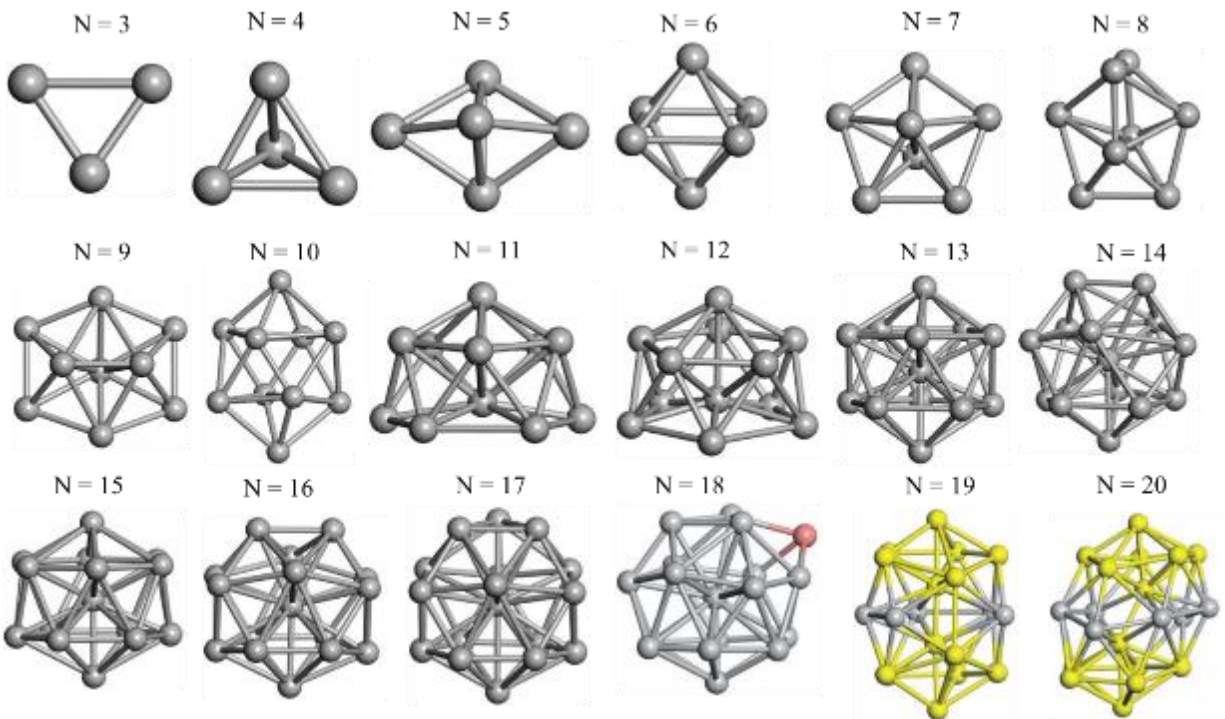


Figure 4.3: Tentative global minima of Ti_N , $N = 3-20$ clusters. As discussed in the main text, for structural analysis of the biggest clusters $N = 18-20$, the following colouring was used: atoms from icosahedra are coloured yellow and capping atoms are coloured pink.

The study of Ti_2 shows a linear geometry as the lowest energy configuration with a bond length of 1.892 \AA in agreement with the previous experimental value of 1.943 \AA Doverstål *et al.* [13], this value is considerably shorter than the experimental value of 2.95 \AA for hcp – Ti in bulk [Kittel *et al.* [248]], showing that the properties of these small clusters are very different from those of bulk

titanium. However, the binding energy of the dimer is found to be 2.73 eV which is in agreement with the experimental value of 2.10 eV Haslett *et al.* [64]. The ground-state structure for Ti_3 is a scalene triangle (D_{3h}) with an average bond length of 2.176 Å. Due to the John-Teller effect, the distorted tetrahedron (D_{2d}) is the lowest energy configuration geometry for Ti_4 with an average bond length of 2.478 Å instead of the equilateral triangle structure with C_{3v} symmetry reported by Wei *et al.* [12]. The energy difference between these latter structures is 1 eV. Moreover, the same structure was reported by Sun *et al.* [11] and has an energy difference of 0.99 eV in comparison with our current predictions. The most stable structure for Ti_5 is found to be the triangular bipyramid (D_{3h}) with an average bond length of 2.487 Å.

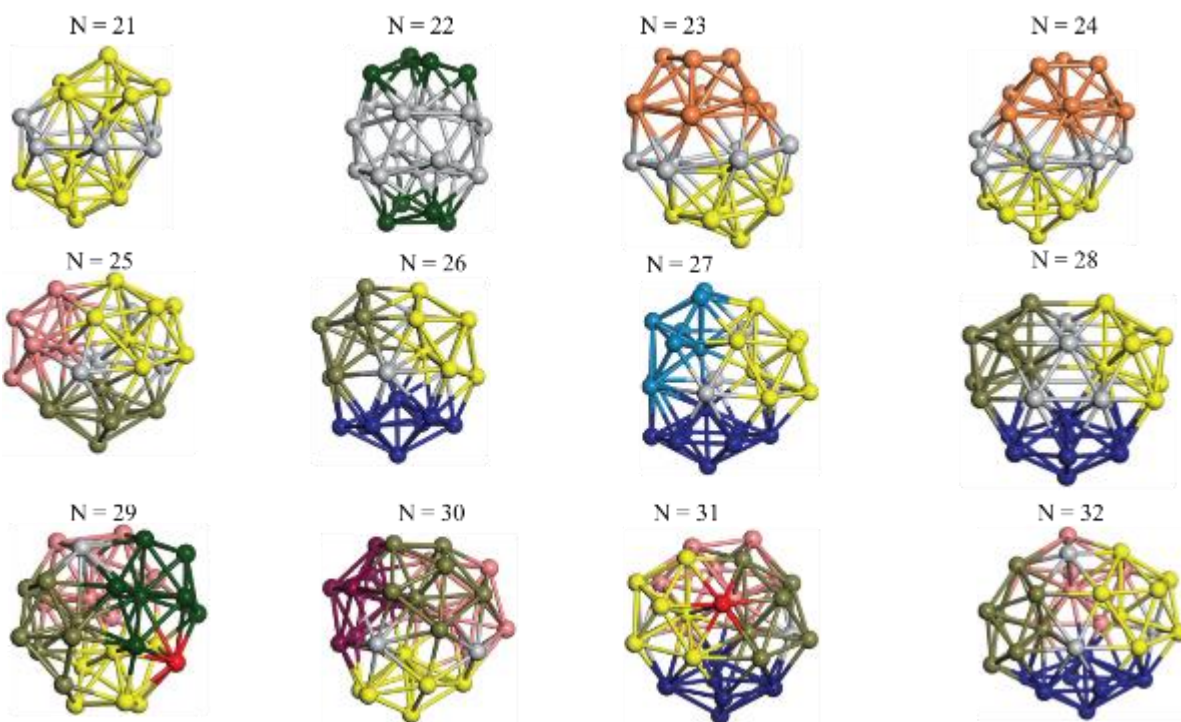


Figure 4.4: Tentative global minima of Ti_N , $N = 21-32$ clustersThe following colouring was used: atoms from icosahedra are coloured yellow (or khaki or pink), from sixfold icositetrahedra – blue (or light blue) and from the Z15 Frank–Kasper polyhedra – orange. Atoms shared by neighbouring fragments are coloured red.

For Ti_6 , the distorted octahedron (D_{4h}) is the one that appears to be the most stable geometry with an average bond length of 2.556 Å. The pentagonal bipyramid (D_{5h}) is found as the lowest energy configuration geometry for Ti_7 . For, Ti_8 the bi-capped octahedron (C_s) is found as the most stable structure, the pentagonal bipyramid with two of its faces capped by one atom (C_{2v}) is the lowest configuration energy for Ti_9 . For $N = 10$, our tentative ground state is a bicapped quadrilateral antiprism (D_2) and is the second-lowest energy structure in ref. 36. Starting from $N = 11$, we can see a clear trend of how the Ti_N cluster is evolving with size. In the case of $N = 11$ (C_{2v}), the lowest energy structure is a tetra-capped pentagonal bipyramid, and by adding an atom to the tetra-cap, the ground state of $N = 12$ – a penta-capped pentagonal bipyramid is obtained. By continuing this process we form the ground states of $N = 13$ and $N = 14$ – an icosahedron (I_h) and a capped (capping one atom over a triangular face) icosahedron, with bond lengths varying from 2.907 Å to 2.765 Å respectively. The following three tentative GM are a sixfold icositetrahedron (D_{6d}), or Z14 Frank–Kasper polyhedron; Z15; and Z16 Frank–Kasper polyhedral (C_{3v}). For $N = 18$, the ground state is a capped Z16 Frank–Kasper polyhedron (C_{2v}); the capping atom is coloured pink in Fig. 4.3.

Starting from $N = 19$, the ground states are formed by at least two interpenetrating fragments of higher symmetry configurations (C_s), such as icosahedra and Frank–Kasper polyhedra. To highlight which fragments were detected in tentative ground states, the following colouring was used in Fig. 4.3 and Fig. 4.4: the atoms forming icosahedron fragments are coloured yellow (or khaki or pink), the atoms from sixfold icositetrahedra are coloured blue (or light blue) and the atoms from the Z15 Frank–Kasper polyhedron fragment are shown in orange. Using this colour map, we observe that the ground states of $N = 19$ and $N = 20$ are two interpenetrating icosahedra with the latter having an extra atom filling a vacant site. Overall, our results for $N = 3–20$

corroborate the report by ref. [11] with only one exception of $N = 10$, where the two lowest energy structures are inter changed.

This change in ranking might be an effect of using different functional and/or different convergence criteria, as the energy differences between the two competing isomers are small, < 0.03 eV in our calculations and < 0.2 eV in ref. [11]. The perfect agreement in the remaining ground states for $N = 3$ – 20 using two independent methods and implementations gives high confidence in the predicted tentative GM. Above $N = 21$, there are no reports of the ground or low energy states of Ti_N clusters. Hence, we could only compare our predicted structures with those reported for other transition metals.

In fact, a reasonable comparison could be made only with palladium clusters reported in ref. 69 as discussed below. Similar to $N = 19$ and $N = 20$, the Ti_{21} structure is also formed of two interpenetrating icosahedra with extra atoms filling vacant sites of the parent structure. For $N = 22$, the ground state is a structure of two tetra-capped (highlighted in green) hexagonal rings, which can be thought of as fragments of capped Z16 Frank–Kasper polyhedra ($N = 18$). The $N = 23$ and $N = 24$ clusters are interpenetrating icosahedra with a tricapped top of Z16 Frank–Kasper polyhedron as the latter has an extra atom filling a vacant site.

For GM structures of size $N = 25$ – 28 , a new growth pattern can be observed based on three interpenetrating fragments. Starting from $N = 25$, the ground state is formed by three interpenetrating icosahedral fragments; at $N = 26$ one of the icosahedral fragments expands to a sixfold icositetrahedral fragment; at $N = 27$, two of the $N = 25$ icosahedral fragments expand to sixfold icositetrahedral fragments; whereas for $N = 28$, the ground state is composed of one icositetrahedral and two interpenetrating icosahedral fragments with two triangular faces

connecting the interpenetrating parts. From $N = 29$ to $N = 32$, the growth pattern, based on four interpenetrating fragments, continues.

The $N = 29$ ground state has four interpenetrating icosahedral fragments, two of which (yellow and dark green) share an atom (red); as for $N = 30$, the four interpenetrating icosahedra fragments do not share atoms between them. Similar results are obtained for $N = 31$ and $N = 32$, except that one of the icosahedral fragments is replaced with an icositetrahedral fragment. Finally, we note that the atomic structures predicted here for Ti_{23} and Ti_{29} closely resemble the corresponding palladium structures [75].

In the following analysis, we will use notation based on the descriptions given above for configurations of the GM: clusters with sizes from $N = 2$ to 10 do not have inner coordination centres (0-c.c.), clusters with sizes from $N = 11$ to 18 will be addressed as having one coordination centre (1-c.c.), for $N = 19-24$ – two coordination centres (2-c.c.), from $N = 25$ to 28 – three (3-c.c.), and lastly, Ti clusters with sizes from $N = 29$ to 32 as having four coordination centres (4-c.c.).

From the above discussion, we can deduce the patterns in the cluster size ranges from 3 to 32. One is based on the tetrahedron structure (N4), namely the triangle of $Ti_3 \rightarrow N4a \rightarrow N5a \rightarrow N6a$. This structural sequence denoted in a's are the most stable ground state of Ti_n clusters ($N = 3 - 6$). The second growth pattern is based on the octahedron structure (N6a), i.e., $N6a \rightarrow N7a \rightarrow N8a \rightarrow N9d \rightarrow N10d$. The third is the pentagonal bipyramid (N7) or icosahedron derived structural sequence, namely, $N7a \rightarrow N8d \rightarrow N9a \rightarrow N10b \rightarrow N11a \rightarrow N12a \rightarrow N13a \rightarrow N14a$. This sequence also appears again for clusters $N19, N20, N21$ and $N22$. However, the sequence appears in more than half of the lowest energy structures for Ti_N ($N = 3-22$).

The fourth pattern is based on the icosahedral type with pentagonal rings replaced by hexagonal ones (N15) –derived structural sequence, i.e., N11c → N12b → N13c → N14a → N15a → N16a → N17a → N18a → N19b → N20d → N21a → N22b. The fifth growth pattern is based on the double interpenetrating icosahedron (N19), i.e., N19a → N20d → N21a → N22b → N23d → N24a → N25c → n26a → N27a → N28d → N29c → N30b → N31b respectively.

Table 4.5: The binding energy per atom E_b (eV), the average coordination number n_0 , the average bond lengths r_0 (Å) for Ti_n ($n= 2-32$), and reported lowest energy structures a_0 , second-lowest energy a_1 of other transition metal clusters.

N	Symmetry	E_b	n_0	r_0	Sun et al [33]	Du et al [58]	Böyükta et al [129]	Datta et al [249]	Reddy et al [250]	Bodadov a-Parvano vaet al [251]
2	Linear	-2.731	1.00	1.89	a_0		a_0	a_0	a_0	a_0
3	D_{3h}	-3.331	2.00	2.34	a_0	a_0	a_0	a_0	a_0	a_0
4	D_{2d}	-3.958	3.00	2.48	a_0	a_0	a_0	a_0	a_0	a_0
	D_{2h}	-3.845	2.50	2.35						
5	D_{3h}	-4.441	3.60	2.49	a_0	a_0	a_0	a_1		a_0
	C_{2v}	-4.042	2.80	2.34						
6	D_{4h}	-4.467	4.00	2.55	a_0		a_0	a_0	a_0	a_0
	C_{2v}	-4.620	4.00	2.51						
7	D_{5h}	-4.928	5.57	2.57	a_0	a_0	a_0	a_0	a_0	a_0
	C_s	-4.730	4.29	2.56						
8	C_s	-4.936	4.75	2.59	a_0	a_0	a_0	a_0	a_0	a_1
	D_{2d}	-4.933	4.50	2.57						
	C_s	-4.926	4.75	2.60						
	D_{6h}	-4.889	4.45	2.58						
	C_{2v}	-4.882	4.50	2.55						
	C_{2h}	-4.824	4.75	2.61						
9	C_{2v}	-5.060	5.11	2.60		a_0			a_0	a_0
	C_2	-5.059	4.80	2.59						
	C_{4v}	-4.994	4.44	2.57						
	C_s	-4.987	4.67	2.57						
10	D_2	-5.140	5.20	2.62						
	C_{3v}	-5.109	5.40	2.63						
	D_{2h}	-5.105	5.20	2.61						
	C_2	-5.088	5.00	2.59					a_0	

11	C _{2v}	-5.197	5.64	2.64						
	C ₂	-5.195	5.27	2.61						
	C _s	-5.184	5.64	2.68						
12	C _s	-5.318	6.00	2.67	a ₀		a ₀		a ₀	a ₀
	C _{2v}	-5.260	5.00	2.62						
	C ₁	-5.258	5.50	2.63						
13	I _h	-5.406	6.46	2.68	a ₀	a ₀	a ₀	a ₀	a ₀	a ₀
	C _s	-5.373	6.00	2.66						
	C _{2v}	-5.347	5.85	2.64						
14	C _s	-5.506	6.67	2.29						
	C _{2v}	-5.498	6.57	2.69						
	C _s	-5.479	6.00	2.65						
15	D _{6d}	-5.560	6.69	2.67	a ₀	a ₀	a ₀			
	C ₁	-5.494	6.27	2.67						
	C ₂	-5.488	6.27	2.66						
16	C _s	-5.640	6.69	2.75	a ₀					
	C _{2v}	-5.640	6.50	2.67						
	C ₂	-5.596	6.38	2.67						
17	C _{3v}	-5.692	6.69	2.82	a ₀					
	C _{2v}	-5.652	6.59	2.67						
	C _s	-5.650	6.35	2.65						
18	C _{2v}	-5.684	6.67	2.44	a ₀					
	C ₁	-5.683	6.44	2.67						
	C _s	-5.662	6.67	2.69						
19	C _s	-5.715	6.71	2.95	a ₀		a ₀	a ₁		
	C _{2v}	-5.714	7.05	2.70						
	C _s	-5.686	6.53	2.67						
20	C ₁	-5.769	6.68	2.80	a ₀		a ₀	a ₁		
	C ₂	-5.764	6.60	2.67						
	D _{3d}	-5.764	6.70	2.68						
21	C ₁	-5.798	7.14	2.71						
	C ₁	-5.797	6.86	2.69						
	C ₁	-5.797	6.86	2.69						
22	D _{2d}	-5.821	7.82	2.68						
	C ₂	-5.816	7.18	2.71						
	C ₁	-5.815	7.09	2.70						
23	C ₂	-5.848	7.13	2.70						
	C ₁	-5.835	7.13	2.70						
	C _{2v}	-5.823	7.22	2.71						
24	C ₂	-5.850	7.08	2.70						
	C ₂	-5.843	7.08	2.69						

	C _{3v}	-5.842	6.92	2.69					
25	C ₂	-5.854	7.44	2.73					
	C ₁	-5.852	7.28	2.72					
	C ₁	-5.852	7.60	2.74					
26	C ₁	-5.880	7.38	2.73					
	C ₁	-5.876	7.31	2.72					
	C _s	-5.875	7.69	2.75					
27	C _s	-5.894	7.48	2.72					
	C ₁	-5.893	7.33	2.71					
	C _s	-5.892	7.33	2.72					
28	C _s	-5.920	7.35	2.73					
	C ₁	-5.946	7.43	2.72					
	C ₁	-5.943	7.36	2.72					
29	C ₁	-5.907	7.52	2.71					
	C ₂	-5.903	7.43	2.72					
	C ₁	-5.902	7.72	2.75					
30	C ₁	-5.928	7.53	2.73					
	C ₁	-5.924	7.60	2.74					
	C ₁	-5.924	7.67	2.74					
31	C ₂	-5.941	7.74	2.73					
	C ₁	-5.941	7.48	2.73					
	C ₁	-5.940	7.61	2.73					
32	C ₁	-5.950	7.94	2.74					
	C ₁	-5.949	8.06	2.77					
	C ₁	-5.949	7.88	2.76					

4.4.2 Spin polarization

In fact, in most of the cases when $N \geq 10$, the lowest energy structure on the PBEsol energy landscape is different from the IP PES lowest energy structure. We have further investigated the fifty lowest PBEsol spin non-polarised energy structures using the PBEsol functional with spin polarization and the tight basis set. Based on a preliminary study, three overall spin moments, S , were used: 1, 2 and 3 \hbar . Exploratory calculations for higher spin values consistently yielded much higher energies. The results from spin unpolarised and polarized calculations are juxtaposed in

Fig. 4.5. As can be seen from Fig. 4.5, a majority of smaller clusters ($N < 19$) stabilize with higher overall spin moments. Exceptions are clusters of size $N = 6, 7, 10,$ and 14 , whose tentative GM structures are non-magnetic.

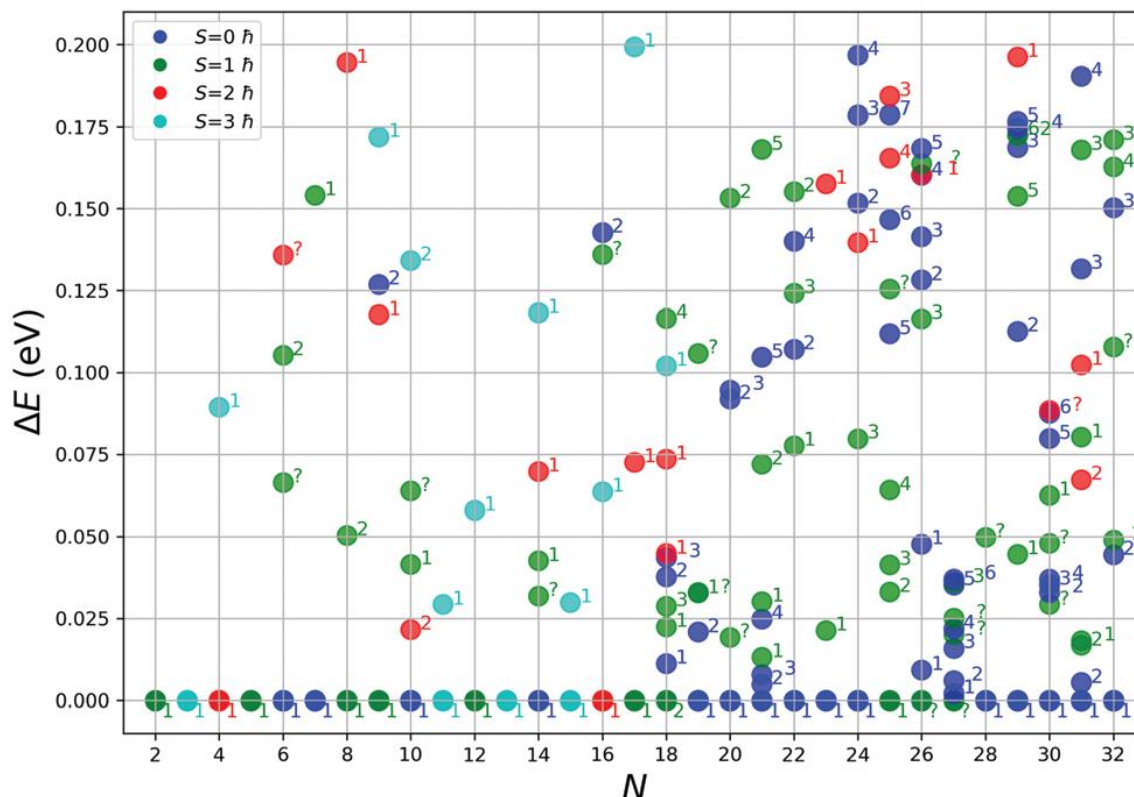


Figure 4.5: Relative energies of LM within a range of 0.2 eV energy range from the tentative GM, $\Delta E = E(\text{GM}) - E(\text{LM})$, for all the cluster sizes considered. The data points are coloured according to the cluster spin moment; the data label shows the energy rank in the initial spin unpolarised calculation. “?” marks new configurations.

For bigger clusters ($N > 23$), most of the tentative GM structures have an overall spin moment of 0, except for $N = 25, 26$ and 27 . For $N = 25$, the GM is only the second-lowest energy structure from the GA search, whereas, for $N = 26$ and 27 , the GM spin-polarised structures optimised to new configurations, which were not found during the GA search.

For the smaller clusters ($N < 19$), the energy difference between the spin-polarised tentative GM and higher energy spin unpolarised lowest energy LM is more pronounced than for bigger clusters ($N \geq 19$), which suggests that for the bigger clusters there will be greater competition for the ground state as there are more configurations of different spin with similar energy.

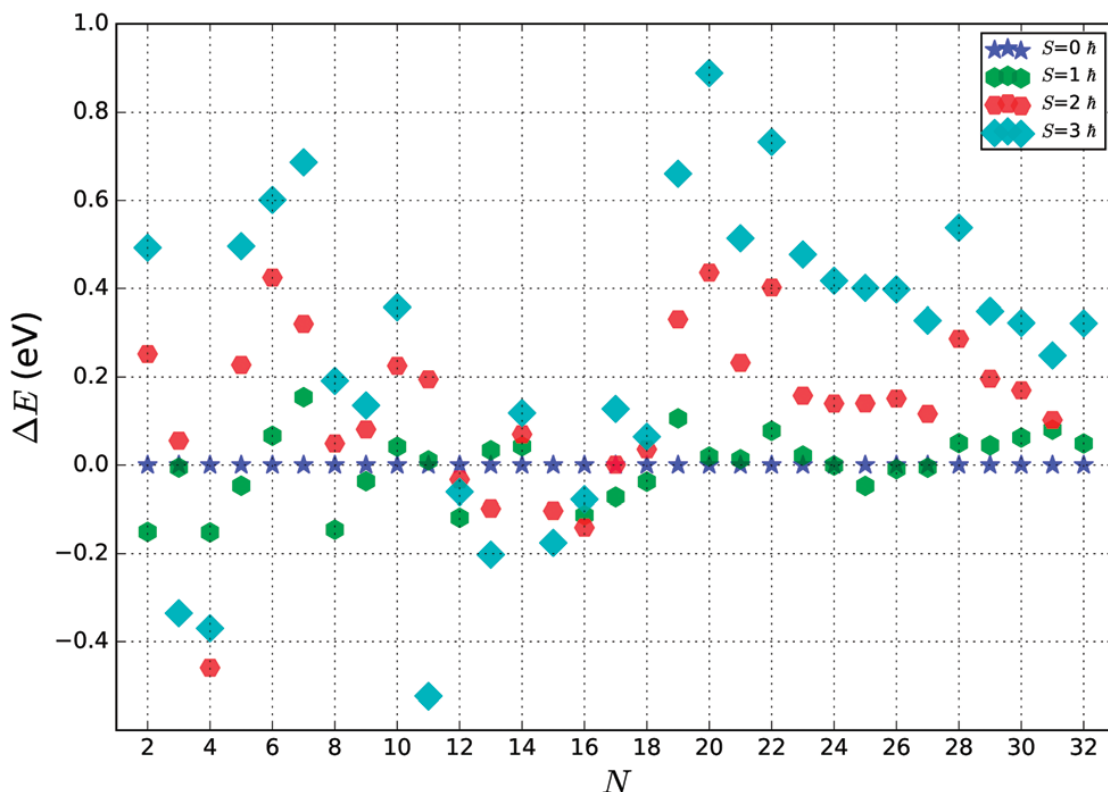


Figure 4.6: Spin polarization energies of tentative GM structures ($\Delta E = E(S) - E(0)$).

In most of the cases, the topology (as shown by atomic coordination) of the tentative GM is unchanged on refinement with spin-polarised calculations, except for $N = 18$, whose new spin-polarised tentative GM had the second-lowest energy during the spin unpolarised GA search and the new $N = 26$ and 27 tentative GM, which were not found during the GA search. In Fig. 4-6 we show the effect of spin polarization on the energy of tentative GM structures. The results clearly indicate the tendency for the small ($N < 19$) Ti_N clusters to stabilize in a magnetic state, whereas

bigger ($N \geq 19$) Ti_N clusters prove to be non-magnetic in the ground state with the exceptions described above. The resultant tentative GM configurations were investigated further by studying the evolution of structural patterns adopted by small GM Ti_N clusters with cluster size, N .

4.4.3 Stability of the Ti_N ($N = 2-32$) clusters.

After finding the geometries up to Ti_{32} , the magic behaviour of these clusters was investigated. The binding energies versus the clusters size were plotted for the putative stable structures in Fig. 4.7. As the clusters size increases the average binding energy per atom decreases. This exponential-like decay is known as a common behaviour almost for all transition metal clusters [252, 253].

A central issue in cluster physics is to identify particularly stable sizes. A detailed structural picture and the nonmonotonic variation in the properties of clusters can be obtained by locating the global minimum as a function of size. This can then give information about the abundance of particularly stable clusters [21]. The average binding energy per atom in the cluster may, therefore, expressed as a function of the cluster size.

$$\Delta^2(N) = E_N - \frac{E_{N+1} + E_{N-1}}{2}, \quad (4-2)$$

$$\Delta^1(N) = E_N - E_{N-1} - E_1 \quad (4-3)$$

and

$$E_B(N) = \frac{(E_N - NE_1)}{N}, \quad (4-4)$$

where E_N is the total energy, E_1 is the energy of a single atom, and $E_B(N)$ is the binding energy,

$\Delta^1(N)$ is the first-order energy and $\Delta^2(N)$ is the second energy order energy. In Fig. 4.7

the binding energy steadily improves with cluster size with an asymptotic value of -5.155 eV, which is about 1.006 eV less stable than the bulk hcp Ti metal's value of -6.161 eV, represented by the blue line at the bottom, which is close to the calculated value of -6.040 eV reported by ref. [254] (*cf.* the standard enthalpy of formation of 4.824 eV is over 1.2 eV smaller than the magnitude of either calculated values and, thus showing that the GGA calculations do overestimate significantly the binding energy for Ti as is well known for a wide range of chemical compounds [234, 255, 256]). The difference between the asymptotic cluster value and the bulk energy can be assigned essentially to the shell structure of the clusters: the majority of the atoms are actually on the cluster surface, e.g. 28 surface atoms compared to 4 c.c. atoms for $N = 32$.

The GM of the largest titanium cluster in this work, Ti_{32} , has a binding energy of 4.838 eV, which is still 1.323 eV above the calculated bulk value. We note that the binding energies of Ti_{18} and Ti_{29} clusters are slightly higher than their respective nearest neighbour Ti_{17} and Ti_{28} , indicating an instability with respect to size.

On the other hand, binding energies of $N = 7$ and 13 almost plateau with neighbouring larger size clusters, and for $N = 17$ and 28, the binding energies are lower than those of the neighbouring larger size clusters, thus indicating the relative stability and prospect for these clusters being magic. Interestingly, two out of four tentative magic numbers are in the 0 and 1-c.c. region and the largest one is from the 3-c.c. region. Particular stability of magic number clusters can be correlated with their geometrical parameters such as coordination numbers.

Thus, the energy convergence seems to be approaching that of bulk as the number of clusters increases but the transition of these clusters to bulk properties is still large.

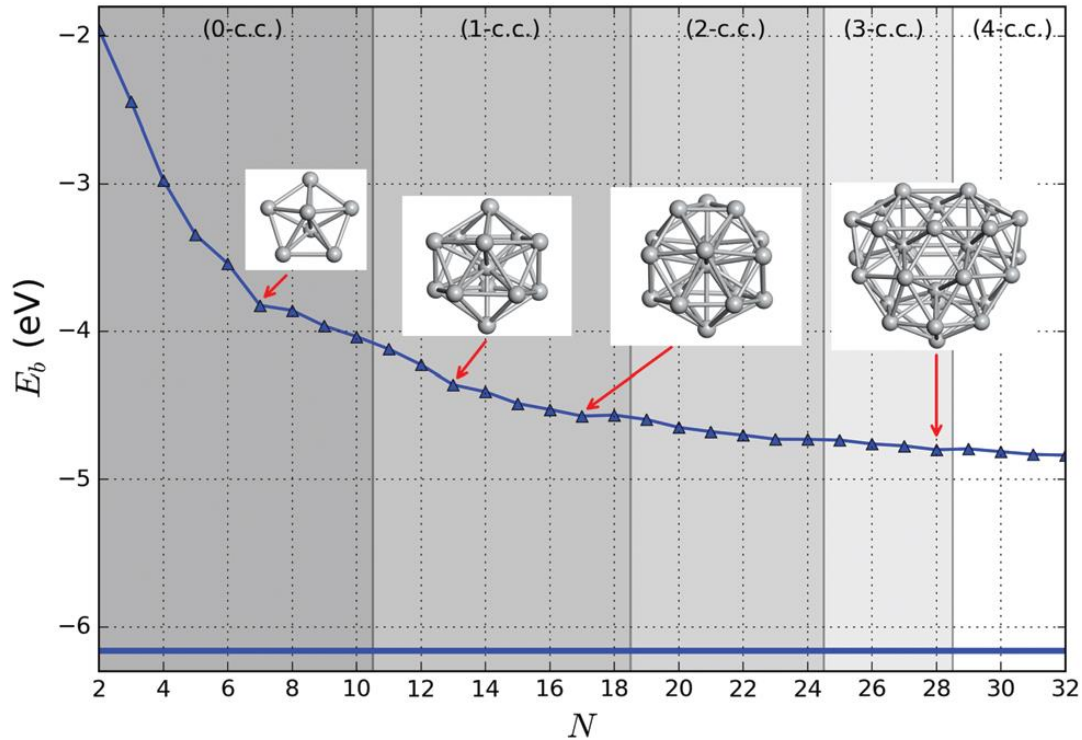


Figure 4.7: Binding energy of the tentative GM PBEsol PES. The horizontal bold line at the bottom represents the calculated binding energy of the bulk hcp (hexagonal close-packed) Ti metal. The background bands indicate the number of coordination centres (c.c.) in the tentative GM. Ball and stick models are also shown for 4 magic sized tentative GM.

The energy difference for clusters $n > 22$ is very small, which suggests that the larger clusters could alternatively exist at moderate temperatures. Fig. 4.8 shows the examinations of the first and second-order energy differences which allow us to identify the more stable structures. Higher stability clusters are classified as the magic numbers or the magic clusters, where the former indicates energetics growth or nucleation: the lower the value, the more favourable the nucleation; whereas the negative value in the latter implies greater stability of a cluster compared to clusters of neighbouring sizes, as described in ref. [33].

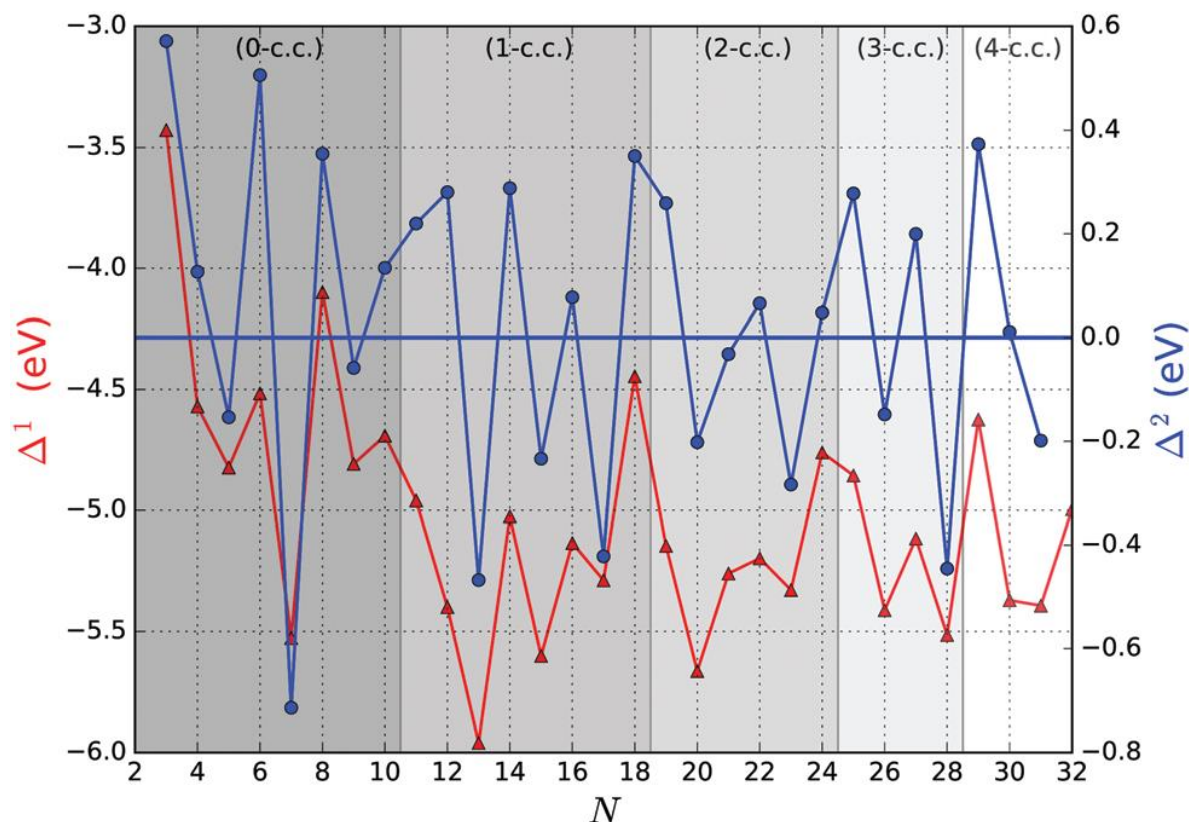


Figure 4.8: First and second-order energy differences of the tentative GM (red triangles, left vertical axis and blue circles, right vertical axis, respectively). The background bands indicate the number of coordination centres (c.c.) in the tentative GM.

Clusters with the lowest negative $\Delta^1(N)$ and $\Delta^2(N)$ values would maintain the overall stability and therefore abundance in observed mass spectra for certain sizes, also known as magic numbers. We note that $N = 5, 7^*, 9, 13^*, 15, 17^*, 20, 23, 26, 28^*$, and 31 $\Delta^1(N)$ values are in local minima, which match LM found for $\Delta^2(N)$. We mark those with particularly negative $\Delta^2(N)$ with a “*”. Magic number assignment for sizes $N = 7$ and 13 correlating to pentagonal bi-pyramid and Icosahedral isomers is in agreement with previous theoretical and experimental studies [33, 59, 247].

Significantly, the current results suggest that $N = 13$. Usually, the magic clusters are due to the geometric or electronic shell effect. If the electronic shell electronic effect dominates the bonding

of Ti clusters, the difference in the total number of electrons ought to change the magic number [257].

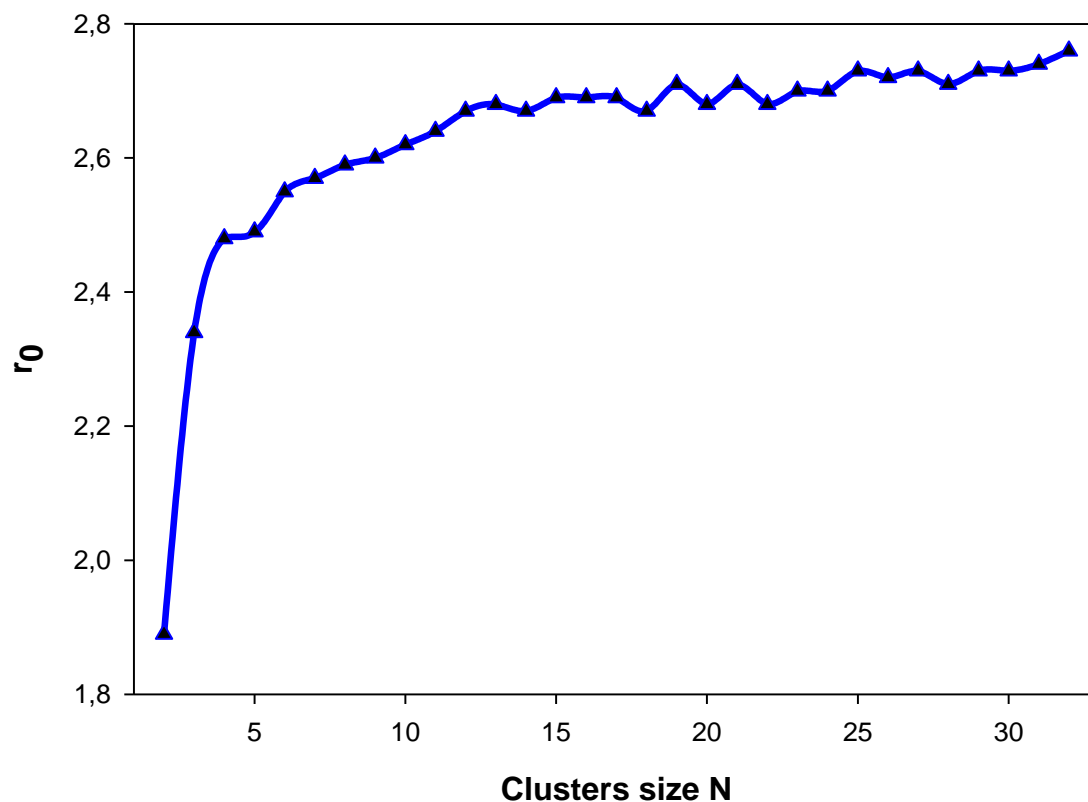


Figure 4.9: Average bonding distance varies with the cluster size.

Now, Fig. 4.9 show the average bond length r_0 as a function of cluster size N which helps to analyse the increasing average bond lengths and the increasing coordination number $\langle N_{coord} \rangle$ with cluster size and to determine how small titanium clusters progressively evolve into the bulk properties. We see that the average bond length increase monotonically with cluster size until $N = 32$ except for $N = 5, 14, 18, 20, 22, 25$ and 27 . This indicates that with the shrinking of the average bond length, these clusters would enhance their binding energy and arrive at a stable structure.

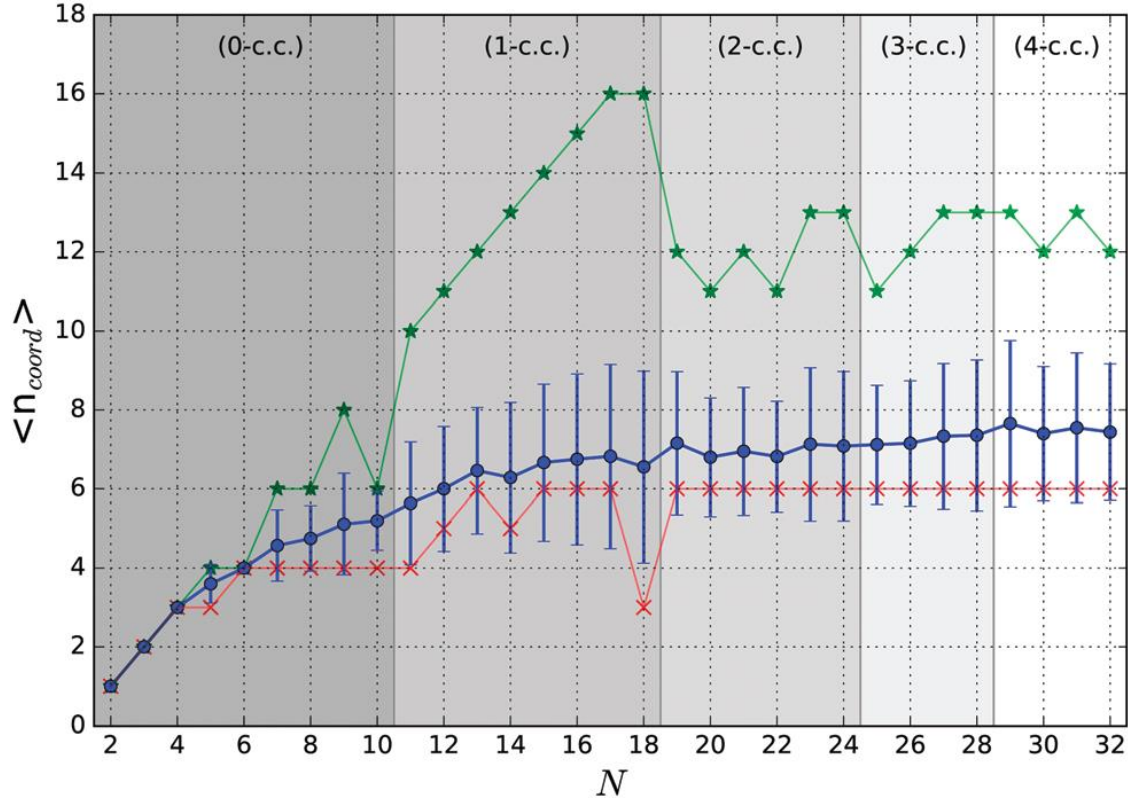


Figure 4.10: Average coordination number of the tentative GM. The blue line shows the average coordination number with 1σ error bars. The red and green lines show the minimum and maximum coordination numbers, respectively. The background bands indicate the number of coordination centres (c.c.) in the tentative GM.

In addition, an increase in the average bond length leads to a decrease in the binding energy. The dependence of the average coordination numbers $\langle N_{coord} \rangle$ on cluster size is shown in Fig. 4.10 for all tentative GM. For simplicity, we consider atoms within a range of 3.1 \AA of another atom to have a coordination bond. As expected, $\langle N_{coord} \rangle$ shows a nearly steady increase with the GM size towards the bulk hcp Ti value of 12. It is observed that there is a relationship between the average bond length and coordination number showing a similar trend and can be understood from the geometrical effects. Generally, compact transition metal clusters tend to make the structure stable by forming maximum coordination numbers with the shorter possible bond length. The coordination number increases with cluster size, in line with the increase of the binding energy.

More informative, however, are the dependencies on cluster size of the minimum and maximum coordination numbers. Starting from $N = 13$, with the exceptions for $N = 14$ and 18 , the minimum coordination number of 6 is associated with the central atom of a pentagonal ring, which, as can be seen from Fig. 4-3 and 4-4, is the main building block forming the outer shell of the clusters presented in this work. For the 0 and 1-c.c. cases, we can see almost a linear increase in the maximum coordination number, which reaches 16 at $N = 17$ for the central atom of the Z15 Frank–Kasper polyhedron. On adding an additional atom, to $N = 18$, as it was described in Fig. 4-4 an extra atom is added on one of the faces of the Z15 Frank–Kasper polyhedron.

The change in the structural motif results in the reduction of $\langle N_{coord} \rangle$ as the added atom has a coordination number of 3, as seen in the drop of the minimum coordination number which explains the reduction of the binding energy at $N = 18$. Moreover, for $N = 13$ and 17 , the neighbouring sizes have lower average coordination numbers, which indicates the possible stability of these sizes. Within the 2-c.c. region, the highest average coordination number is found for $N = 19$ cluster, which, like the $N = 21$ structure, is formed by two interpenetrating icosahedra and also has a higher $\langle N_{coord} \rangle$ than its neighbours.

A similar observation can be made for $N = 23$, but the lack of a stable trend in the coordination numbers implies no particular stability within this region. Similarly to the 1-c.c., in the 3-c.c. region we observe a steady increase in the average and maximum coordination numbers, where both reach peak values at $N = 28$, again implying the potential stability of this size. Within the 4-c.c. region, similar trends to those described for the 2-c.c. region are observed – the smallest cluster in the region has the maximum average coordination number and the consecutive sizes do not show any particular trends, thus no particular stability in the region should be expected. For Ti clusters, the adoption of high coordination structures, favours compact arrangement, presumably

due to the fact that some of the d states are empty and their energy can be lowered by increasing the coordination number.

4.4.4 Energetic distribution and surface area.

A further measure of stability can be gleaned from the energy distribution for each cluster size. The spread of energies ($E_{rel} = E_{LM}(N) - E_{GM}(N))/N$) can be seen in Fig. 4.11 for all cluster sizes.

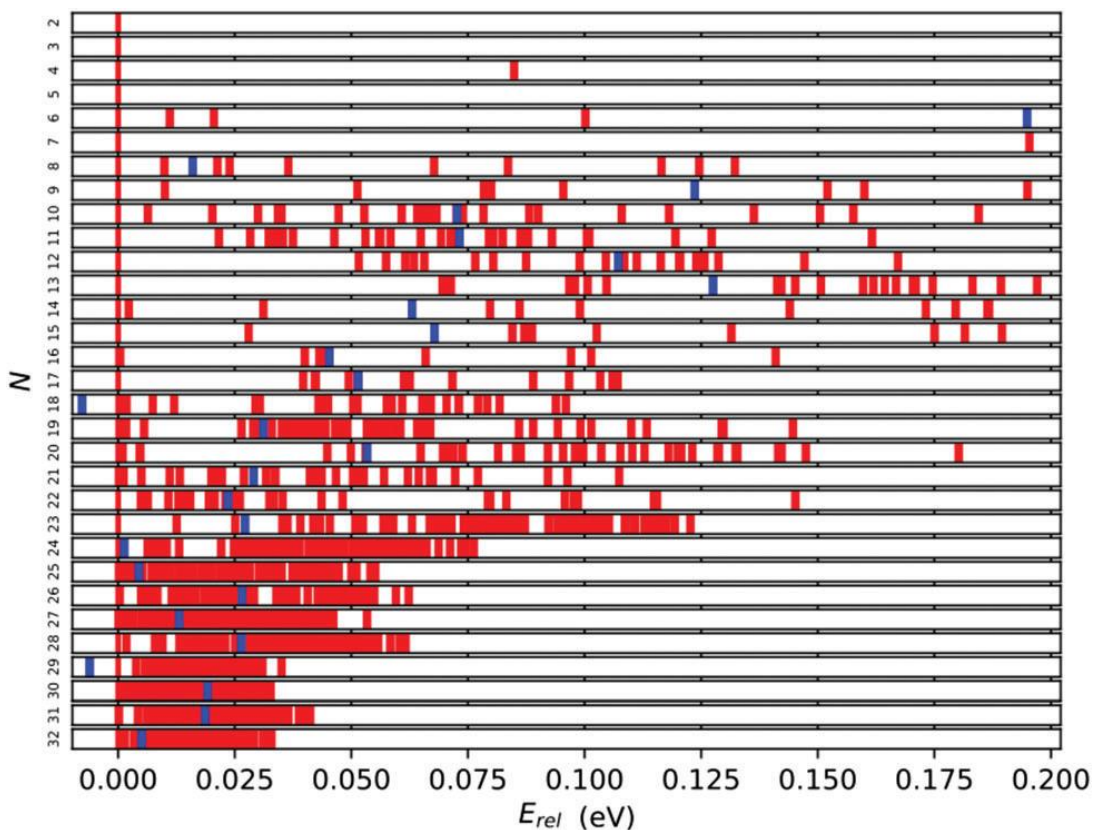


Figure 4.11: Relative LM energies per atom with respect to the tentative GM structure. The red bars represent the relative energies of the LM and the blue bars represent $[E_{rel} = E_{GM}(N-1)/(N-1) - E_{GM}(N)/N]$ for the $N-1$ tentative GM.

We expect that the wider the gap between the tentative GM (the red bar on the 0.00 eV mark) and the first lowest energy LM, the more stable the GM. From this perspective the most stable tentative GM are Ti₇, Ti₁₂, Ti₁₃, Ti₁₇, Ti₂₃, Ti₂₄ and Ti₂₉ with the relative energy gaps per atom of 0.195,

0.052, 0.070, 0.040, 0.013, 0.006 and 0.004 eV, respectively. As expected, the E_{rel} distribution narrows with cluster size, and the relative stability of the tentative GM decreases, as there are an increasing number of LM that are energetically close.

In Fig. 4.11, the blue bars indicate the relative energy of the tentative GM for size $N - 1$; the further to the left, the more stable Ti_{N-1} is with respect to Ti_N . For $N = 18$ and 29 , the tentative GM has a higher energy per atom than the corresponding $N - 1$ GM, i.e. $N = 17$ and 28 . This energetic distribution corroborates the tentative assignment of magic numbers made previously based on the binding energies and energy differences: for small Ti clusters, Ti_7 and Ti_{13} , due to the significant energy difference between the best two LM of each size, and for larger Ti clusters, Ti_{17} and Ti_{28} , owing to the unfavourable Ti_{N+1} energies.

It is useful to compare surface areas as metal clusters are often compared with liquid droplets. Such droplets are more stable when they adopt spherical shapes in order to minimise their surface area. For large clusters, we can expect the larger fraction of atoms to be located inside the cluster with the remainder exposed at the surface, which warrants a $\sim N^{2/3}$ asymptotic behaviour of the surface area, a regime we have not yet reached. For smaller clusters where the majority of atoms are on the surface, the surface area should depend on N linearly. The coefficient in the linear dependence will be determined mostly by the number of bulk atoms, or atoms playing the role of coordination centres as discussed previously. In the presence of such centres, we should also expect that the stability of a cluster will be determined both by the requirement of minimizing the surface area and maximising the average coordination number.

To check this hypothesis, we have analysed the surface area of the five lowest energy LM as a function of cluster size, shown in Fig. 4.12. Figure 4.12, indeed, shows the expected behaviour – increasing A_{surf}/N with N .

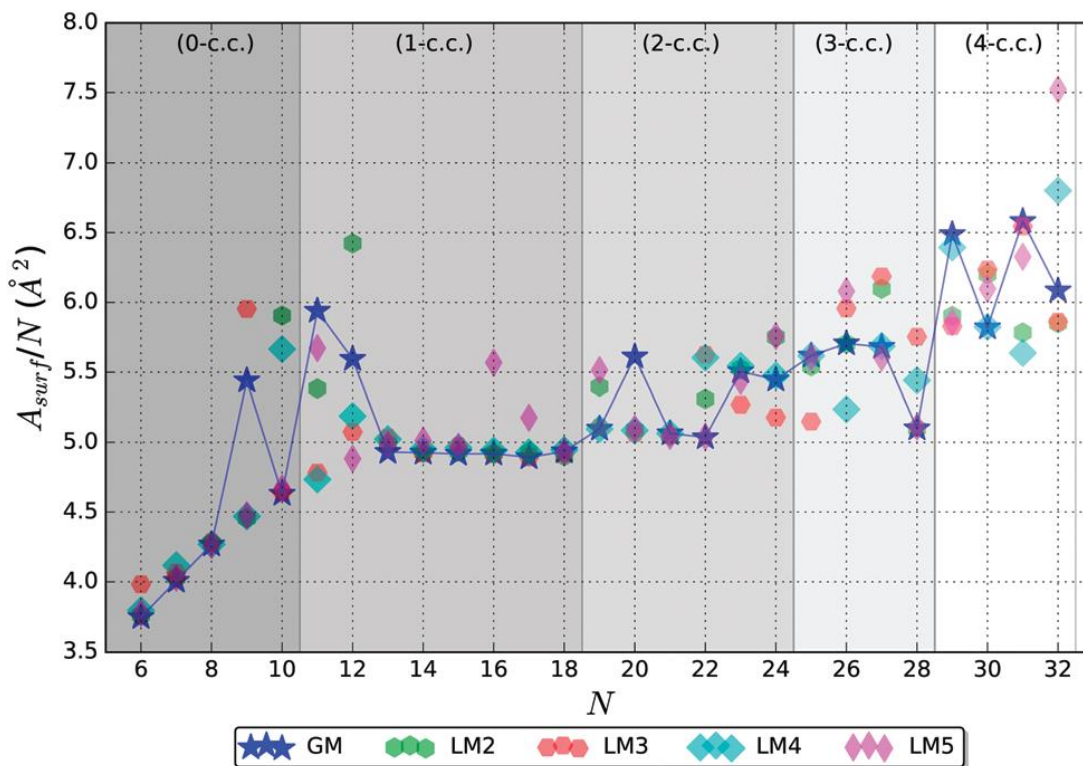


Figure 4.12: Surface area per atom for the five lowest energy LM structures. The blue line connecting the GM is a guide for the eye. The background bands indicate the number of coordination centres (c.c.) in the tentative GM.

Curiously, the lowest energy structure does not always have the lowest A_{surf}/N , and, in many cases, higher energy LM have A_{surf}/N lower than that of GM, especially for $N > 22$. Nonetheless, the A_{surf}/N correlates well with average coordination numbers and energetic measures of stability.

A spheroid concept is not applicable at the lowest end of the size scale, N , and becomes meaningful, perhaps, only from $\sim N = 6$ (*cf.* graphs in Fig. 4.3, 4.12 and 4.10). In the 0-c.c. region,

the surface is formed by a gradual increase in the number of triangular facets from 4 to 16. Before the average coordination number of surface atoms is saturated, the facet growth is faster than that of the expected spheroid area. With cluster growth, however, the discrete faceted surface resembles and approximates a spheroid more accurately. The $N = 9$ GM cluster shows a first indication of forming a coordination centre with one of the atoms increasing its coordination number to 8, while preserving coordination of the remaining atoms.

This break in the trend can clearly be seen in the increased A_{surf}/N . The 1-c.c. region thus starts with two clusters of greater surface area than expected ($N = 11$ and 12), as the GM stabilization originates from the formation of the c.c. In common with $N = 9$, the GM structures of $N = 11$ and 12 shares a similar configurational property – one pentagonal cap, which expands clusters and maximizes their surface area. From $N = 13$, the tentative GM have a more symmetrical main building block, as described in section 4.4.1, and we observe a plateau in A_{surf}/N , where it slowly decreases until $N = 17$, which, again, suggests possible stability of this particular size. In the 2-c.c. region, A_{surf}/N shows a decreasing trend reaching the lowest value at $N = 22$, except for $N = 20$. At $N = 23$, the trend is broken, which correlates with the dramatic increase in the maximum coordination number, which clearly describes the environment of the two coordination centres.

Thus we observe an interplay between the surface and bulk coordination trends, as hypothesized at the beginning of this subsection. In the 3-c.c. region, a very low A_{surf}/N GM is seen at $N = 28$, whereas the data points for the other three sizes form a rough plateau. As the sustainable coordination number $\{ \langle N_{\text{coord}} \rangle = 13$ in this c.c. region $\}$ is reached, the $N = 28$ GM adopts the first available minimum surface area configuration, which also gives a possible explanation for stability. In the 4-c.c. region, we cannot deduce any particular trends in A_{surf}/N from the available data points. The seemingly erratic behaviour can, however, be related to the increasingly intricate

balance between the surface and bulk coordination trends. As the number of c.c. increases, we expect an emergence of greater scale features that average over irregularities at neighbouring sizes. Each new c.c. centre should give rise to a new plateau until a saturation surface to bulk ratio is reached, after which the surface area per atom should show a decreasing trend with the $\sim N^{-1/3}$ asymptote and a stepwise behaviour close to the expected maximum of A_{surf}/N . We expect that this theory will be confirmed by future larger size cluster studies.

4.4.5. Refinement and electronic properties.

As the GGA exchange-correlation functionals prove to be only moderately accurate in reproducing the binding energies (compared to experiment as can be seen from a significantly better reproduction of bulk and molecular dimer energies), the tentative GM structures for each size were refined using hybrid functional (PBEsol0) single-point calculations. The PBEsol0 energies obtained were used to calculate binding energies and first and second-order energy differences.

PBEsol0 binding energy (Fig. 4.13) shows a similar behaviour with cluster size to that of the PBEsol level of theory. The match is potentially good within the 0-c.c. and 1-c.c. regions and provides further support of the stability of $N = 7, 13$ and 17 GM; likewise, the match is good within the 2-c.c. region although here the graphs are both featureless. A pronounced difference between the two levels of theory can be observed, however, within the 3-c.c. and 4-c.c. regions. On the PBEsol PES, $N = 28$ is the only size showing particular stability, whereas, on the PBEsol0 PES, it is a maximum between two tentative magic numbers: $N = 26$ in the 3-c.c. and $N = 31$ in the 4-c.c. regions, respectively. Following a similar procedure employed to assist in the assignment of magic numbers in Fig. 4.14, we now identify values of N that correspond to low LM of $\Delta^2(N)$ as measured using PBEsol0.

These are cluster sizes $N = 7^*$, 9, 13*, 15, 17, 20*, 23, 26* and 30*, where those marked with a “*” also have low LM in Δ^1 . Apart from $N = 30$, which has similar stability to $N = 31$, the remaining eight sizes matched those found previously for PBEsol GM. This includes the originally assigned $N = 7$ and 13 magic numbers.

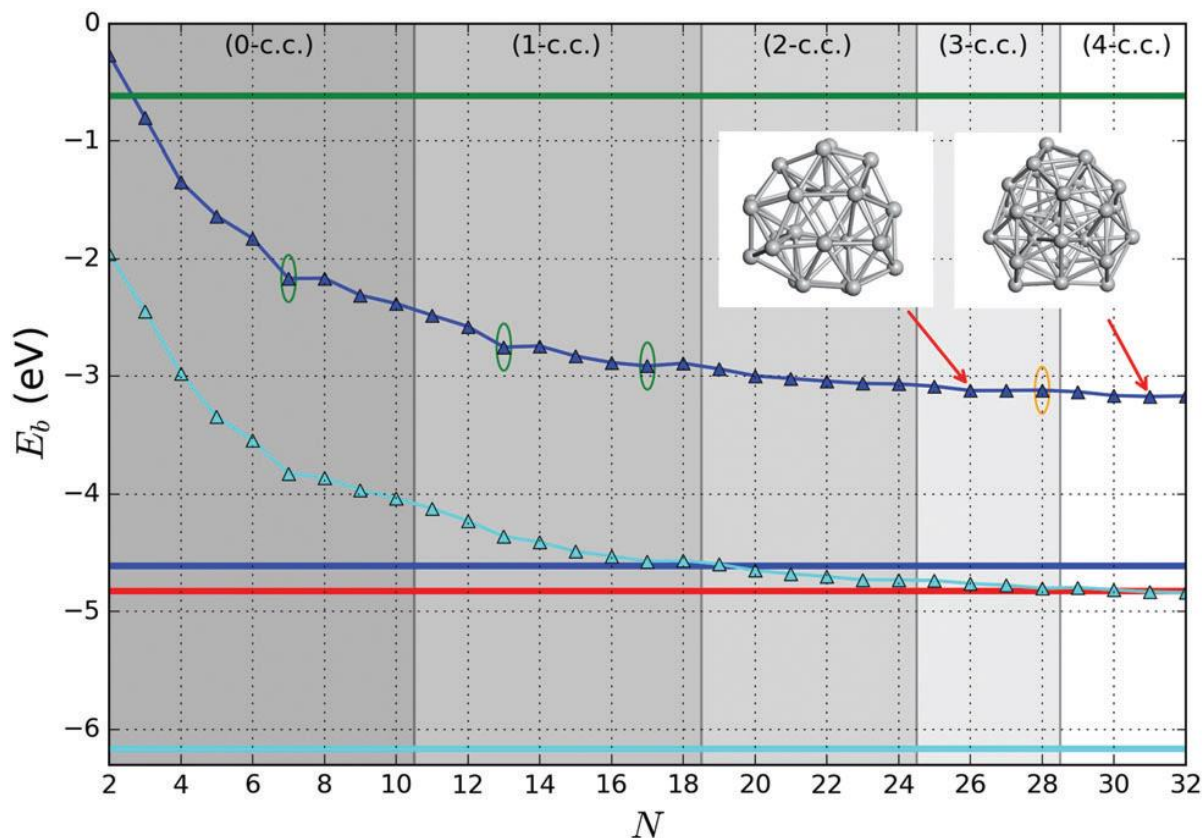


Figure 4.13: Binding energy of the tentative GM on the PBEsol0 PES (dark blue lines and triangles). The green (orange) ellipses highlight key sizes where greater stability is predicted (not) to be the same using both levels of theory. Two ball and stick models of key GM configurations on the PBEsol0 PES are marked with arrows. Bounds on the data shown are provided by the binding energies for the smallest ($N = 2$) and largest (bulk) are shown with horizontal lines: the experimental dissociation energy of Ti_2 is shown in green; [30] PBEsol0 for bulk in blue; PBEsol for bulk in cyan; and the experimental value of cohesive energy is indicated in red. [248] The background bands indicate the number of coordination centres (c.c.) in the tentative GM.

Two sizes did, however, disappear, namely $N = 5$ and 28. As the hybrid approach corrects the over binding by the PBEsol functional, the overall average slope in Fig. 4.14 decreases and so does the scale for Δ^1 . Curiously the scale for Δ^2 increases indicating the greater stability of certain size GM.

It is well known that the gap between the highest occupied molecular orbital (HOMO) and the lowest unoccupied molecular orbital (LUMO) are generally considered as a useful quantity to estimate the stability of one system.

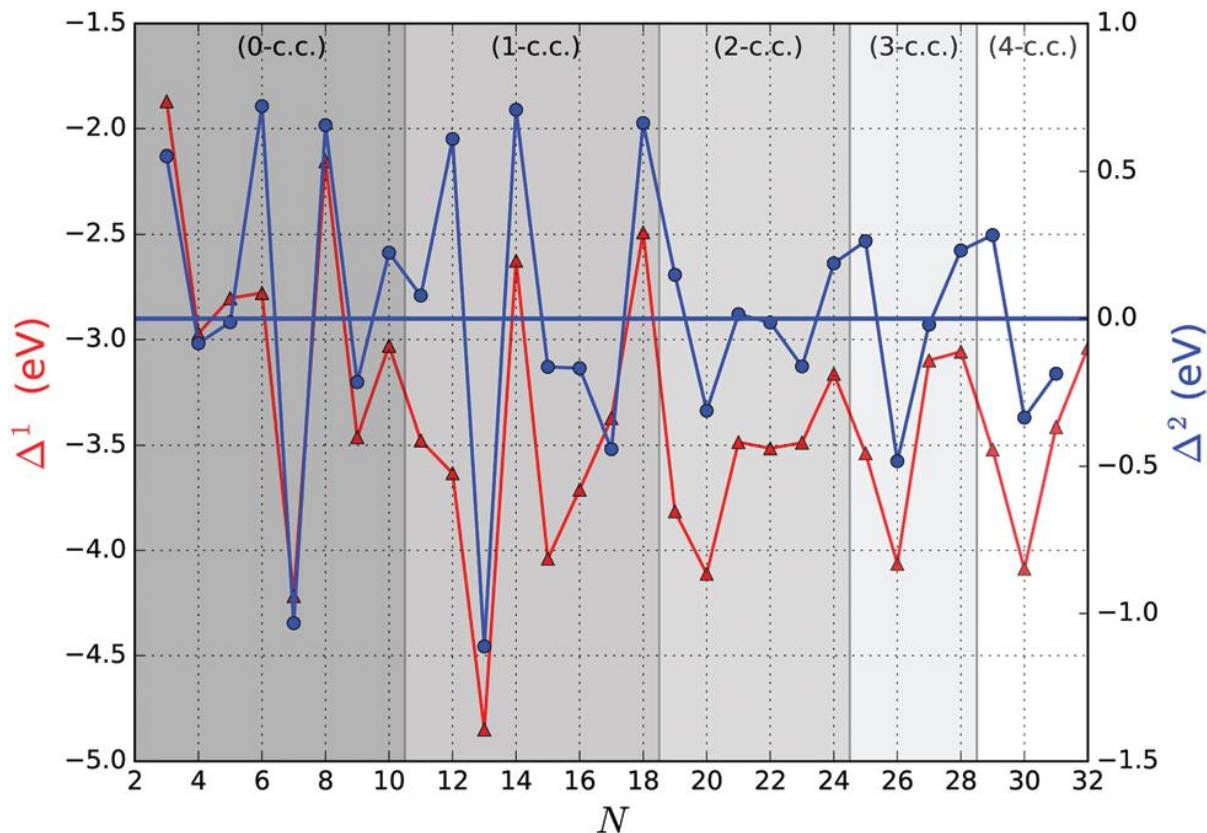


Figure 4.14: First and second-order energy differences of the tentative GM (red line, primary y-axis and blue lines, secondary y-axis, respectively) on the PBEsol0 PES. The background bands indicate the number of coordination centres (c.c.) in the tentative GM.

In Fig. 4.15 we show the energies of the highest occupied (HOMO) and the lowest unoccupied (LUMO) molecular orbitals for the two levels of theory, and in Fig. 4.15, we present the calculated HOMO–LUMO gap, ΔE . As expected, ΔE decreases with increasing cluster size.

This trend is evident in the PBEsol results but is more pronounced when employing the PBEsol0 functional. From the HOMO and LUMO energies, we observe that this decrease in ΔE is mainly a consequence of the lowering of the LUMO energy; as the cluster size increases, the quantum

confinement effect on the more diffuse conduction-band-like states decreases and the LUMO becomes more stable.

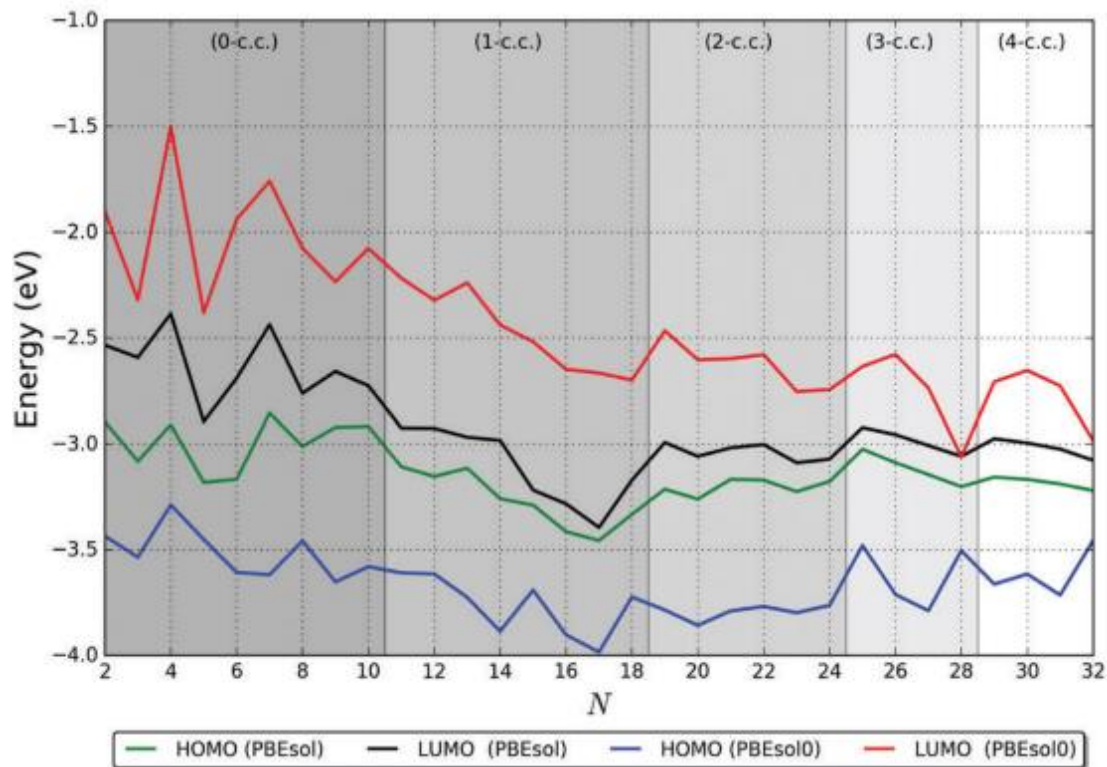


Figure 4.15: Electronic properties of tentative GM Ti_N clusters at two levels of theory: PBEsol and PBEsol0. The background bands indicate the number of coordination centres (c.c.) in the tentative GM. The HOMO and LUMO states.

The HOMO energy, however, remains relatively constant as N increases. We expect that ΔE will reduce to zero when the HOMO and LUMO energies lie between 3.5 and 4 eV, relative to vacuum, but closer to the 3.5 eV end of this range (from the PBEsol0 results). Such a value of the HOMO energy would result in a work function somewhat lower than the experimental value for bulk Ti (3.95 eV from thermionic emission, 4.06 eV from photoelectric emission;⁷⁵ note the positive sign convention for the work function, which is opposite to our convention for electronic levels relative to vacuum).

This difference can be attributed to the fact that the clusters studied here are composed of Ti atoms that are typically on the surface of the cluster as opposed to atoms coordinated in a bulk-like fashion. As a consequence, the HOMO is composed mostly of states on surface atoms and is hence less stable than it would be if the majority of atoms were bulk-like. If N were increased much further, so that the surface to volume ratio of the clusters reduced significantly and most of the atoms were coordinated as in bulk Ti, then we would expect the HOMO energy to lower and the work function to be closer to the experimental values.

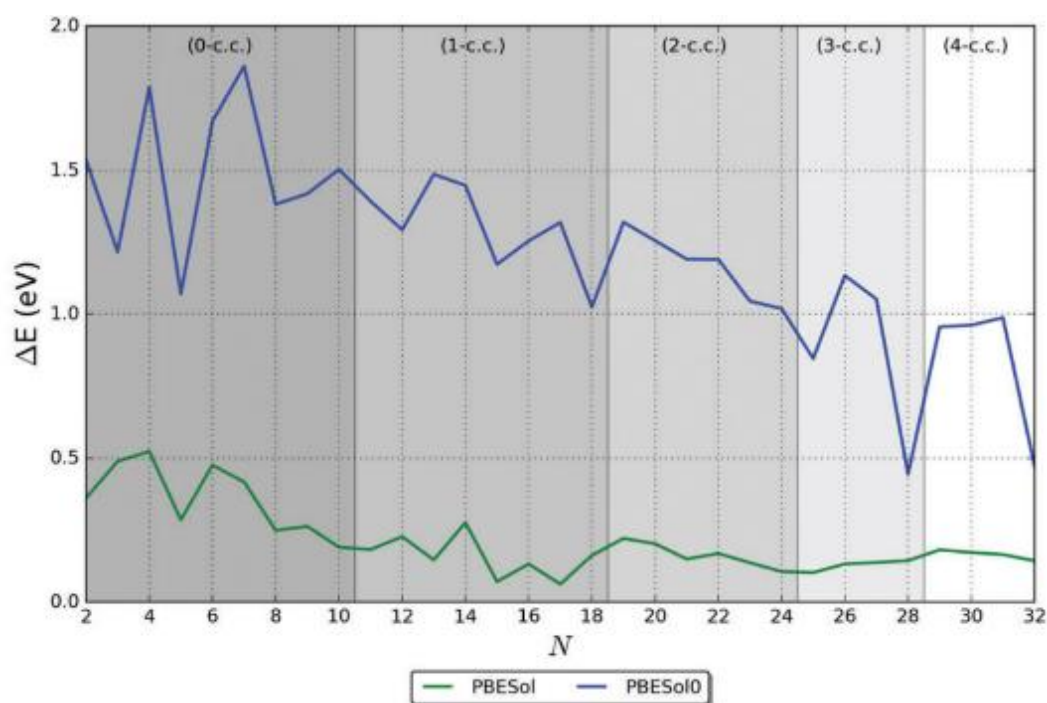


Figure 4.16: The energy difference between HOMO-LUMO

Although there is a clear overall trend in the energy of electronic states with cluster size, there is a high degree of fluctuation within this trend. It is difficult to attribute this variation to specific structural properties of the clusters, but the surface morphology, Ti coordination and ratio of surface to bulk-like atoms will all play a role. In Fig. 4.15 and 4.16, we have indicated the filling

of coordination centres by different levels of shading; we see that, from the PBEsol0 results, apart from the 0-c.c. case, whenever an inner centre becomes fully coordinated (at the right-most point of each shaded region), the gap reduces, and then increases with additional atoms forming an additional c.c.

This effect indicates a degree of stabilisation of the LUMO and destabilisation of the HOMO as the centre becomes coordinated, which may be related to (i) a reduction of the quantum confinement effect on LUMO states as more of the diffuse electron density can reside within the cluster on metallic bonds, and (ii) a decrease in the predominance of covalency.

There is no simple correlation between the ΔE and the stability ($\Delta^1(N)$ and $\Delta^2(N)$) for both exchange-correlation. Particularly, the highest maxima for $\Delta^2(N)$ (PBEsol0) are found at $N = 7, 13$ and 26 and $N = 7, 13, 17, 23, 28$ for PBEsol, whereas the ΔE shows steep for $N = 5, 12, 18$ and 28 respectively. However, from these results and the fact that the stable clusters obtained in the present study have geometrically closed structures, it is concluded that the extraordinary stability in Ti_N clusters at $N = 7$, and 13 is ascribed to the geometrical shell effect. It was reported by Chauhan *et al.* [258] that, such peaks in the $\Delta^2(N)$ without any accompanying peaks in the HOMO-LUMO gap indicate enhanced stability due to geometric effects rather than electronic effects. This work has been published in the open literature [228].

CHAPTER 5

Effect of Temperature on Ti_N nanoclusters

In this chapter, we investigate the effect of temperature on the most stable titanium nanocluster discussed in Chapter 4. The following properties: radial distribution functions (RDFs), density profiles, and mean square displacement will be investigated to evaluate the effect of temperature on the nanoclusters. Particularly, to understand how the atoms vibrate and evolved into new structural phases as the temperature is increased.

5.1 Molecular dynamics study of the stable titanium nanoclusters

Molecular dynamics calculations were performed using DL_POLY to investigate the effect of temperature on three stable nanoclusters, i.e. Ti_7 , Ti_{13} and Ti_{17} . The nanoclusters were found to form stable geometries at 0 K (as discussed in chapter 4). Two sets of calculations are considered: firstly the nanoclusters are calculated in a vacuum and secondly in the presents of Argon gas, which is done to check how the isomers are affected in different conditions.

Previously, experimental work was done to determine the metal nanoclusters, structural and dynamical properties under realistic conditions [259]. They investigated the geometry changes in Pd clusters when it is exposed to oxygen at high temperatures. The particles *ex-situ* via high-resolution electron microscopy (HRTEM) and weak beam dark field (WBDF) imaging were observed. It was found that shape changes induced after exposing Pd clusters to oxidizing environments at around 550°C are reversible after being under a reducing atmosphere. It was

observed that when the temperature is high enough to enable the surface atoms to diffuse, the cluster recovers its original equilibrium structure. Therefore, the dependence of the shape and structural changes of the nanoclusters on the temperature could bring very important knowledge and understanding for future applications.

5.2 DL_POLY parameter and settings

The MD calculations are carried out in the canonical ensemble (NVT) using Berendsen [38], Hoover [36] and Andersen [37] thermostats. The equilibration time was set at 300 ps and the production time was set at 600 ps. Periodic boundary conditions were applied in the x, y and z directions. The equation of motion is the Verlet leapfrog algorithm [230] with a time step of 0.001 ps. Simulations are performed on nanoclusters with 7, 13, 17, and 32 atoms of Ti and also supported by 100 atoms of argon gas. All simulations are made by the DL_POLY 2.20 [130] and DL_POLY 4.07 [35] packages. The equation of motion in the Argon environment was derived on the basis of the extended Lennard – Jones [260] as the effective pair potential. These parameters were chosen to monitor the inert gas effect on the Ti nanoclusters. The Gupta and Lennard-Jones parameters used in the MD calculations are shown in table 5.1. To simulate properly the thermodynamics properties of the nanoclusters, the EAM and the Born-Mayer interatomic potentials [228] were incorporated together to express the total internal energy of pure metals in terms of Gupta potentials [125].

Table 5.1 The Gupta and Lennard – Jones potential parameters

Parameters	A (eV/Å)	r₀ (Å)	p	B (eV)	q
Gupta	0.0741	2.8791	11.418	2.0059	1.643
	ε				
Parameters	(kJ/mol)	σ (Å)	-	-	-
LJ	0.996073	3.405	-	-	-

One independent MD run was performed for each twenty-three fixed temperatures, with 300 K as our lowest chosen temperature and 2400 K our highest. A run time of 300 ps was employed to equilibrate the cluster before collecting data for 600 ps. We also carry out a series of cooling processes in the temperature range 2400 – 300 K with the same equilibration and production times as in the heating process.

5.3 The search for the most effective ensemble on Ti₁₃ nanocluster in a vacuum

In this section, we search for the most effective ensemble by calculating the effect of temperature on the 13 atoms nanocluster using three ensembles (Hoover, Andersen and Berendsen) and compare their efficiency when they are employed to thermally agitate the nanocluster in a vacuum. Thereafter, we employ the most efficient thermostat to investigate the thermal agitation on the Ti₇ and Ti₁₇ nanoclusters.

5.3.1. The thermal agitated phase transition of Ti₁₃ employing Hoover thermostat

The temperature dependence on the calculated global minima nanocluster for Ti₁₃ is shown in Fig. 5.1. Recall that the Ti₁₃ nanocluster has an icosahedral configuration (discussed in chapter 4). The temperature is varied from 300 – 2400 K, above the melting point of bulk Ti. We observe no change in the morphology of the nanoclusters at a temperature from 300 – 2000K. However at 2100 K the snapshot depicts a change in the geometry. The icosahedral unit which is 1-5-1-5-1

layered stacking geometry transitions into a two interpenetrating pentagonal bi-pyramid in maroon and blue with two atoms in lime green bonded to the other pentagonal bi-pyramid.

At 2200 K we observe the atoms of the Ti_{13} geometry being redistributed into its original or equilibrium geometry, whereas at 2300 K the structural change deduces a three interpenetrating triangular-bipyramids (blue, maroon and lime green) or two interpenetrating pentagonal bi-pyramid (Blue and lime green) connected by two atoms in maroon.

The transient for 2400 K is observed to be a pentagonal bi-pyramid (grey) connected to two interpenetrating triangular bi-pyramid (gold and light blue). The most dominant unit deduced as the building block for these thermal transitions is the pentagonal bi-pyramid which has been found as the meta-stable configuration in discussed in chapter 3 and it also forms part of the building block for the formation of the icosahedron unit. These cluster transitions show the structural transition behaviour at higher temperatures above the bulk Ti melting point of 1941.15 K.

However, the behaviour of other nanoclusters was reported to have melting points decreasing with decreasing nanocluster size [261, 262]. This is contrary to our current findings; the nanoclusters are observed to have solid-liquid features at 2100 K above the bulk Ti melting point. This might be ascribed to the facets or planes at the tip of the cluster that make the cluster to be compact and remain almost unaffected.

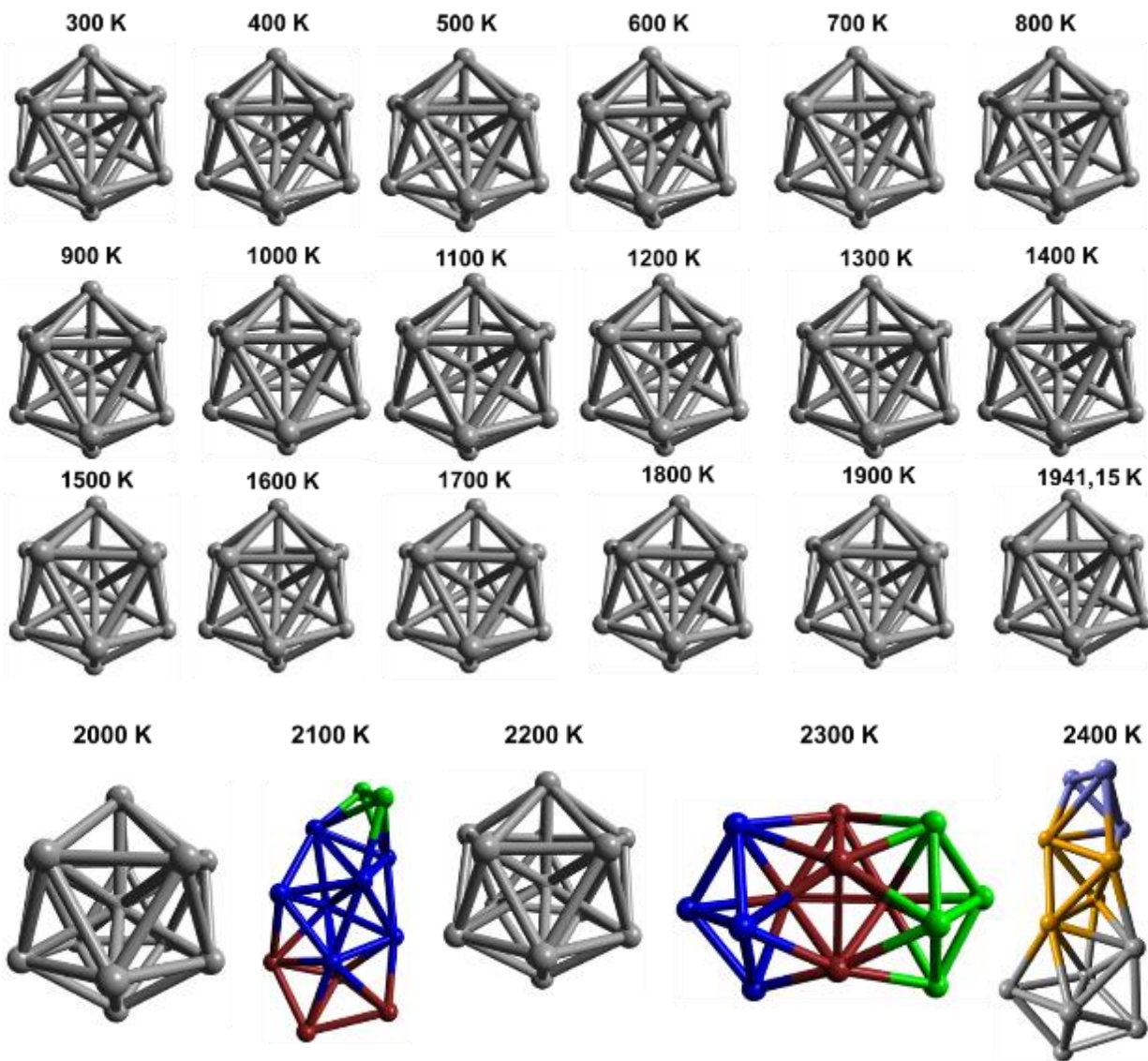


Figure 5.1: Ti_{13} nanocluster in the vacuum at various temperatures.

5.3.2. The thermal agitated phase transition of Ti_{13} employing Andersen thermostat

In the case of Andersen thermostat in Fig. 5.2, some of the icosahedral geometries are observed to have distortion features that involve the stretching of the nanocluster at 1100 – 1600 K.

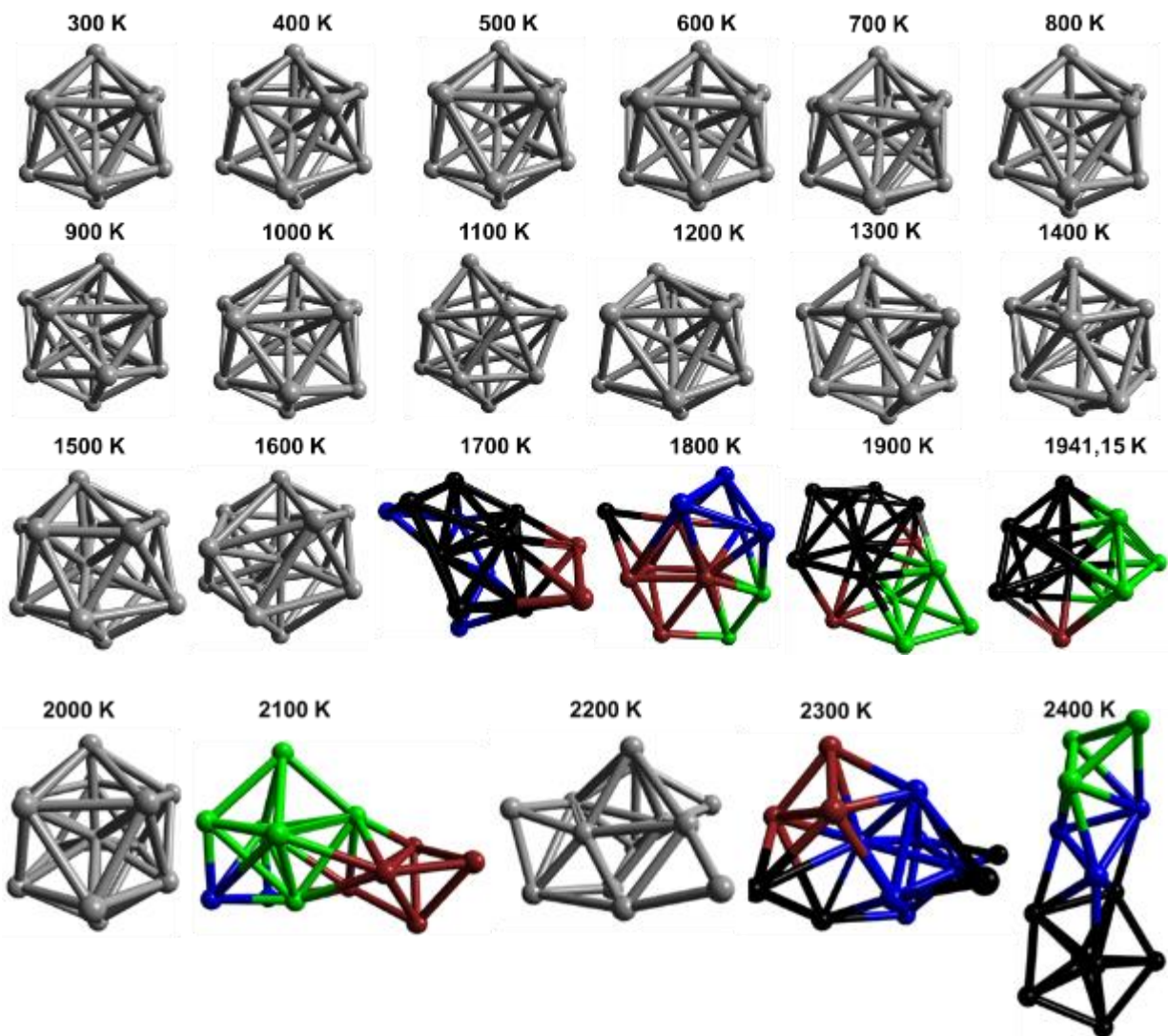


Figure 5.2: Snapshots Ti_{13} nanocluster in vacuum showing changes in the geometry at elevated temperatures.

These observations were not found for Hoover thermostat at such temperatures. However, the Hoover thermostat showed structural distortions at $T > 2000$ K. In the case of Andersen thermostat, the minimal icosahedral distortions are observed at 700 K. This behaviour might be ascribed to the algorithm that decorrelates velocities of the atoms in the cluster and giving dynamics that is actually not physical as compared to Hoover. The distortions in the system appear to be enhanced as the temperature is increased. We observe the nanocluster transitioning into two interpenetrating pentagonal bi-pyramid (black and maroon) with penta-atoms (lime green) connected to them at 1700 K. The thermal agitation on the metal nanoclusters is frequently reported to show melting like features below the bulk melting point. The same phenomena is observed with the Andersen thermostat.

The transient for 1800 K is observed to be two interpenetrating octahedral units (blue and Maroon) with an atom (black) connected to the maroon isomer and two atoms (lime green) connected to both of the isomers. At 1900 K, the thermal agitation is observed to have changed the nanocluster into pentagonal bi-pyramid (black) interpenetrating with octahedral unit (lime green) connected to two atoms (maroon).

The thermal agitation at 1941.15 K deduce a partial redistribution of atoms into the original shape which yielded in the atoms of the nanocluster being completely redistributed into its original morphology at 2000 K. The transient for 1941.15 K is observed to be a pentagonal bi-pyramid (black) coexisting with octahedral isomer (green) which are connected to an atom (maroon). The 2100 K thermal agitation is observed to transient the nanocluster into octahedral (lime green) isomer coexisting with triangular bi-pyramidal (maroon) with an atom (blue) connected to the octahedral unit. At 2200 K, we observed distorted icosahedra dominated by the building blocks of all the nanoclusters; the triangular fragmentation.

5.3.3. The thermal agitated phase transition of Ti_{13} employing Berendsen thermostat

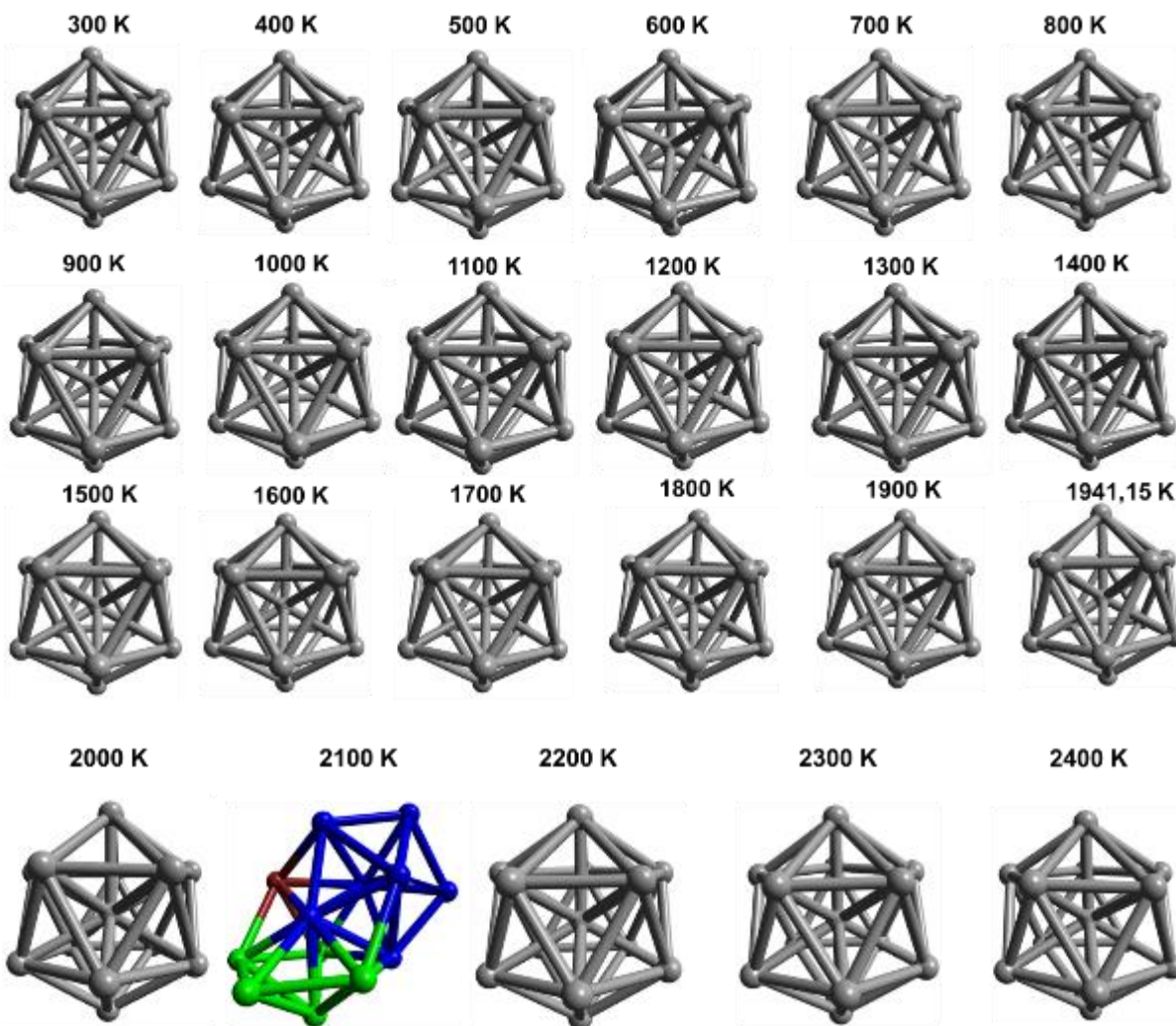


Figure 5.3: Snapshots for Ti_{13} nanoclusters showing configurational changes as a function of temperature.

The transition at 2300 K is observed to be the octahedron (lime green) coexisting with triangular bi-pyramidal (maroon) and tetrahedral units (black) with two atoms (black) connected to the lime green unit. Moreover, the transient for 2400 K is observed to be a pentagonal bi-pyramid (black) coexisting with two interpenetrating triangular bi-pyramidal (blue and lime green). At 2400 K,

Hoover and Anderson's thermostat appears to have similar thermal transients. However, Andersen thermostat is observed to have a structural transition at 1700 K compared to 2100 K for Hoover thermostat.

In the case of Berendsen thermostat, there are no distortions observed on the icosahedra unit at $T < 2100$ K and $T > 2100$ K. Andersen thermostat appeared to have minor distortions or structural deformation at 600 K. However, total distortions were observed at 1700 K. Hoover thermostat appeared to have distortions at $T > 2000$ K and $T > 2100$ K. The Berendsen thermostat depicts a structural change from icosahedron to a two coexisting pentagonal bi-pyramid (lime green and blue) with an atom (maroon) connected to both pentagonal units at 2100 K which is similarly depicted with Hoover thermostat. Moreover, the redistribution of atoms to its equilibrium geometry is observed at $T > 2200$ K.

5.3.4. The potential energy (heating and cooling) on Ti_{13} nanocluster

Figure 5.4 shows the variation in potential energy for the 13-atom icosahedral shaped Ti nanocluster. The potential energy is used as the indicator for solid-liquid (melting point) transitions of a cluster. As reported in the literature [124], the melting point is defined as the transition temperature corresponding to the temperature of observed phase change during heating and cooling.

The potential energies for the Hoover thermostat show linearity in the energy between 300 K and 2000 K. However, after 2000 K there is a significant deviation from linearity at 2100 K with the potential energy of -52.70 eV. This phenomenon is also observed in Fig. 5.1 where the Ti_{13} geometry is found to transition into a new unit.

This could be attributed to the transformation of the nanocluster from the solid phase to a liquid phase. However, the melting behaviour is observed to be higher than that of the bulk melting point of 1941.15 K. The same observations were reported by Chacko *et al.* [263], they found that Tin and Gallium nanoclusters remained solid above the melting point, which was attributed to structures having bonding that are significantly different from the bulk [263].

The plot depicts a sudden drop of the energy at 2200 K which affirms the behaviour of 13-atoms redistributing into their original geometry in Fig 5.1 that is observed at $T < 2000$ K. Hence the energy appears to follow the linearity trend at $T < 2100$ K.

Upon cooling, the nanocluster undergoes a liquid-solid transition and shows a more negative drop in the potential energy at 2100 K. The increase of the energy is minimized. The drop in potential energy upon cooling shows a rather strong hysteresis loop, where the melting-freezing transition is not unusual and is expected both theoretically [264] and experimentally reported in the study of Pb [265] and Na [266].

Chausak and Bartell [267] reported that the structural changes resulting from cooling and melting also influences the phase transition and result in hysteresis. However, the potential energy of the new solid phase does not show much difference with the solid phase during heating at a temperature below 1400 K. Although they show a difference at a temperature above 1400 K.

The Andersen thermostat contributions in the melting are also observed by a sharp jump in the potential energy. At 500 K, we observe a smaller jump which suggests early distortions of the nanocluster. The melting transition of Ti_{13} nanocluster from solid to liquid occurs at 2200 K which is above the bulk melting temperature of 1941.15 K.

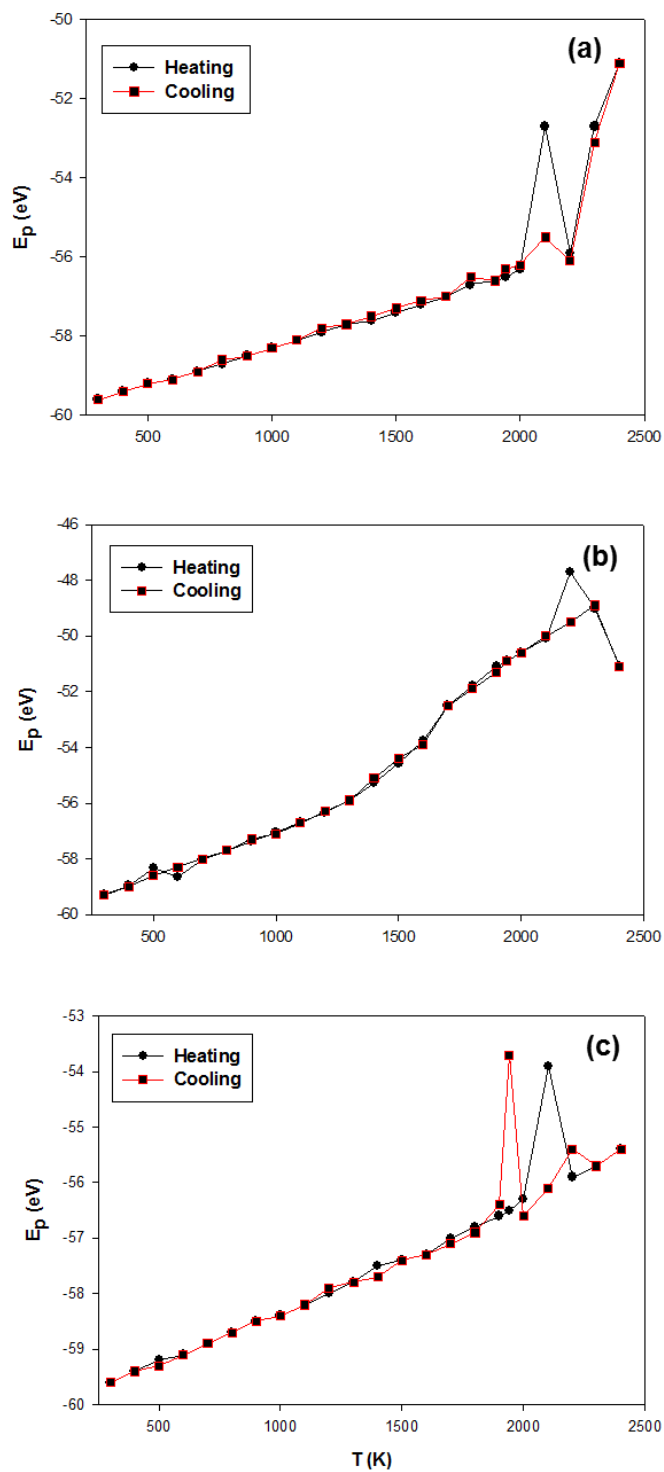


Figure 5.4: The potential energy (E_p) for the heating and cooling using (a) Hoover, (b) Andersen and (c) Berendsen thermostats.

However at 1800 K, 1900 K and 1941.15 K we observe no indication of the melting behaviour and similar results were observed for the Hoover thermostat. The Hoover thermostat appeared to have a liquid-like behaviour at 2100 K compared to 2200 K for the Andersen thermostat.

As the nanoclusters undergo cooling, the energies are observed to be enhanced at 2300 – 2100 K. We observe a drop in the energy at 2200 K showing a more negative compared to heating. This may be ascribed to the formation of new stable phases as the system is cooled. Most Andersen energies have similar heating-cooling energies as compared to Hoover energies.

The hysteresis at 2000 K does not appear reduced or lowered similarly with Hoover energies. Moreover, the potential energy of the new solid phase is slightly different at 600 K compared to the energy during heating.

In the case of the Berendsen thermostat, the potential energy shows linearity and the loss of stability as the temperature increases. Although the nanoclusters also show no distortions, the potential energy depicts energy gain which frequently has to do with the loss of structural morphologies. However, at 2100 K we notice a sudden jump which may be attributed to structural transitions. This phenomenon is as well depicted in Fig 5.2. Furthermore, the linearity in the potential energy may be ascribed to nanoclusters having minimal distortions due to energy gain but structurally intact.

The geometry was observed have transitioned at 2100 K and its atoms being redistributed into their original morphology at 2200 K which is associated with the sudden drop in the potential energy at 2200 K. The potential energies during cooling show similar trends at temperatures below 1900 K. There is energy gain observed at 2200 K which is attributed to instability and the formation of a new phase. However, the lowering in energy at 2100 K may be attributed to the formation of

a new stable phase. Furthermore, temperature decreases, we observe a jump in the energy at 1941.15 K not at 2100 K as observed during the heating. This phenomenon is attributed to the energy gain and the formation of a new unstable phase as compared to heating. The Hoover and Berendsen thermostat are observed to have similar potential energy (-60 eV) at 300 K.

The Andersen thermostat is observed to have higher potential energy at 300 K valuing at -59.7 eV. However, at 2100 K and 2200 K temperatures (where they appear to have solid-liquid like features), the Berendsen thermostat is observed to have enhanced energy (-57.2 eV) while Andersen displayed the highest energy value of -51.1 eV.

5.3.5. Mean square displacement (MSD) for Ti₁₃ nanocluster at various temperatures

The melting temperature indicator of the system is through the mean square displacement (MSD) of ions. The MSD is a combination of how far the atoms inside the nanocluster moved. Figure 5.5 shows the mean square displacement at varied temperature. The mean square displacements for the Hoover thermostat is observed to be of higher magnitude than Berendsen thermostat. We observe fluctuations of the MSD at 300 – 900 K and the nanoclusters stabilizing at 1000 – 1800 K. However, at 1900 – 2400 K we observe higher fluctuations which are ascribed to high vibrations of the atoms as the nanocluster is thermally agitated.

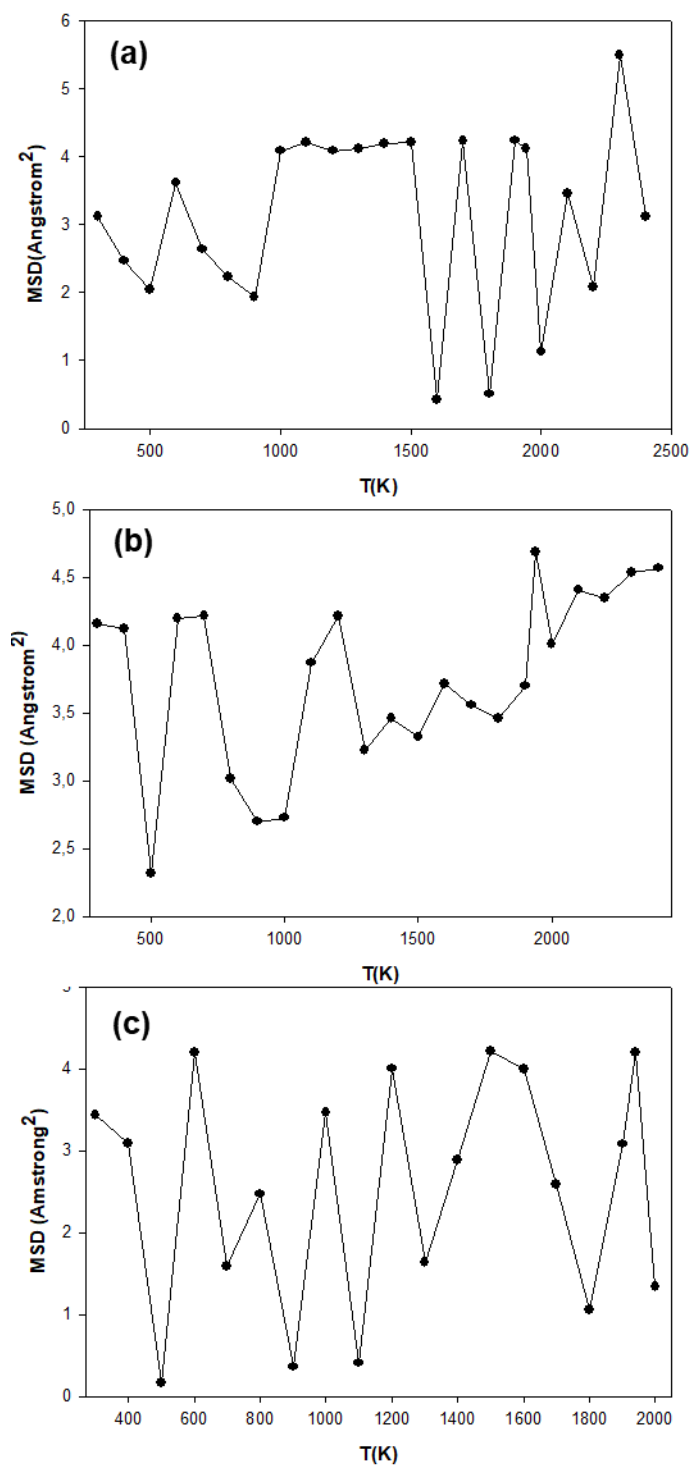


Figure 5.5: Mean square displacement (MSD) for Ti_{13} nanoclusters at various temperatures for (a) Hoover, (b) Andersen and (c) Berendsen ensembles.

These fluctuations might be due to the nanocluster exhibiting molecular behaviour since it is below 500 atoms. Qi *et al.* [268] reported that Ni nanoclusters exhibit a molecular behaviour below 500 atoms, but have well-defined bulk and surface properties above 750 atoms.

The MSD for Andersen thermostat are observed to have vibrational instability at 300 – 900 K and stabilizes at 1400 – 2400 K. There is a smooth vibrational activity as the temperature is elevated. The Berendsen thermostat is observed to have MSD values that are of lesser magnitude compared to the thermostats. There is a higher degree of fluctuations observed which alludes to the high vibrational activity of atoms in the nanocluster.

All the thermostats show the Ti mobility decreasing and increasing. This is ascribed to the displacement of surface atoms which are more mobile than core atoms and the nanocluster evolving towards a more stable structure that is lower in energy through the diffusion of the atoms. Similar observations were reported by Lamas and Balbuena [269].

5.3.6. The radial distribution function for Ti₁₃ nanocluster

Fig. 5.6 shows the RDFs of the Ti₁₃ nanocluster at different temperatures. There is a similar trend observed for both the thermostat (Hoover and Andersen). The radial distances of the nanocluster change as the temperature is increased as observed in all the peaks. For Hoover and Berendsen thermostats, the first peaks correspond to the radial distance of 0.25 Angstroms. However, at 2400K the radial distance change to 0.36 Angstroms. This is indicated by the broadening of the peaks at increased temperatures.

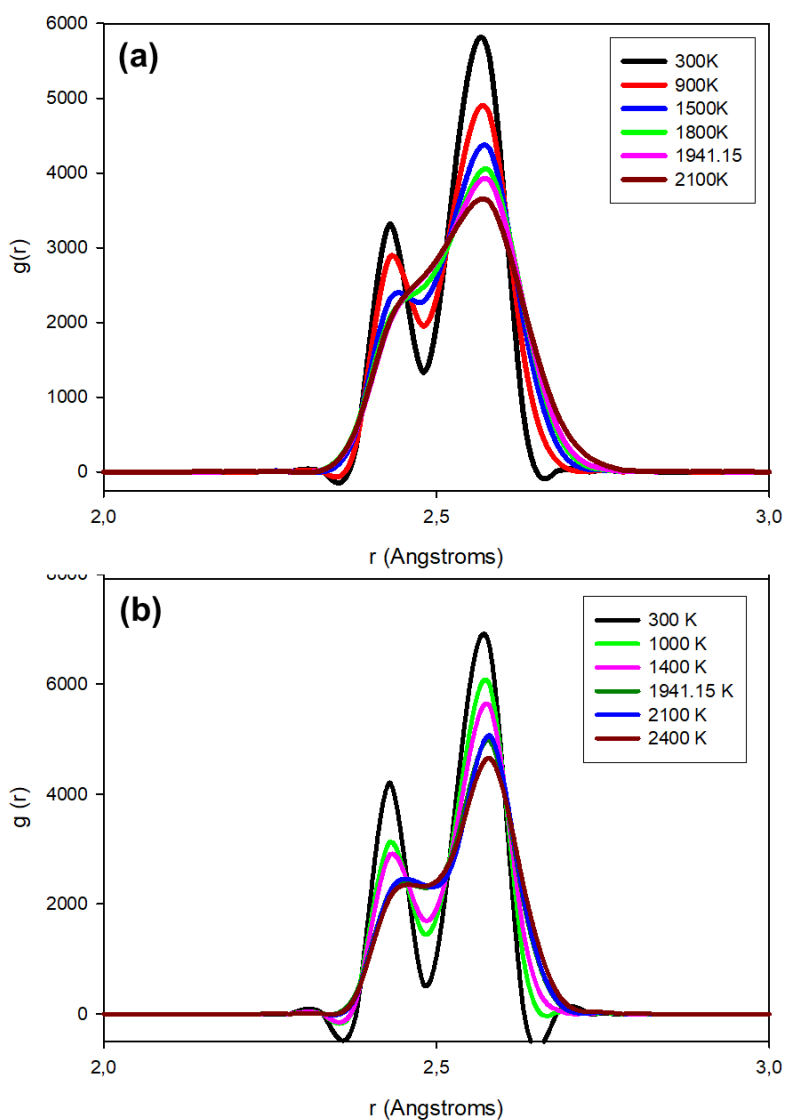


Figure 5.6: The radial distribution functions (RDFs) of the Ti_{13} at various temperatures for (a) Hoover and (b) Berendsen thermostats.

At 300 K and 900 K, we observe sharp peaks and pre-melting peaks with higher magnitude implying that the morphology of the structure is still crystalline. We observe that at 300 K the RDF have a sharp peak, however at 1800 K to 2100 K the peaks become broader. Moreover, at 1941.15 K the melting point of the bulk titanium, we observe the magnitude of the peaks decreasing which

is indicative of the morphology transition and the system approaching a melting point. Additionally, at 1941.45 K and 2100 K, the pre-melting peaks are depicted disappeared which also illustrates that the nanocluster is approaching the solid-liquid phase transitions.

5.3.7. Density profiles for Ti₁₃ nanoclusters at various temperatures

Figure 5.7 shows the atomic distribution of atoms during the melting process for the Ti₁₃ nanocluster along the z-axis using Hoover and Berendsen as the thermostats. Note that similarly at lower temperatures (300 – 900 K), solid-like features are preserved as suggested by the distinct peaks or atoms have higher distribution. As the temperature increases, the peaks at the centre decreases.

However, an emerging higher temperature peak appears at 1941.15 K which is the melting temperature for Ti bulk. These phenomena might be due to the nanocluster thermally affected the same as geometries at $T < 1500$ K. However, at temperatures 1800 K and 2100 K the peaks are no longer distinct at the centre and the higher degree of fluctuation are reduced.

In the case of Berendsen, we investigate the effect of thermal agitation beyond 1941.15 K. The Hoover and Berendsen thermostat showed similar trends in Fig. 5.6. The same is observed with density profiles. Hence we carried out this calculation to have more insight into what transpires beyond the melting point. The nanoclusters which are still orderly orientated shows the solid-like features which are indicated by the distinct peaks.

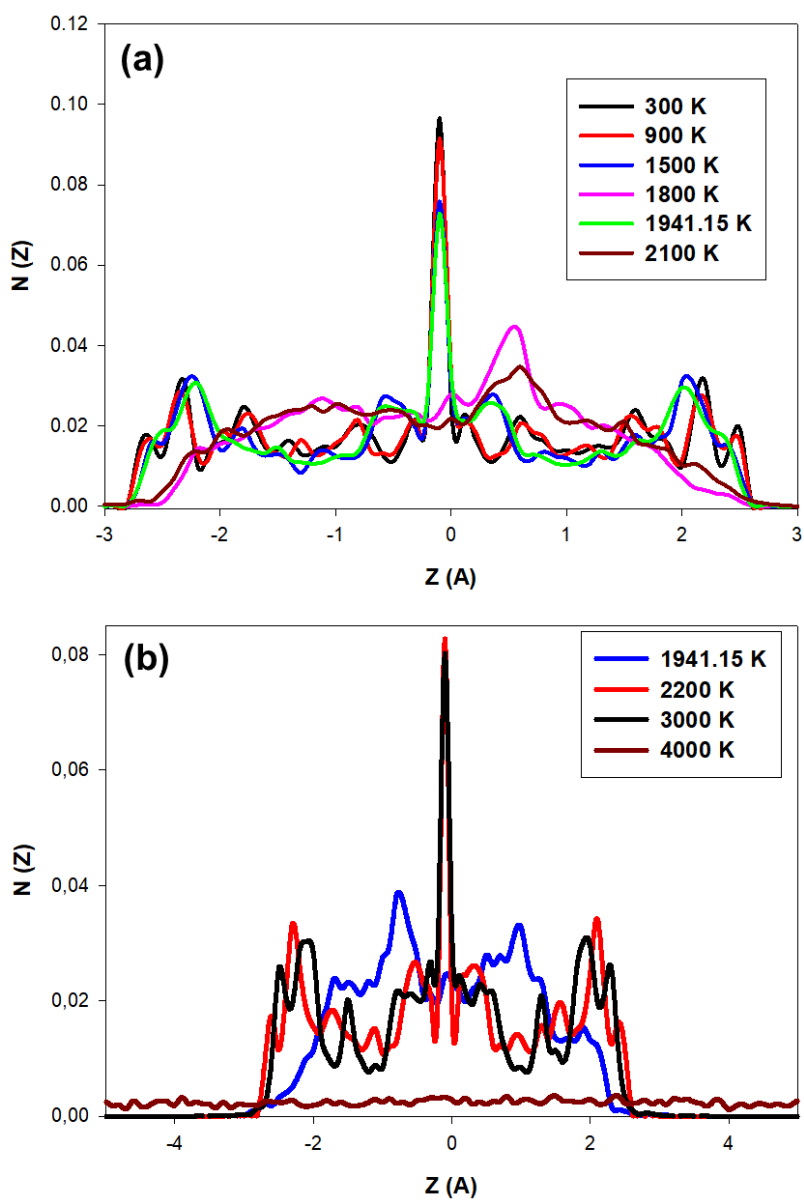


Figure 5.7: Comparison of Ti_{13} nanocluster atomic distribution for (a) Hoover and (b) Berendsen ensembles along a Cartesian coordinate (z) at different temperatures.

The atomic distribution depicts an overlap of the peaks at 2000 K and 3000 K which suggests solid-like features. However, the peak at 1941.15 K shows a reduced magnitude of the peak which suggests a liquid-like feature indicating the formation of a new phase. Furthermore, at 4000 K

beyond the Ti bulk melting temperature, the atomic distribution peak becomes extensively flattened which alludes to a liquid phase.

5.4 The search for the most effective ensemble on Ti₁₃ nanoclusters in an Argon gas environment

In this section, we carry out a systematic classical molecular dynamics (MD) study of the pressure effect exerted by the Ar environment on a 13-atom Ti nanocluster at various temperatures. In the previous section, the observations for Hoover and Berendsen thermostats showed N = 13 nanocluster in a vacuum having melting like features above bulk Ti melting point. The inert gas with 100 atoms is introduced to increase the kinetic energy of the thermally agitated nanocluster. This, in turn, is expected to result in the nanocluster having features like melting behaviour below Ti bulk melting point.

The Argon gas is widely used to produce an inert atmosphere in Ti casting machines. It is capable of allowing arc melting to be carried at lower temperatures or pressures, reducing casting defects. Argon gas can escape easier through the pores of the material [270]. The effect of gas adsorption on the nanoclusters was investigated by Graoui [259], Hansen *et al.*, [271] and Wu *et al.*, [272], it was found that the geometry of their nanoclusters is influenced by the nature of the substrate and gas atmosphere. Furthermore, reversible changes are strongly dependent on the nature of the gas phase [269].

5.4.1. The thermal agitated phase transition of Ti_{13} employing Hoover thermostat in an inert gas

In the case of Hoover thermostat, at 300 K an orderly structure still observed. However, as the temperature increases, we observe the structure gradually losing the coordination of atoms which may be attributed to the influence of the Argon gas and its kinetic energies

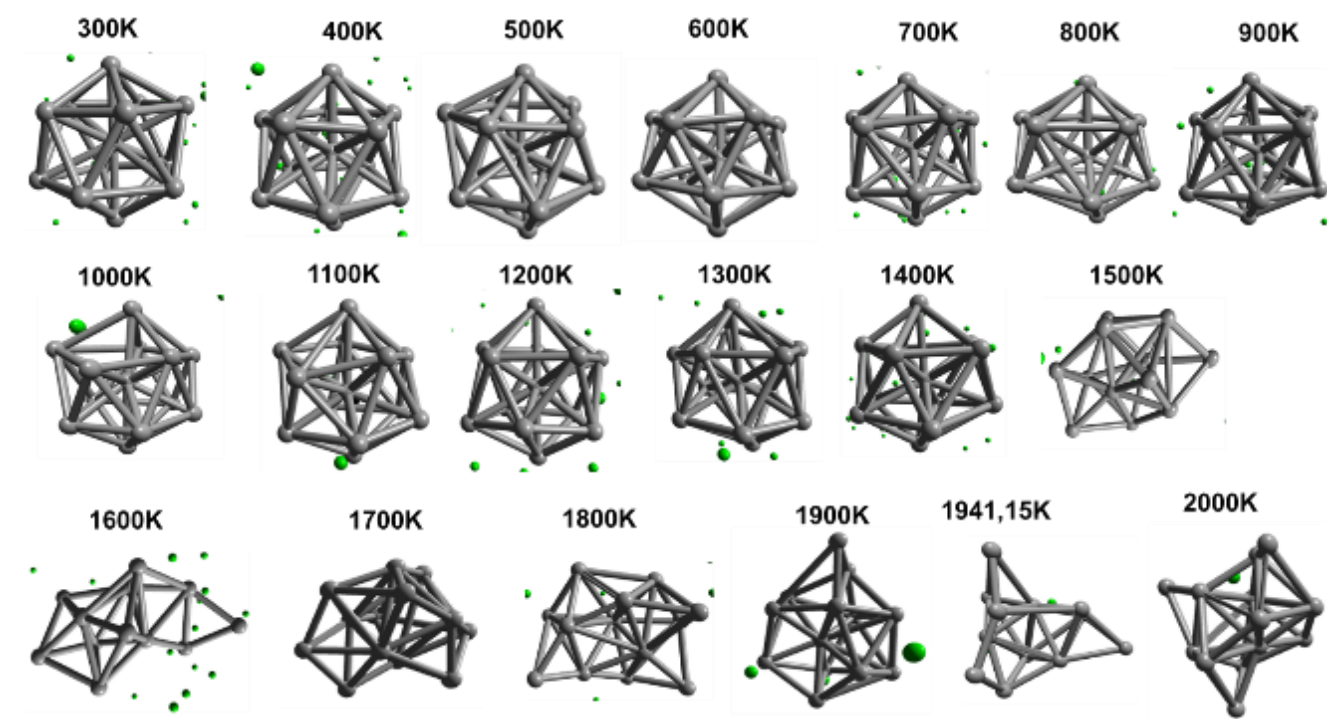


Figure 5.8: The Ti_{13} nanocluster inserted in an inert gas at various, where the green circles represents Ar atoms temperatures.

on the nanocluster at lower temperatures due to the Argon gas-liquid state (83.81 K). The nanocluster show features of distorted icosahedra at a mere 300 K. This phenomena is expected due to the greater mass of Argon atoms, which may lead to larger momentum influenced by its liquid state. Therefore, it exerts a stronger impact on the top 5-layer in the 1-5-1-5-1 layered stacking or on the surface of the nanocluster.

Furthermore, the bonding of the Ti-Ti layered atoms shows distortions on the geometry at temperatures below the melting of Ti bulk. This is consistent with the fact that the higher temperatures give the inert gas more kinetic energy and this effect result in the Ti nanocluster losing their morphology and reduced melting features as compared to vacuum.

At $T > 1000$ K, the nanoclusters are showing features that are associated with liquid-like behaviour that involves the stretching of the nanocluster at $\langle 112 \rangle$ direction. The temperature range 300 – 2000 K depicts the distortion of the equilibrium structural shape at 1500K which is reasonably not far from the melting temperature of Ti as compared to Ti_{13} nanocluster in a vacuum. The melting temperature is reduced upon thermally subjecting the nanocluster into the Argon environment.

5.4.2. The thermal agitated phase transition of Ti_{13} employing Andersen thermostat in an inert gas

In the case of the nanocluster insertion in the Argon gas shown in Fig. 5.9, the same effects (structural distortions) are also observed with the Andersen thermostat. At 300 K and temperatures up to 900 K, an orderly icosahedral structure is observed.

There are no distortions observed on the icosahedral isomer at $T < 1000$ K. At $T > 1000$ K we observe a distortion at the bottom coordination affecting the 1-5-1 layered stacking which yielded structure at 1300 K to lose its ordered structure. However, from 1400 – 1500 K, the nanocluster appears to have transitioned back into its initial configuration. Furthermore, we also observe a complete distortion of the nanocluster at $T > 1600$ K which did not result in the formation of a new phase that forms part of the building block of the nanocluster as it is thermally agitated.

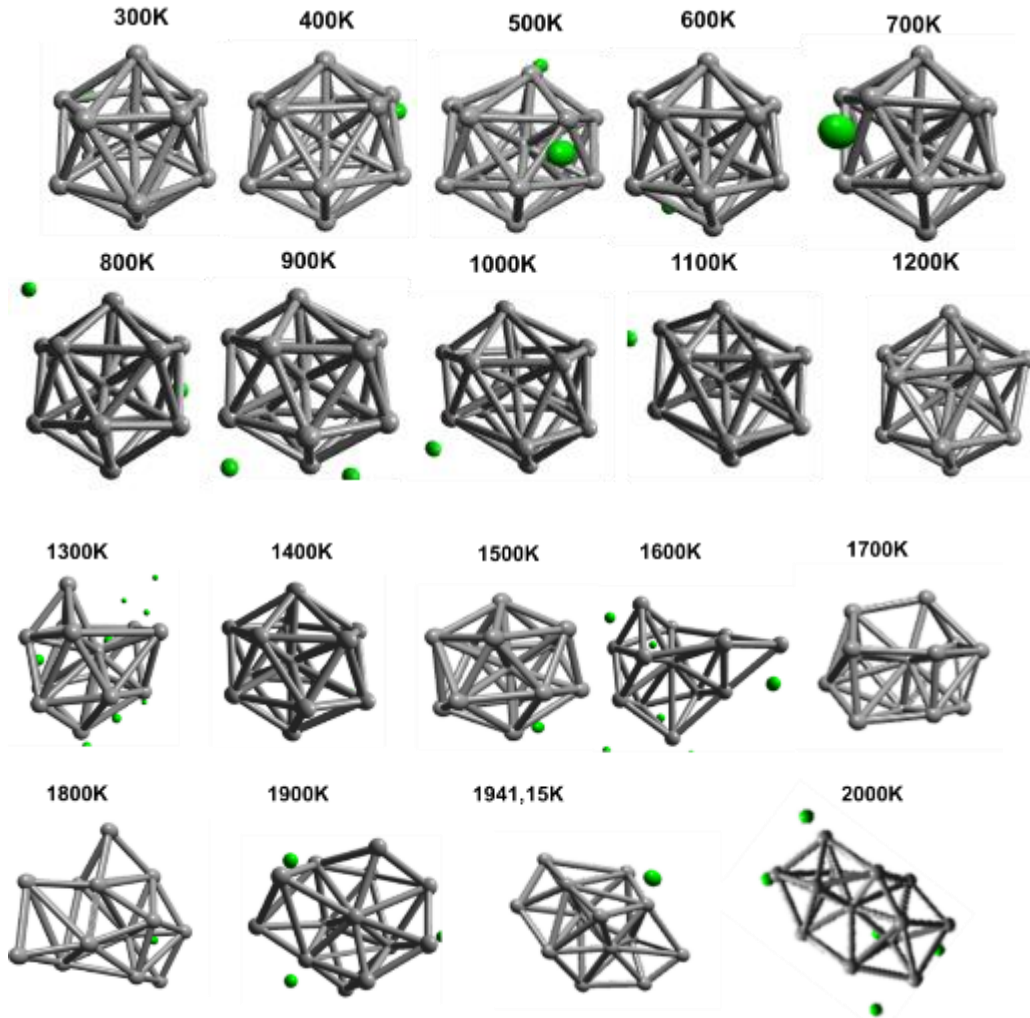


Figure 5.9: The Ti_{13} nanocluster inserted in an inert gas at various temperatures, where the green circles represents Ar atoms.

There is no stable fragment observed in this new phase. The results are reasonable as compared to the Ti bulk melting point of 1941.15 K. In comparison with Hoover thermostat, Hoover exhibits structural distortion at $T < 1000$ K which are complemented by the stretching of upper $\{111\}$ surface at 1000 K.

5.4.3. The thermal agitated phase transition of Ti_{13} employing Berendsen thermostat in an inert gas

In Fig. 5.10 we consider the temperature effect on the nanocluster in the Argon environment using Berendsen thermostat.

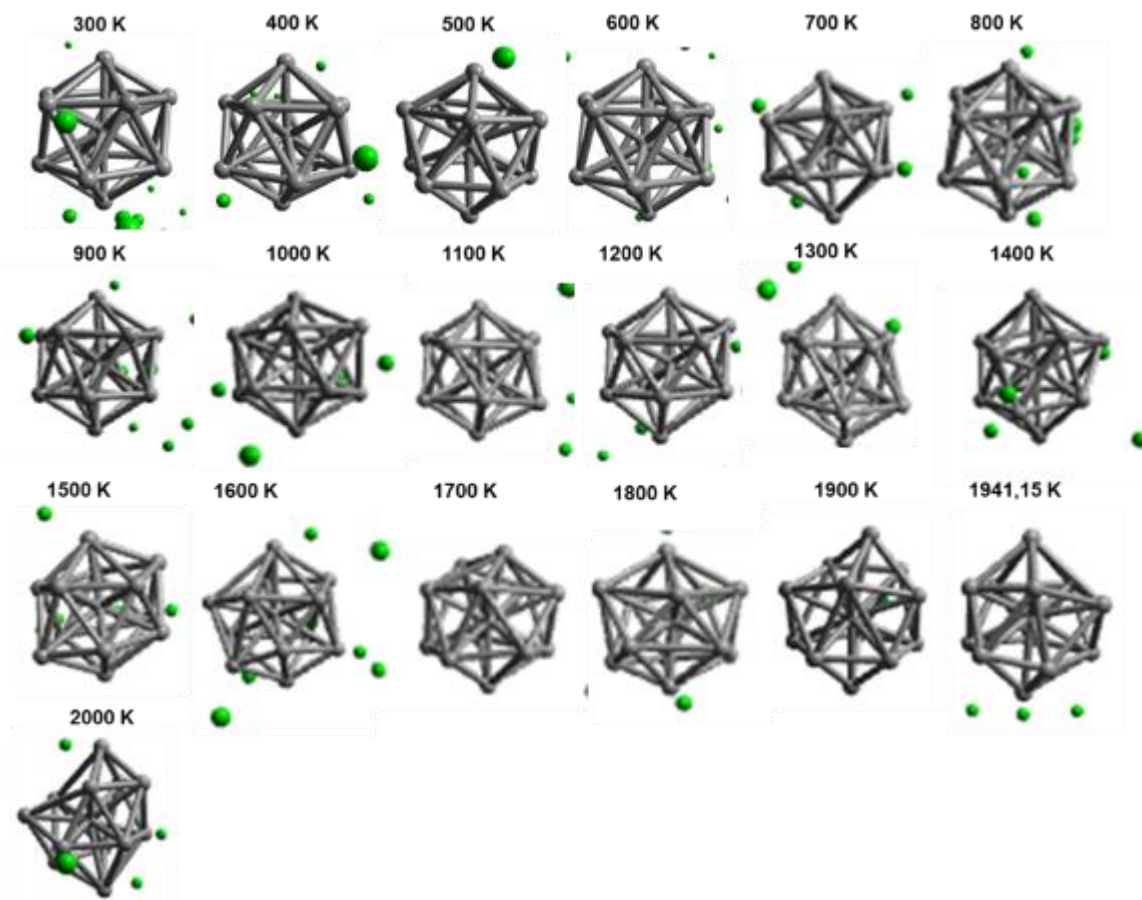


Figure 5.10: The Ti_{13} nanocluster inserted in an inert gas at various temperatures, where the green circles represents Ar atoms .

The snapshots of the nanocluster are shown at various temperatures. Here we observe a phenomenon where the vibrations in the nanocluster gain momentum at lower temperatures. Structural distortions are observed at $T > 1900$ K. However, there are minimal distortions observed

at $T < 1900$ K. These phenomena may also be expected for the greater mass of Argon atoms, which may lead to larger momentum and the nanocluster being greatly and widely opened or squeezed at smaller temperature.

The gas phase changes the geometry and causes it to stretch at the top 5 layered stacking arrangement of atoms, i.e., Ti_{13} is a 1-5-1-5-1 layered stacking configuration. The top layer of 5 layered arrangements of atoms is observed to be opening up at temperatures close to the melting temperatures.

This phenomenon might be indicative of the solid-liquid like features as the nanocluster approaches the melting point. In the vacuum environment, the distortions are observed at 2100 K compared to inert gas (1400 K) impact on the nanocluster. The inert gas impact on the nanocluster reduces its distortions to temperatures below the melting point of the bulk Ti which agrees well with what is reported in the literature [263].

5.4.4. The potential energy of the Ti_{13} nanocluster in an inert gas

Figure 5.11 shows the potential energies for Ti_{13} nanocluster as a function of temperature using different ensembles. The potential energies are varied with temperatures. At 300 K, the Hoover thermostat potential energy is observed to be -111.181 eV compared to -59.9600 eV in a vacuum. The Andersen thermostat is observed to be -89.5463 eV compared to -59.2696 eV in a vacuum. The Berendsen thermostat is observed to be -109.0000 eV compared to -60.1000 eV. However, the Andersen thermostat is observed to have more negative energy at 1400 K.

This phenomenon might be due to the escape of the nanocluster from the higher energy to the lower energy pool.

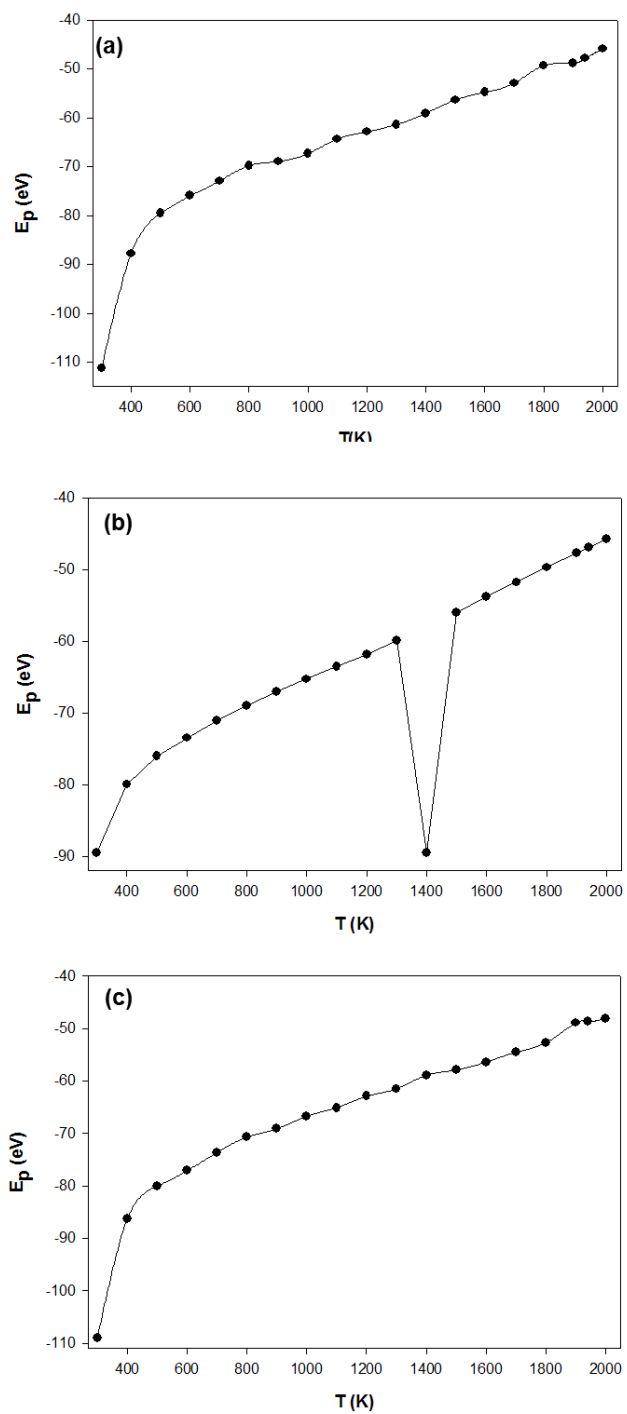


Figure 5.11: The potential energy vs temperature for Ti_{13} nanoclusters inserted in the inert gas at various temperatures for (a) Hoover, (b) Andersen and (c) Berendsen ensembles.

The ability of the Argon gas to enhance the energies of the nanocluster might be ascribed to its melting temperature. The melting point of Argon gas is 83.81 K. At 300 K the inert gas is already in its molten state. The number of Argon atoms might have contributed significantly to the distortions of the nanocluster at a mere 300 K. The nanocluster surface atoms are redistributed in order to favour the interactions with the gas-phase atoms driving the nanocluster to a lower energy state.

5.4.5. Mean square displacement (MSD) for the Ti_{13} nanocluster inserted in the inert gas at various temperatures

Figure 5.12 shows the mean square displacement (MSD) as a function of temperature. The Hoover thermostat shows the atomic vibrations reduced in the presents of inert gas. The highest vibrational activities are observed at 700 K, 1400 K and 1941.15 K. The lowest is found to be at 500 K, 900 – 1000 K, 1600 K and 2000 K. However, with the Andersen thermostat we observe the reduced degree of fluctuations. The MSD values are of a lower magnitude than the other ensembles.

The nano-system is observed to have atomic vibrations which stabilise at 500 – 700 K and 1000 – 1400 K. At elevated temperature (1500 – 2000 K), the atomic vibrations increases. Furthermore, the lowest vibrations are observed at 300 K, 800 K and 1400 K whilst the highest at contributing at 600 K, 1000 K, 1600 K, 1800 K and 2400 K. The atomic vibrations for the Berendsen thermostat increases with temperature.

However, there is a minimal degree of fluctuations at 1100 – 2000 K. Berendsen - At $T < 700$ K, we observe is minimal vibrations of atoms. However, there is a drop of the diffusivity at 800 K which is followed by a high degree of fluctuations from $T > 900$ K. At 1700 K, we observe the highest peak which might be associated with the structural transitions attributed to the solid-like phase.

5.4.6. The radial distribution functions (RDFs) for Ti_{13} nanocluster in an inert gas

In order to obtain the specific details on the effect of an inert gas on the nanocluster, we calculate the radial distribution functions (RDFs) of the nanocluster at different temperatures as shown in Fig. 5.13 below. For the Hoover thermostat, the RDFs depicts the structural changes at varying temperatures.

In the case of Hoover thermostat, the nanocluster in temperature 300 K has well-defined peaks and the magnitude of the peaks reduces with temperature up to 1400 K. However, the magnitude of the peaks at $T > 1400$ K is observed to be greater than at 800 K.

There are no pre-melting peaks observed when the nanocluster is inserted in the inert gas. However, we notice two peaks at 1400 K and 2000K which superimposed each other. This phenomenon may be ascribed to Argon gas not having a considerable effect on the nanocluster due to its atoms behaving like free molecules at elevated temperatures. At $T > 500$ K, the Argon atoms are depicted far away from the nanocluster in Fig 5.8.

Although, as the temperature increases the peaks start to be broader, observing some emerging peaks near 4 angstroms which have a similar resemblance as the peaks in a vacuum. Furthermore, near and above the melting point, it may be that the inert gas does not have a considerable effect on the dynamics of the nanocluster due to the high atomic motion in the liquid phase.

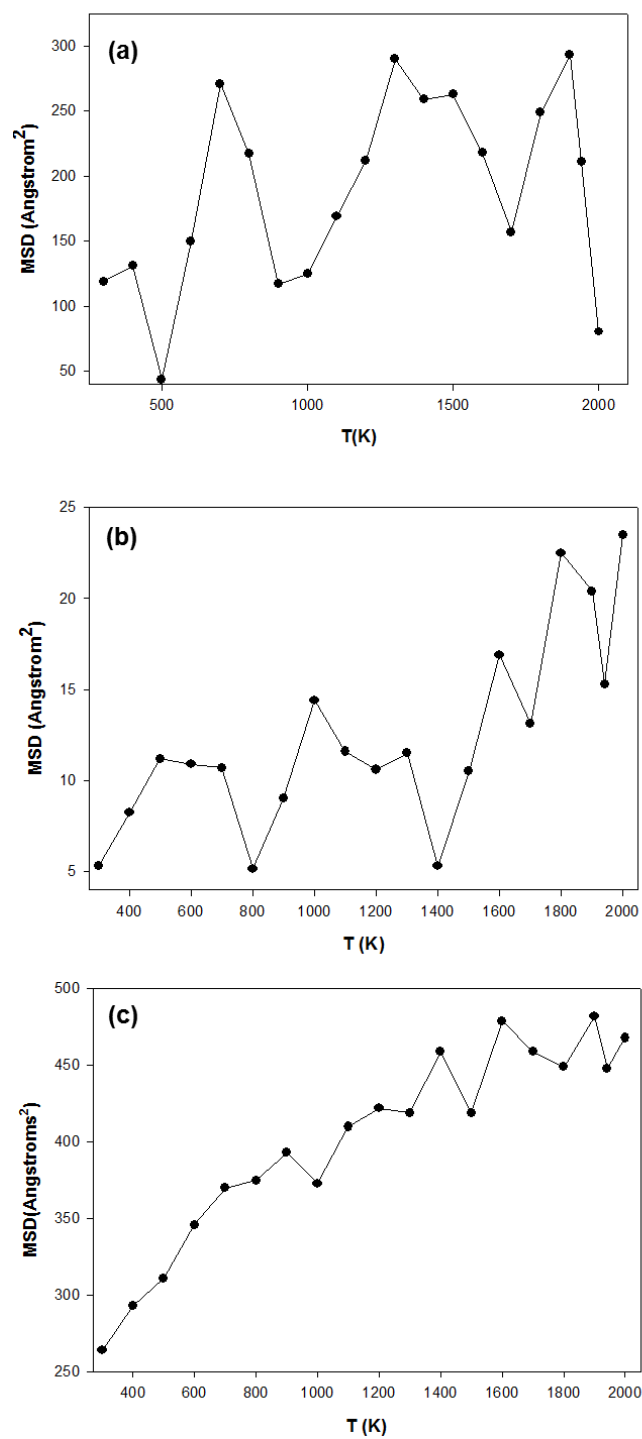


Figure 5.12: Mean square displacement (MSD) of Ti_{13} nanoclusters inserted in the inert gas at various temperatures for (a) Hoover, (b) Andersen and (c) Berendsen ensembles.

In the case of the Berendsen thermostat, the peaks at 300, 800 and 1000 K are observed to have a lower magnitude than the peaks at $T > 1900$ K. Similar features were observed with the Hoover thermostat except at 300 K.

We observe that as the temperature increases the peaks start to be broader, we notice the RDFs being bouncy and becoming flattened around 3 angstroms as the temperature approaches the melting point. The peaks at 4 angstroms become sharp and superimpose each other at temperatures 1400 K, 1900 K and 2000 K respectively.

5.4.7. The density profiles for Ti_{13} nanoclusters in an inert gas at various temperatures

In Fig. 5.14, we observe that at lower temperature 300 K, we find the solid-like features preserved suggested by the distinct peaks or atoms have higher distribution only at certain distances from the centre. For Hoover thermostat, as the temperature increases, the peaks at the centre decreases and the density probability fluctuations decrease as well. However, at temperatures 1400 K, 1900 K and 2000 K we find the peaks flattening indicating smooth phase transition from a solid phase to a liquid phase due to the uniform distribution of atoms in a liquid phase. Figure 5.8 and 5.13 illustrates that there may have occurred two transitions where one is influenced by the inert gas at $T < 1000$ K and when the inert gas is highly distributed at $T > 1400$ K, behaving like a free molecule.

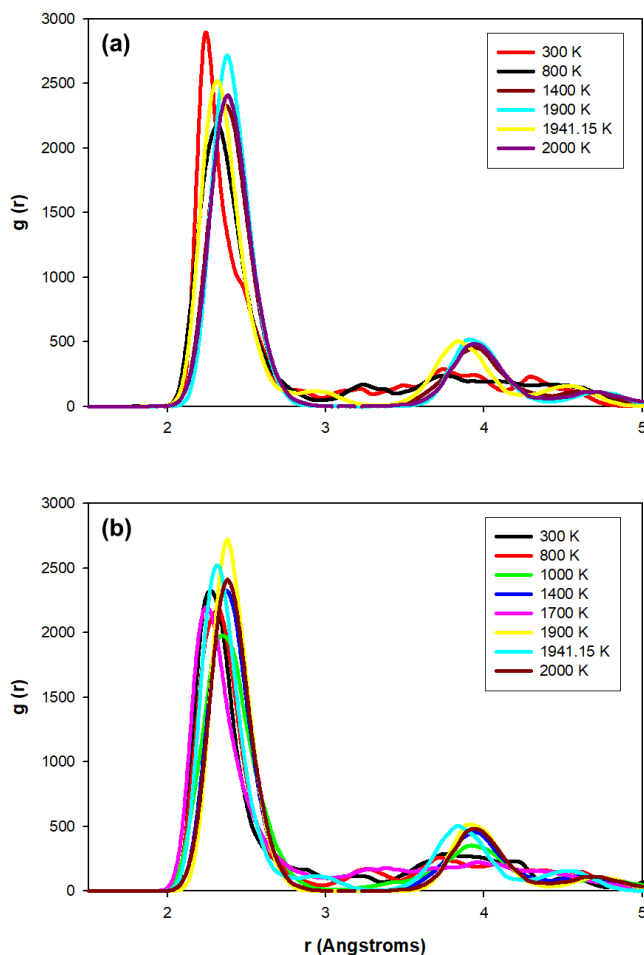


Figure 5.13: The radial distribution functions (RDFs) of the Ti_{13} at various temperatures for (a) Hoover and (b) Berendsen thermostats.

At $T > 1400$ K, the Ti_{13} nanocluster behaves similarly when it is thermally agitated in a vacuum. However, the Berendsen thermostat show solid-like features at 800 K and 1400 K with higher distribution magnitude next to the 300 K distribution peak. At 1900 K the peak is observed flattened. The peaks at 2000 K for both the thermostats are observed to have a similar trend.

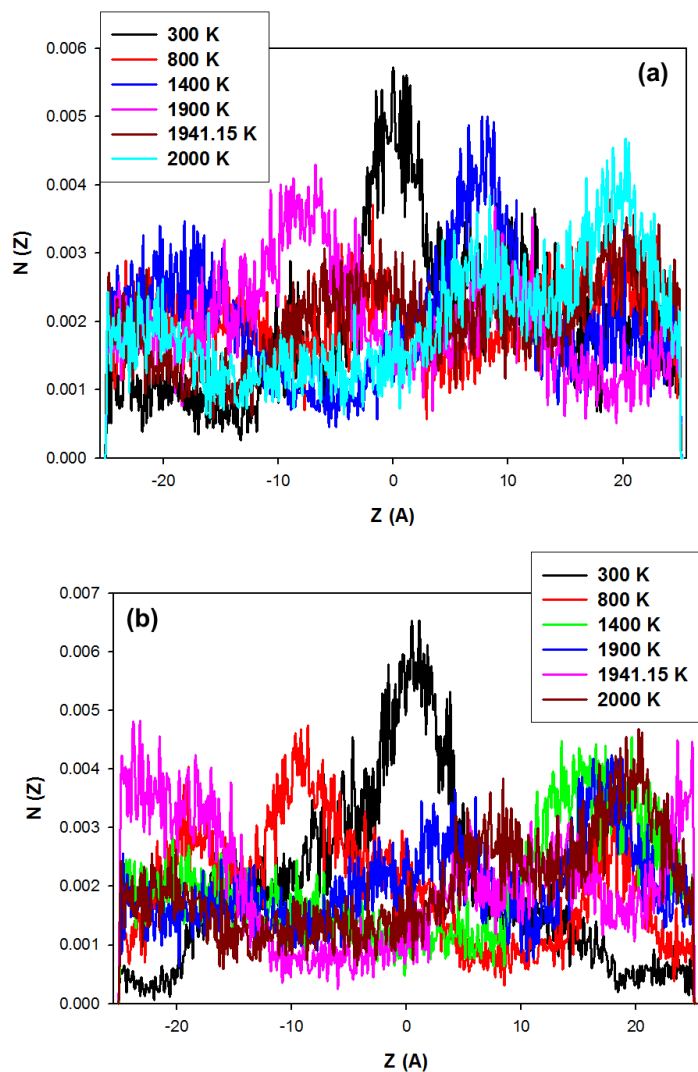


Figure 5.14: Comparison of Ti_{13} atomic distribution along a Cartesian coordinate (z) at different temperatures in an argon environment for (a) Hoover and (b) Berendsen thermostats.

Moreover, the large fluctuations observed may be due to Ar-Ti interacting at a small distance. This may be ascribed to the movement of the inert gas molecules within a certain equilibrium distance. Some of the gas atoms which are located at a longer distance from the nanocluster behave like a free molecule in a gas phase, in turn resulting in large fluctuations.

5.5 The thermal agitated phase transition on the Ti_N ($N = 7$ & 17) nanocluster in a vacuum

In this section, we investigate the thermal agitation on the Ti_{17} and Ti_7 nanoclusters using Nose' Hoover thermostat. The Hoover thermostat was considered efficient in the previous discussion. Although Andersen thermostat showed melting features below Ti bulk, it does not produce RDFs and density profiles. Hence the Hoover thermostat is considered in the current thermal investigations.

5.5.1. The thermal agitated phase transition of Ti_7 nanocluster

We have analysed the Ti_{13} nanocluster using Nose' Hoover thermostat. We observed that the Hoover thermostat generates results that are most comparable with the literature. We, therefore, employ Hoover thermostat to carry out thermodynamics calculations for Ti_7 and Ti_{17} nanocluster. Figure 5.15 show the configurations of the Ti_7 nanocluster at a variety of temperatures. The configuration appears to have the same morphology and no distortions at $T < 1000$ K and $T > 1200$ K. At 1100 K we notice the abrupt changes in the morphology.

The original nanocluster transitioned into capped octahedron which is the first meta-stable nanocluster among the DFT calculated nanoclusters for Ti_7 . Moreover, the pentagonal bi-pyramid atoms redistributed and evolved into the most stable isomer for Ti_6 which is observed to be capped with an atom. This observation showed that the Ti_7 nanocluster is more intact with stable geometry above the bulk melting point. This may be due to its $\{111\}$ and $\{100\}$ facets. The geometry has ten $\{111\}$ stable facets and five $\{100\}$ facets. The ten $\{111\}$ facets at the tip remain almost

unaffected and these planes are thermodynamically unfavourable [273, 274]. The Ti_7 geometry showed distortions at 1100 K while Ti_{13} showed distortions at 2100 K.

5.5.2. The thermal agitated phase transition of Ti_{17} nanocluster

In the case of Ti_{17} nanoclusters in Fig 5.16, we observe a similar thermal agitation effect from 300 – 500 K, where the Ti_{17} configuration change to tetra-capped (lime green) icosahedral isomer (grey).

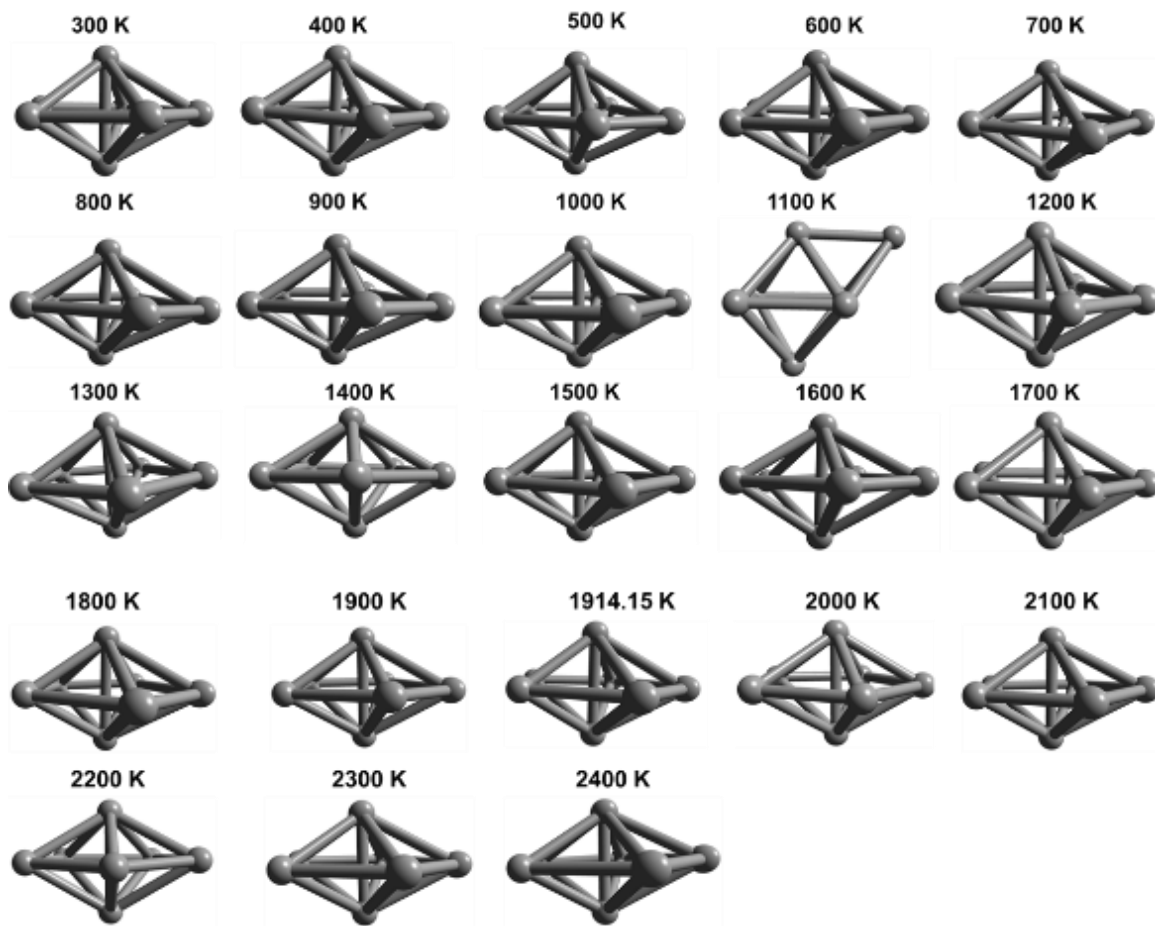


Figure 5.15: The Ti_7 nanocluster in the vacuum at various temperatures.

These changes in configuration at lower temperatures may be attributed to its instability when compared with Ti_{13} nanoclusters.

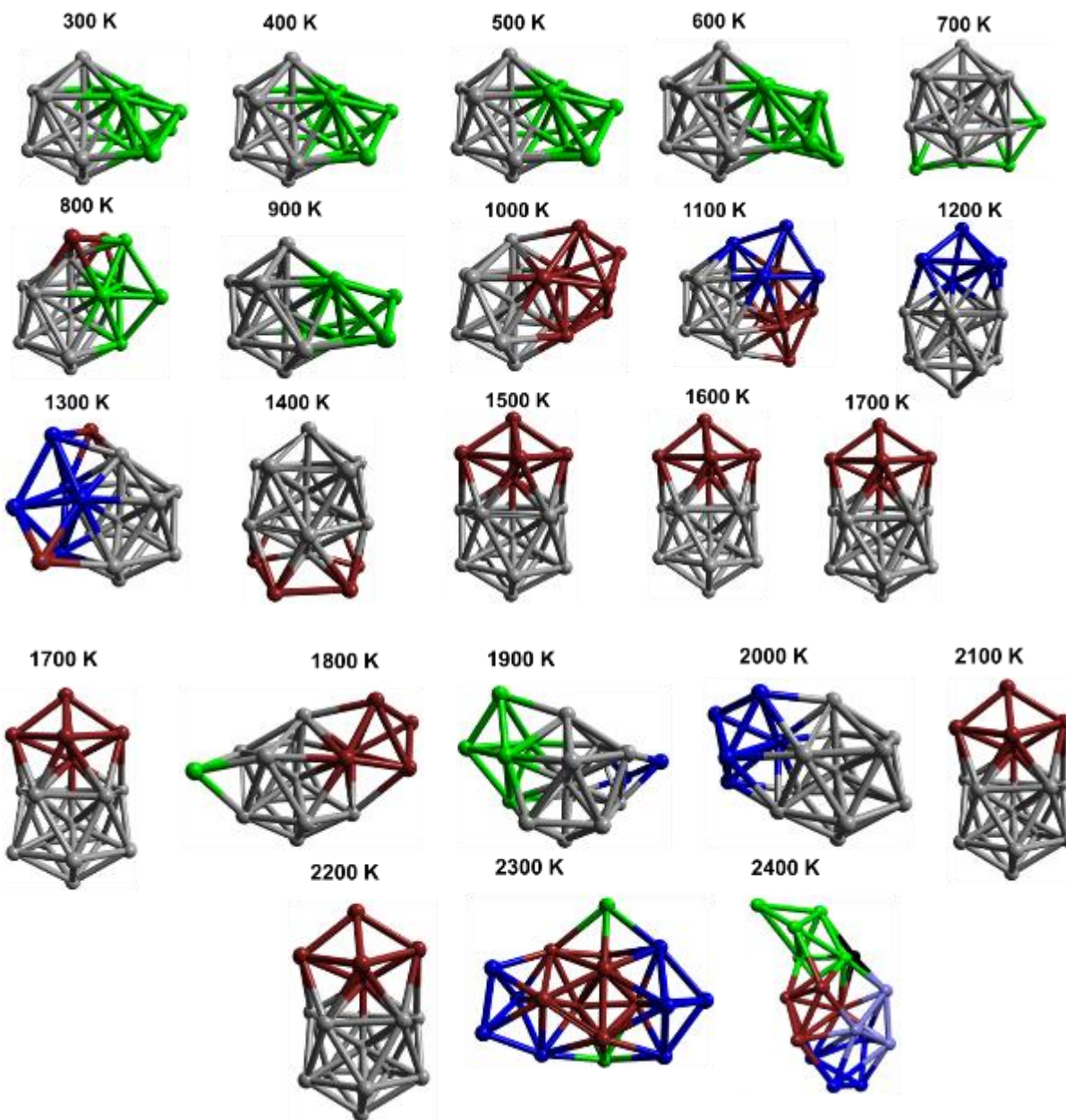


Figure 5.16: Snapshot of Ti_{17} nanoclusters in the vacuum at various temperatures.

The transient at 600 K is observed to be an icosahedral (grey) interpenetrating with a pentagonal bi-pyramid (lime green). At 700 K, the nanocluster to have transitioned to a tetra-capped (lime green) icosahedral (grey). The transient for 800 K is observed to be icosahedral (grey) interpenetrating with triangular bi-pyramidal (lime green) coexisting with two atoms (maroon).

At 900 K, the structural changes are observed to be icosahedral (grey) coexisting with tetra-capped atoms (lime green). The thermal agitation at 1000 K deduces a pentagonal bi-pyramid (maroon) interpenetrating with icosahedral isomer (grey). At 1100 K, the transition of the nanocluster is observed to be icosahedral (grey) coexisting with two triangular bi-pyramidal (blue and maroon).

The 1200 K structure is observed to be icosahedral unit (grey) interpenetrating with triangular bi-pyramidal (blue). At 1300 K, the transient is observed to be icosahedral (grey) coexisting with triangular bi-pyramidal (blue) connected to two atoms (maroon). The 1400 K transient is observed to be the tetra-capped (maroon) icosahedral unit. At 1500 – 1700 K, the transients are observed to be icosahedral interpenetrating with triangular bi-pyramidal. The transition at 1800 K is found to be icosahedral (grey) coexisting with triangular bi-pyramidal (maroon) and an atom (lime green) connected to the grey isomer.

The 1900 K transient is also observed to be the icosahedral unit (grey) coexisting with triangular bi-pyramidal (lime green) and an atom connected on the grey unit. At 2000 K, the structural transitions are observed to be icosahedral unit (grey) interpenetrating with triangular bi-pyramidal unit (blue). For 2100 – 2200 K, the transients are also observed to be icosahedral (grey) interpenetrating with triangular bi-pyramidal (maroon). The pentagonal bi-pyramid (maroon) coexisting with two triangular bi-pyramidal (blue) connected to two atoms (lime green) is found to be the transient for 2300 K. The transition for 2400 K is observed to be dominated by triangular bi-pyramid coloured lime green, maroon, blue and light blue. The Ti_{17} geometry showed

distortions at 300 K while Ti_{13} showed distortions at 2100 K. This may be ascribed to the instability nature of the Ti_{17} nanocluster as compared to the Ti_{13} nanocluster.

5.5.3. The potential energy (heating and cooling) for Ti_N ($N = 7 \text{ \& } 17$) nanoclusters

In Fig. 5.17 we show the potential energies for Ti_N ($N = 7$, and 17). The energies increase with increasing temperature.

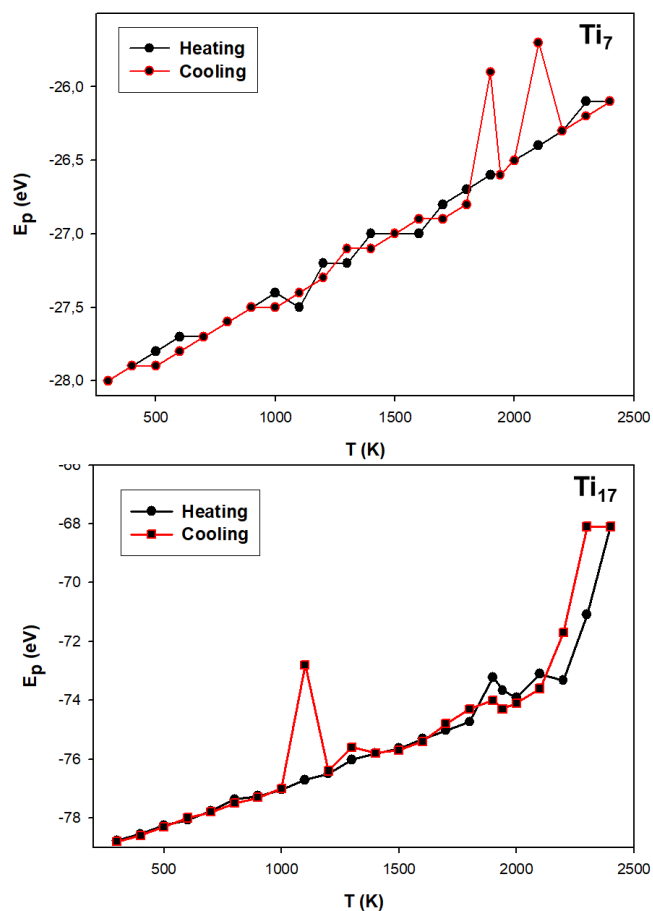


Figure 5.17: Variation of potential energy with temperature for Ti_N ($N= 7 \text{ \& } 17$) nanocluster.

In the case of the potential energy for $N = 7$, we observe linearity between 300 K – 1000 K and an abrupt drop in the energy is noticed at 1100 K. This is the temperature where 7-atoms redistributed into a capped octahedron shown in Fig. 5.15. This phenomena might be attributed to an escape of the nanocluster into the lowest energy pool which resulted in its stabilisation.

At 1600 K, a small drop in energy is depicted. However, the shape of the geometry was not affected as compared to the drop in energy at 1100 K. At 1900 K and 1941.15 K, we observe no differences. This illustrates that the influence of temperature did not change the morphology of the nanocluster. The gain in energy at 2300 K also had no contribution in the transitioning of the nanocluster.

In the case of cooling, we observe lower energies at temperatures 500 K – 600 K, 1000 K, 1200 K, 1400 K, 1700 – 1800 K which are associated with stability and the formation of new phases. However, we also observe the high energies at 1300 K, 1600 K, 1900 K and 2100 K which is associated with instability and the formation of a new phase.

At 1900 K and 2100 K, we observe the gain in energy which influence a change in the morphology of the nanocluster to two interpenetrating triangular bi-pyramid and a bicapped triangular bi-pyramidal respectively. Furthermore, for $T < 1800$ K, most of the cooling energies are observed to be below the heating energies.

For Ti_{17} at 1900 K, we observe a sharp simple jump which is indicative of the melting point of the nanocluster. The nanoclusters are known to exhibit melting behaviour below the melting point of bulk metals. This simple jump suggests that there might be a transition from solid to liquid occurring at that temperature. The deviation from linearity is observed only at 1900 K and followed by the second simple jump at 2100K lower in energy than the first jump.

5.5.4. The mean square displacement (MSD) for Ti_N ($N = 7$ & 17) nanoclusters at various temperatures

Upon cooling, we observe a sudden jump in the energy at 1100 K with a higher magnitude. This may be due to the formation of a new unstable fragment that escaped from the lowest energy to the highest energy pool. We also observe lower energies at 1300 K, 1800 K, 2200 and 2300 K which are attributed to stability and the formation of a new phase.

The higher energies are observed at 1900 and 2100 K which is also due to destabilization of the nano-system and the formation of the new unstable fragmentations. At 1700 – 1600 K and 900 – 300 K, the potential energies are observed to have relatively the same energies. This may be ascribed to the atoms of the cooled nanocluster being redistributed and formed fragmentations that are equivalent to the heated nanoclusters. The Ti_7 formed new unstable geometries at 1900 K and 2100 K during cooling, while Ti_{13} formed the new unstable isomer at 1941.15 K when we used the Berendsen thermostat.

Figure 5.18 shows atomic movement in the nanocluster at various temperatures. Both the nanoclusters are observed to have a higher degree of fluctuations. However, the values of the MSD for Ti_{17} nanocluster is observed to be of higher magnitude compared to Ti_7 nanocluster. The vibrational activities are observed to be lower at 800 – 900 K and 1941.15 K. Furthermore, the atomic vibrations at 2000 – 2400 K are observed to be smooth compared to Ti_7 and Ti_{13} nanoclusters. In the case of the Ti_{17} nanocluster, the lowest vibrational activity is observed at 800 K and 1400 – 1500 K.

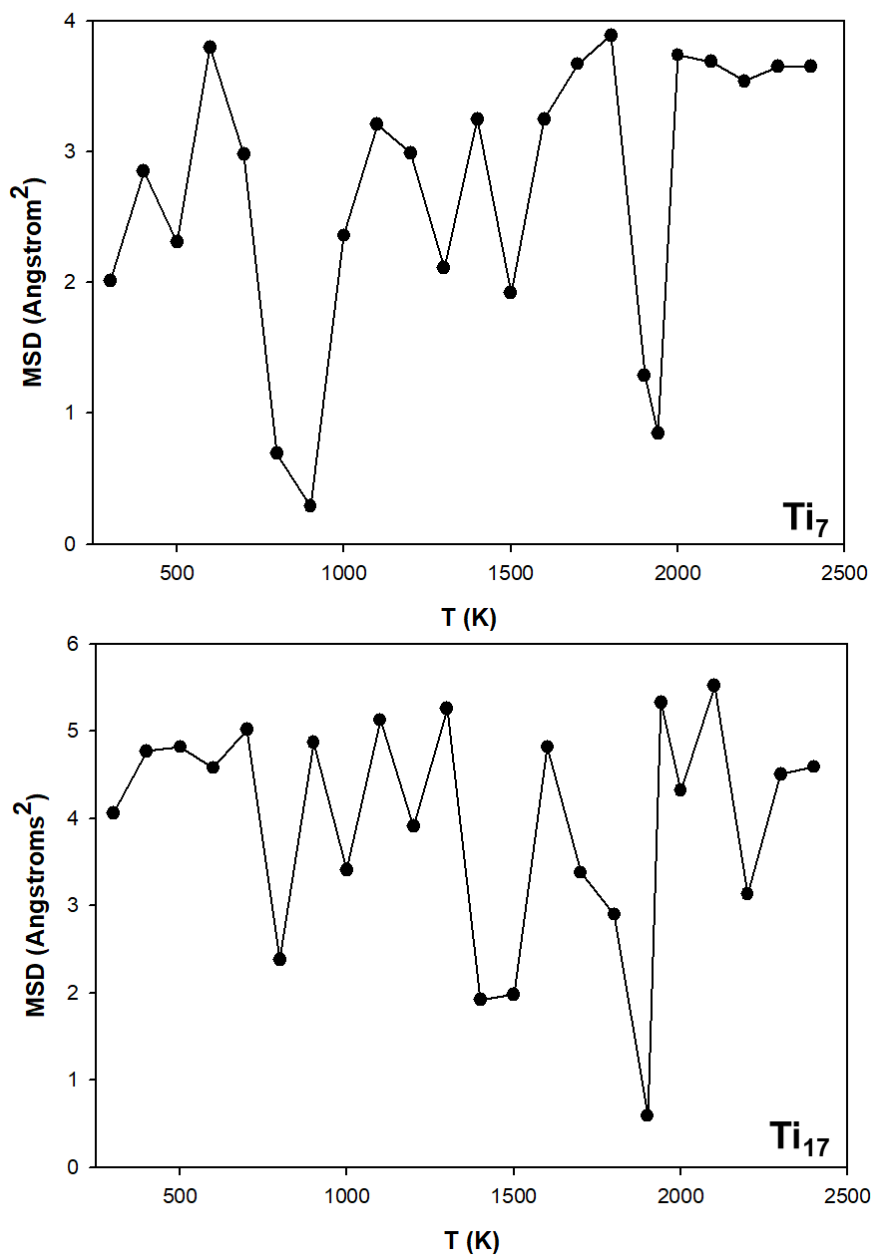


Figure 5.18: The MSD for the Ti_N ($N = 7$ & 17) nanocluster at various temperatures.

Almost all temperatures are observed to have the highest atomic vibrations as the nanoclusters are thermally agitated. However, stabilized atomic vibrations are observed at 300 – 700 K.

5.5.5. The radial distribution function (RDFs) for Ti_N ($N = 7$ & 17) nanoclusters

In order to obtain specific details on the local configuration of Ti_7 , and Ti_{17} nanoclusters we calculated the radial distribution functions shown in Fig. 5.19. These peaks are observed to superimpose each other which suggests that the nanocluster is still solid and atomic orientations are still intact for the Ti_7 nanocluster.

The magnitude of the peak at 1400 K is observed to be lower than the peak at 1900 K. This phenomena might be due to the nanocluster showing solid-like features similar to the nanocluster at 800 – 1000 K. Particularly since the nanocluster at 1400 K is potentially depicted as having higher energy than other temperatures which is attributed to the instability of the nano-system. At 1941.15 K and 2000 K, the peaks are observed to decrease with temperature.

In the case of the Ti_{17} nanocluster, at 300 K the peaks reveal ordered atoms having the highest peak implying that the nanocluster is still highly structured. However, the peaks at 300 K is observed to have a shoulder. This may illustrate the early transition of the nanocluster as observed in Fig. 5.16. As the temperature increase, the peaks decreases in magnitude and becomes broader depicting the disorder of the atoms due to the random distribution of atoms at higher temperatures (1900 – 2000 K).

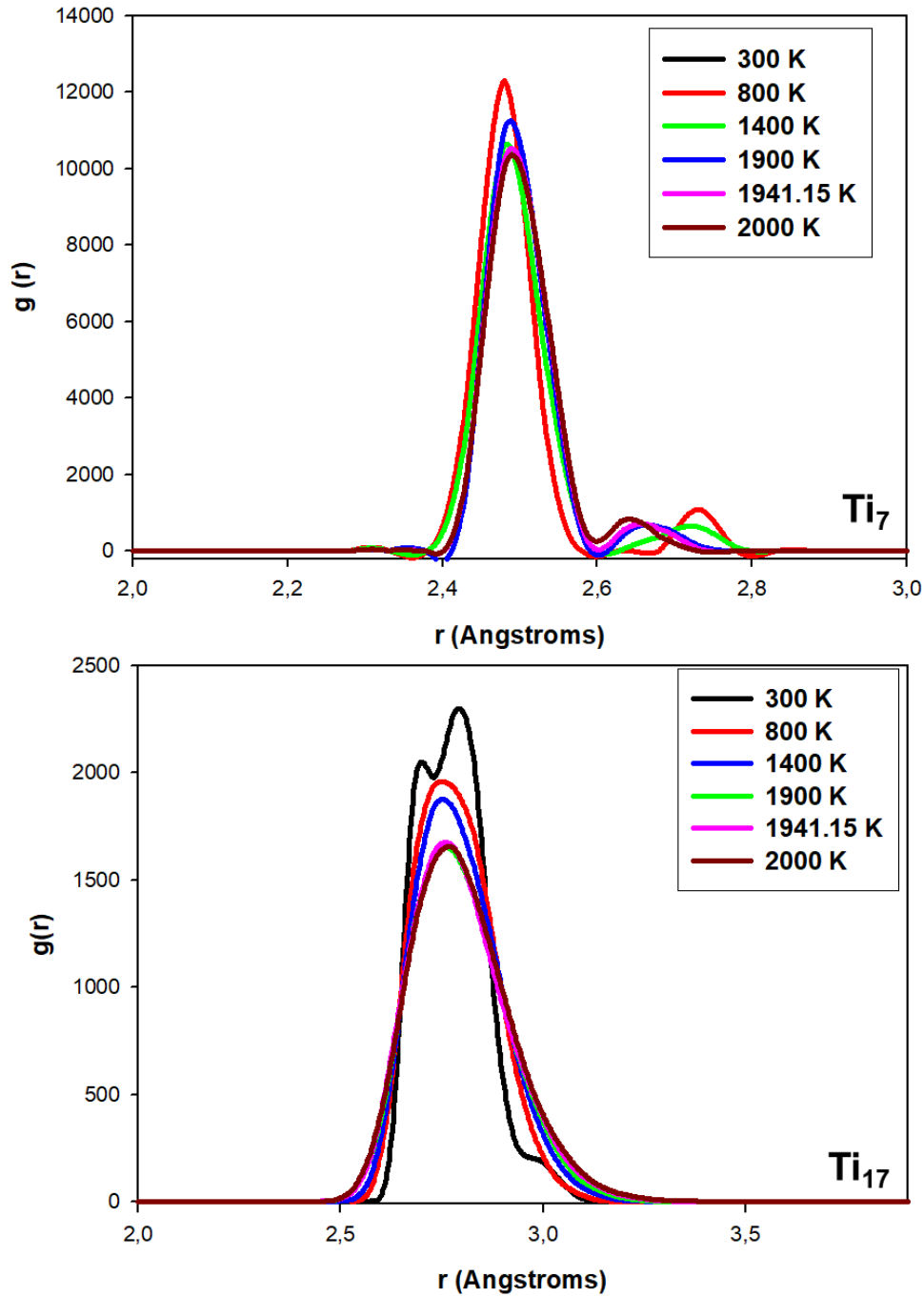


Figure 5.19: The radial distribution function of the Ti_N (7 & 17) at various temperatures.

5.5.6. The density profiles for Ti_N ($N = 7$ & 17) nanoclusters at various temperatures

Figure 5.20 shows the atomic distribution of Ti_7 and Ti_{17} nanoclusters along the axis at different temperatures.

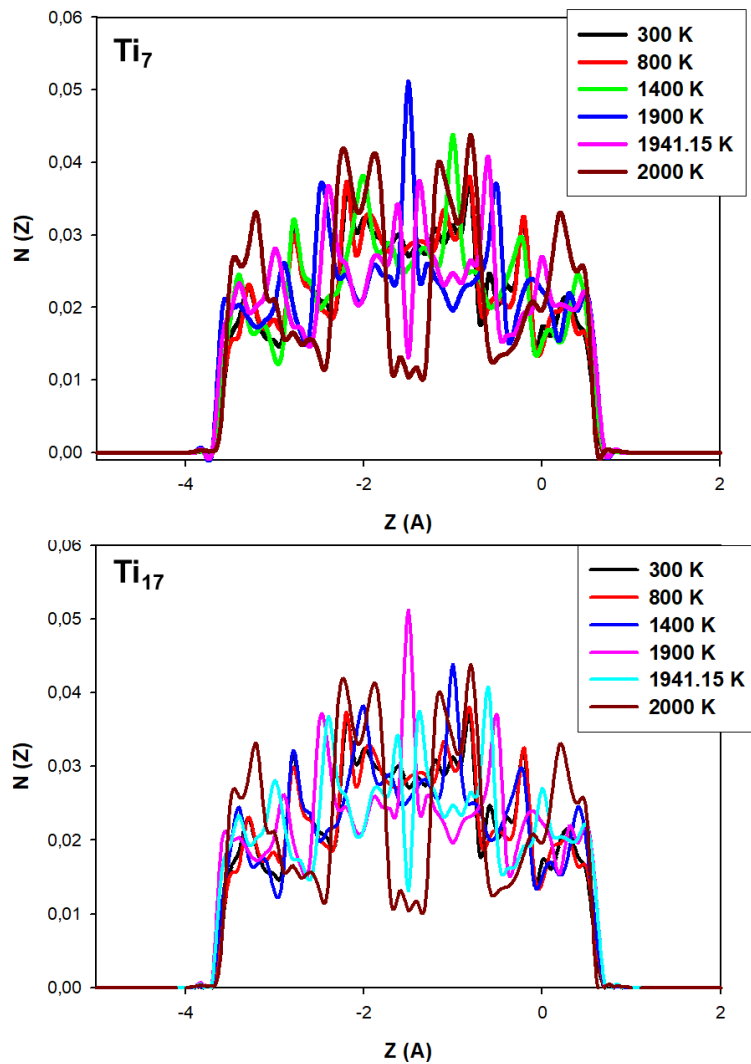


Figure 5.20: The comparison of Ti_N ($N = 7$ & 17) atomic distribution along a Cartesian coordinate (z) at different temperatures.

The atomic distribution of both the nanoclusters depicts similar thermal agitation. At lower temperatures, we do not observe a distinct peak at 300 K rather the overlap of peaks at 300 K, 800 K and 1400 K.

The magnitude of the peaks at 1900 K illustrated at the centre is observed to be higher. The peaks at 1941.15 K and 2000 K are observed to decrease with temperature. These phenomena might be ascribed to the higher degree of distortions on the nanoclusters at elevated thermal agitation.

5.6. The thermal agitated phase transition on the Ti_N ($N = 7$ & 17) nanocluster inert gas insertion

In this section, we consider thermal agitation on the nanocluster of Ti_7 and Ti_{17} in the presence of inert gas. We are investigating how the inert gas affect the nanoclusters and their energies as the temperature is increased. Recall that in a vacuum, Ti_7 maintained its equilibrium geometry above the bulk Ti melting point.

5.6.1. The thermal agitated phase transition of Ti_7 in an inert gas

Figure 5.21 show minimal distortions on the nanocluster at $T < 700$ K. At 800 K, we observe the nanocluster having transitioned into a bi-capped triangular bi-pyramidal. At 900 – 1000 K, the nanocluster is observed to have regained its original configuration. At 1200 K, the thermal transient is observed to be a bi-capped triangular bi-pyramidal. However, at 1300 – 1500 K the 7-atoms are observed to have redistributed into their original morphology but distorted at 1500 K.

The structural transients are observed to be a capped octahedron at 1700 K and bi-capped triangular bi-pyramidal at 1800 K. At 1900 K the distorted Ti_7 was observed. At 1941.15 – 2400 K, we observe the unit being structurally transitioned to tricapped tetrahedral, bicapped triangular bi-

pyramidal, tetrahedral interpenetrating with triangular bipyramid and two interpenetrating tetrahedral units capped by one atom.

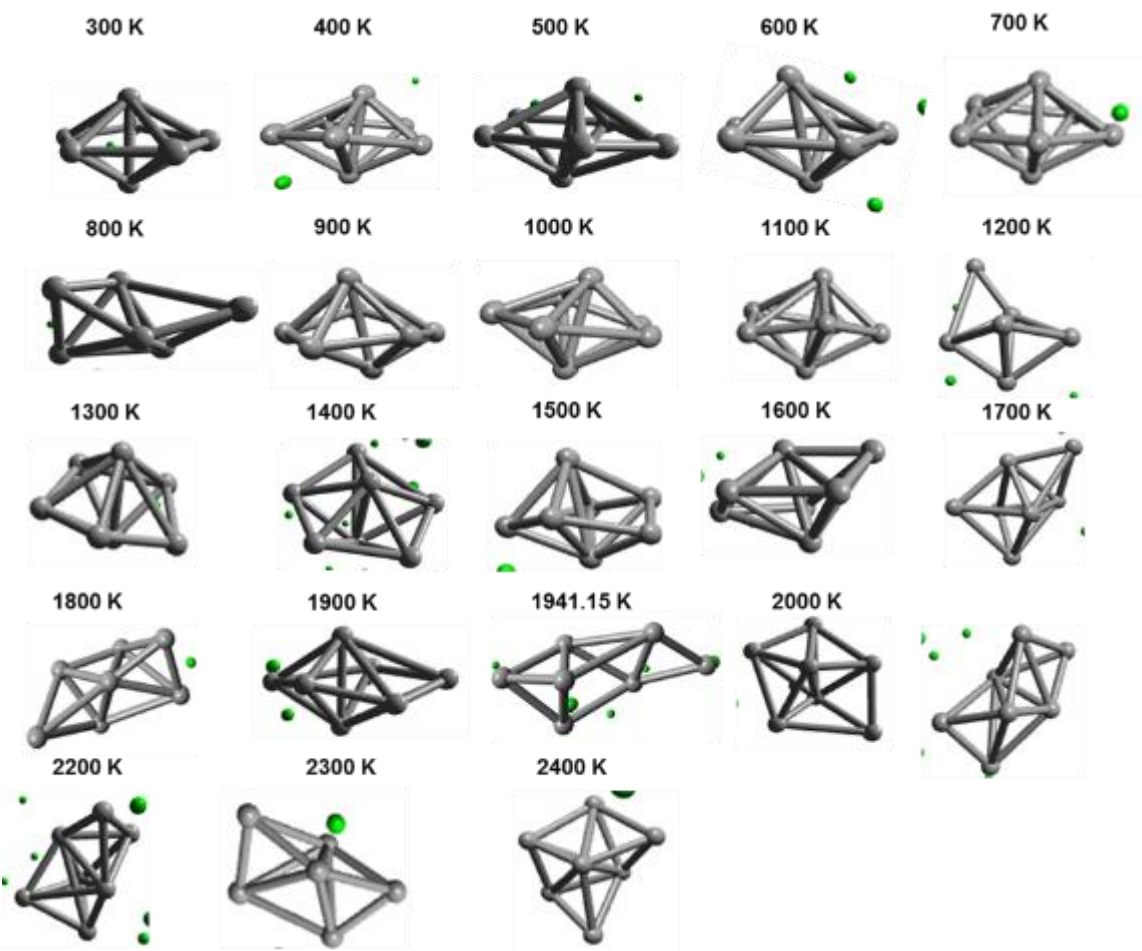


Figure 5.21: Snapshots of Ti₇ nanoclusters inserted in an inert gas environment at various temperatures, where the green circles represents Ar atoms .

We notice that as the temperature is increased in an Argon environment the distortions appears at lower temperatures in comparison with the nanocluster in a vacuum which might be attributed to the Argon atoms' kinetic energies dominating since their number is greater yielding in the increase of the Ti nanocluster's energy.

5.6.2. The thermal agitated phase transition of Ti_{17} in an inert gas

The insertion of a 17 atom titanium cluster in an argon environment shows a phenomenon where the nanocluster begins to lose its morphology at temperatures as low as 300 K. These observations become more evident when the cluster changed its original shape to tetra-capped icosahedral configuration, also observed at 400 K. This transition is observed at 300 – 400 K, 600 K and 800 K. At 1000 K we observe the configuration changing to icosahedral structure interpenetrating with triangular bi-pyramidal unit.

We observe a similar configuration at 1100 K. The tetra-capped pentagonal bipyramid interpenetrating with triangular bipyramid 500 K and 700 K. At 1200 K the transients are found to be icosahedral unit interpenetrating with triangular bi-pyramidal with capped atoms.

The 1300 K geometry transition is observed to be a capped Z15 Frank-Casper polyhedral. The dominance of the icosahedra as the building block fragmentation is observed diminished at 1400 K. There are total distortions in the fragmentations for the Ti_{17} nanocluster.

The nanocluster is observed to approach the melting point. This phenomenon is observed at $T > 1400$ K. The nanoclusters are exhibiting features that are associated with a higher degree of distortions. At $T > 1900$ K, the nanocluster no longer exhibits features that are associated with the icosahedral unit. The melting behaviour is observed below the 1941.15 K bulk Ti melting point.

At a temperature near the melting point, we observe the nanocluster having a total loss of the original structure.

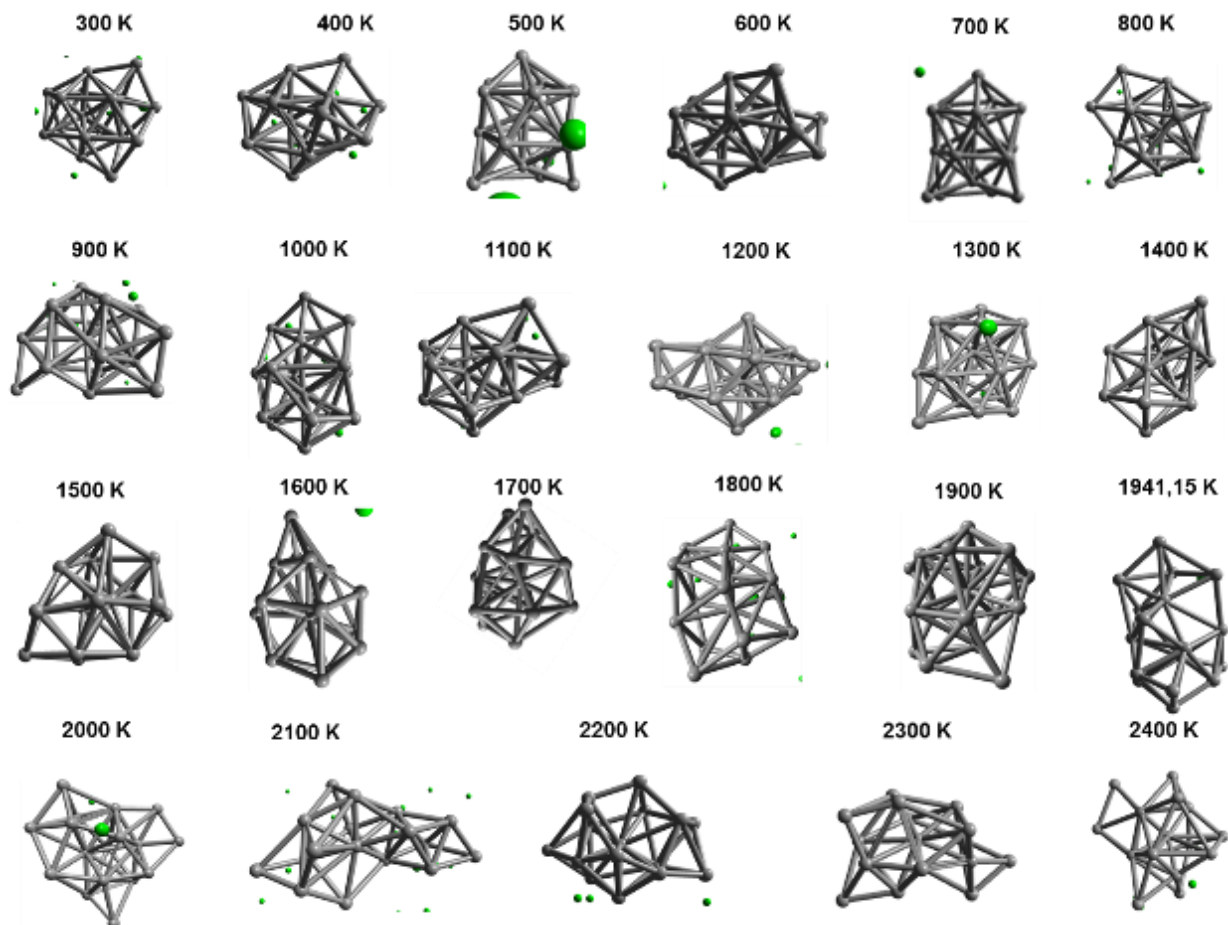


Figure 5.22: The Ti_{17} nanocluster inserted in an inert gas at various temperatures.

These early changes of the nanocluster may be attributed to an increase in the kinetic energy and nature of the nanocluster. This phenomenon is observed for all the nanocluster which are inserted into the Argon gas.

5.6.3. The potential energy of the Ti_N ($N = 7$ & 17) nanocluster in an inert gas

Figure 5.23 depicts a smooth curve in the energy from 300 K to 400 K with the potential energy of -83, 2238 eV at 300 K for Ti_7 . Although the trend is the same compared to all nanoclusters inserted an inert gas. There is a minimal loss in energy and no gain in energy as the temperature

increases as compared to pure Ti. We observe the energy gap closing up and depicting a drop in the energy at 1700 K with the energy of -24, 200 eV.

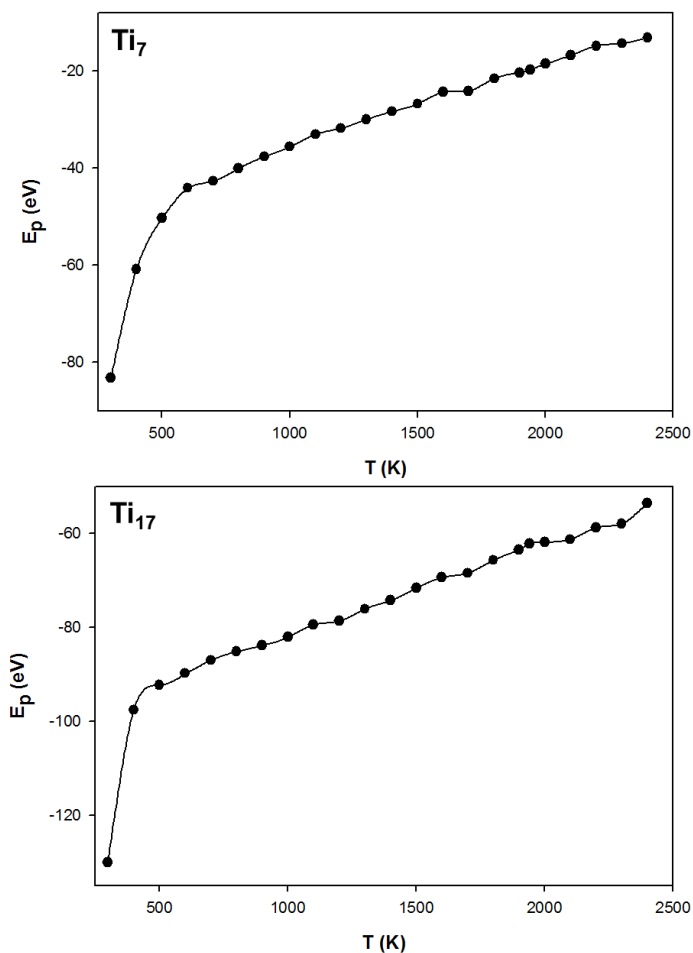


Figure 5.23: The potential energy vs temperature for Ti_N ($N = 7$ & 17) nanocluster inserted in inert gas environment.

There is no temperature with high magnitude in the potential energy observed. For Ti_{17} , the plot depicts the same trend as the observed for Ti_7 and Ti_{13} where it shows energy increment at 300 K. However, we observe more energy as compared to Ti_7 and Ti_{13} with energy -130.481eV compared to -111.181eV for Ti_{13} . This increase in the energy can be attributed to the increase in the kinetic

energy increasing the momentum of the atoms at lower temperatures. At 1100 K we observe a drop in the energy as observed with the Ti_{13} nanocluster.

5.6.4. The mean square displacement (MSD) for Ti_N ($N = 7$ & 17) nanoclusters in an inert gas at various temperatures

Figure 5.24 shows the mean square displacement at varied temperatures.

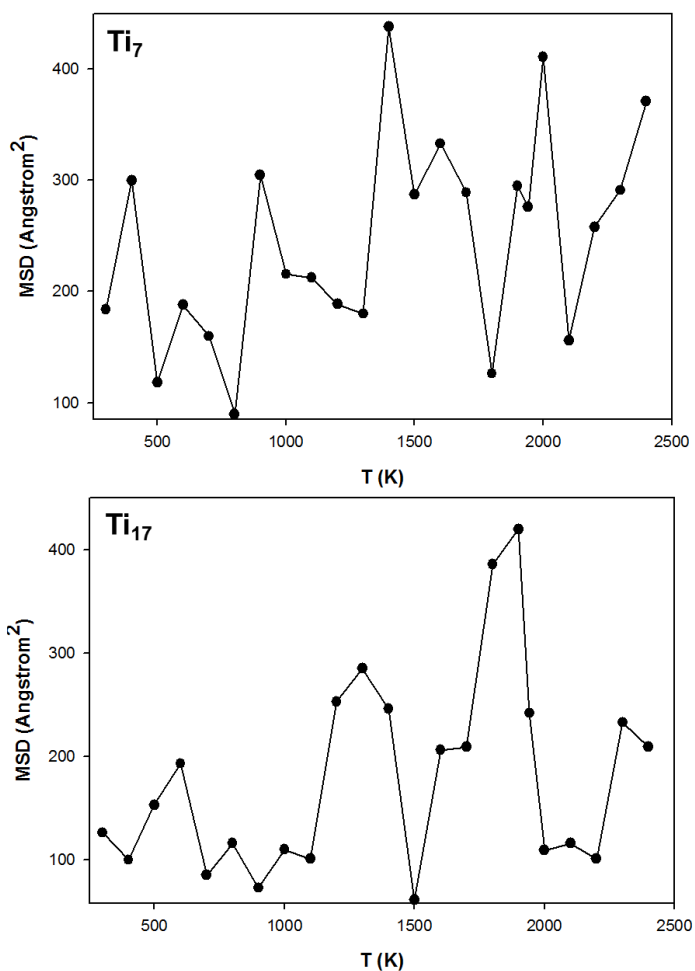


Figure 5.24: The MSD of Ti_N ($N = 7$ & 17) nanocluster inserted in inert gas at various temperatures.

The atomic vibrations for Ti_7 are observed to have reduced fluctuations as compared to vacuum. At 300 – 800 K the vibrational activity is observed to have stabilised. The atomic vibrations at 900 – 1300 K are observed to have smoothly stabilised.

However, they show higher instability at 1400 – 2400 K. With Ti_{17} the atomic vibrations are also observed to have reduced fluctuations. The vibrational activity for this nanocluster is observed to stabilise at 300 – 1100 K and becomes greatly unstable at 1400 – 2400 K. Furthermore, the inert gas influences the nanocluster to have lower atomic vibrations activities as compared to vacuum.

5.6.5. The radial distribution function (RDFs) for Ti_N ($N = 7$ & 17) nanoclusters in an inert gas

The RDFs in Fig. 5.25 depicts a high magnitude peak at 300 K suggesting a well-ordered structure. The same trend is observed. However, at 800 – 1400 K we observe the decrease in the magnitude of the peaks followed by the broadening of the peaks, which is attributed to the nanoclusters losing their morphology by exhibiting features that are associated with solid-liquid like transitions.

Furthermore, at temperatures 1900 K, 1941.15 K and 2000 K which is closer to the melting temperature of bulk titanium, we observe the peaks superimposing each at 2.53 – 2.4 and 3.2 – 4.0 Angstroms. At 2.6 Angstroms, the magnitude of the peak at 1941.15 K is observed to be below the magnitude of the peaks at 1900 K and 2000 K.

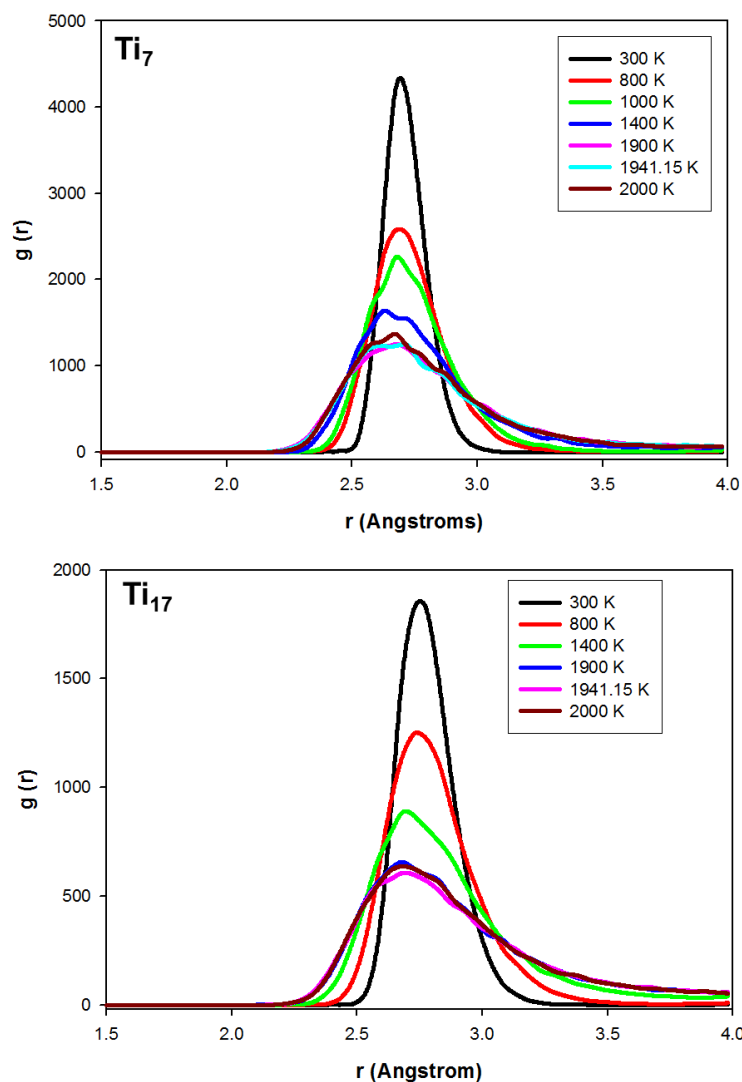


Figure 5.25: The radial distribution function for Ti_N ($N = 7$ & 17) at various temperatures.

The magnitude of the peaks becomes lesser as the number of Ti atoms is increased. The Argon effect on the nanocluster declines as the Ti atoms increases. The impact of the Argon gas on the nanocluster depends on the number of Argon gas atoms inserted as well as the Ti atoms.

5.6.6. The density profiles for Ti_N ($N = 7$ & 17) nanoclusters in an inert gas at various temperatures

The atomic distribution plot in Fig. 5.26 shows the distribution of atoms along the z-direction having solid features indicated by the distinct peaks.

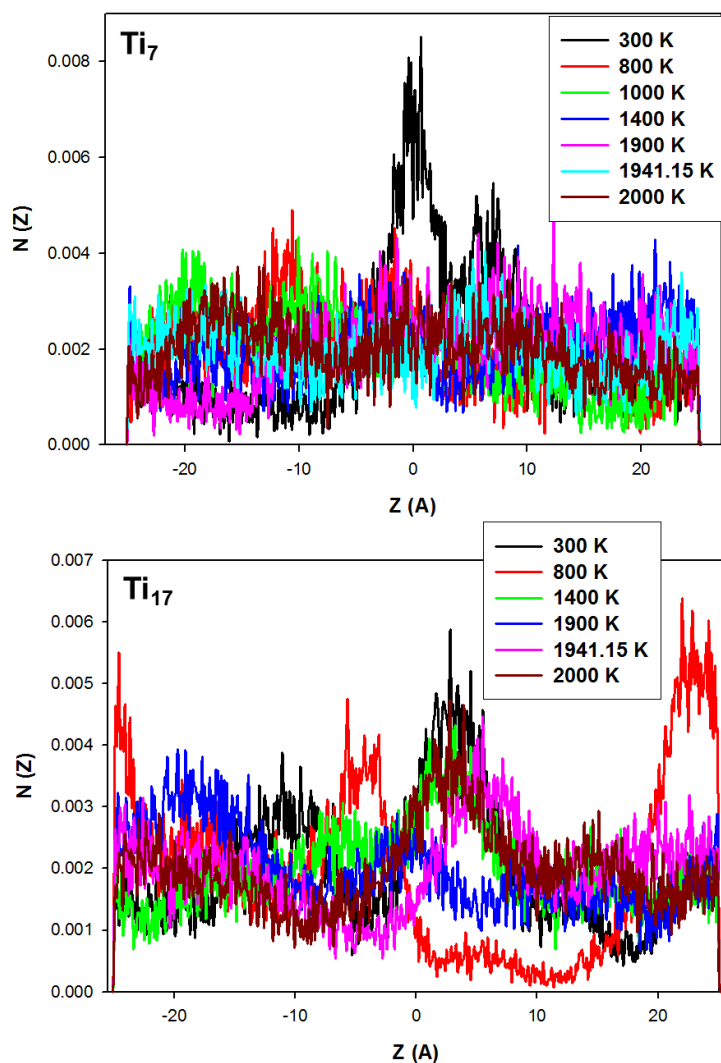


Figure 5.26: The comparison of Ti_N ($N = 7$ & 17) atomic distribution along a Cartesian coordinate (z) at different temperatures in an inert gas.

For Ti_7 and Ti_{17} we observe a distinct peak at 300 K suggesting that the morphology of the system is still ordered which is also observed with the RDF. However, we also notice that at a temperature from 800 K to 2000 K, the distinct peaks along the z-direction decreases resulting in the flattening of the peak at 2000K which might be attributed to the phase change of the nanocluster from a solid phase to a liquid phase.

For Ti_{17} the peak at 800 K is observed to have a high degree of fluctuations. Furthermore, at 1400 K and 1914.15 K we observe the peaks exhibiting features that have the same behaviour as the peak at 300 K. This phenomena may be attributed to the uniform distribution of Argon atoms in a liquid phase which exposes the nanocluster to thermal agitation. At elevated temperature, the inert gas is already in a liquid form and it might be evaporating and isolating from nanocluster. Moreover, at 1900 K the peak is observed to be flattened.

CHAPTER 6

The effect of the thermal agitation on Ti_N ($N = 32, 57, 80$ & 89) using molecular dynamics simulation

In this chapter we study the thermodynamic properties of the nanocluster and how the geometry and shape of bigger titanium nanoclusters ($N = 32, 57, 80$ and 89) are thermally affected using the molecular dynamic computational method. The molecular dynamics code (DL_POLY 4.08) was used to investigate the effect of temperature on four stable nanoclusters, i.e. Ti_{32} , Ti_{57} , Ti_{80} and Ti_{89} . The Ti_{32} will be treated in both vacuum and Ar environment and the Argon gas will not be captured for Ti_{57} , Ti_{80} and Ti_{89} . We will discuss the geometry evolution of nanoclusters, then their RDFs, potential energy, mean square displacement and density profiles.

6.1. The thermal agitated phase transition on the Ti_{32} nanocluster

In this section, we evaluate the thermal agitated phase transition to gain more insights regarding the structural transition as a function of temperature, the snapshots of the thermally agitated Ti_{32} nanocluster are analysed as shown in Fig. 6.1. The structural transients are shown in different colour coding as the structure of Ti_{32} nanocluster changes as a function of temperature. Note that the (Ti_{32}) nanocluster shows various geometrical configurations as the temperature is increased.

The configurational transitions as the temperature increases involve distortion or displacement of atoms in the Ti_{32} nanocluster. The distortion of the Ti_{32} nanocluster becomes more frequent from lower temperatures and increasingly severe with increasing temperature. The initial or non-thermal agitated configuration starts as interpenetrating icosahedra where one of the icosahedra is replaced with icositetrahedra geometry.

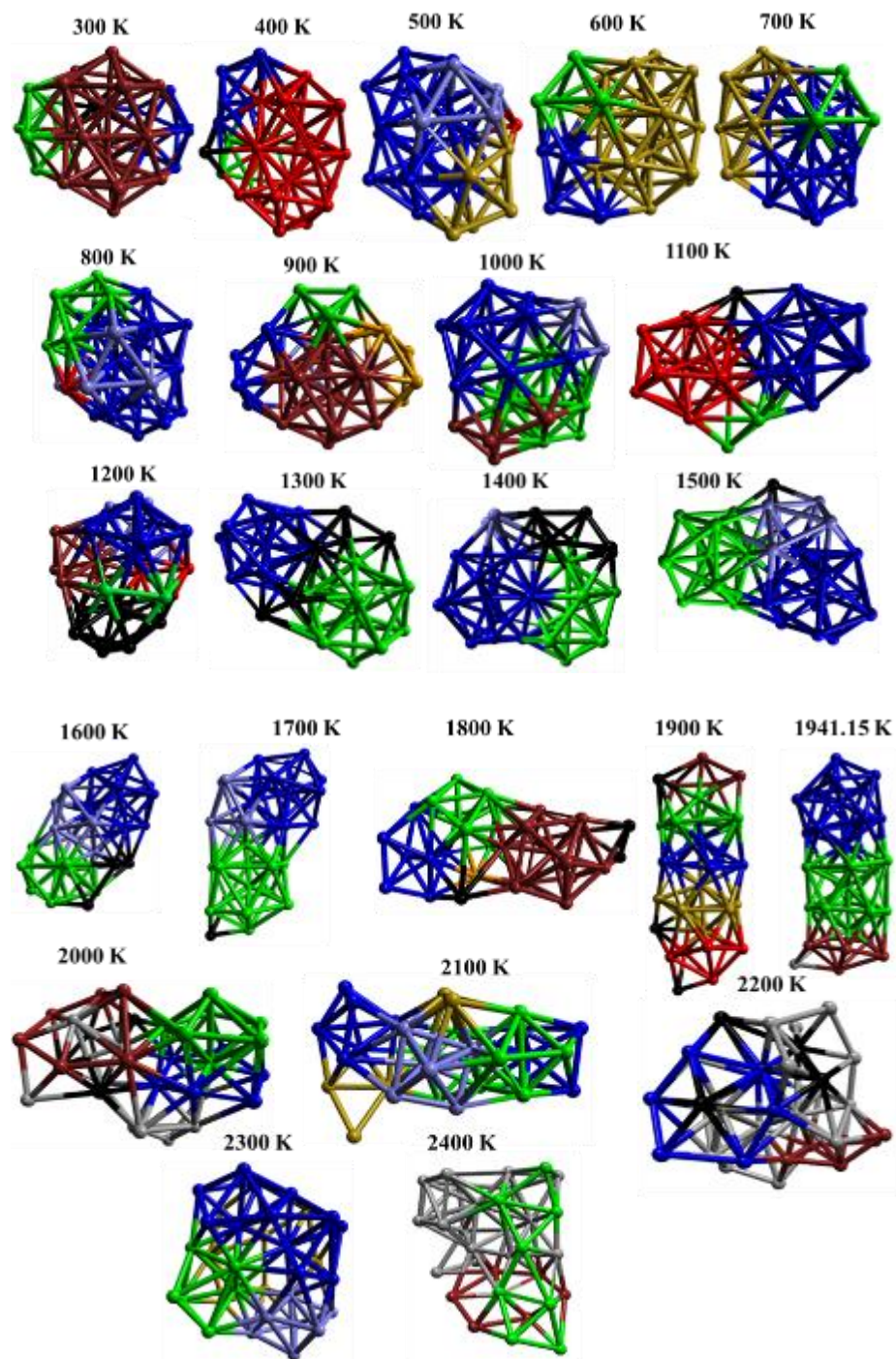


Figure 6.1 Ti_{32} nanoclusters in the vacuum at various temperatures.

At 300 K, the dominant configurations take a triangular bi-pyramidal Ti_5 (lime green), octahedral Ti_6 (lime green and maroon), pentagonal bi-pyramid Ti_7 (blue), icosahedra Ti_{13} (black and maroon), interpenetrating icosahedra Ti_{19} (maroon). As the temperature increases, the atomic displacement about the initial positions increases and lead to a change in the morphology of the nanocluster at 400 K to a Ti_{19} (red) interpenetrating with two pentagonal bi-pyramids, the Ti_7 (blue and lime green) is added on the sites of the Ti_{19} .

The transition of the nanocluster at 500 K is observed to have Ti_{20} (blue) polyhedron interpenetrating with icosahedra (gold), triangular bi-pyramidal (violet) and an atom (red) connecting the triangular pyramidal and the icosahedra units or nanocluster. At 600 K the nanocluster transitions to Ti_{19} (gold) polyhedron interpenetrating with Z13 Frank Casper polyhedron, Ti_{14} (blue) and triangular bi-pyramidal (lime green).

The effect of thermal agitation at 700 K appears to change the Ti_{32} morphology into two interpenetrating Ti_{19} polyhedron (gold and blue) with a triangular unit connected on the Ti_{19} polyhedra described by the blue colour. At 800 K, the two Z12 Frank Kasper polyhedral, Ti_{13} (green and blue) form the transient unit interconnected to pentagonal bi-pyramidal (lime green), triangular unit (violet) and an atom (red).

The Ti_{13} nanocluster (maroon) is observed to coexist with four pentagonal bi-pyramids (blue, green, and gold) at 900 K. Two interpenetrating icosahedra (lime green and blue) complemented by tetra-capped atoms (violet and maroon) on the sides are found to be the transient for 1000 K. The transition occurring at 1100 K leads to two icosahedra connected by dimers (black and lime green).

Furthermore, for higher thermal agitation, these fragmentation patterns reveal the existence of a stable building block namely an icosahedral or interpenetrating pentagonal bi-pyramid. At 1200 K, we observe the coexistence of three pentagonal bi-pyramid (blue, black and maroon) and triangular unit connecting all the penta-shaped isomers or nanoclusters with dimer (lime green) connecting the blue, maroon and black penta-shaped units.

The transient observed for 1300 K comprises two icosahedral units (blue and lime green) connected by six atoms. However, at 1400 K the two interpenetrating icosahedra (blue and green) are found to coexist with a triangular bi-pyramid unit as well as complementing dimer connecting the other fragments. The structural transformation precursor at 1500 K is found to be two icosahedral fragments (lime green and blue) connected by the hexagonal ring (violet, lime green and black) or triangular bi-pyramidal (violet) with an atom (black) connecting the icosahedra and triangular bi-pyramidal.

Furthermore, the structural transition for 1600 K is noted to be two icosahedral units connected by triangular bi-pyramid shaped nanocluster (violet) and triangular unit (black). At 1700 K we observe two interpenetrating icosahedra (blue and violet) connected on top of the icosahedral configuration (lime green) with an atom (black) capped on its face. The transient for 1800 K is found to be the icosahedron (maroon) bi-pentagonal bi-pyramid (blue and green) with tetra-coordinated capping atoms (black) completing the structure.

At 1900 K the nanocluster transitions into three interpenetrating icosahedra capped by an atom (black) which can also be seen as four interpenetrating pentagonal bi-pyramids (lime green, gold, blue and red) with triangular unit (maroon) capping the top of the pentagonal bi-pyramid (lime green) and three further single complementing atoms (black). However, at 1941.15 K which is the melting temperature for bulk titanium [275], the structural transition is observed as two

interpenetrating icosahedra (blue and green) capped pentagonal bi-pyramid (maroon) with one (grey) capping atom completing the structure. At 2000 K we observe three hexagonal rings (black, blue and red) coexisting with pentagonal bi-pyramid (lime green) capping with grey atoms completing the structure.

This transition did not follow the same pattern with icosahedral dominated configurations, and the behaviour might be attributed to the configuration having a higher symmetry structure. Furthermore, at 2100 K we observe three octahedral units (lime green, blue and violet) coexisting with eight atoms (gold and green). The 2200 K structural transition is observed to be two interpenetrating hexagonal rings (blue and black) coexisting with a pentagonal ring (maroon) and the surrounding atoms (grey). The same is observed where the nanocluster did not follow the pentagonal dominated pattern.

At 2300 K and 2400 K the thermal agitated structural transitions are observed to be hexagonal and pentagonal shaped dominated configurations (blue, lime green, violet and gold) whereas for 2400 K is observed to form a hexagonal ring (maroon) and triangular unit dominated transition. As discussed, above 2000 K there is appreciable atomic mobility confirming the molten state.

6.1.1. The potential energy (heating and cooling) on Ti₃₂ nanocluster

Figure 6.2 shows the potential energy at varied temperatures when the Ti₃₂ nanocluster is thermally agitated. This evaluation reflects the melting behaviour of the system. Particularly, the melting transition of the cluster from the rigid or solid form in which atoms merely oscillate about the equilibrium unit to a liquid or fluid form characterized by uncorrelated motion of atoms is spread over a range of temperatures from 300 - 2400 K. We observe a linear increase in energy varying

smoothly as the temperature is increased up to 1941.15 K. The plot depicts a jump in the potential energy at 2000 K above to the melting temperature (1941.15 K) of bulk Ti.

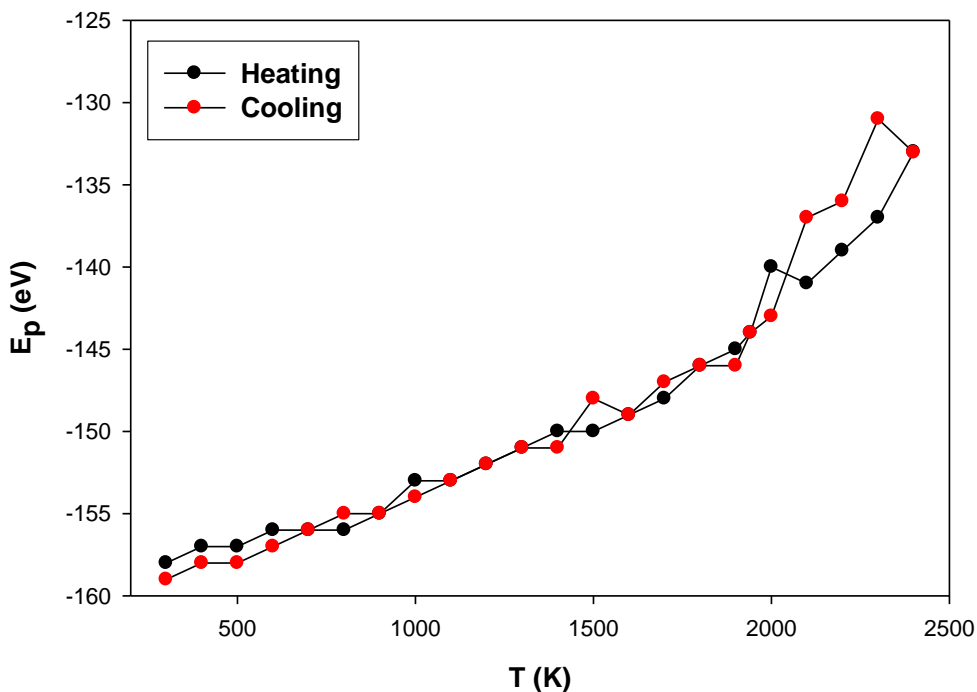


Figure 6.2: The potential energy at various temperature cooling for Ti_{32} nanocluster.

Additionally, the plot also shows smaller peaks at temperatures 400 K, 600 K and 1000 K with the potentials energies -157.0 eV, -156.0 eV and -153.0 eV. These may be attributed to the cluster losing its original orientation of atoms at lower temperatures or showing the characteristics of solid to a liquid phase transition. We also notice linearity of the energies at 600 – 800 K, 1100K – 1400 K, 1500 K – 1900 K and 2100 K – 2400 K respectively. The most striking feature is that the maximum potential energy occurs at a temperature above the bulk melting point. In addition, there

have been theoretical reports that small nanoclusters have elevated melting temperatures [276, 277].

In the case of the cooling process, the nanocluster undergoes a liquid-solid transition and more negative energies are observed at 300 K – 600 K, 1000 K, 1400 K, 1900 K and 2000 K suggesting the formation of a new stable configuration. There are cooling energies higher than heating energies observed at 800 K, 1500 K, 1700 K, 2100 K, 2200 K and 2300 K, suggesting the transition of less stable configurations.

The solid-liquid and liquid-solid transitions are observed to have similar energies at 700 K, 900 K, 1100 K - 1300 K, 1600 K, 1800 K and 1941.15 K suggesting the assemble of configurations that are similar to the heated configurations. We notice a weak hysteresis at 2000 K due to the structural changes as we cool the temperature from higher to lower temperature.

This influences the phase transition which results in hysteresis suggesting a phase change accompanied by the formation of a new geometry. The melting-quenching cycle discloses that it is easier for the nanocluster to go from the solid-liquid phase than the liquid-solid phase.

6.1.2. Configuration energy of the thermal agitated Ti_{32} nanocluster

Figure 6.3 depicts the configuration energy at varied temperature for the Ti_{32} nanocluster. The configuration energy is analysed to study the arrangement of atoms in the nanocluster as the system is thermally agitated. This plot shows a step by step wise trend as the temperature is increased from 300 – 2400 K.

It is observed that at temperatures 300 -700 K, the energies are constantly followed by a steeper depth at 800 K which resulted in lower energy nanocluster compared to other temperatures.

However, we observe a sudden jump in the energy from 800 – 1000 K which is followed by the linearity of the energies from 1000 – 1200 K.

Furthermore, we note the stepwise constant energies at temperatures from 1300 – 2300 K where we observe an abrupt jump in the energy at 1941.15 K which is higher as compared to other temperatures. The abrupt jump may be attributed to the phase transition of the nanocluster from a solid phase to a liquid phase. These observations are consistent with the potential energies of the nanocluster at varied temperatures.

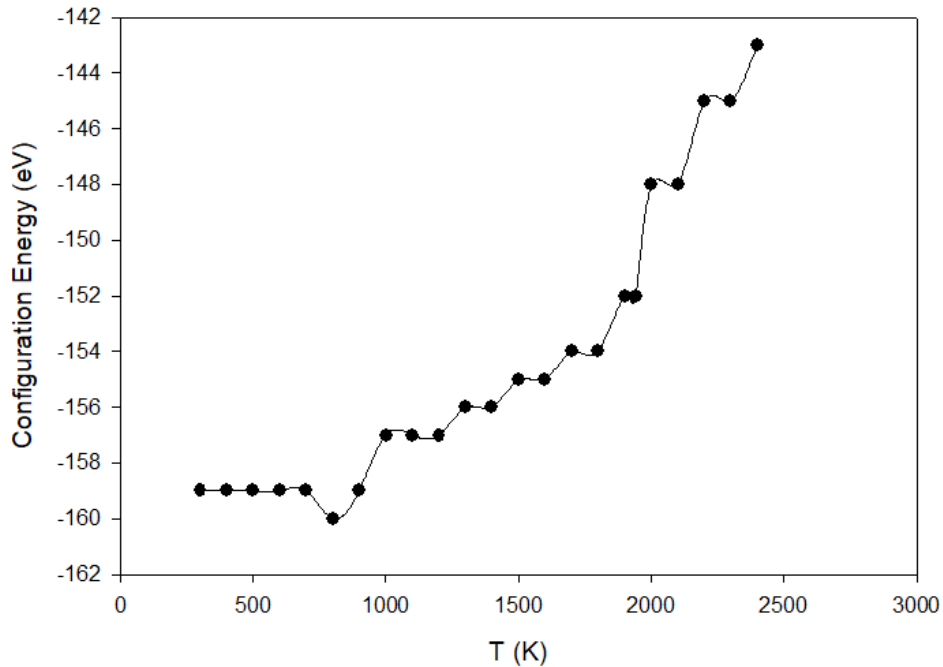


Figure 6.3: Configuration energy against temperature for Ti_{32} nanocluster.

6.1.3. Diffusion coefficient for thermal agitated Ti_{32} nanocluster

In Fig. 6.4, we discuss the diffusivity of Ti_{32} nanocluster as the temperature is increased above melting temperature. It can be seen that there is no movement of atoms at temperatures lower than 1941.15 K, where the diffusivity reverts to zero. However, at 2000 K the atoms appear to have a noticeable movement followed by a jump in the diffusivity at 2100 K which might be indicative of a solid-liquid transition of this cluster.

These observed transitions are justifiable since the melting temperature for Ti bulk is at 1941.15 K. It is also noticed that as the nanocluster is subjected to thermal agitation, the diffusivity of the cluster reverts to zero until the melting temperature is reached at 1941.15 K. The change in the slope of the diffusion coefficient against temperature plot is well defined as compared to nanoclusters with a smaller number of atoms as discussed in chapter 5.

Similar behaviour was noted for Pd-Pt clusters [278]. Their transition temperature was observed to be in the range 800-1200 K corresponding to the surface melting stage. However, both Pd and Pt diffusion coefficients show a tendency to increase with temperature whilst a decline is observed in our current study.

The decline behaviour might be due to atoms being smaller as compared to the number of atoms in their study. It is reported that small cluster shows a non-monotonic variation of the melting temperature and latent heat with cluster size [279, 280] and complete-shell icosahedral clusters melt at higher temperatures than incomplete-shell sizes. It was also reported that tin cluster ions with 10 – 30 atoms melt above the bulk metal [281]. Our results also suggest that the melting mechanism behaviour depends on the relative orientation of the core structure.

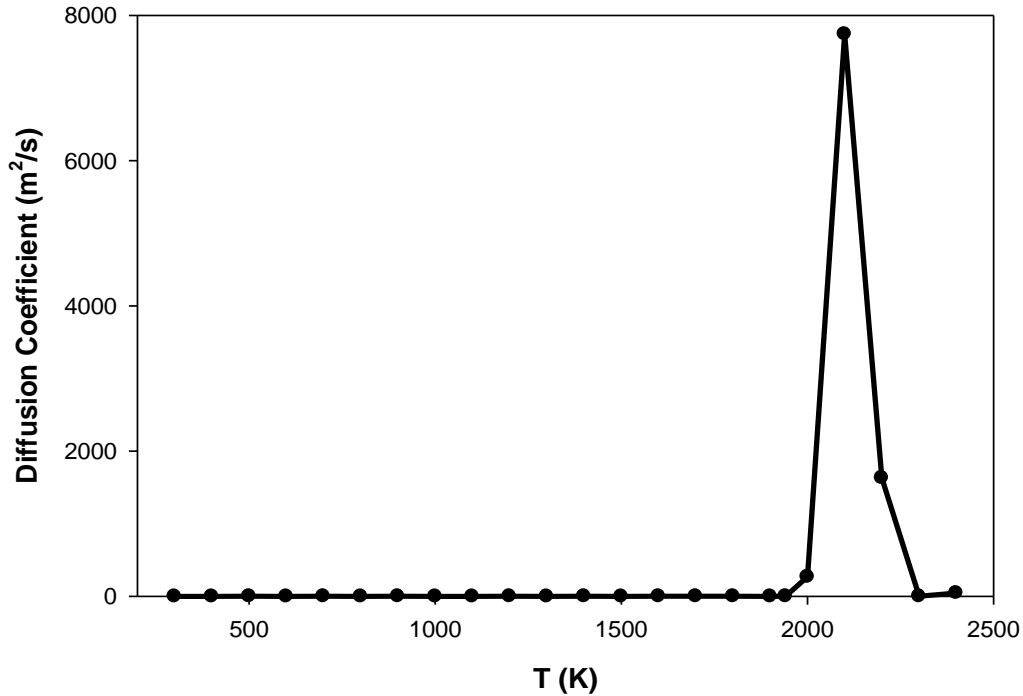


Figure 6.4: Diffusion coefficient as a function of temperature for Ti_{32} nanocluster.

6.1.4. Mean square displacement (MSD) for Ti_{32} nanocluster

In Fig. 6.5, we have also determined the mean square displacement (MSD) to determine the pre-melting behaviour of the Ti_{32} nanocluster. There is no observed signature indicating the surface melting of the nanocluster from 300 – 1900 K. After the melting temperature, both MSD and diffusivity depicts an abrupt jump reflecting the first-order melting transition of the nanocluster. However, beyond the melting temperature, both MSD and diffusivity fluctuate but tend to increase when the temperature is elevated.

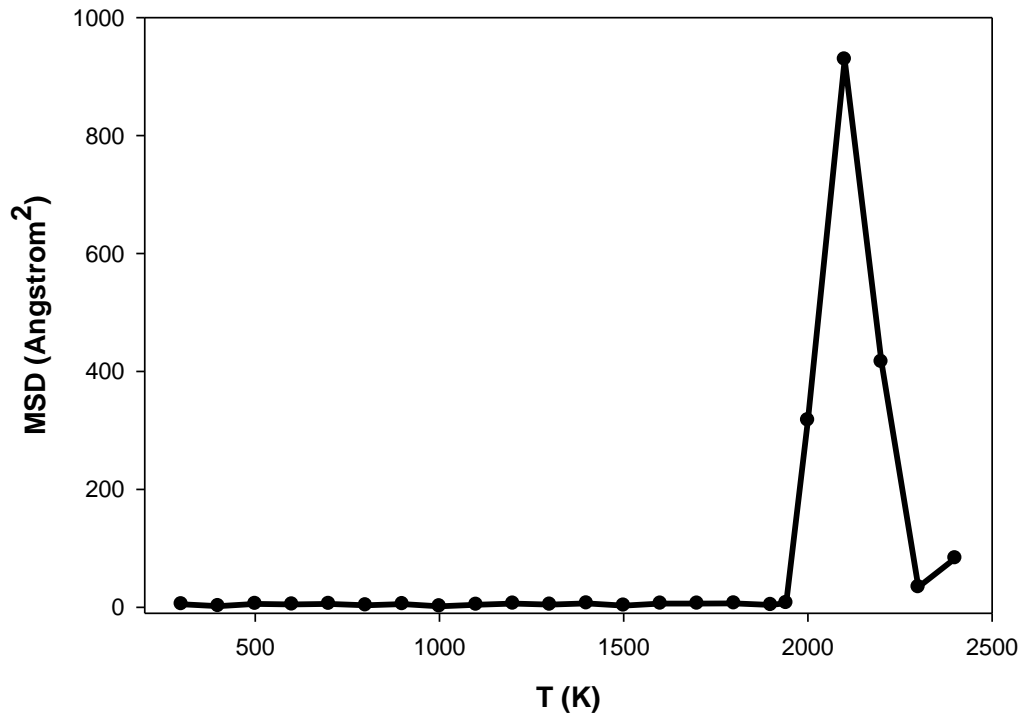


Figure 6.5: MSD for Ti₃₂ nanocluster at various temperatures.

6.1.5. Radial distribution function for Ti₃₂ nanocluster

The radial distribution curves at different temperatures are shown in Fig. 6.6. At 300 K the nanocluster is still solid as illustrated by the distinct peak. However, with the temperature range of 300 – 700 K, the nanocluster maintains a well-defined solid-like structure. As the temperature is increased, the surface melting or disorientation of atoms appears at $T > 800$ K.

This is observed through the broadening of the peaks which indicate the diffusion of atoms from the surface to the core which can be clearly illustrated by the uniformity of the distribution. The reduction in the peak size may be ascribed to nanocluster changing phases or fragments which at

some point reflect solid-liquid transitions at an elevated temperature near or above the melting point.

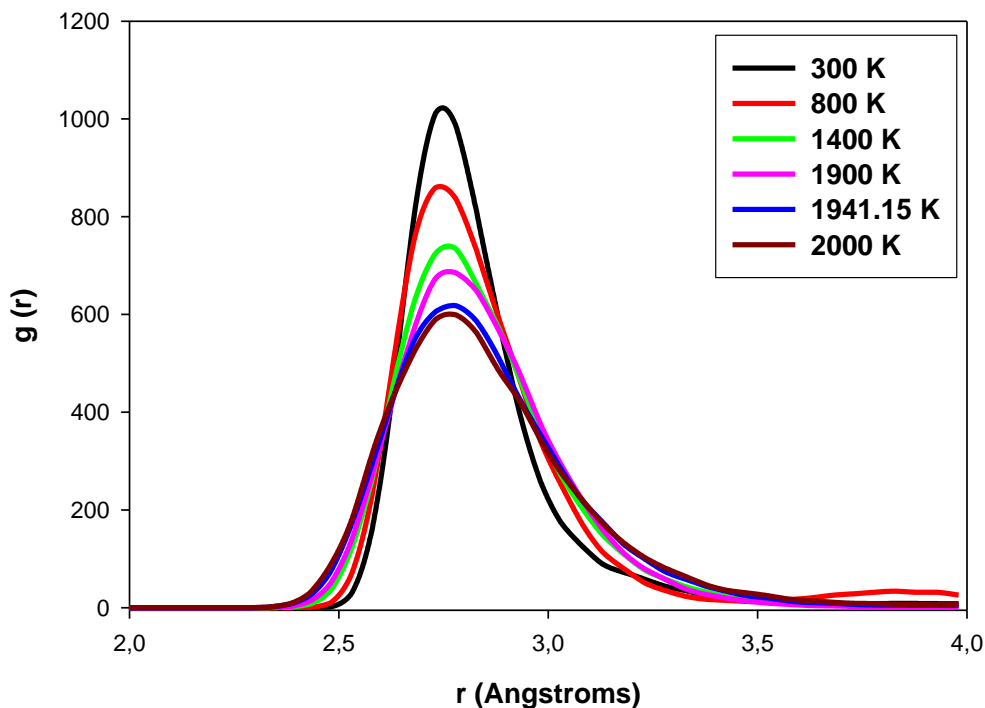


Figure 6.6: The radial distribution function for Ti_{32} nanocluster at various temperatures.

6.1.6. Density profiles for Ti_{32} nanocluster

In the case of the density profile plot, the atomic distribution of Ti_{32} nanocluster along the Z-axis at different temperatures shows various trends in Fig. 6.7. At lower temperatures, the solid-like features are indicated by the distinct peaks, where atoms have higher distribution at a certain distance from the centre.

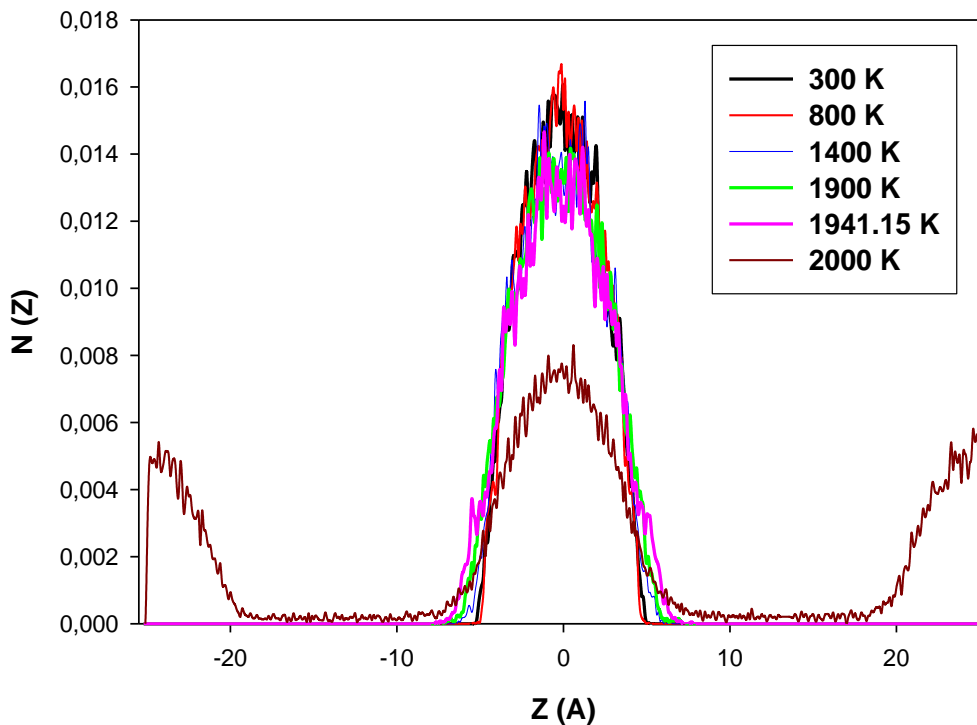


Figure 6.7: Comparison of Ti_{32} nanocluster atomic distribution along a Cartesian coordinate (z) at different temperatures.

This figure depicts an overlap of the peaks at 300 K and 800 K suggesting that the cluster retains its solid structural pattern within this temperature range. However, from 1400 – 1941.15 K the peaks are observed to decrease and overlapping indicating a similar initial surface melting process.

Furthermore, it becomes easier to observe the changes along the Z (Å) axis. As the temperature increases, the peaks becomes broader, showing a decrease in the size of the peak due to uniformly distributed atoms which is illustrated by the liquid characteristics. Moreover, at 2000 K beyond the Ti bulk melting temperature, atomic distribution becomes extensively shorter and the new peaks emerge which alludes to a liquid phase formation. These observations agree with the RDFs in Fig. 6.6.

6.2. The thermal agitated phase transition on the argon gas inserted Ti_{32} nanocluster

In Fig. 6.8, we further discuss the temperature dependence of Ti_{32} nanocluster in an inert gas environment to investigate the impact of the gas on nanocluster as they are thermally agitated at various temperatures. As the temperature increases, we notice small changes in the morphology of the nanocluster at a lower temperature below 600 K. Although for the pure Ti_{32} nanocluster, it was observed that the structural changes were at 400 K.

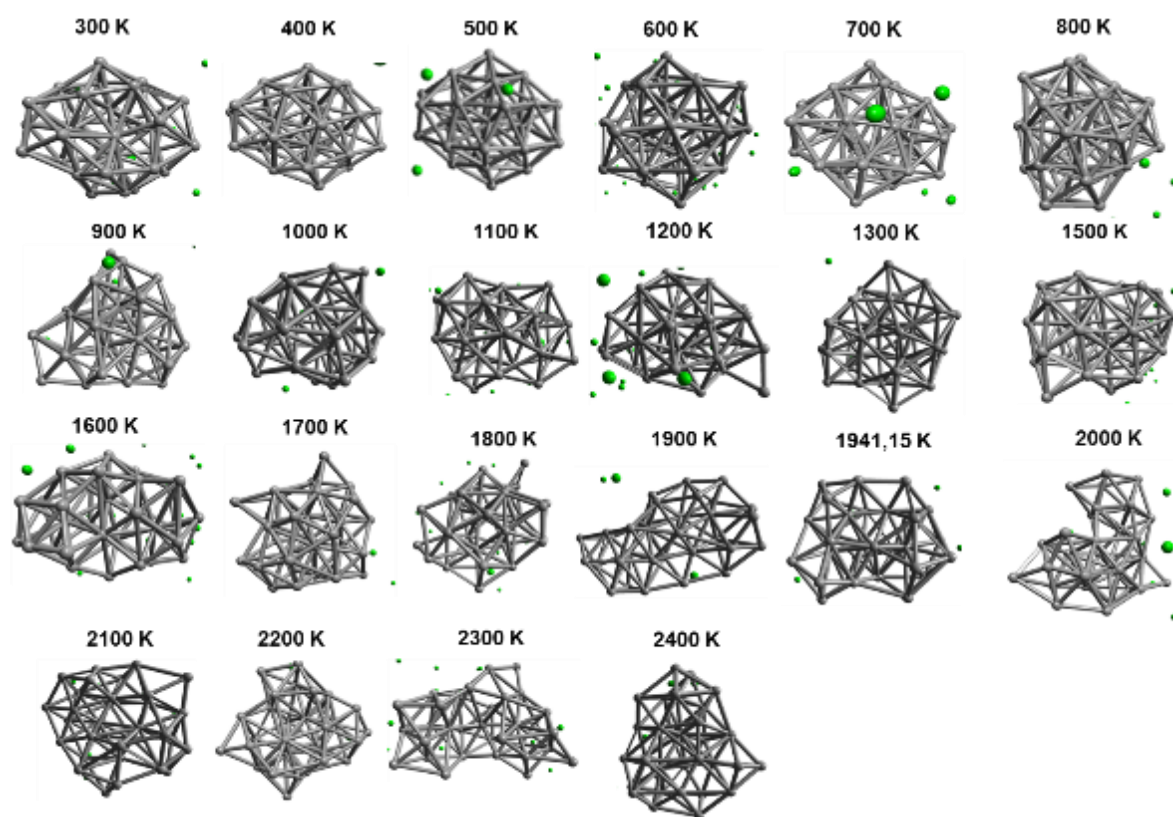


Figure 6.8: Ti_{32} nanoclusters in an inert gas environment at various temperatures, where the green circles represents Ar atoms.

This may suggest that the inert gas seem to be mobilizing the atoms and maintaining its original morphology. In contrast, the atomic distribution of the inert is initially having a great impact on the surface of the nanocluster. However, at $T > 1500$ K the inert gas is observed to have a great impact in the nanocluster core and becomes liquid-like for $T > 1700$ K indicated by the loss of the morphology.

Additionally, as the temperature increases, we notice the dominance in the kinetic energies of the inert gas from 800 – 2400 K resulting in stronger distortions of the nanocluster at elevated temperatures. For instance, at 800 – 1600 K we observe the capping of two interpenetrating Ti_{19} followed by a total distortion of the original morphology for all temperature close to the melting temperature of titanium.

6.2.1. The potential energy for Ti_{32} nanocluster in an argon gas environment

In Fig. 6.9, we show the potential energy at various temperatures in an argon environment. We observe the reduction of the potential energy jump at temperatures 300 K to 400 K in comparison with the energies for Ti_7 , Ti_{13} and Ti_{17} . These could be attributed to the increase in the number of atoms, which are likely to reduce the vibrational speed at lower temperatures.

We also notice the linearity of the energies at 500 – 2000 K interfered by a small jump at 1600 K which may be due to the atomic distribution of argon gas into the core of the structure resulting in the Ti nanocluster its structural stability. Furthermore, we observe a jump in the potential energy at 2100 K which is above the melting temperature of bulk Ti suggesting a transition from a solid phase to a liquid phase of the nanocluster.

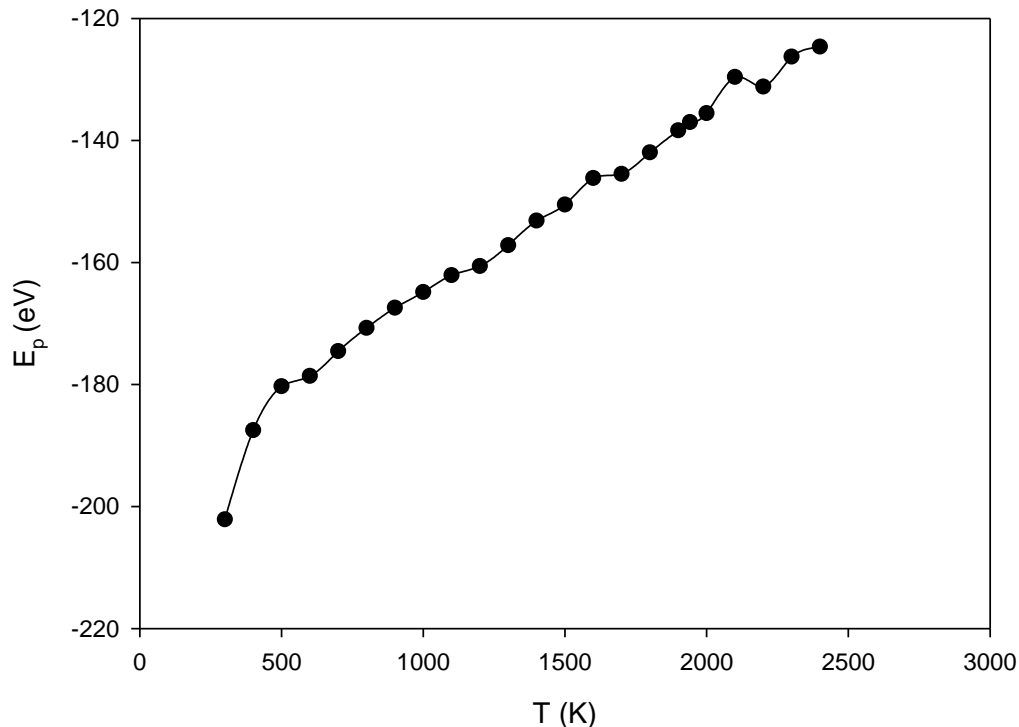


Figure 6.9: Variation of the potential energy with temperature for Ti_{32} nanocluster in an argon environment.

The higher surface melting temperature corresponds to the nanocluster with a lower percentage of the Argon atoms being a distance away from the Ti cluster as depicted in Fig. 6.8. The Argon molecules behave like free molecule at higher temperatures.

6.2.2. Diffusion coefficient for thermal agitated Ti_{32} nanocluster in an inert gas environment

In the case of the diffusion coefficient in Fig. 6.10, the plot depicts the movement of atoms at various temperatures. There is a lack of movement of atoms at 700 K, 800 K, 900 K, 1300 K, 1500 K and 2300 K where the diffusivity is observed to revert to zero. In comparison with the diffusivity in a vacuum environment, we observed that the effect of an inert gas results in the movement of atoms at lower temperatures, 300 – 500 K.

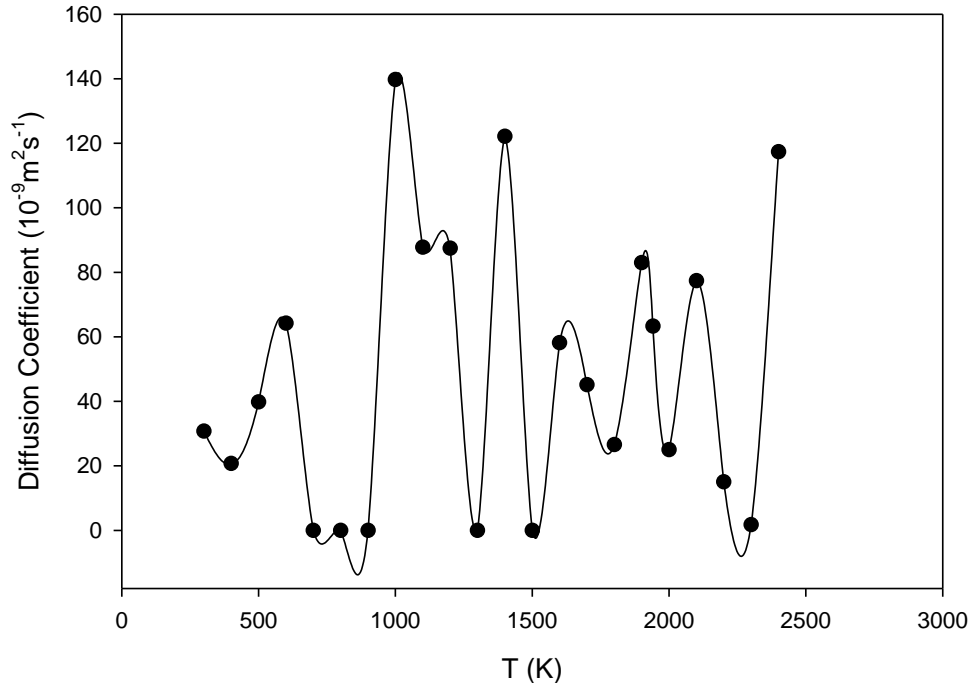


Figure 6.10: Diffusion coefficient as a function of temperature for Ti_{32} nanocluster in an inert gas environment.

We further observe the highest diffusivity peaks at 1000 K, 1400 K and 2400 K, which might be influenced by the effect of inert gas on the nanocluster by increasing the kinetic energies of the atoms.

6.2.3. Mean square displacement (MSD) for Ti_{32} nanocluster

Figure 6.11, depicts the total Mean square displacement as a function of temperature. We also observe the movement of atoms on the Ti_{32} nanocluster for all the temperatures.

We observe the highest peaks at 500 K, 1000K, 1400K and 2400 K which indicates higher fluctuations of atomic distribution of atoms. However, we observe the highest peak at 2400 K as compared to 2100 K for pure nanocluster in Figure. 6.5. Furthermore, the 1400 K is also observed

to be the second-highest peak for this nanocluster. The inert gas had a great impact mostly on the surface of the cluster as compared to the inner core atoms. This impact can be clearly seen in Fig. 6.8. The nanocluster displays disorder on the outermost periphery.

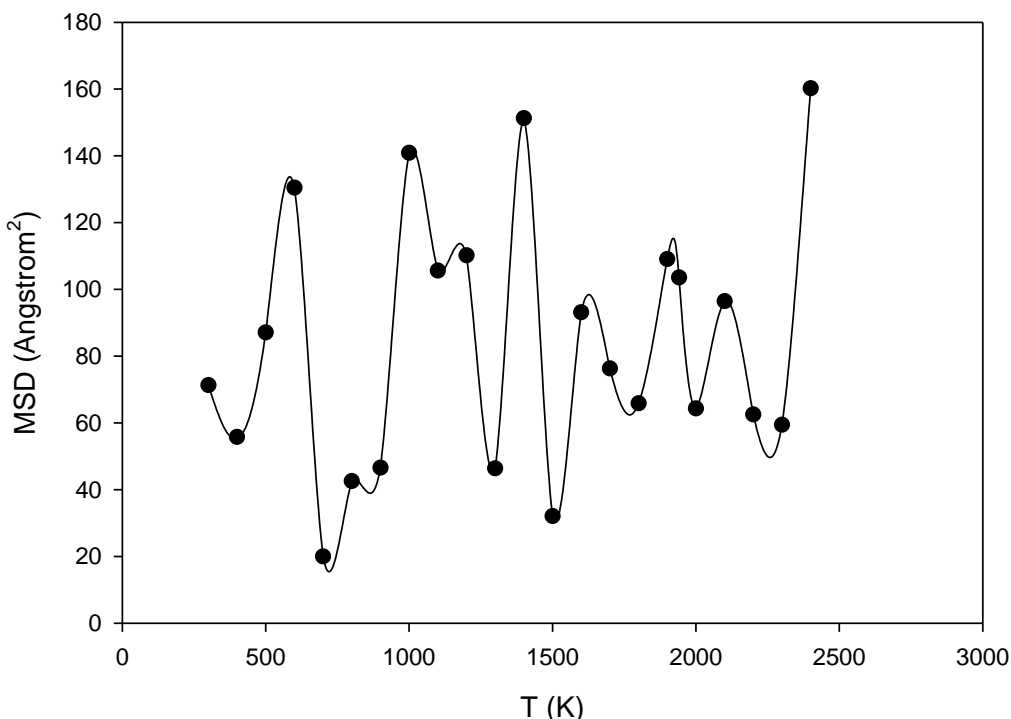


Figure 6.11: The MSD of Ti₃₂ nanocluster in an inert gas environment.

6.2.4. Radial distribution function for Ti₃₂ nanocluster

Figure 6.12 shows the radial distribution function for Ti₃₂ at varied temperatures. The peaks are observed decreasing with increasing temperature. The first peak shows that the nanocluster has a well-ordered structure or the atoms are localized on the surface but the patterns start to appear as the temperature elevates. As observed in pure Ti₃₂ nanocluster, the 300 K and 800 K peaks are slightly higher in probability when the nanocluster is inserted in an Argon environment. However,

as the temperature increases, the peaks becomes broader and decreases except for 1900 – 2000 K temperatures, where the peaks are observed to superimpose each other.

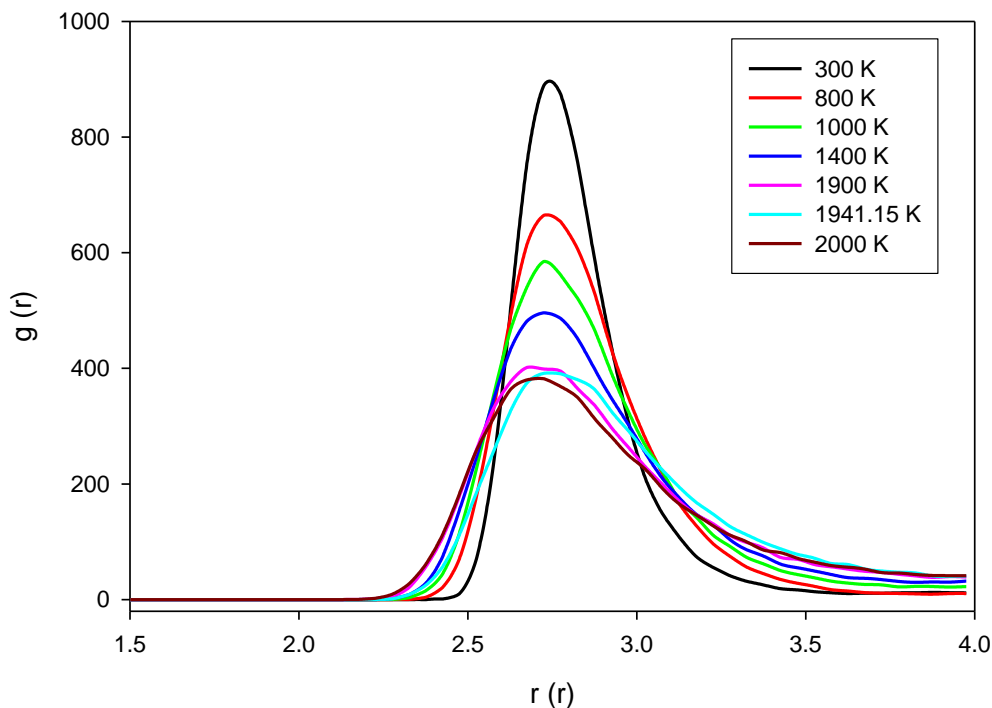


Figure 6.12: The radial distribution function of the Ti_{32} in an inert gas environment at various temperatures.

These phenomena may be due to the nanocluster displaying Ar – Ti isolation caused by the Ar gas-liquid state transition state resulting in Ti cluster nanocluster freely exposed to thermal agitation. The surface melting is observed to take place at 800 K and 900 K.

6.2.5. Density profiles for Ti_{32} nanocluster

Figure 6.13 show the density distribution at varying temperatures. At a lower temperature of 300 K, we observe that the solid-like features are preserved suggested. This is continued by the distinct peak showing higher distribution only at certain distances from the centre. As the temperature

increases, the peaks at the centre shift to the right and decreases in size. We observe an emerging higher temperature peaks at 2000 K which was also seen for pure Ti_{32} nanocluster in Fig. 6.7.

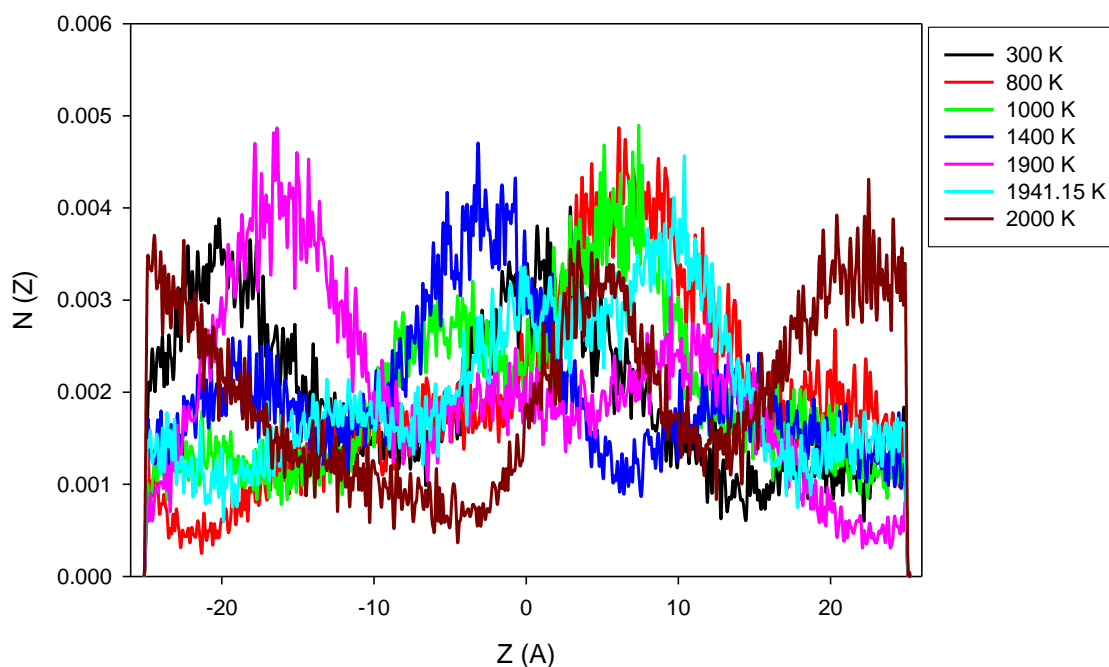


Figure 6.13: Comparison of Ti_{32} atomic distribution along a Cartesian coordinate (z) at different temperatures in inert gas.

This could be due to the argon gas having an inconsiderable effect at higher temperature as a result of high atomic motion in a liquid phase. However, as the temperature increases, the peaks decreasing in size indicating that the temperature increment may result in the magnitude of the peaks flattened. This suggests that the phase transition from a solid phase to a liquid phase occurred due to the uniform distribution of atoms in a liquid phase. The fluctuations of the density profiles become lower beyond a melting point (1941.15 K) corresponding to the solid-liquid melting first-order transition taking place.

6.3. Structural evolution and thermal transitions on Ti_N ($N = 57, 80$ & 89)

In this section, we discuss the structural and thermal transitions for Ti_N ($N = 57, 68, 80$ and 89). The intentions are to bring more insight into the structural evolution of bigger nanoclusters as they are thermally stressed. We compare their strength by analysing their potential energies, mean square displacement, radial distribution function and density profiles as they approach the molten state. The discussion will also follow that of the Ti_{32} nanocluster above. However, the evaluation for the Argon gas environment will not be captured. Firstly, we will analyse the thermal agitation of each nanocluster separately and compared their thermodynamics properties.

6.3.1. The thermal agitated phase transition of Ti_{57}

The thermal agitated structural transitions at 300 K are observed to be two interpenetrating icosahedral units Ti_{19} (lime green) coexisting with pentagonal bi-pyramid (maroon) sharing existence with triangular bi-pyramidal (black) which is connected to icosahedral unit (blue). The Ti_{19} is also observed to be connected to Ti_{13} (blue) and hexagonal shape isomer (light brown) with a 1 – 6 – 1 layered stacking by three atoms (grey).

The transition at 400 K is observed to have three icosahedral configurations (blue, maroon and black) coexisting with three pentagonal bi-pyramid (gold and lime green) having the upper layered staking connected to 4 atoms (blue and maroon). The two lime green atoms connect both the icosahedral configuration (blue and black) which forms pentagonal units (black and lime green) and (blue, gold and black).

The effect of thermal agitation at 500 K appears to change the Ti_{57} morphology into an unit having Ti_{19} isomer (blue and gold) coexisting with Ti_{13} (blue), pentagonal bi-pyramid (gold, lime green, and red). The gold pentagonal bi-pyramid coexists with pentagonal units (black and maroon).

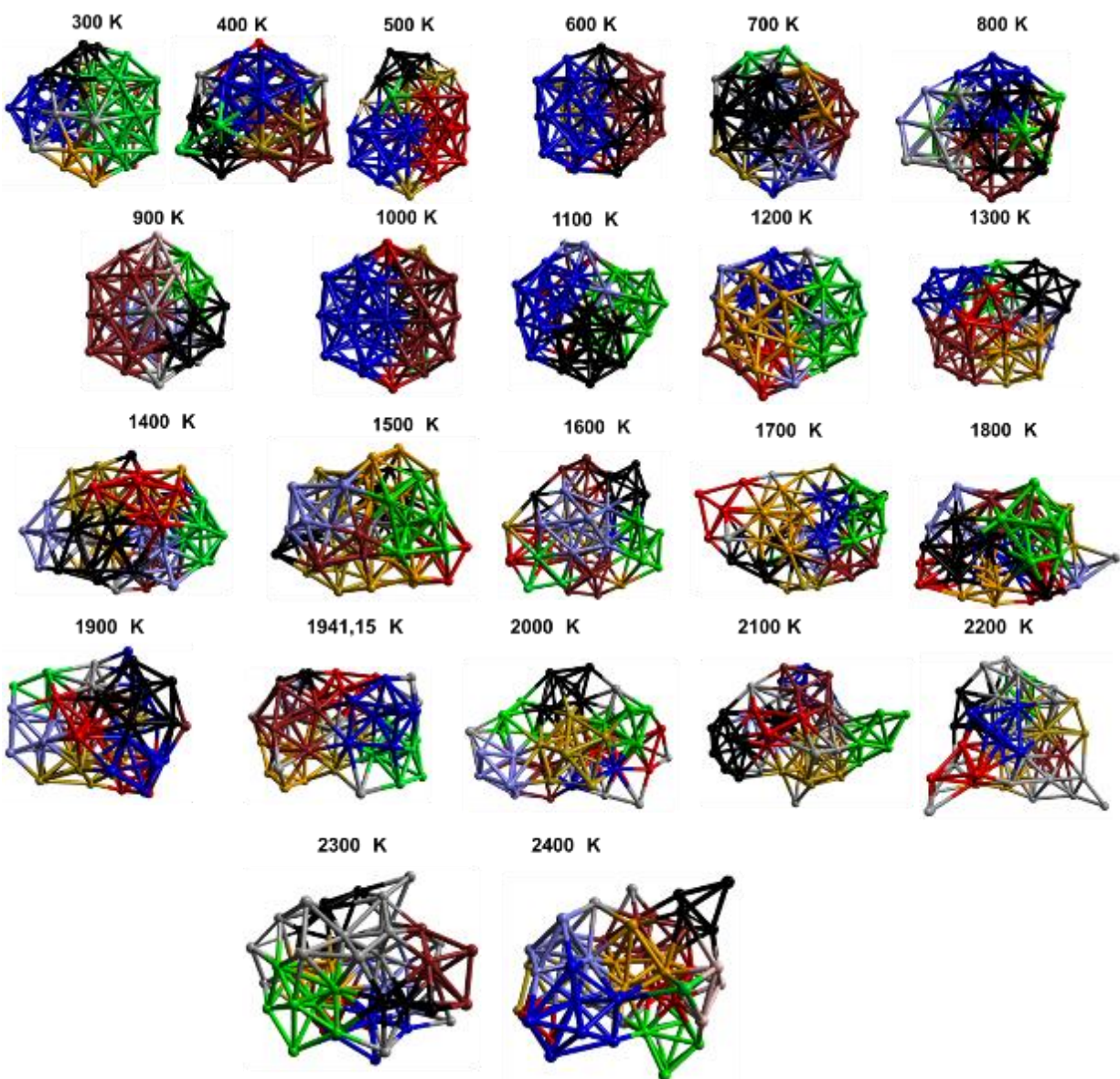


Figure 6.14: The Ti_{57} nanoclusters in the vacuum at various temperatures.

At 600 K we observe the nanocluster transitioning into three Ti_{19} isomers (blue, maroon and gold) where maroon and blue Ti_{19} are connected to each other by five atoms (black) whilst the Ti_{19} (gold) is connected to both Ti_{19} (blue and maroon) units.

Furthermore, the structural transition for 700 K is noted to be three icosahedral configurations (violet, maroon and black) coexisting with pentagonal units (lime green, light brown and blue). At 800 K we observe icosahedral thermal agitated precursors (blue and maroon) interconnected to two hexagonal rings (black, lime green and violet). The Ti_{19} geometry (maroon) is observed to interconnect with icosahedral unit (black) by two atoms grey atoms.

The other configurations involved in the building block of the nano-system is icosahedron unit (violet) interconnected to pentagonal bi-pyramid geometry (lime green) and Ti_{13} (maroon) by 9 atoms (grey). The transient observed for 1000 K comprises of three Ti_{19} stoichiometry (blue, maroon and red) connected to each other, whilst the other is highlighted with a red atom on the upper and lower layered stacking.

The Ti_{19} isomer (black) coexist with the other Ti_{19} isomers (maroon, red and blue) with two atoms (lime green and gold) creating pentagonal units coexistence.

At 1100 K we observe the nanocluster having been transitioned to Ti_{19} configurations (lime green and blue) coexisting with Ti_{13} black. Ti_{19} (lime green) is observed to interconnect with pentagonal units (gold and violet). However, Ti_{19} units (blue and lime green) are connected to each other by 4 atoms (red). The transient for 1200 K is found to be the Ti_{19} (lime green) and Ti_{13} (blue) coexisting with hexagonal unit with a 1 – 6 – 1 layered stacking (light brown), pentagonal bi-pyramid (gold) and octahedron configurations (black, red and maroon).

The structural transformation precursors at 1300 K is observed to have a coexistence of pentagonal bi-pyramid configurations (blue, black, violet, lime green and gold). However, other pentagonal shaped units are highlighted in different colours, interconnecting with a hexagonal unit (maroon). At 1400 K, we observe the coexistence of pentagonal isomers (black, red, and lime green, blue and maroon). The other coexisting configurations are tri-angular bi-pyramidal (violet) and octahedral (gold). Pentagonal bi-pyramidal seems to be the dominant building block isomers at elevated temperatures.

The thermal agitated transient at 1500 K is observed to be a pentagonal units (black, gold, violet and lime green) coexisting with triangular bi-pyramidal structure (red) and other units highlighted in different shades. At 1600 K, the structural transition is observed to be dominated by pentagonal and icosahedral geometries. The pentagonal units (violet, gold and lime green) are observed to coexist with octahedral units (black, and red) with others expressed in different shades.

The thermal transient at 1700 K is observed to be the pentagonal units (lime green, light brown, black and maroon) coexisting with triangular bi-pyramidal (black and red) as well as other configurations which are highlighted with different colours. At 1800 K, the structural transformations are observed and found the nano-system transitioned to three pentagonal units, triangular bi-pyramidal and octahedral geometries highlighted in different colours. However, the thermal agitation at 1900 K is observed to have transitioned into a pentagonal bi-pyramidal unit (black, red and gold), coexisting with a capped pentagonal (violet) and other triangular units expressed with different colours.

The pentagonal bi-pyramid (blue, maroon, lime green and red) at 1941.15 K, were found to be the dominating configurations coexisting with triangular bi-pyramidal. However, at 2000 K, we observed the structures having been transitioned to pentagonal bi-pyramid configurations (gold

and black) interconnecting with the octahedron and tri-angular bi-pyramidal units. At 2100 K, the pentagonal bi-pyramid units (black and gold) coexist with octahedral geometries (violet, light brown) and Ti_5 (red).

The transient at 2200 K is found to be an octahedral unit coexisting with Ti_5 highlighted in different colours as well as other atoms. At 2300 K and 2400 K, we observed Ti_7 (lime green), octahedral structure (violet and red), triangular bi-pyramidal (maroon, light brown and black) whilst the highest temperature depicts a pentagonal geometry (blue), and triangular bi-pyramidal coexisting with other inclusive of the other atoms which can't be expressed as fundamental fragmentations. This cluster is observed to segregate to cluster surface below 1300 K and becomes more uniformly distributed in the surface and interior at higher temperatures.

6.3.2. The thermal agitated phase transition of Ti_{80}

The structural transition at 300 K is observed to be the three interpenetrating icosahedral stoichiometry (lime green) coexisting with Ti_{19} (maroon) with three atoms (black) connecting them with pentagonal bi-pyramid (light brown) and the icosahedral unit (violet) connected to lime green and light brown geometries by four grey atoms, which as well coexist with pentagonal bi-pyramid (gold). Red atoms connect all the building block fragmentations.

At 400 K, the thermal transient is found to be three interpenetrating icosahedral geometries (lime green) which are interconnected to Ti_{19} (black) and icosahedral unit (gold) coexisting with pentagonal bi-pyramid configurations (red, blue and maroon) and triangular bi-pyramidal (violet). However, at 500 K, the structural changes are observed to have three icosahedra (blue, light pink, lime green and red) coexisting with each other, having pentagonal bi-pyramid units (maroon and

gold) interconnected to blue geometry and another pentagonal geometry connected to the three icosahedral configurations (light pink, lime green and red).

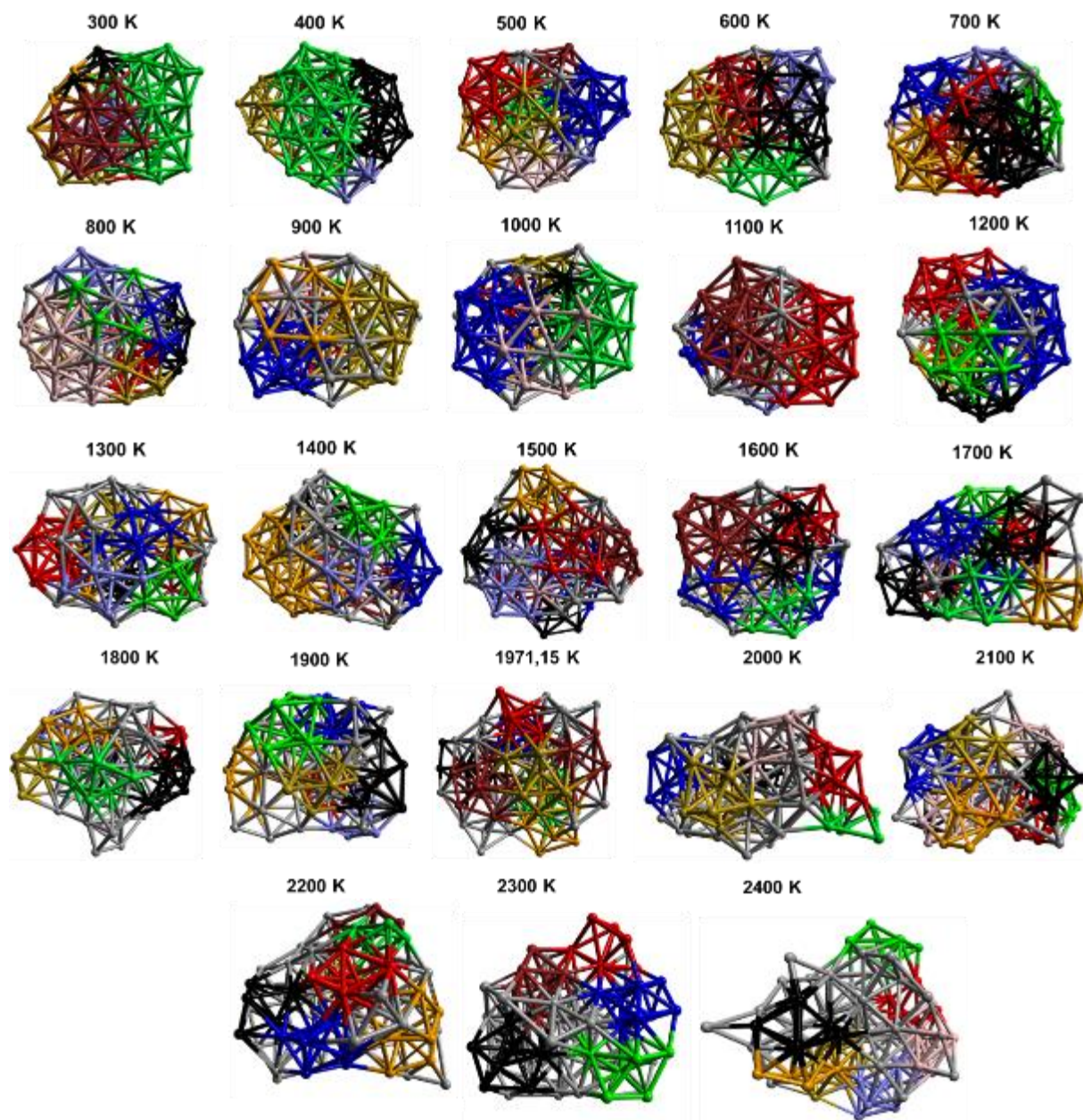


Figure 6.15: The Ti₈₀ nanoclusters in the vacuum at various temperatures.

At 600 K, we observe Ti_{19} (gold) connected to Ti_{19} (black and violet) by three maroon atoms and coexisting with an icosahedron (lime green) with icosahedral isomer (violet) interpenetrating with Ti_{19} (black) where the Ti_{19} (red) interconnects with every unit.

The Ti_{13} unit (light brown) and Ti_7 (blue) is found to be connected to Ti_{13} (black) by 6 atoms (red) at 700 K. Two icosahedral configurations (maroon) are found to coexist with hexagonal shaped structure (lime green) and octahedral unit (violet).

At 800 K, we observe the thermal agitated structure changing to Ti_{19} units (light pink and violet) connected to each other by the hexagonal ring (gold) and two grey atoms. There are three hexagonal rings (black, blue and lime green) interconnecting pentagonal bi-pyramid (red) with the larger units.

The structural transition at 900 K is found to have the icosahedral unit (blue) connected to Ti_{19} (gold) by the hexagonal ring (light brown) and other atoms (grey). Two hexagonal rings (red and black) are found to coexist with the icosahedron (light pink) with Ti_{19} isomer (gold) and Ti_{13} (Blue).

The transient for thermal agitation at 1000 K is observed to be Ti_{19} geometries (blue and lime green) interconnected by the hexagonal ring (light pink), coexisting with pentagonal units (red, black and light brown), Ti_5 (gold) and several grey atoms. At 1100 K, the Ti_{19} is found to be connected to Ti_{19} (maroon) by two grey atoms, coexisting with octahedral unit (black), pentagonal bi-pyramid (violet) and Ti_5 (lime green). All the atoms in grey form part of the interconnection between the desired fragmentations.

At 1200 K, the Ti_{19} unit (blue) is found to interconnect with Ti_{13} (lime green) and Ti_7 (black) and coexisting with Ti_{13} (red), two Ti_7 (light brown and lime green) and the hexagonal ring (gold). The

1300 K transient is observed to be dominated by icosahedron (red, light brown and gold) and pentagonal bi-pyramid (blue, maroon and light brown) precursors coexisting with octahedral unit (lime-green). Ti_5 configuration (violet) and hexagonal-shaped structure (violet, blue and red). At 1400 K, the thermal transient is observed to be a Ti_{19} isomer coexisting with five pentagonal bi-pyramid (maroon, blue, lime green and red), Ti_5 (violet) and other atoms in grey.

At 1500 K, the structural transitions are observed to Ti_{19} (black and violet) interconnecting with icosahedral geometry (blue) and coexisting with four pentagonal units (maroon, red, black and light brown) and other additional atoms (grey). The thermal transient at 1600 K is observed to be an icosahedral unit (maroon) coexisting with four Ti_7 geometries (black, blue, gold and blue-maroon), Ti_5 units (lime green, violet-gold and light brown) and hexagonal-shaped structure (red).

The thermal agitation at 1700 K is found to have the Ti_7 unit as the dominance configuration. The structural transformation is observed to have pentagonal bi-pyramid fragmentations (blue, light brown, lime green, black, maroon and gold-red-lime green). The other fragmentations forming part of the building block are Ti_5 (black, red, lime green and violet Ti_6 (red-lime green)).

At 1800 K, there is a high degree of structural distortions. It might be due to the fact that the temperature is closer to the melting point. We observe structural changes to be the coexistence of Ti_7 geometries (black, lime green, violet, light brown, gold and red) and hexagonal-shaped structure (black).

The other atoms (grey) are interconnection for $N < 5$. At 1900 K, the structural changes are observed to have the coexistence of pentagonal isomer (black, blue, light brown, lime green, violet, red and gold-lime green) and octahedral configuration (violet). We observe the coexistence of

pentagonal isomers (black, blue, gold-red-maroon, lime green, light brown-lime green and maroon, octahedral units (red and maroon) at 1941.15 K.

The structural changes observed at 2000 K, are pentagonal bi-pyramid units (blue, gold, red, red-lime green, light brown and black) coexisting with octahedral unit (light pink).

At elevated temperatures 2100 – 2400 K, we observe an icosahedral geometry (blue) coexisting with Ti_7 units highlighted in different colours. There exists pentagonal dominated fragmentation with a higher level of distortions. This cluster is observed to segregate to cluster surface below 1600 K and becomes more uniformly distributed in the surface and interior at higher temperatures.

6.3.3. The thermal agitated phase transition of Ti_{89}

The thermal agitated structural transitions at 300 K are observed to be three interpenetrating icosahedra (lime green) connected to Ti_{19} (maroon) by two hexagonal rings (lime green-grey and red-grey-lime green), coexisting with Ti_{19} (blue) Ti_7 (light brown) and hexagonal rings (black and gold). At 400 K, the structural transformation is observed to be three interpenetrating icosahedra (lime green) interconnected and connected to Ti_{19} (maroon) coexisting with Ti_{19} (blue), Ti_7 (maroon) and hexagonal rings (black and gold).

At 500 K, the transient is observed to have Ti_{19} (gold and lime green) connected to the hexagonal ring by one atom (grey) and coexisting with two Ti_7 (red and black). The Ti_{19} unit (blue) is found to interpenetrate with three interpenetrating hexagonal-shaped structures (black). The structural changes observed at 600 K, Ti_{19} (blue) is found to interpenetrate with icosahedral geometry (lime green) with four atoms (grey) the geometry with icosahedral unit (red).

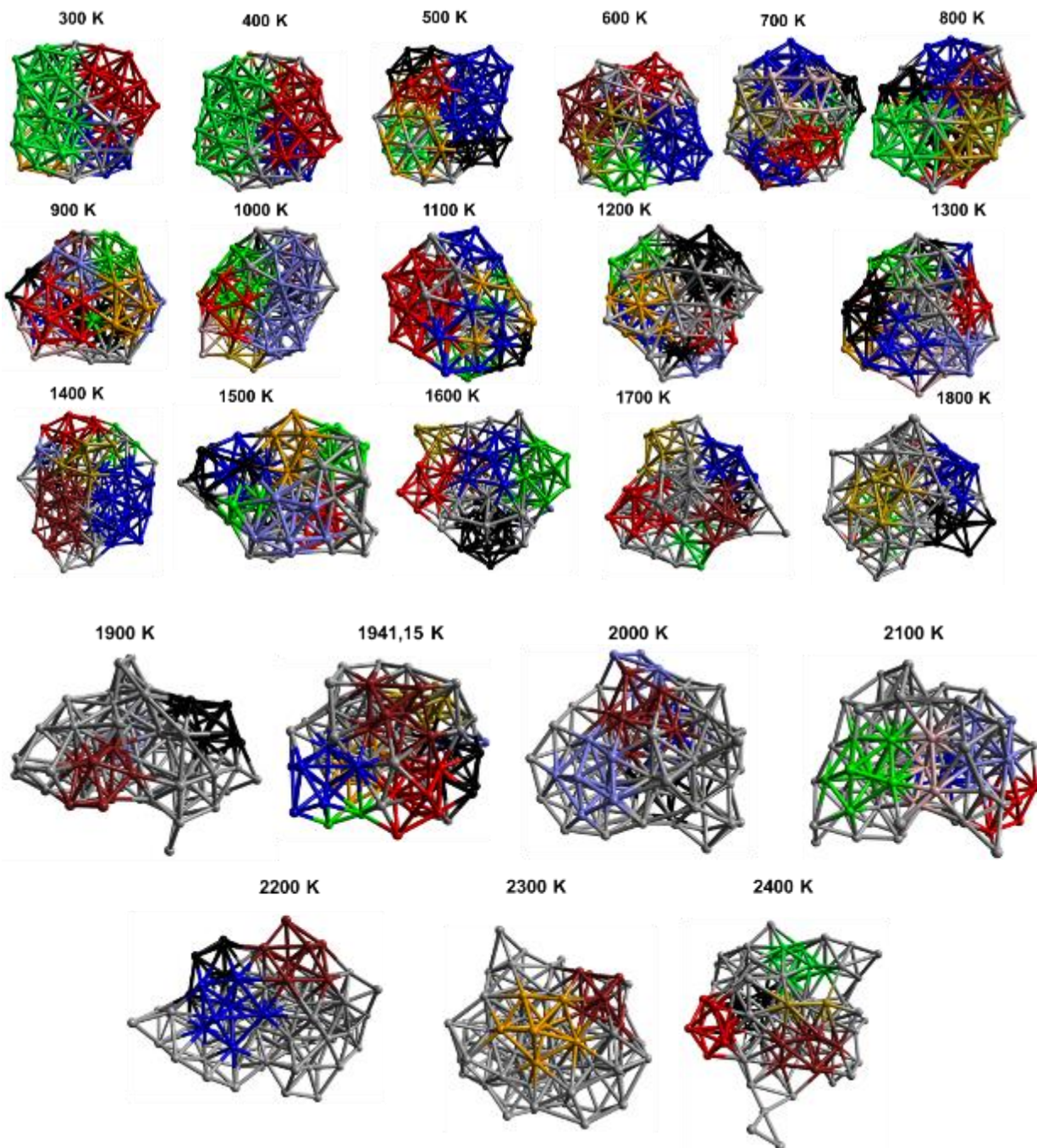


Figure 6.16: The Ti_{89} nanoclusters in the vacuum at various temperatures.

The distorted Ti_{19} (maroon) is observed to coexist with bi-capped Ti_7 (black), hexagonal ring (gold) and Ti_7 (violet-black-red).

The thermal agitation at 700 K, is found to have three icosahedral units (blue, lime green and gold), coexisting with pentagonal units (black-green, light pink-blue, red, maroon and maroon-blue). At 800 K, the structure transitioned into Ti_{13} (lime green) coexisting with Ti_{10} (gold) connected to Ti_{13} fragmentation (gold) by three atoms (black) and Ti_7 units (light brown and maroon) by single atoms (grey). Three pentagonal bi-pyramids (black, maroon and lime green) are found to interconnect with each other.

The transient at 900 K is observed to have its configuration transformed to a nanocluster dominated by pentagonal bi-pyramid geometries (red, maroon, lime green, black, blue, light brown, violet-grey-lime green and red-light pink-blue) coexisting with icosahedral unit (black). Most of the atoms (grey) are connecting the geometries which are the centres of the structural evolution pattern observed in chapter three.

The thermal agitation at 1000 K is observed to be Ti_{25} geometry (violet), interconnected to Ti_{13} (lime green) coexisting with three Ti_7 units (red-green-light pink, gold and gold-light pink). The Ti_7 (black-maroon) is observed to be connected to Ti_7 (maroon) with the rest of the atoms connecting all the fragmentation for crystal isomerization. At 1100 K, the structural transition is found to be Ti_{19} (red) connected to Ti_7 unit (blue) by three atoms (grey) and two hexagonal rings (blue and gold), where the other ring (blue) is connected with two Ti_7 (green and black) coexisting with octahedral unit (lime green), Ti_7 units (violet and light pink-violet).

At 1200 K, we observe the structural transformation having Ti_{13} (black) coexisting with distorted Ti_{13} (light pink-red-black) and five Ti_7 (light brown, lime green, gold-light pink, and blue). However, other atoms (grey) possesses the ability to transition into triangular bi-pyramidal. The 1300 K transient is observed to have hexagonal-shaped geometry (light pink), pentagonal bi-

pyramid units (blue, red, lime green, black, maroon, gold, violet, light brown-maroon-light pink and blue-red) coexisting with other atoms (grey).

The transient at 1400 K is observed to have two Ti_{19} units (maroon and blue), coexisting with three pentagonal bi-pyramid (lime green, red, black violet and gold-red) and other atoms interconnecting the building block fragmentations. At 1500 K, the most stable fragmentations observed to coexist with the other atoms (grey) is the dominance of Ti_7 units (red, black, lime green, violet, blue-black, light brown-blue and violet-lime green-black). The transient at 1600 K is observed to have Ti_{13} configurations (black and green) coexisting with five Ti_7 (red, blue, gold, maroon and violet) and other atoms (grey).

At 1700 K, the pentagonal bi-pyramid isomers (blue, maroon, gold, black, red and maroon-lime green) are observed to be the fundamental building block fragmentations. The transient at 1800 K is observed to have five pentagon bi-pyramid (black, blue, gold, lime green and red). At 1900 K, we observe three pentagonal bi-pyramid (black, violet and maroon). The transient at 1941.15 K is found to have Ti_7 units (blue, maroon, light brown, blue-light pink, black-red, gold, lime green-red-light brown) coexisting with other atoms (grey).

The transient at 2000 K we observe a higher degree of distortions where the pentagonal bi-pyramid dominance is found to coexist with the triangular bi-pyramid dominated configurations (grey). At 2100 K, the structural transition is observed to have five pentagonal bi-pyramid (lime green, red, violet, blue and light pink-lime green-violet). However, the 2200 K is found to have three Ti_7 units (blue, maroon and black). At 2300 K, the transient is observed to have two Ti_7 fragmentations whilst at 2400 K five Ti_7 geometries (maroon, lime green, red, black and gold-maroon) are observed. This cluster is observed to segregate to cluster surface below 1800 K and becomes more uniformly distributed in the surface and interior at higher temperatures.

6.3.4. The dominant configurations for Ti_N ($N = 32, 57, 80, 89$) nanoclusters

In this section, we are discussing the geometries which are considered the most dominant building blocks fragmentations for Ti_N ($N = 32, 57, 80, 89$) nanoclusters. Table 6.1 show the most common isomers observed at the melting point of these nanoclusters. The geometries which are the building blocks at the melting point are highlighted in the table below.

Table 6.1: Dominant geometries for Ti_N ($N = 57, 80, 89$) as a function of temperature

	Ti_{32}	Ti_{57}	Ti_{80}	Ti_{89}
Temperature (K)	Dominant clusters	Dominant clusters	Dominant clusters	Dominant clusters
300	Ti_{13}	$Ti_{19}, Ti_{13}, Ti_7, Ti_5$	Ti_{19}, Ti_3, Ti_7	Ti_{19}, Ti_{13}, Ti_7
400	Ti_{19}, Ti_7	Ti_{13}, Ti_7	$Ti_{19}, Ti_{13}, Ti_7, Ti_5$	Ti_{19}, Ti_{13}, Ti_7
500	Capped Ti_{19}, Ti_{13}, Ti_5	Ti_{19}, Ti_{13}, Ti_7	Ti_{13}, Ti_7	Ti_{19}, Ti_7
600	Ti_{19}, Ti_{14}, Ti_5	Ti_{19}	Ti_{19}	Ti_{19}, Ti_{13}, Ti_7
700	Ti_{19}, Ti_5	Ti_{13}, Ti_7	Ti_{13}, Ti_7	Ti_{13}, Ti_7
800	Ti_{13}, Ti_7, Ti_5	Ti_{13}	Ti_{19}, Ti_7	Ti_{19}, Ti_{10}, Ti_7
900	Ti_{13}, Ti_7	Ti_{19}, Ti_{13}	Ti_{19}, Ti_{13}	Ti_{13}, Ti_7
1000	Ti_{13}	Ti_{19}, Ti_7	Ti_{19}, Ti_7, Ti_5	Ti_{25}, Ti_{13}, Ti_7
1100	Ti_{13}	Ti_{19}, Ti_{13}, Ti_7	Ti_{19}, Ti_7, Ti_5	Ti_{19}, Ti_7, Ti_6
1200	Ti_7, Ti_5	$Ti_{19}, Ti_{13}, Ti_7, Ti_6$	Ti_{19}, Ti_7, Ti_5	Ti_{13}, Ti_7, Ti_5
1300	Ti_{13}	Ti_7	Ti_{13}, Ti_7, Ti_5	Ti_7
1400	Ti_{13}, Ti_5	Ti_7, Ti_5, Ti_6	Ti_{19}, Ti_7, Ti_5	Ti_{19}, Ti_7
1500	Ti_{13}, Ti_5	Ti_7, Ti_5	Ti_{19}, Ti_7	Ti_7
1600	Ti_{13}, Ti_5	Ti_{13}, Ti_7	Ti_{13}, Ti_7, Ti_5	Ti_{13}, Ti_7
1700	Ti_{19}, Ti_{13}	Ti_7, Ti_5	Ti_7, Ti_6, Ti_5	Ti_7
1800	Ti_{13}, Ti_7	Ti_7, Ti_5, Ti_6	Ti_7	Ti_7
1900	Ti_{19}, Ti_5, Ti_7	Ti_7, Ti_5	Ti_7, Ti_6	Ti_7
1941,15	Ti_{19}, Ti_7	Ti_7, Ti_5	Ti_7, Ti_6	Ti_7
2000	Ti_7	Ti_7, Ti_6, Ti_5	Ti_7, Ti_6	Ti_7, Ti_5
2100	Ti_6	Ti_7, Ti_6, Ti_5	Ti_{13}, Ti_6	Ti_7
2200	Ti_7	Ti_6, Ti_5	Ti_{13}, Ti_6	Ti_7
2300	Ti_7	Ti_7, Ti_6, Ti_5	Ti_{13}, Ti_6	Ti_7
2400	Ti_7	Ti_7, Ti_6, Ti_5	Ti_{13}, Ti_6	Ti_7

The most dominant configurations forming part of the building blocks during thermal agitation are mostly observed to have a pentagonal Ti_7 and icosahedron Ti_{13} isomerization for all Ti_N ($N = 32, 57, 80, 89$) nanoclusters. The icosahedral units (Ti_{13}) are formed by two interpenetrating pentagonal (Ti_7) shapes and Ti_{19} is a three interpenetrating pentagonal units or two interpenetrating icosahedral geometries (Ti_{13}).

In Fig. 6.17, we show snapshots for the most dominant units as they are subjected to thermal stress. The pentagonal bi-pyramid (Ti_7) is observed to be the most dominant unit at the melting point for all the systems. The most dominant unit for Ti_{32} nanocluster at the melting point (1941.15 K) is Ti_{19} and Ti_7 . The Ti_{57} nanocluster is observed to have Ti_7 and Ti_5 as the dominant units. The octahedron geometry (Ti_6) is found to be dominant at 1700 – 2400 K for Ti_{80} nanocluster with Ti_7 as one of the dominant units at 1941.15 K. However, the Ti_7 unit is observed to be the only dominant geometry for Ti_{89} nanocluster.

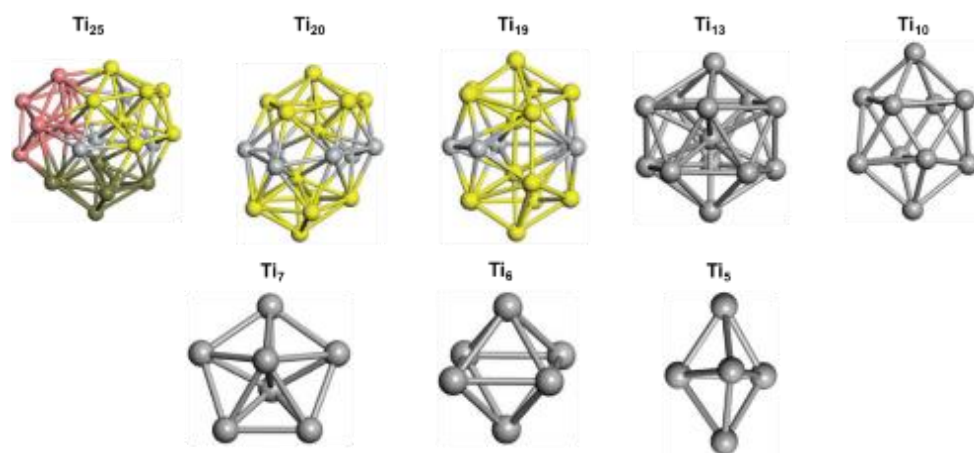


Figure 6.17: The most dominant geometries forming part of the building block fragmentations for Ti_N ($N = 32, 57, 80$ & 89).

6.3.5. The potential energy for Ti_N ($N = 32, 57, 80, 89$) nanoclusters

The thermal agitation transitions from the solid to liquid phase and vice versa is usually identified by studying the variation in the thermodynamic properties such as total energy or potential energy [128]. In Fig. 6.18 we show the potential energies for Ti_N ($N = 32, 57, 80, 89$). The melting transition of the nanoparticle from the solid form in which atoms merely oscillate about the equilibrium isomer to a liquid form characterized by uncorrelated motion of atoms is spread over a range of temperatures from 300 - 2400 K. Note that is included for comparison. In the case of all Ti nano-systems, we observe a smooth linear variation of the potential energies as the temperature is increased.

The Ti_{57} nanocluster energy varies linearly with temperature up to 1900 K where it depicts a small jump in the potential energies at 1941.15 K, 2100 K and 2300 K, which may be attributed to a phase change as the thermal agitation of the system is elevated. The Ti_5 , Ti_6 , and Ti_7 dominant geometries were observed at this temperature range. However, the energy for Ti_{80} also linearly varies with temperature up to 1941.15 K where it depicts a slight jump in the potential energy which is consistent with the observed Ti_{32} and Ti_{57} thermal responses at 1941.15 K.

This suggests that the thermal agitation on the nanocluster possesses the same reaction on the melting temperature of Ti bulk. There is a depicted slight steep at 1400 K with the potential energy of -394 eV which is different from that of Ti_{32} and Ti_{57} suggesting different attributes when it comes to cluster stabilization. This is confirmed by the emergence of different geometry for the three nanoclusters. Particularly, the Ti_{19} geometry is observed for Ti_{80} .

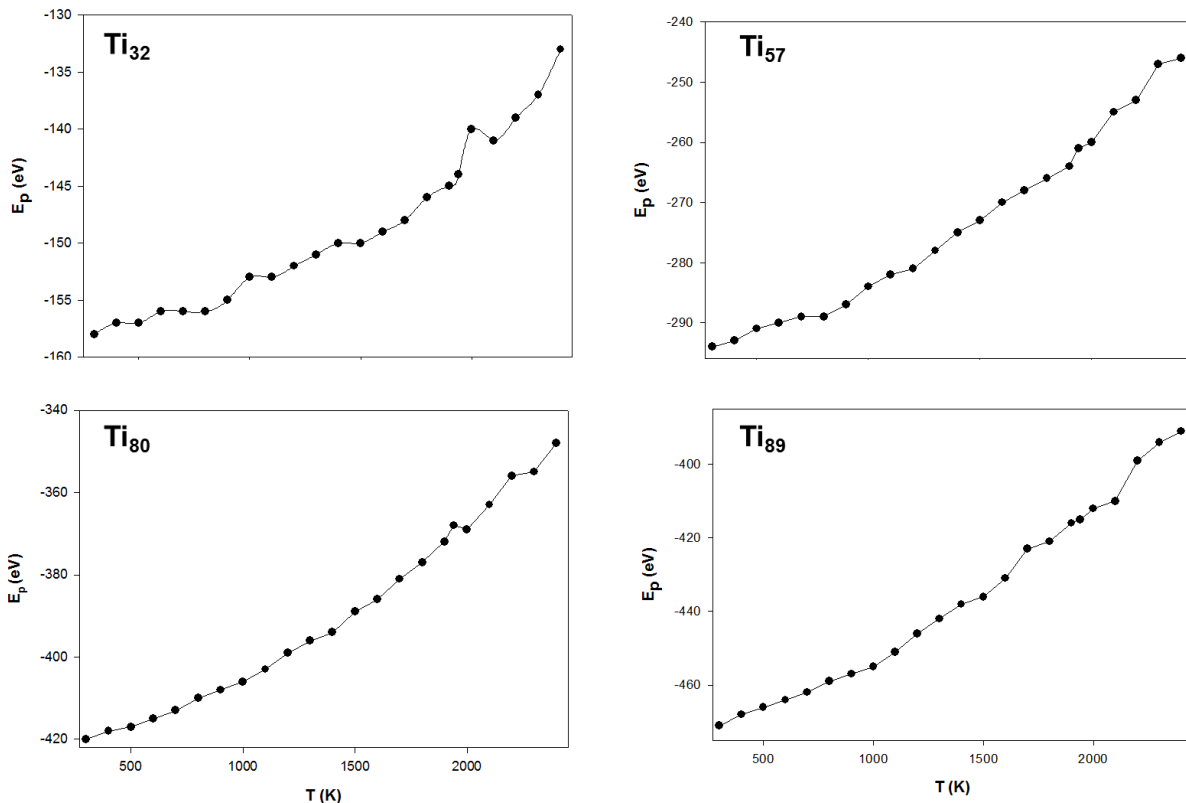


Figure 6.18: The potential energy of the Ti_N ($N = 32, 57, 80, 89$) showing smooth variation as the temperature increase. The Ti_{32} is inserted for comparison.

At 2200 K, we observe another crystalline formation of a new phase that is lower in energy which might be attributed to distributed atoms having characteristics that are prime to those of neighbouring thermal agitation.

In the case of Ti_{89} , there is an abrupt increase in the energy at 1500K and 2100 K which suggest a stable morphology formation at those projected temperatures. The emerging stable geometry was Ti_7 configuration. The behaviour at 1941.15 K is different as compared to the other nanoclusters. There is no small jump observed for this nanocluster.

This nanocluster shows molten state characteristics which are elevated more than that of bulk. However, other reports found that nanoclusters with 450 atoms and above decreases with

decreasing cluster size [282]. Comparing the potential energies, a small inflection was detected in the potential energy against the temperature curve for Ti_{57} and Ti_{80} except for Ti_{89} where the inflection was detected at 1700 K indicative of the melting transition proximity.

6.3.6. The configuration energy of the thermal agitated Ti_N ($N = 57, 80, 89$) nanoclusters

The thermal agitation transitions from the solid to liquid phase and vice versa is usually identified by studying the variation in the thermodynamic properties such as configuration energy to validate the structural transitions obtained from the potential energy [128].

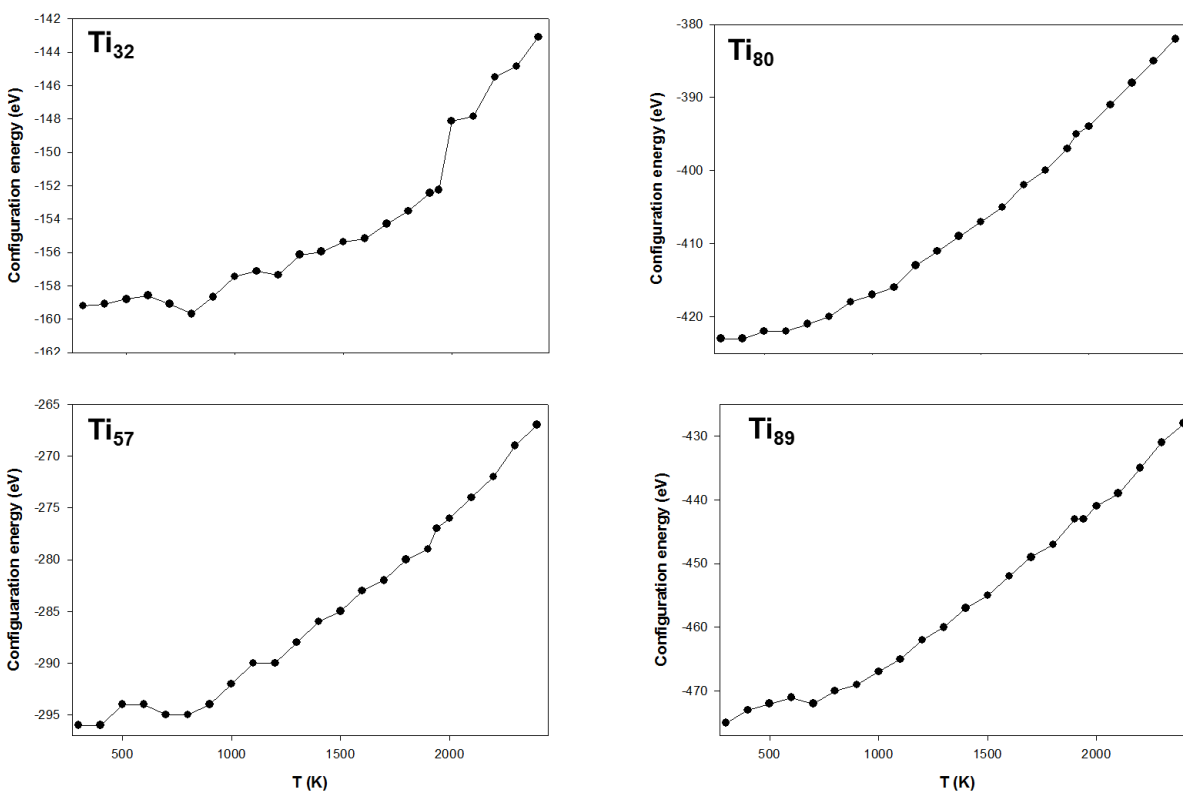


Figure 6.19: The configuration energy of the Ti_N ($N = 57, 80, 89$) at various temperatures.

In this case, we compare the configuration energy for Ti_N nanoclusters. The configuration energies are also observed to increase with temperature for Ti_N ($N = 32, 57, 80, 89$). It is clearly seen that

Ti₃₂ is slightly varying compared to other nanoclusters. Ti₅₇ slowly varies with configuration energy at a lower temperature below 1000 K. Above this temperature, we observe linearity in energy as the temperature is increased. The destabilization attributed to the loss of energies are observed from 500 – 600 K and stabilize from 700 – 800 K. However, we observe a slight steep at 1200 K indicative of the formation of a new stable configuration compared to its neighbours. The slight jump at 1900 K is also observed which may be attributed to fragmentation transition.

The configuration energy with temperature for Ti₈₀ nanocluster to liquid-like phase reveals that the energies increase linearly with increasing temperature. No steeper energies are observed as compared to Ti₅₇ nanocluster suggesting that configurational changes. However, we observe a slight jump in the energy at 1941.15 K which is followed by the linearity of the energies from 2000 – 2400 K.

The Ti₈₉ nanocluster energy smoothly increases at lower temperatures and a sudden drop at about 800 K. The sudden drop in the energy at 800 K may be attributed to stabilization in energy as the fragmentation is thermodynamically evolved, featuring the formation of a new stabilized unit. Furthermore, we also observe an energy drop at 1941.15 K followed by a linear increase in the energy towards the elevated thermal agitation. The drop in the energy may be attributed to the solid-liquid phase transition of the nanocluster.

6.3.7. Mean square displacement (MSD) for Ti_N (N = 57, 80 & 89) nanoclusters

The mean square displacement (MSD) for the Ti_N nanoclusters are compared in Fig. 6.20. This is important to deduce the melting temperature. The melting temperature of metal nanoclusters can be obtained by monitoring the variation of the MSD as a function of temperature during diffusion.

In the case of the Ti_{57} nanocluster, we observe a high degree of fluctuations from 300 – 1300 K and the nanoclusters stabilizing at 1400 – 2400 K temperature range.

At 800 K and 1900 K the fluctuations are observed to be slightly steep more than their neighbouring thermal agitated configurations. These may be due to the nanocluster exhibiting molecular behaviour since the nanoclusters are below 500 atoms. This observation is consistent with the previous work. Qi *et al.*, [268] reported that Ni nanoclusters exhibit a molecular behaviour below 500 atoms, but have well-defined bulk and surface properties above 750 atoms. In the case of the Ti_{80} nanocluster, we observed a minimal movement of atoms at temperatures lower than 2300 K. We also observe the diffusivity jump that maximises at an abrupt rate at $T > 2300$ K. A similar trend has been observed for Ti_{32} nanocluster at 300 – 1900 K, suggesting that these nanoclusters may have the same building blocks which have the potential of responding similarly to thermal agitation. The three interpenetrating pentagonal bi-pyramid (Ti_{19}) and pentagonal bipyramid were observed to be the most dominant units at 1900 K. At 400 K the diffusivity appears to have reverted to zero.

These observed transitions are justifiable since the melting temperature for Ti bulk is 1941.15 K and nanoclusters melts at prime temperatures to that of bulk Ti. It is also observed that the diffusivity of the cluster is likely to revert to zero with a slight peak at 1941.15 K indicative of the initial phase transition towards the liquid-like phase. Moreover, Ti_{89} shows a higher degree of fluctuation at temperatures from 300 – 1000 K. However, from 1200 K the movement of atoms increases smoothly with increasing temperature. At 1941.15 K the diffusivity appears to have a steeper diffusivity than the other temperature indicative of the effect of thermal pressure at melting signature for Ti bulk.

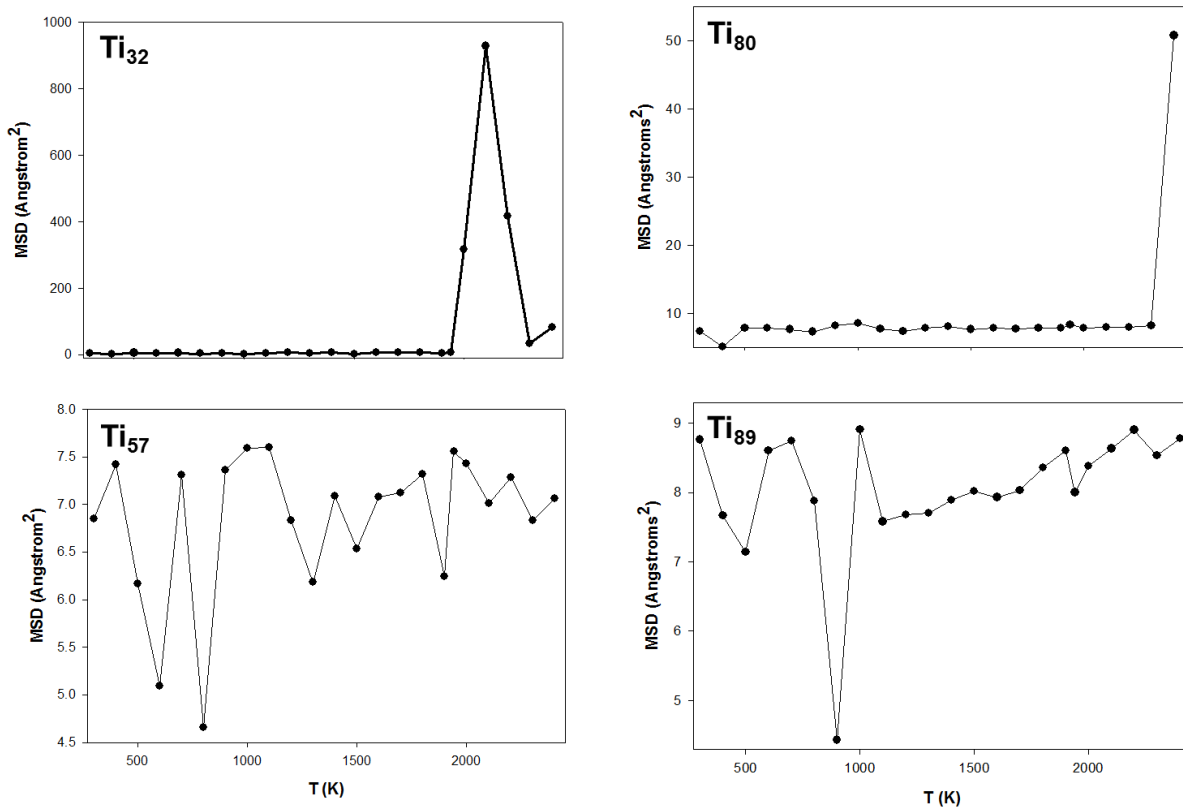


Figure 6.20: Dynamics properties for Ti_N ($N = 57, 80 \text{ \& } 89$). Temperature effect on these nanoclusters mean square displacement.

6.3.8. Radial distribution function for Ti_N ($N = 32, 57, 80, 89$) nanocluster

The radial distribution function are compared for Ti_N ($N = 32, 57, 80 \text{ \& } 89$) as shown in Fig. 6.21. This is important to evaluate the atomic order and disorder as the temperature is increased. The magnitude of the peaks is high for the Ti_{32} followed by Ti_{57} , Ti_{80} and the Ti_{89} nanocluster. This show that as the number of atoms increases, the probability of finding an electron becomes lower. It would be very difficult to locate an electron in smaller nanoclusters.

The Ti_{57} nanocluster shows well ordered thermally agitated fragmentations at 300 and 800 K. However, as the temperature increases the peaks decreases and becomes broader suggesting a phase change or a diffusion dynamics is thermally activated. The reduction in the probability of

the peaks from 1900 – 2100 K may be ascribed to the crystal order of the nanocluster broken and the melting state reached. At every temperature, a new phase emerges by reflecting distinct peaks suggesting that the nanocluster is crystalline, although it depicts features that highlight the nanocluster approaching a liquid-like phase.

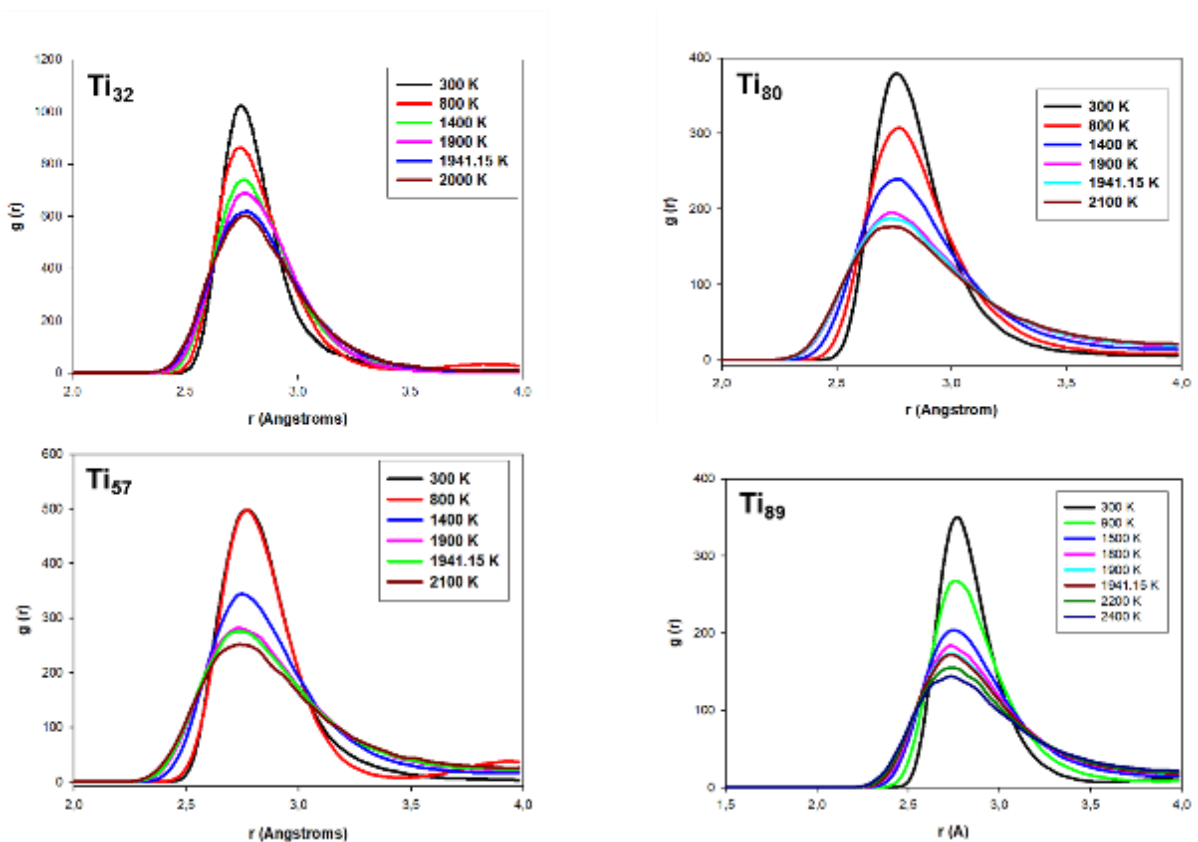


Figure 6.21: The radial distribution functions from the integral-equation theory, showing the increase of short-ranged order as a function of temperature.

These phenomena were also reported by Kart *et al.* [283]. They found that at elevated temperature, the peaks broadened, lowered and disappeared indicating that the metal nanocluster approaches the liquid state.

The Ti_{80} atomic distribution curve against temperature shows the 300 K peak having a well-ordered structure. These observations are different from those of Ti_{57} , where the probability at 300

K and 800 K are found to superimpose or overlap each other indicative of highly ordered clusters. There is also a clear broadening of the peaks as the peaks height decreases indicating a possible phase change from solid to liquid. The 300 K peak for the Ti_{89} nanocluster shows a well-ordered structure. The trend in the reduction of the peaks as the temperature is elevated shows consistency with that of Ti_{80} and different to those of Ti_{57} . The peak at 800 K for the Ti_{57} nanocluster shows more crystalline features than the 300 K peak. This phenomenon is disclosed by their distribution radius.

6.3.9. Density profiles for Ti_N ($N = 32, 57, 80, 89$) clusters at various temperatures

The density profiles in Fig. 6.22 show the comparison of the atomic distribution along the axis at varying temperatures for Ti_N ($N = 32, 57, 80 \& 89$). The peaks at 300 K for Ti_N ($N = 32, 57, 80$) nanoclusters depicts solid-like features indicated by the distinct peaks, where atoms have a higher distribution peak at a certain distance from the centre.

The position of the peaks at 300 K and 800 K remains relatively similar, but the atomic distribution at 300 K shifts from 4.7 Å to 5.8 Å as the temperature reaches 1400 K for Ti_{57} nanocluster. The peaks – peak separation is not that clear but there is a slight reduction in the magnitude of the peaks. The 2100 K peak is observed to have a reduced magnitude and shifted from 4.7 Å at 300 K to 7 Å at 2100 K along the z-axis, signaling the existence of solid-liquid transition above the melting point. In the case of the Ti_{80} nanocluster, the atomic distribution deduces a similar trend as the Ti_{57} nanocluster. The atomic distribution at 300 K and 800 K shift from 5.6 Å to 6.3 Å as the temperature reaches 1400 K. The peak-peak separation is also not observed with this nanocluster.

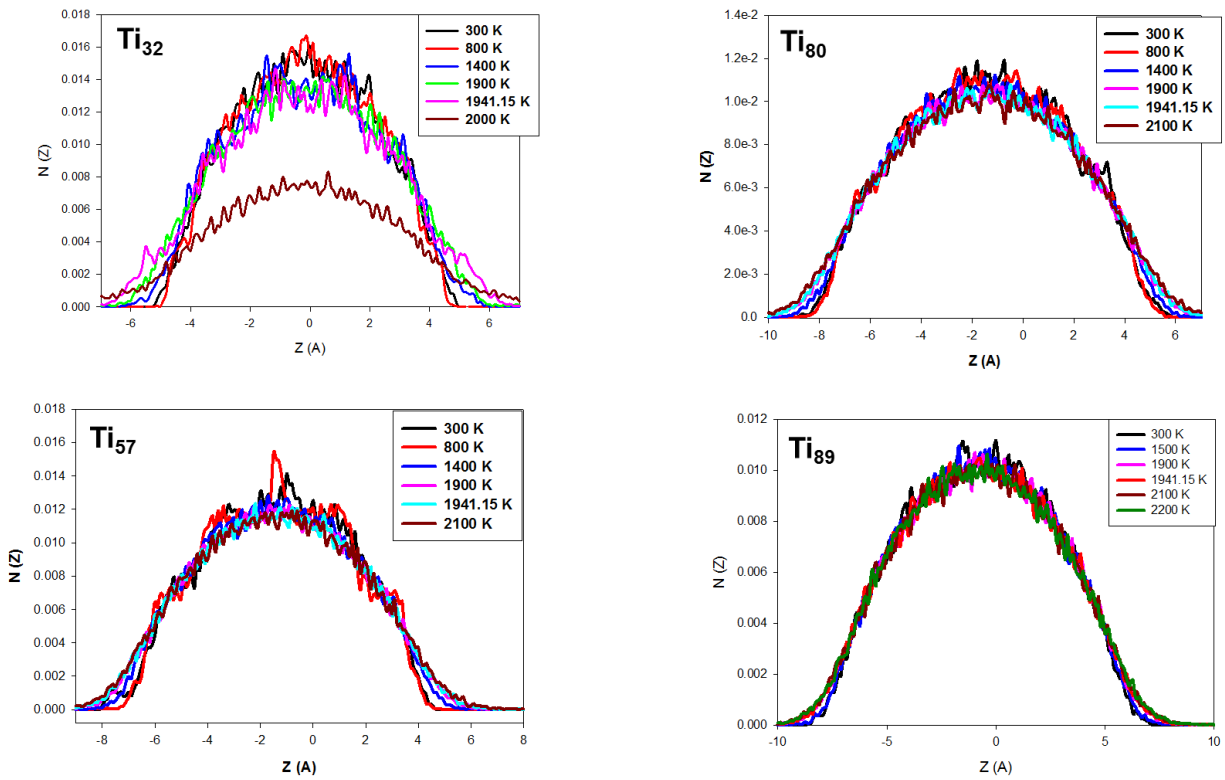


Figure 6.22: Atomic density profile $N(Z)$ as a function of temperature, in the direction perpendicular of the substrate located at $z = 0$, in Ti_N ($N = 32, 57, 80, 89$).

At 2100 K, the peak is also observed broadened and it shifts from 5.6 Å at 300 K to 7.8 Å at 2100 K. The oscillating density profiles becomes broader as compared to Ti_{57} nanocluster. The increase in the number of atoms from 57 – 80 atoms during thermal agitation, enhanced the mobility of the atoms in the Ti_{80} nanocluster.

In the case of Ti_{89} nanocluster, the position of the peaks at 300 K and 1500 K remains relatively similar, contrary to the behaviour shown by Ti_N ($N = 32, 57, \text{ and } 80$) atomic distributions. At $T > 1500$ K, the nanocluster undergoes large structural changes. The atomic distribution above the melting point slightly broadens along the z -axis.

This phenomenon might be ascribed to the population of Ti atoms expanding and moving out of the core due to the increase of the atomic disorder acquiring liquid features passing an intermediate state where the nanocluster fluctuates between solid and liquid behaviour. The same observations were previously reported by Cleveland *et al.* [284].

CHAPTER 7

Structural characterization of Ti-doped Ti_{N-1}M ($\text{M} = \text{Pt}, \text{Ni}, \text{Ir}, \text{Pd}$) nanoclusters

In this chapter we employ the first principle method based on density functional theory FHI – aims to understand the interplay between electronic and geometric effects in bimetallic nanoclusters. We generated the stable Ti_{N-1}M bimetallic nanoclusters by hand for a given cluster size by replacing the Ti atoms with M impurity in all Ti positions or sites for energetically selected nanoclusters from $N = 2 - 16$. We investigate the Ti nanocluster reactivity and the impact when it is doped with Pt, Ni, Ir and Pd impurities. The stable geometrical structures and structural properties such as binding energy, relative stability, dissociation energy, HOMO – LUMO and density of states (DOS) will be discussed in detail.

7.1. Background knowledge on bimetallic transition metal nanoclusters

Metal nanoparticles have been reported to exhibit unusual chemical and physical properties different from those of bulk metal [285]. They possess fascinating potential applications in catalyses [14, 286]. Their physical, chemical and electronic properties have received more attention from the research community due to their large fraction of surface metal atoms ranging from 1 – 10 nm and their ability to strongly depend on their size, shape and composition.

Particularly, since the bimetallic nanoparticles are widely used in the catalysis industry, their knowledge of the size and shape distribution, surface composition, and crystalline structure for some metals have not been thoroughly investigated and analysed. Bimetallic systems such as TiPt,

TiIr, TiPd and TiNi clusters have not yet received a vast approach to understand their chemical and physical behaviour and which may lead to improvement of their catalytic selectivity or activity [285, 287]. Thus, we are currently exploring the reactivity and electronic properties of the $Ti_{N-1}M$ nanoclusters when they are modified by a different impurity element. Note that Pt impurity will be used to locate the most stable position. Then, the same position will be used to investigate the electronic properties of other impurities.

7.2. Structure and characterization for $Ti_{N-1}Pt$

The most energetic favoured isomer for $Ti_{N-1}Pt$ clusters obtained by the FHI-aims technique are presented in Fig. 7.1. The clusters with the most stable Pt substitution are analysed in detail and shown in table 7.1. The $N = 3$ cluster is an isosceles isomer that is observed to have Pt impurity capping on the Ti_2 isomer. This position is observed to be mostly energetically favoured compared to others. At $N = 4$, the Pt atom is found to be more stable on the capped atom of the isosceles isomer or the Pt atom caps the surface of the three equilateral triangle Ti atoms, whereas $N = 5$ cluster is a triangular bi-pyramidal configuration which is a 1 – 3 – 1 layered stacking and the Pt atom staying at 1 – 2 (Pt) – 1 layer. This is a face capped isomer with Pt atom capped on the opposite and adjacent faces of Ti atoms.

The octahedral isomer $N = 6$ is 1 – 4 – 1 layered stacking where Pt atom is placed at 1 – 3(Pt) – 1 layered. This configuration also has the Pt impurity capped on the face. For $N = 7$, the pentagonal bi-pyramidal isomer is 1 – 5 – 1 layered stacking and the Pt atom is found to be favoured at Pt – 5 – 1 layer. This isomer is observed to have its impurity staying on the apex and the surface. For $N = 8$ is a capped pentagonal bi-pyramid which is observed to have Pt atom placed on the capped atom of the pentagonal bipyramid or the Pt atom forming part of the pentagonal ring.

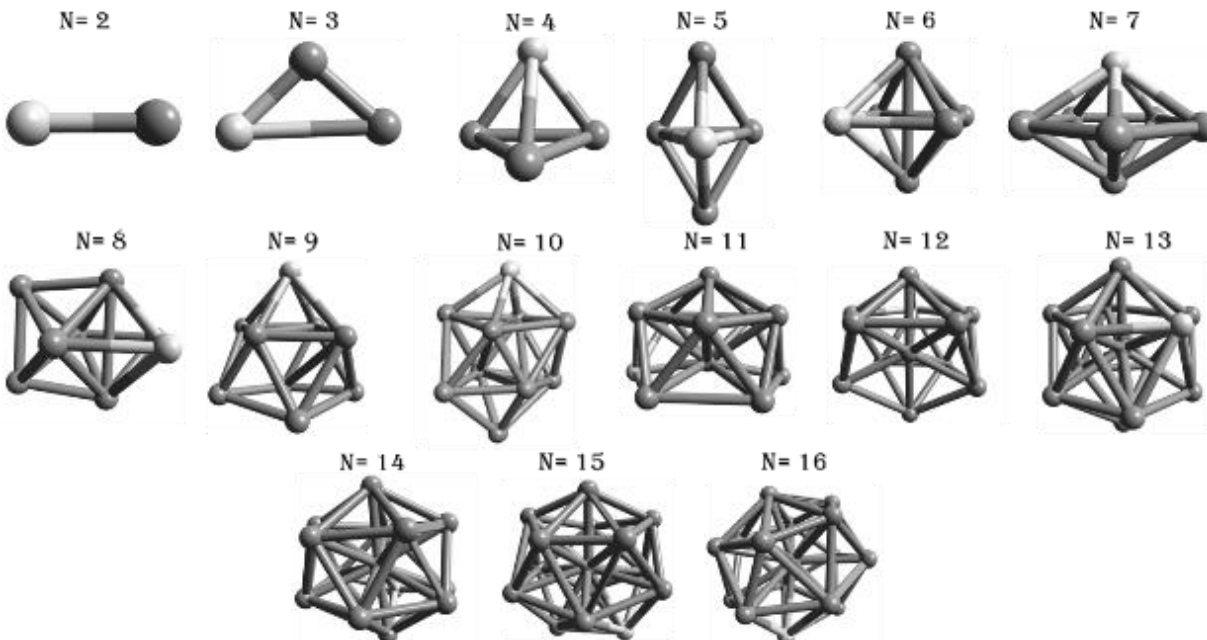


Figure 7.1: The $Ti_{N-1}Pt$ ($N = 2-16$) configurations showing the lowest energy positions where grey atoms represents Ti and white atoms represents Pt.

For $N = 9$, Pt atom is found to be placed on the apex of the Two-faced capped pentagonal. The $N = 10$ is observed to have its atom on the apex replaced with Pt atom. Similar observations were found for $N = 9$. The $N = 11$ is a $1 - 5 - 1 - 4$ layered stacking where Pt atom is placed on the $1 - 5 - 1 - 3(Pt)$ layered stack. The Pt atom is placed on one of the tetra atoms which are capped on the pentagonal bi-pyramid. For $N = 12$ the most favoured substituting is observed at $1 - 4(Pt) - 1 - 4 - 1$ layered stacking. The Pt atom is capped on the face of the pentagonal bi-pyramid.

The Z12 Frank-Casper polyhedral or icosahedral isomer is a $1 - 5 - 1 - 5 - 1$ layered stacking and the Pt atom was found to be more stable at $1 - 4(Pt) - 1 - 5 - 1$ layered stacking. The Pt impurity is placed on this precursor similarly with $N = 12$. The $N = 14$ is a Z13 Frank Casper polyhedral isomer which has the Pt atom staying at $1 - 5 - 1 - 5(Pt) - 1$ layered stacking. The Pt atom is capped on the pentagon ring. The Z14 Frank Casper polyhedral is found to have the most favoured

site at 1 – 5 – 1 – 6 – 1 (Pt). Here, the Pt atom is observed to be placed on one of the two atoms which are capped on the apex of the pentagonal geometry. For N = 16, the Z15 Frank Casper polyhedral is a 1 – 6 – 1 – 7 – 1 layered stacking and the Pt impurity placed at 1 – 6 – 1 – 7 – Pt. The Pt atom is observed to be placed on the atom which is capped on the Z14 Frank Casper polyhedral.

Table 7.1: The cluster number, isomer identification and substituted Pt stable sites on $Ti_{N-1}M$ nanoclusters.

Cluster Size N	ID	Pt sub-site
2	Liner	1 - Pt
3	Isoceles	2 - Pt
4	Tetrahedral isomer	3 - Pt
5	triangular bipyramid	1 – 2 (Pt) – 1
6	Octahedron	1 – 3(Pt) – 1
7	Pentagonal bi-pyramid	Pt – 5 – 1
8	bi-capped octahedron	1(Pt) - 4 - 2
9	Two faced capped pentagonal	Pt - 4 - 4
10	bicapped quadrilateral antiprism	Pt - 4 - 4 - 1
11	Tetra-capped pentagonal	1 – 5 – 1 – 3(Pt)
12	Penta-capped pentagonal	1 – 4(Pt) – 1 – 4 – 1
13	Icosahedron	1 – 4(Pt) – 1 – 5 – 1
14	Z13 Polyhedron	1 – 5 – 1 – 5(Pt) – 1
15	Z14 Polyhedron	1 – 5 – 1 – 6 – 1 (Pt)
16	Z15 Polyhedron	1 – 6 – 1 – 7 – Pt

7.3. Electronic and structural properties of $Ti_{N-1}Pt$

In this section, we evaluate the structural and electronic properties of $Ti_{N-1}Pt$. The stability of $Ti_{N-1}Pt$ nanoclusters is explored by calculating the binding energy per atom (E_b) in order to measure the amount of energy required to remove a particle from a system. The relative stability (D_2E) is

evaluated to determine the most stable isomers amongst the other clusters and the dissociation energy (E_d) to measure the strength of bond energy. These quantities are defined as:

$$E_b[Ti_NPt] = (NE_T[Ti] + E_T[Pt] - E_T[Ti_NPt]) / (N + 1), \quad (N = 1, 2, \dots, 16) \dots \dots \dots (7-1)$$

$$D_2E[Ti_NPt] = E_T[Ti_{N+1}Pt] + E_T[Ti_{N-1}Pt] - 2E_T[Ti_NPt] \dots \dots \dots (7-2)$$

and

$$E_d[Ti_NPt] = E_T[Ti_{N+1}Pt] + E_T[Ti] - E_T[Ti_NPt] \dots \dots \dots (7-3)$$

where, $E_T[Ti_NPt]$ is the total energies of the Ti_NPt doped nanoclusters, while n denotes the number of Ti atoms in the nanocluster, respectively.

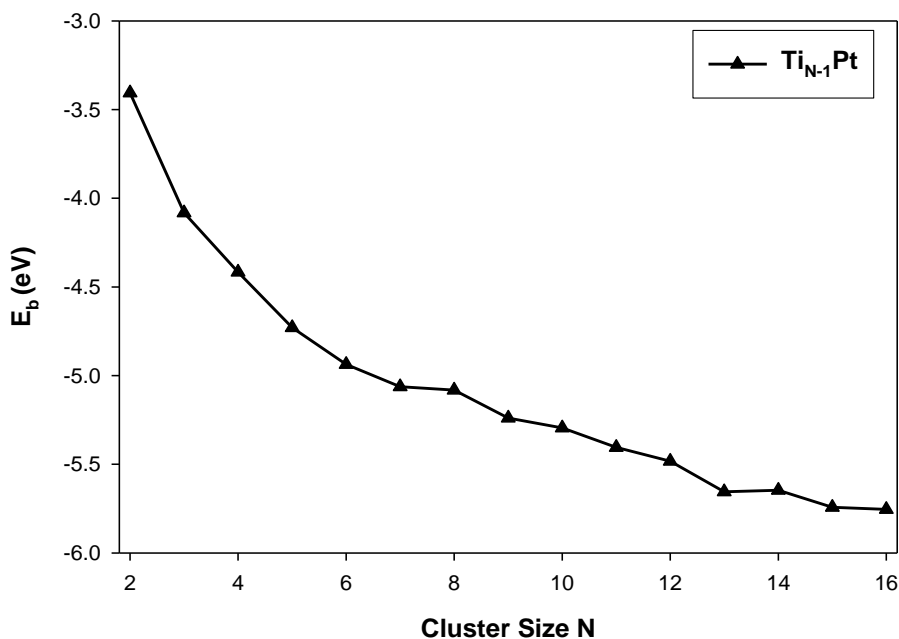


Figure 7.2: The binding energies of $Ti_{N-1}Pt$ nanoclusters.

Figure 7.2 shows the binding energy curve as a function of cluster size. The binding energy gives information about the abundance of, particularly stable geometries. It can be clearly seen (in table 7.2) that the binding energy decreases with cluster size and rapidly down at $N \leq 7$; then the size dependence becomes smooth at $N > 7$. The decrease in energy suggests that $Ti_{N-1}Pt$ becomes more stable for larger clusters. However, for $Ti_{12}Pt$ ($N = 13$) and its neighbours, the binding energy is slightly lowered while for $N = 15$ onwards the nanocluster become more stable. The increase in the stability of the $Ti_{12}Pt$ cluster can be understood by the nature of the icosahedral structure.

Table 7.2: The binding energy (E_b) for $Ti_{N-1}M$ ($M = Pt, Ni, Ir, Pd$) and pure Ti.

Cluster size N	Binding energy (eV)				
	TiPt	TiNi	TiIr	TiPd	Pure Ti
2	-3.406	-2.556	-4.787	-2.047	-2.847
3	-4.082	-3.440	-4.804	-3.194	-3.434
4	-4.416	-3.958	-4.997	-3.741	-3.962
5	-4.730	-4.374	-5.253	-4.127	-4.447
6	-4.937	-4.630	-5.351	-4.464	-4.640
7	-5.063	-4.813	-5.473	-4.655	-4.924
8	-5.082	-4.980	-5.489	-4.828	-4.930
9	-5.239	-5.047	-5.524	-4.929	-5.054
10	-5.295	-5.104	-5.552	-4.998	-5.136
11	-5.404	-5.225	-5.623	-5.138	-5.210
12	-5.482	-5.324	-5.702	-5.233	-5.317
13	-5.655	-5.488	-5.854	-5.418	-5.437
14	-5.646	-5.512	-5.834	-5.433	-5.507
15	-5.742	-5.604	-5.921	-5.534	-5.575
16	-5.754	-5.629	-5.930	-5.561	-5.620

The high stability of the regular icosahedral structure usually occurs for transition-metal cluster due to their $\{111\}$ surface facets. This behaviour was also reported by Kessler *et al.* [32, 257] and it was found that the icosahedral structure possesses a special reactivity when compared to the less coordinated neighbouring structures. A similar trend was observed for pure Ti. The $Ti_{N-1}Pt$ binding energies were found to be enhanced as compared to pure Ti clusters. The second-order energy D_2E in Fig. 7.3 is used to determine the relative stability of $Ti_{N-1}Pt$ clusters. Higher stability is associated with the lower negative value in energy that is ascribed to favourable nucleation. The corresponding relative energy data is listed in table 7.4.

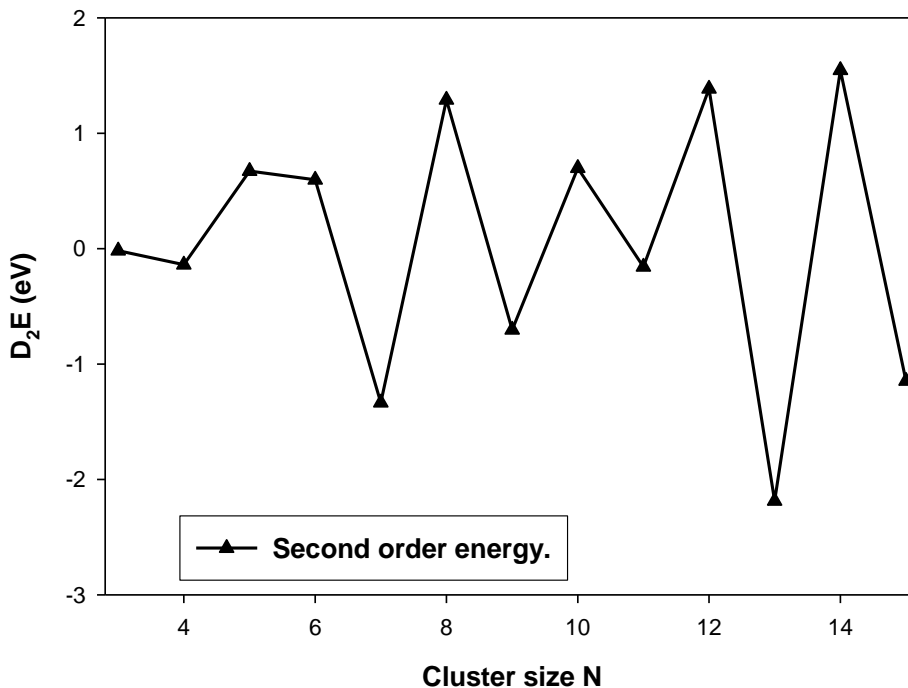


Figure 7.3 : Relative Stability (D_2E) of the most stable $Ti_{N-1}Pt$ site as a function of N .

We note that for D_2E , an odd-even pattern is shown with the lowest values for Ti_6Pt ($N = 7$) and $Ti_{12}Pt$ ($N = 13$) clusters, implying greater stability of the cluster compared to its neighbouring sizes. This suggests that these isomers are the magic clusters. These magic clusters correlate to pentagonal bipyramid and icosahedral isomers, in agreement with the previous report by Kessler *et al.* [32]. We also note clusters with particularly negative D_2E for $N = 3, 7^*, 9, 11, 13^*$ and 15^* . The clusters with more particularly negative D_2E are marked with “*”. Figure 7-4 shows an examination of the first-order energy or dissociation energy which also allow us to identify stable bonded clusters. The higher stability clusters are noted for $N = 7, 9, 11, 13^*$ and 15^* .

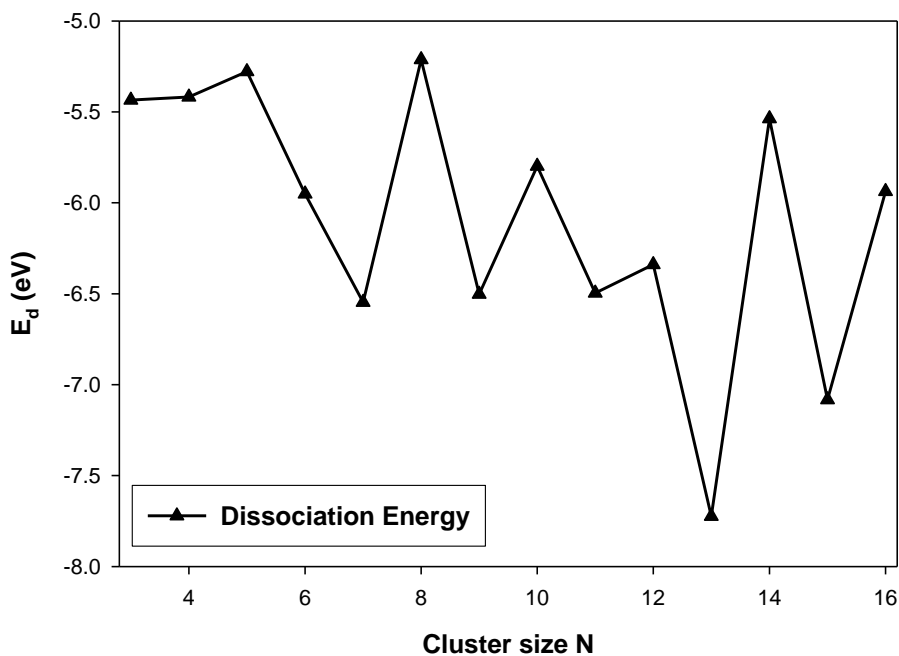


Figure 7.4: The dissociation energy of the most stable $Ti_{N-1}Pt$ sites as a function of N.

The dissociation energy and relative stability exhibit similar magic clusters for $N = 7, 9, 11, 13^*$ and 15^* . However, the bonding strength for the Ti_6Pt ($N = 7$) cluster is observed to be weaker as compared $Ti_{14}Pt$ ($N = 15$) cluster. This contrary to the relative stability. Figure 7.5, shows the energy gap (E_g) of the highest occupied (HOMO), the lowest unoccupied (LUMO) molecular orbitals as the cluster size is increased up to $N = 16$. The average HOMO-LUMO gaps are also presented in Fig. 7.5. From the HOMO and LUMO energies, we observe a decrease in E_g resulting in the lowering of the HOMO energy as the cluster size increases. This behaviour is also observed for pure Ti nanoclusters discussed in chapter 4 section 4.4.5.

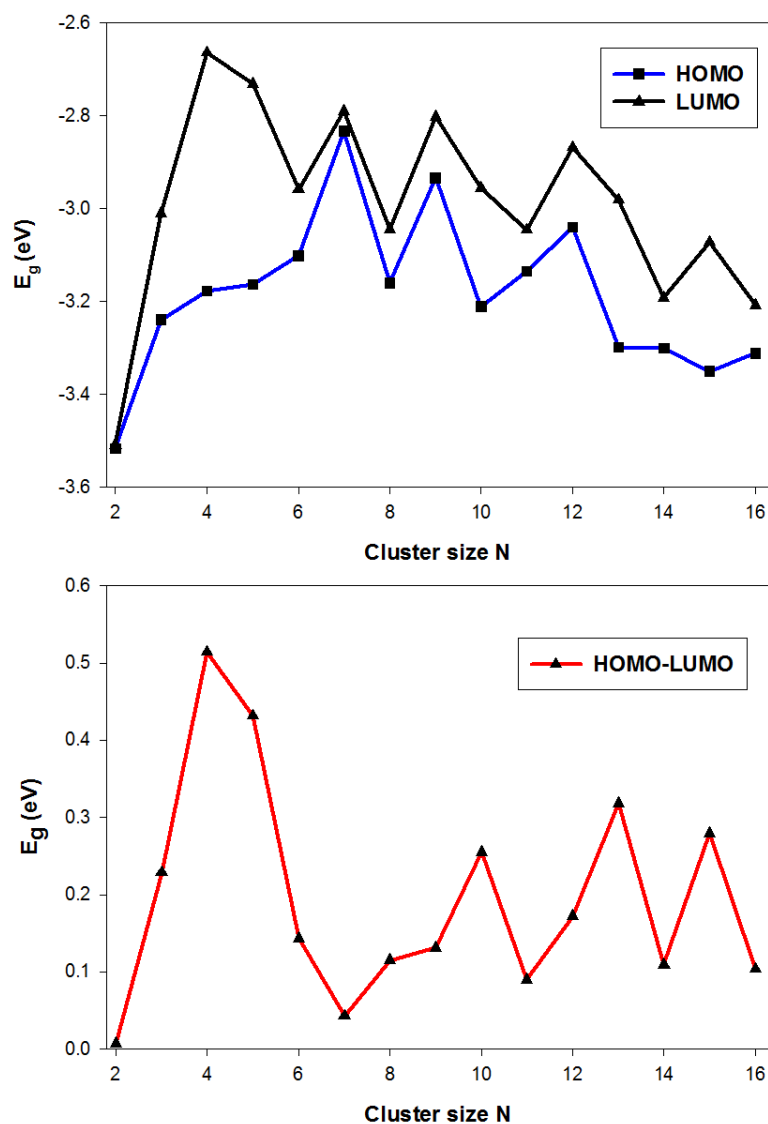


Figure 7.5: The HOMO and LUMO energy gap for $Ti_{N-1}Pt$ clusters, where N is the number of substituted Pt atoms.

The HOMO and LUMO are largest at $N < 9$ and this is as a result of quantum confinement. This effect is observed when the size of the particle is too small compared to the wavelength of the electron. The smaller the nanoparticle, the closer the two charges (electron and hole) [288]. The HOMO and LUMO have smaller energy gaps at $N = 7 - 9$ and 11, however, larger at $N = 12 - 16$.

Table 7.3: The calculated HOMO and LUMO gabs) for $Ti_{N-1}M$ (M = Pt, Ni, Ir and Pd).

Cluster size N	HOMO (eV)				LUMO (eV)			
	TiPt	TiNi	TiIr	TiPd	TiPt	TiNi	TiIr	TiPd
2	-4.937	-3.067	-5.457	-4.937	-3.047	-3.064	-3020	-3.047
3	-3.063	-2.825	-3.200	-3.063	-2.896	-2.709	-2.897	-2.896
4	-3.200	-3.109	-3.325	-3.200	0.524	-2.773	-2.825	0.524
5	-3.115	-3.089	-3.102	-3.115	-2.795	-2.820	-2.603	-2.795
6	-3.083	-3.072	-3.287	-3.083	-2.947	-2.998	-3.079	-2.947
7	-2.971	-3.044	-3.192	-2.971	-2.829	-2.982	-2.744	-2.829
8	-3.096	-3.096	-3.028	-3.096	-2.742	-2.741	-2.645	-2.742
9	-2.946	-2.983	-3.097	-2.946	-2.715	-2.889	-2.812	-2.715
10	-3.180	-3.135	-3.069	-3.180	-2.895	-2.929	-3.069	-2.895
11	-3.117	-3.086	-3.129	-3.117	-3.028	-3.008	-2.984	-3.028
12	-3.055	-3.034	-3.027	-3.055	-2.764	-2.880	-2.945	-2.764
13	-3.269	-3.243	-3.288	-3.269	-2.853	-2.904	-3.219	-2.853
14	-3.288	-3.285	-3.171	-3.288	-3.181	-3.149	-3.115	-3.181
15	-3.323	-3.338	-3.338	-3.323	-3.044	-3.047	-3.258	-3.044
16	-3.288	-3.296	-3.363	-3.288	-3.193	-3.240	-3.221	-3.193

The HOMO-LUMO energy gap increases for smaller clusters whilst it decreases for larger clusters with the consequence of a high degree of fluctuation observed at the average H-L energy gap. However, there is no simple correlation between the E_g and stability (D_2E and E_d). The highest maxima for D_2E is found at $N = 7, 9, 11, 13$ and 15 , whereas the E_g shows steep for $N = 7, 11, 14$ and 16 . The correlation between the E_g and D_2E only exists for $N = 7$ and 11 .

7.4. Structure and stability of $Ti_{13-N}Pt_N$ nanoclusters

In this subsection, we are investigating the effect of Pt doping on the Ti_{13} nanoclusters, i.e., $Ti_{13-N}Pt_N$.

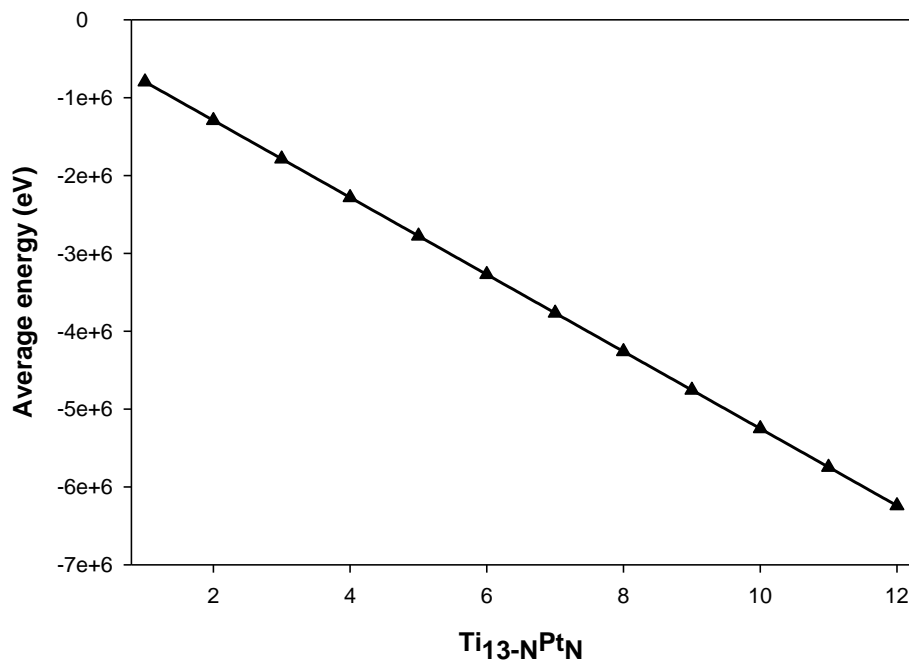


Figure 7.6: The average energy for Ti₁₃-N_{Pt}N composition replaced with Pt at almost all Ti positions of Ti₁₃, where N represents the number of atoms.

The atoms are substituted with Pt impurity to observe doping can influence their potential energy and electronic properties such as the HOMO-LUMO energy gap. Note that the Ti₁₃ cluster was selected since it is a magic nanoparticle and has high stability for a large number of transition metal systems [10].

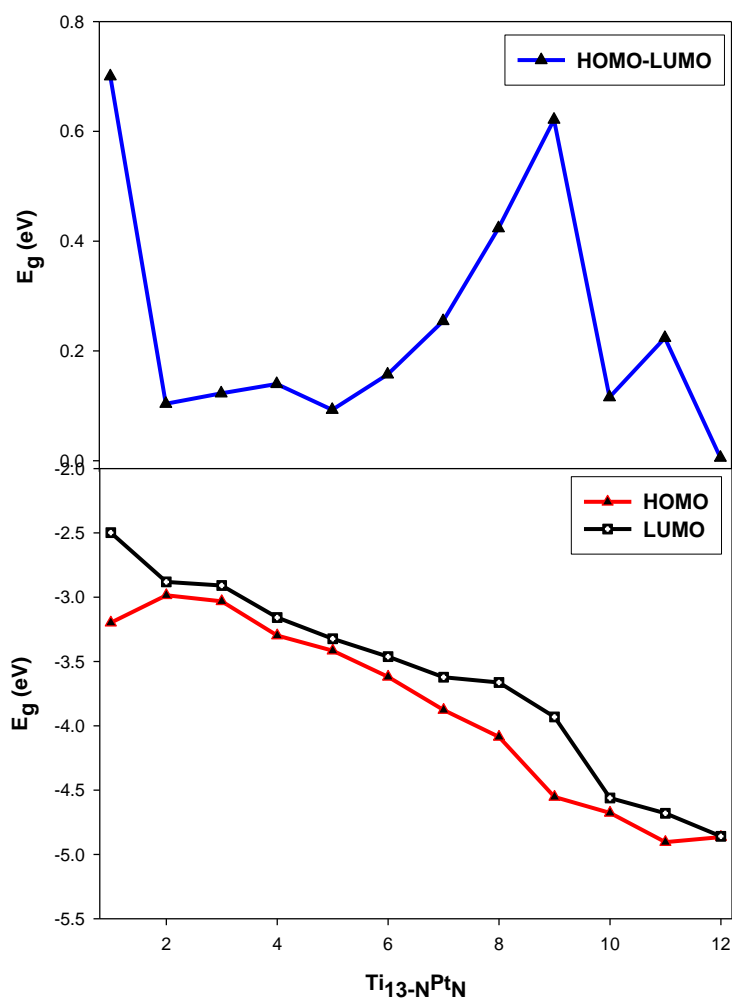


Figure 7.7: The electronic properties (HOMO-LUMO) of $Ti_{13-N}Pt_N$ nanoclusters.

Figure 7.6 shows the potential energy as the Pt atom is substituted in almost all Ti_{13} positions. The plot depicts that the energy decreases linearly with an increase in the Pt atoms.

This suggests that the stability of the $N = 13$ cluster is increased as the number of Pt atoms increases. Figure 7.7 shows the highest occupied molecular orbital (HOMO) and the lowest unoccupied molecular orbital (LUMO) and also present the calculated HOMO–LUMO gap. The HOMO and LUMO decrease as Pt atoms are increased with the HOMO being favoured. The

decrease in energy suggests that Pt substitution enhances the stability of the HOMO and LUMO to a possible similar value of -4.865 eV at $\text{Ti}_1\text{Pt}_{12}$.

This suggests that the LUMO become stabilised as the Pt atoms are increased. The HOMO-LUMO gap displays the lowest gap for $N = 2 - 6$ Pt atoms and the highest energy gap for $N = 7 - 9$ Pt atoms, however, drastically reduced when $N = 10 - 12$ Pt atoms. The HOMO-LUMO gap is also found to increase sharply and reach the highest energy gap (0.622 eV) for the Ti_4Pt_9 cluster. This suggests that it will not be easier for the electrons to move from HOMO into the LUMO states.

For lower energy gaps, the valence electrons in the HOMO can absorb lower energy since they are highly reactive and can easily be excited photo-chemically [289].

7.5. Stability effect of Ti_{N-1}M ($\text{M} = \text{Pd}, \text{Ir}, \text{Ni}$) nanoclusters

In this subsection, we analyse the binding energy, relative stability and dissociation for Ti_{N-1}M ($\text{M} = \text{Pd}, \text{Ir},$ and Ni impurities). We compare the impact of these dopants and how they influence the stability of the Ti_{N-1}M nanoclusters when they are substituted in the same position. Note that N represents the number of Ti atoms and M represents the dopants. We will also compare Pt dopant in this section.

Figure 7.8 shows the binding energy of Ti_{N-1}M doped with Ni, Ir and Pd. We notice that all plots display a similar trend. Their binding energy monotonically or rapidly decreases with cluster size. When the Ti_N ($N = 2 - 16$) clusters are doped with Ni impurity, the size dependence energetically becomes smooth except for Ti_{12}Ni where it is more negative (-5.488 eV) compared to clusters of neighbouring sizes. This particularly more negative is associated with the magic number. The corresponding binding energy data is shown in table 7.2 above. The higher stability of the icosahedron usually occurs for all transition metal cluster [2].

In the case of Ti_{N-1}Ir , the binding energy for Ir dopant also display more negative energy for the Ti_{12}Ir cluster. However, the Ir dopant is observed to enhance the binding energy more for all the nanoclusters. Particularly, for $N = 13$, iridium (-5.854 eV) is observed to enhance the binding energy more compared to nickel impurity. The largest cluster for iridium doped Ti clusters has a binding energy of - 5.930 eV compared to - 5.629 eV for nickel dopant.

Furthermore, for Ti_{N-1}Pd the binding energy as well displays more negative energy for size $N = 13$ (Ti_{12}Pd) and the cluster stabilise for $N = 15$ onwards. The binding energy for Ti_{12}Pd was found to be -5.418 eV and it is the highest binding energy compared to Ni (-5.488 eV), Pt (-5.655 eV) and Ir (-5.854 eV) dopants. The binding energy for the largest cluster with Pd dopant is -5.561 eV which displays it as the weakest dopant compared to other dopants.

In Fig. 7.9, we compare the relative stability (D_2E) for Ti_{N-1}M clusters doped with $M = \text{Ni, Ir, and Pd}$ impurities as the cluster size is increased. The corresponding relative energy data is listed in table 7.5 with the least stable clusters highlighted in green and most stable clusters highlighted in red. In the case of nickel dopant, the clusters with particularly negative D_2E are found for Ti_4Ni ($N = 6$), Ti_7Ni ($N = 8^*$), Ti_{10}Ni ($N = 11$), Ti_{12}Ni ($N = 13^*$) and Ti_{14}Ni ($N = 15^*$). As we observed in section 7.3 and Fig. 7.3, the $N = 13$ is particularly more stable compare to the neighbouring sizes. Magic number assignment for sizes $N = 8, 13$ and 15 correlates to bi-capped octahedron, icosahedron and Z14 Frank–Kasper polyhedron.

Moreover, the most favourable nucleation energy for Ti_{12}Ni is -1.644 eV compared to Ti_{12}Pt (-2.187 eV).

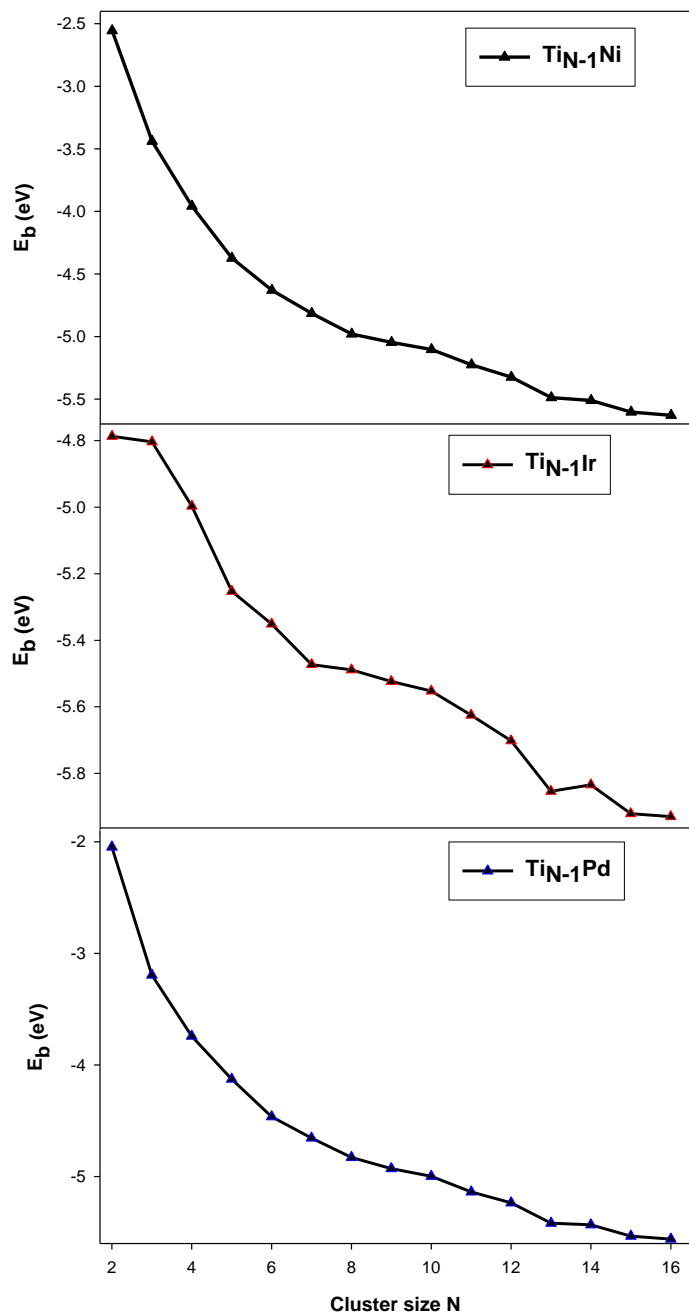


Figure 7.8: The binding energy of $Ti_{N-1}M$ ($M = Ni, Ir, Pd$) against the cluster size.

The latter implies greater stability for platinum compared to nickel impurity. Meanwhile, for iridium dopant, the magic number assignment is observed for Ti_4Ir ($N = 5$), Ti_6Ir ($N = 7^*$),

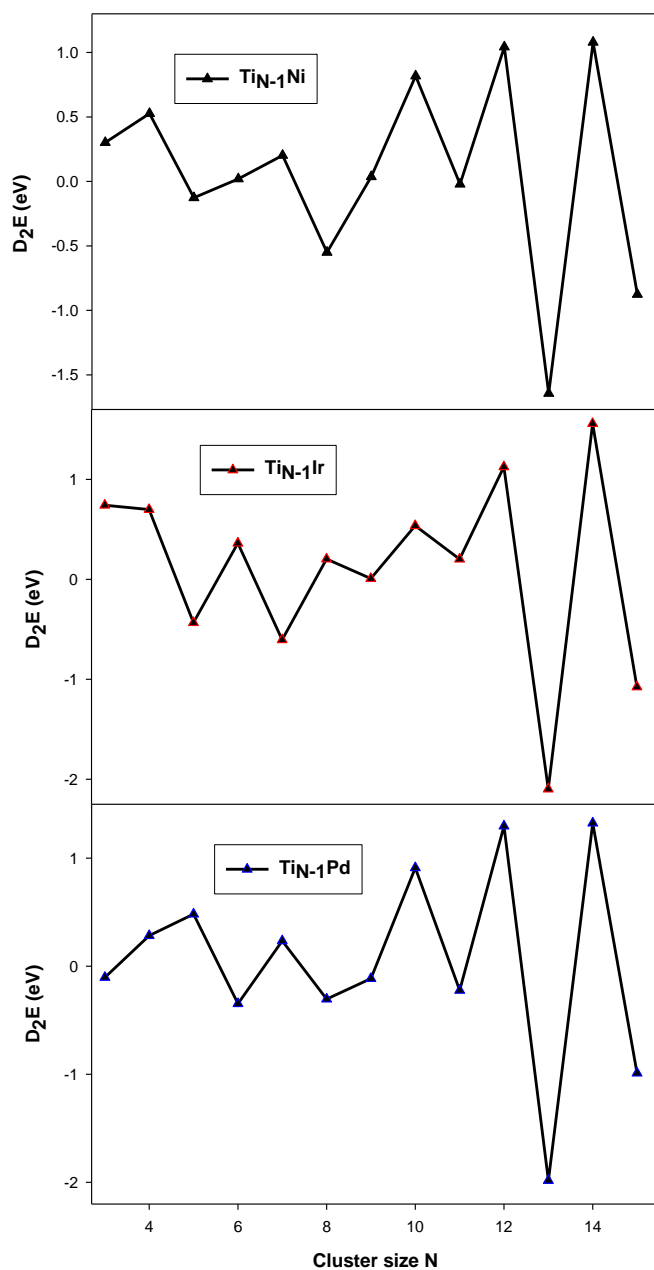


Figure 7.9: The relative Stability (D_2E) as a function of cluster size for $Ti_{N-1}M$ ($M = Ni, Ir, Pd$).

Ti_8Ir ($N = 9$), $Ti_{10}Ir$ ($N = 11$), $Ti_{12}Ir$ ($N = 13^*$) and $Ti_{14}Ir$ ($N = 15^*$) which correlates to triangular bi-pyramid, pentagonal bi-pyramid, pentagonal bipyramid with two of its faces capped by one atom, tetra-capped pentagonal bipyramid, icosahedron and Z14 Frank–Kasper polyhedron. The

D_2E values for $N = 11, 13$ and 15 geometries are in local minima, which match local minima found for nickel and platinum impurities. The higher stability energy value for $N = 13$ compared to clusters of neighbouring sizes is -2.099 eV. This energy is higher compared to platinum impurity and lower compared to nickel dopant.

In the case of palladium dopant, the D_2E more particularly negative values which are associated with the most favourable nucleation (magic numbers) of the isomers are found for $N = 6^*, 8, 11, 13^*$ and 15^* . The $N = 6$ (Ti_5Pd) magic number assignment correlates with octahedral geometry.

Table 7.4: The total relative energies (D_2E) for $Ti_{N-1}M$ ($M = Pt, Ni, Ir, Pd$) and pure Ti.

Cluster size N	Relative energy (eV)				
	TiPt	TiNi	TiIr	TiPd	Pure Ti
2	-	-	-	-	-
3	-0.017	0.301	0.741	-0.104	0.469
4	-0.140	0.526	0.698	0.283	0.418
5	0.673	-0.127	-0.433	0.483	-0.383
6	0.596	0.019	0.362	-0.346	0.506
7	-1.335	0.202	-0.604	0.235	-0.827
8	1.290	-0.550	0.203	-0.304	0.535
9	-0.703	0.036	7.86E-03	-0.113	-0.081
10	0.698	0.818	0.538	0.912	0.031
11	-0.157	-0.021	0.202	-0.222	0.278
12	1.385	1.043	1.126	1.297	0.189
13	-2.187	-1.644	-2.099	-1.983	-0.223
14	1.546	1.079	1.559	1.325	0.047
15	-1.146	-0.876	-1.076	-0.987	-0.115
16	-	-	-	-	-

The $N = 8, 11, 13$ and 15 geometries are in local minima, which match local minima found for nickel, iridium and platinum impurities.

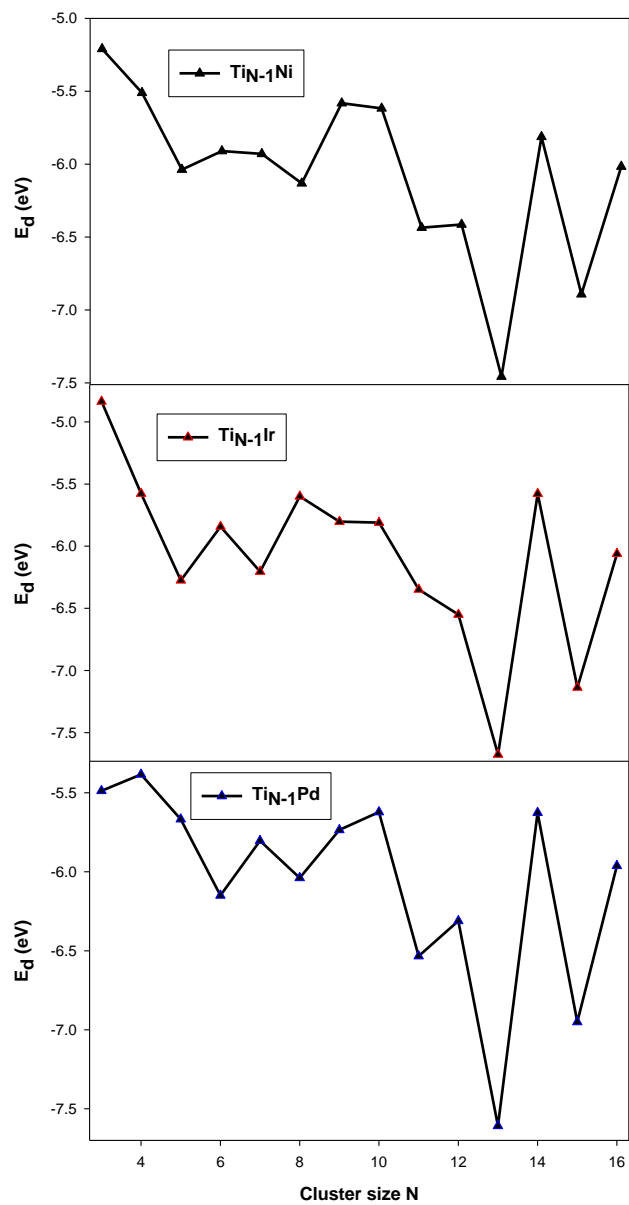


Figure 7.10: The dissociation energy of the most stable $Ti_{N-1}M$ ($M = Ni, Ir, Pd$) sites as a function of N .

The particularly more favoured dopant is observed to be platinum dopant with (-2.187 eV) compared to nickel (-1.644 eV), iridium (-2.099 eV) and palladium (-1.983 eV) dopants for $N = 13$ cluster. In Fig. 7-10, we compare the first-order energy or dissociation energy (E_d) for $Ti_{N-1}M$

clusters doped with M = Ni, Ir, and Pd impurities as the cluster size is increased. The corresponding dissociation energy data is listed in Table 7.5 with the stable cluster highlighted in green. We note that N = 6 (Ti₅Ni), N = 8 (Ti₇Ni), N = 11* (Ti₁₀Ni), N = 13* (Ti₁₂Ni) and N = 15* (Ti₁₄Ni) E_d values are in local minima, which match local minima found for D₂E except for N = 9 (Ti₈Ni). N = 13 is the most favoured isomer with an energy value of -7.457eV.

Table 7.5: The total dissociation energy (E_d) for Ti_{N-1}M (M = Pt, Ni, Ir and Pd) and pure Ti.

Cluster size N	Dissociation energy (eV)				
	TiPt	TiNi	TiIr	TiPd	Pure Ti
2	-	-	-	-	-
3	-5.435	-5.210	-4.836	-5.488	-4.607
4	-5.418	-5.511	-5.577	-5.384	-5.547
5	-5.278	-6.037	-6.276	-5.667	-6.382
6	-5.951	-5.910	-5.843	-6.150	-5.615
7	-6.547	-5.930	-6.204	-5.804	-6.626
8	-5.212	-6.132	-5.600	-6.039	-4.973
9	-6.502	-5.582	-5.803	-5.735	-6.042
10	-5.798	-5.618	-5.811	-5.622	-5.881
11	-6.496	-6.436	-6.349	-6.534	-5.942
12	-6.339	-6.414	-6.551	-6.311	-6.497
13	-7.724	-7.457	-7.677	-7.609	-6.874
14	-5.537	-5.813	-5.578	-5.626	-6.428
15	-7.083	-6.892	-7.137	-6.951	-6.525
16	-5.937	-6.017	-6.061	-5.962	-6.295

In the case of iridium impurity, the higher stability values which are associated with the lower negative values in energy that are attributed to favourable nucleation are noted for N = 5* (Ti₄Ir), N = 7 (Ti₆Ir), N = 13* (Ti₁₂Ir) and N = 15* (Ti₁₄Ir) clusters. These clusters correlate to triangular bi-pyramid, pentagonal bi-pyramid, icosahedron and Z14 Frank–Kasper polyhedron. All values for these magic clusters match the D₂E local minima values. N = 13 is favoured with -7,677 eV as

the lowest energy. Meanwhile, for palladium dopant, the assignment of the magic numbers is found for sizes $N = 6$ (Ti_5Pd), $N = 8$ (Ti_7Pd), $N = 11$ (Ti_{10}Pd), $N = 12$ (Ti_{11}Pd) and $N = 15$ (Ti_{14}Pd) which correlates to octahedron, bi-capped octahedron, tetra-capped pentagonal bi-pyramid, icosahedron and Z14 Frank–Kasper polyhedron. These clusters are also observed to match the D_{2E} local minima values. Furthermore, $N = 13$ is found to be the most stable with the lowest energy of -7.6085 eV. The E_d values in table 7.5 displays that at $N = 13$, $\text{Pt} > \text{Ir} > \text{Pd} > \text{Ni} > \text{Ti}$.

7.6. HOMO – LUMO (H-L) energy gabs of Ti_{N-1}M ($\text{M} = \text{Pd}, \text{Pt}, \text{Ir}$ and Ni)

In this subsection, we analyse and discuss the difference in the energy between the HOMO and LUMO to predict the strength and stability of the bimetallic isomers. The HOMO is normally related to the electron-donating ability of the system and the LUMO is associated with the electron-accepting ability of a system. These orbital energies have energies that are significant indicators of how easily can a molecule be excited photo-chemically.

Figure 7.11 depicts energies of the highest occupied (HOMO) and the lowest unoccupied (LUMO) molecular orbitals, and the calculated average HOMO–LUMO gap for Ti_{N-1}Ni . The HOMO and LUMO energy gaps decrease as the cluster size is increased. The LUMO energy displays the highest peaks at Ti_2Ni ($N = 3$) and Ti_7Ni ($N = 8$), however, stabilise as the cluster size increases.

The largest cluster with the lowest HOMO energy gap is Ti_{14}Ni (-3.30 eV), whereas the largest cluster with the lowest LUMO energy gap is Ti_{15}Ni (-3.24 eV). The corresponding data is listed in Table 7.3. These observations entail that the valence electrons in the HOMO can absorb lower energy which is indicative of higher reactivity and lower stability.

The HOMO-LUMO gap has the highest peaks at $N = 4$ (Ti_3Ni), 8 (Ti_7Ni), 13 (Ti_{12}Ni) and 15 (Ti_{14}Ni). This behaviour illustrates that it would be very difficult for an electron to move from the HOMO into the LUMO.

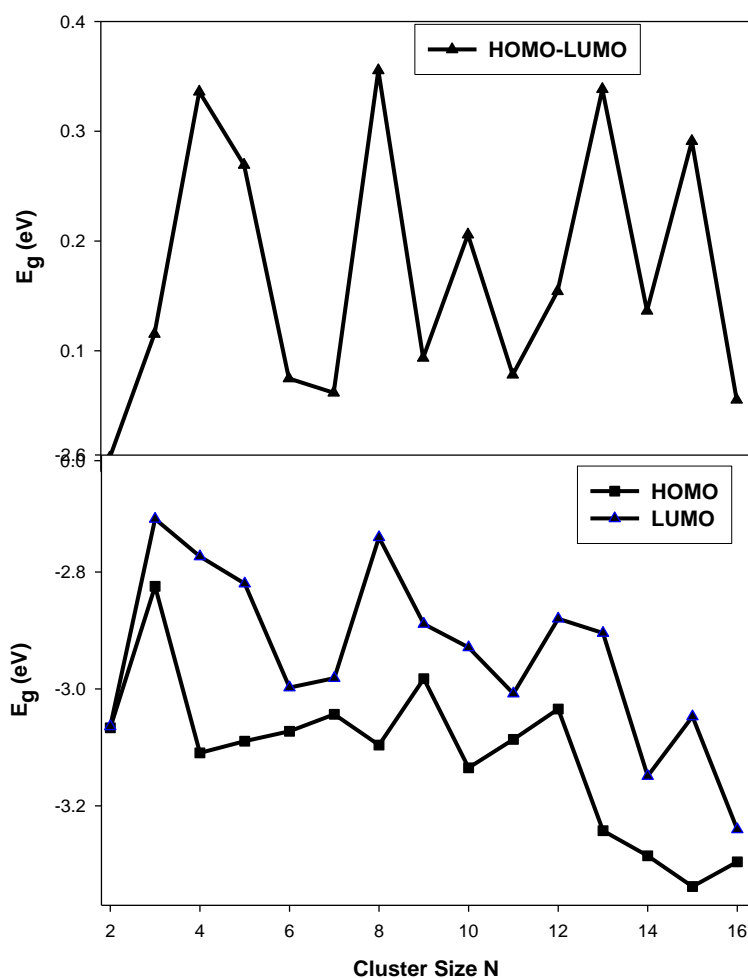


Figure 7.11: The electronic properties (HOMO-LUMO) of Ti_{N-1}Ni nanoclusters.

These clusters behave like they are confined in a delocalised state. The confined states are observed to have relatively higher energies. The effect shifts their bandgap to an optimal value for high energy conservation efficiency.

However, there is no simple correlation between E_g and stability (D_2E and E_d). The highest maxima for D_2E is found at $N = 5, 8, 11, 13$ and 15 , whereas the E_g shows steep for $N = 6, 7, 9, 11$ and 14 . The stability of these clusters is derived from their geometrical shell effect rather than their electronic effect.

In Fig. 7.12 we show the HOMO and LUMO energy and the average HOMO-LUMO energy as a function of cluster size N . The energy gap decreases resulting in the stabilisation of the LUMO energy as the cluster size N increases. The HOMO and LUMO energy gaps show a higher energy difference at Ti_1Ir ($N = 2$). This is attributed to the electron pairs becoming spatially confined when the diameter of the particle approaches the De Broglie wavelength in the conduction band.

At $N < 10$, the LUMO energy stabilises and reduces the energy gap. However, at $N > 10$ the confinement of the electron pairs is reduced. Among the different clusters of a particular size, the HOMO-LUMO shows a steep at Ti_2Ir ($N = 3$), Ti_5Ir ($N = 6$) and Ti_9Ir ($N = 10$). However, the Ti_9Ir ($N = 10$) energy is 0.000 eV.

This happens when the HOMO-LUMO are conjugated or have degenerate energy levels suggesting that the electron in the HOMO would easily move into the LUMO, i.e., electrons are free to move. This observation shows no simple correlation between the E_g and stability (D_2E and E_d). Particularly, the highest maxima for D_2E are found at $N = 5, 7, 9, 11, 13$ and 15 .

In Fig. 7.13 it can clearly be seen that LUMO energy exhibits a greater variation than the HOMO as the cluster size increase. The LUMO displays the highest peak at $N = 4$. This is attributed to the quantum confinement effect on the more diffuse conduction-band-like states increases and the LUMO becomes unstable. The HOMO energy, however, remains relatively constant as cluster size N increases. At $N > 12$, the LUMO and HOMO energies display that clusters with relatively

icosahedral isomerization exhibit shifts of the valence band maximum and conduction band (reduction of quantum confinement).

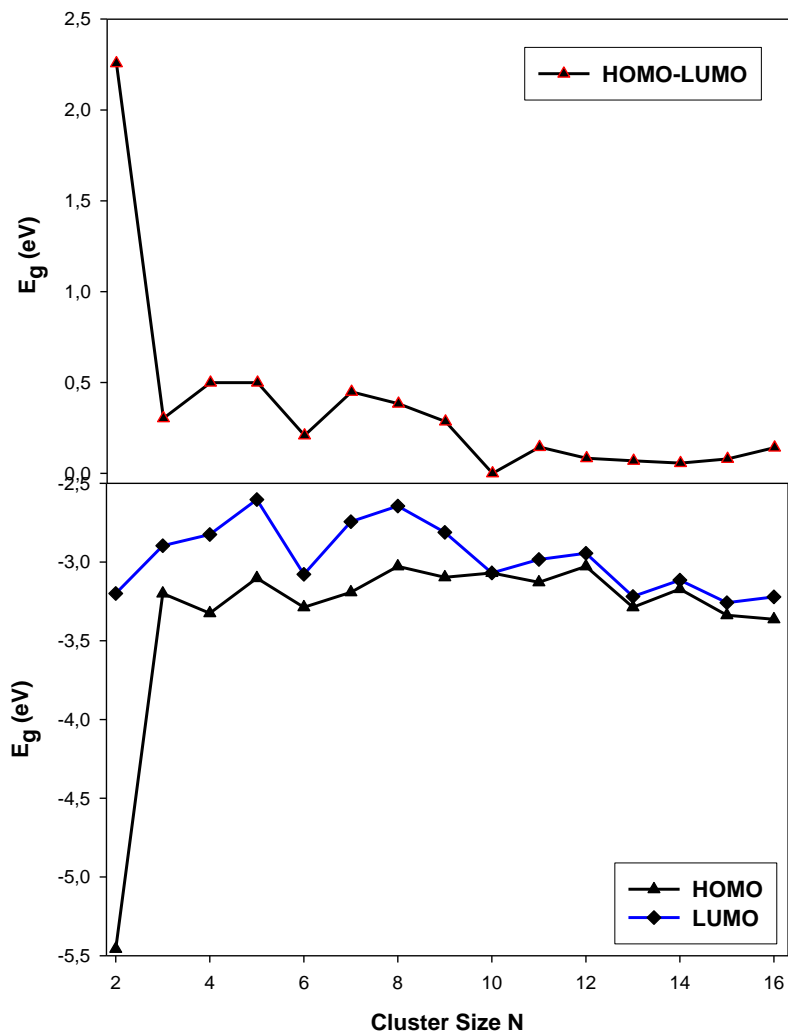


Figure 7.12: The electronic properties (HOMO-LUMO) of $Ti_{N-1}Ir$ nanoclusters.

This behaviour may be linked to eigenstates in the conduction band of the clusters being more sensitive to the addition of atoms. This phenomenon makes the levels discrete and decreases the bandgap and consequently, the band energy also decreases.

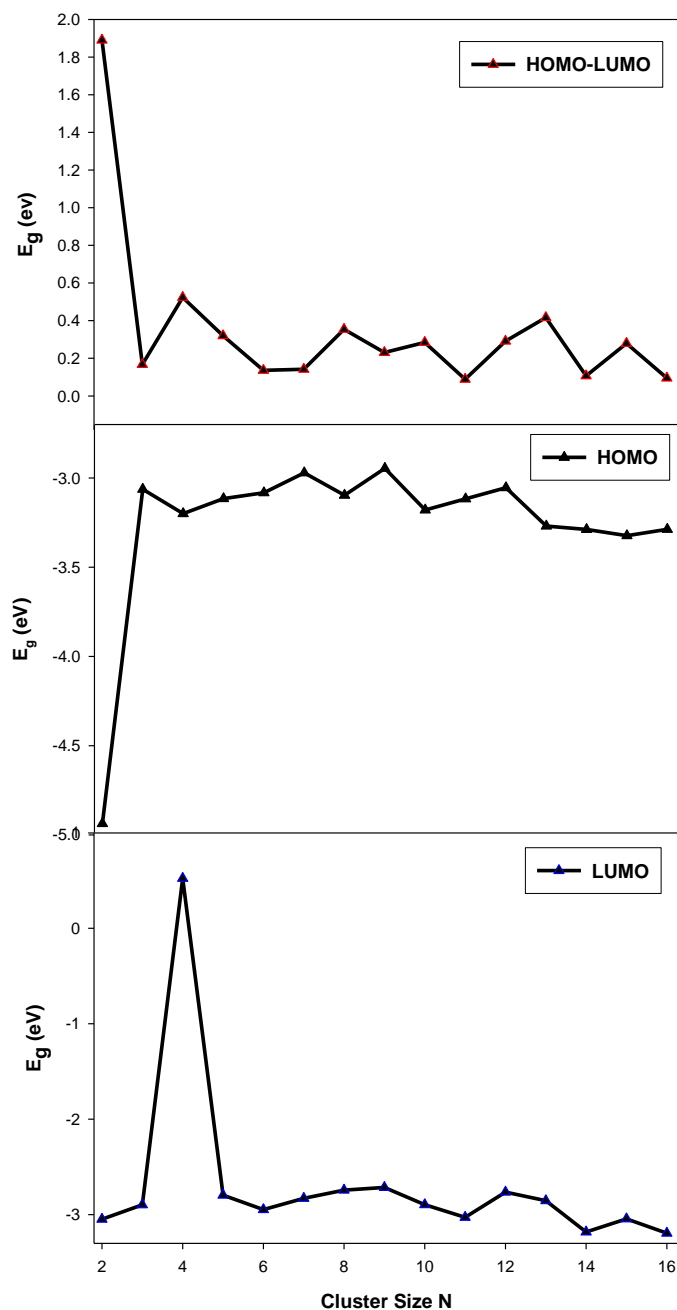


Figure 7.13: The electronic properties (HOMO - LUMO) of Ti_N-1Pd nanoclusters.

The observed trend for the clusters of a decrease in the bandgap with increasing cluster size suggests that it is approaching that of the bulk TiPd bimetallic structure. However, the HOMO-LUMO gap appears to be large for Ti_1Pd , this cluster is more stable in this series. These phenomena may be ascribed to low coordinated atoms in the surface of smaller clusters [290]. Interestingly,

all clusters have a relatively lower bandgap except for Ti_1Pd with a value of 1.89 eV, suggesting that this cluster is the least reactive. The higher energy of Ti_1Pd is indicative of lower reactivity and higher stability. We also note that Ti_3Pd ($N = 4$), Ti_7Pd ($N = 8$), Ti_9Pd ($N = 10$), $Ti_{12}Pd$ ($N = 13$) and $Ti_{14}Pd$ ($N = 15$) have a relatively large gaps than their neighbouring clusters. However, the Ti_3Pd cluster has the highest bandgap than $Ti_{12}Pd$. The latter implies that these clusters are less reactive compared to their neighbouring clusters.

Table 7.6: Average HOMO – LUMO (H-L) energy gaps of $Ti_{N-1}M$ ($M = Pd, Pt, Ir$ and Ni)

Cluster size N	Average HOMO-LUMO (eV)			
	TiPt	TiNi	TiIr	TiPd
-				
2	7.265e-3	0.003	2.250	1.890
3	0.229	0.115	0.303	0.167
4	0.514	0.336	0.499	0.524
5	0.145	0.269	0.499	0.320
6	0.243	0.075	0.208	0.136
7	0.043	0.062	0.449	0.142
8	0.273	0.356	0.383	0.354
9	0.131	0.094	0.285	0.231
10	0.255	0.206	0.000	0.284
11	0.090	0.078	0.145	0.089
12	0.172	0.154	0.083	0.291
13	0.318	0.338	0.069	0.417
14	0.109	0.137	0.056	0.107
15	0.279	0.291	0.080	0.279
16	0.104	0.056	0.142	0.095

This behaviour suggests that in order to excite the electron in the HOMO, light with higher energy is needed. The decrease in confining dimension is observed as we go further to the higher clusters. This observation also shows no simple correlation between the E_g and stability (D_2E and E_d). The

highest maxima for D_2E are found at $N = 6, 8, 11, 13$ and 15 , whereas E_g shows steep for $N = 3, 6, 7, 11, 14$ and 16 .

7.7 Density of states of selected Ti_N clusters doped with Ni, Pt, Ir, Pd

This section intends to correlate the electronic and structural stability of Ti_N ($N = 6, 7, 8, 13$ and 15) when doped with Ni, Pd, Pt and Ir impurities. We compare clusters with the same composition to mimic the stability trend with respect to their behaviour at the Fermi ($E - E_F = 0$). This approach has been previously used on metal alloys [291, 292]. It was suggested that structures with the highest and lowest states at the Fermi (E_F) are considered the least and most stable respectively. This may further be confirmed by observing the trend of the Fermi level with respect to the pseudo-gap and that the system whose states fell in the deep pseudo-gap correspond to the stable system.

Figure 7.14 shows the total density of states (DOS) for the magic numbers of Ti_N ($N = 13$ and 15) clusters when doped with Pd, Pt, Ni and Ir. In Fig. 7.14(a), is clearly seen that Pd and Pt dopants increased the Ti_{13} states at the Fermi with the pseudogap slightly shifted to the right of the Fermi level. Ir and Ni dopants lowered the Ti_{13} states at the Fermi level with pseudogap shifting more to the right of the Fermi level as compared to Pd and Pt dopants. Interestingly, the E_F hit both the Pd and Pt doped Ti_{13} DOS peaks on the left shoulder which is attributed to the stable behaviour. The structural stability trend using density of states is thus; $Ti_{12}Ir > Ti_{12}Ni > Ti_{12}Pt > Ti_{12}Pd > Ti_{13}$, whereas the D_2E found $Pt > Ir > Pd > Ni$ (see section 7.5, figure 7.10).

The density of states also shows no simple correlation between the DOS and stability (D_2E and E_d). Meanwhile, the Ti_{15} cluster in Fig. 7.14(b) shows that the E_F hit the DOS peak at the tip which suggests instability of the cluster. The $Ti_{14}Ir$, $Ti_{14}Pt$ and $Ti_{14}Ni$, however, have their pseudo-gap

shifting slightly to the right of the E_F . The E_F hit the DOS peak of the dopants particularly on the left shoulder which may be ascribed to stability.

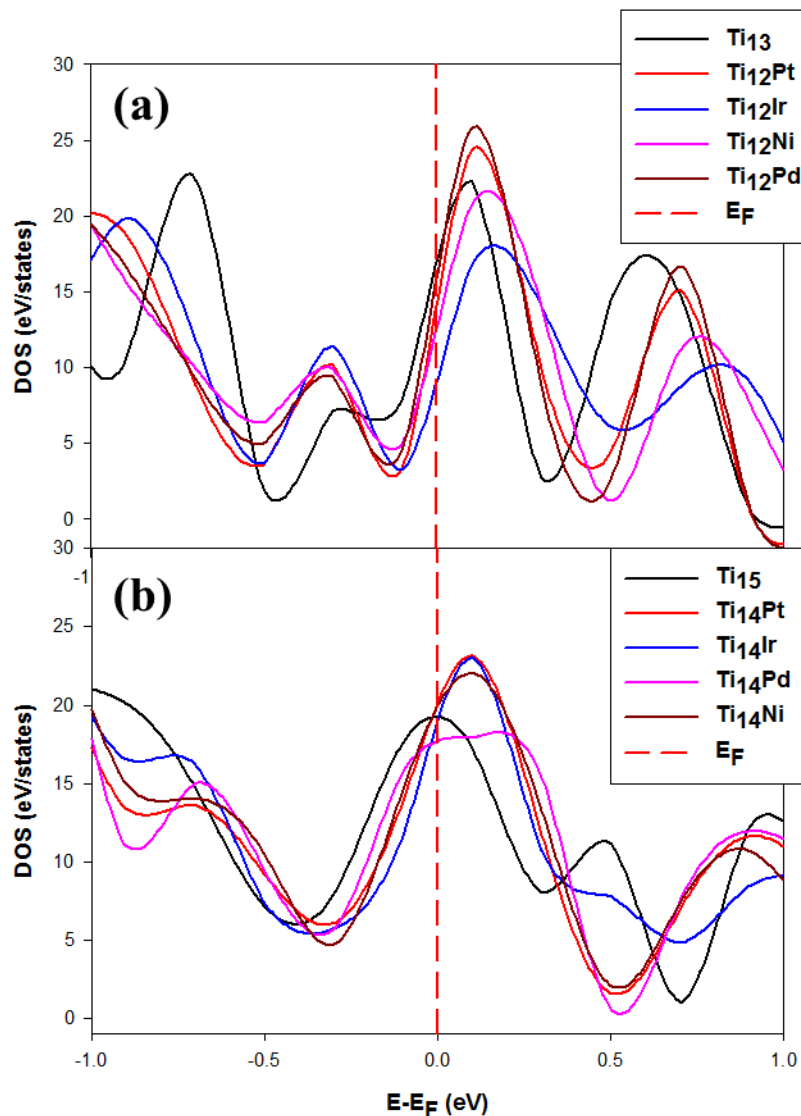


Figure 7.14: Comparison of the total density of states for Pt, Ni, Ir, Ni dopants on Ti_{13} and Ti_{15} .

Although the Pt, Ni and Ir dopants stabilise the Ti_{13} cluster, Ir dopant is more favourable compared to Pt and Ni. This is displayed by the low lying DOS peak of Ir dopant at the E_F .

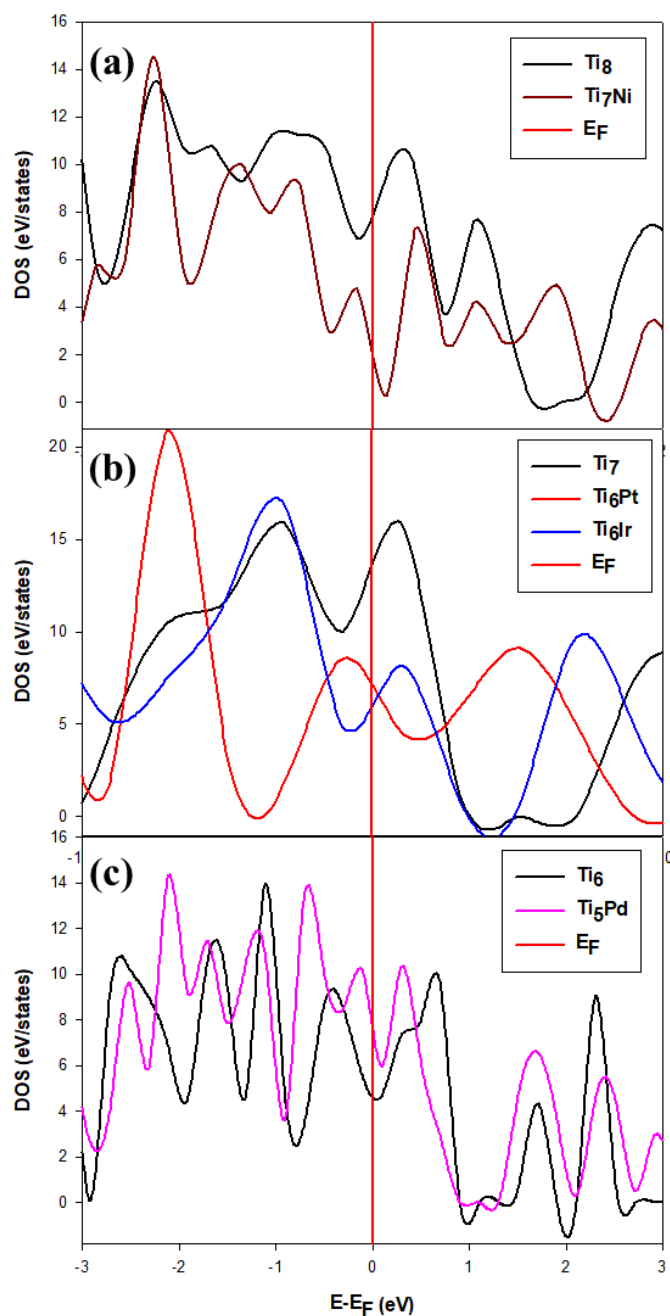


Figure 7.15: Comparison of the total density of states for Ni, Pt, Ir, Pd dopants on Ti₈, Ti₇ and Ti₆ clusters.

We also note that the Ti₁₄Pd DOS are broader at the E_F and its pseudo-gap shifted to the right of the E_F compared to the sharp peak observed for the Ti₁₃ cluster which makes it the least stable.

Figure 7.15 shows the comparison of the density of states for Ti_8 when doped with Ni, Ti_7 with Ir and Pt and Ti_6 with Pd. In Fig. 7.15(a), we show only Ni-doped Ti_8 since it was found to be the only stable dopant. The pure Ti_8 states are higher at E_F as compared to Ti_7Ni states. It is clearly seen the Ni lowered the states and becomes more stable since the E_F fell deep in the pseudo-gap as compared to Ti_8 whose DOS peak shifts slightly to the right of the E_F . The small emergence of a small peak is observed on the left of the E_F , which may be attributed to Ni d-states. The Ti_7 states shown in Fig. 7.15(b) are higher at the Fermi level with its pseudo-gap slightly shifting to the right of E_F , whereas the states for Ti_6Pt are lowered at E_F with its pseudo-gap shifting to the left of the Fermi level. However, for Ti_6Ir , the states are lowered more as compared to Pt dopant. Clearly, both Ir and Pt may stabilise the Ti_7 cluster as confirmed by lowering of DOS at E_F .

The Ti_6 cluster denotes Ir dopant enhancing the stability of the cluster more. It is also noted that for Ti_6Ir , the E_F hit the DOS peak on the shoulder with its pseudo-gap shifting to the right of the Fermi level. In the case of the Ti_6 doped cluster shown in Fig. 7.15(c), the pseudo-gap slightly shifted to the right and their states fell in the slightly deep pseudo-gap. The pure Ti_6 is observed to have higher states compared to the doped Ti_5Pd . Thus, the Pd impurity electronically stabilises the Ti_6 cluster.

7.8. The charge density difference of $Ti_{12}M$ ($M = Ir, Pt, Pd, Ni$)

This section intends to compare the charge density difference for the most stable configuration $Ti_{12}M$ ($M = Ir, Pt, Pd$ and Ni). This approach was previously used on metal surfaces [293] and metal nanostructured titanium dioxide [294]. Bader and Henneker [295] reported that the change in density difference for ionic bonding displays a charge density map that is localised on a single

atom. Figure 7.16 shows the charge density difference of the Ti_{13} cluster doped with (Pt, Pd, Ni and Ir) on the face of the Ti_{13} cluster.

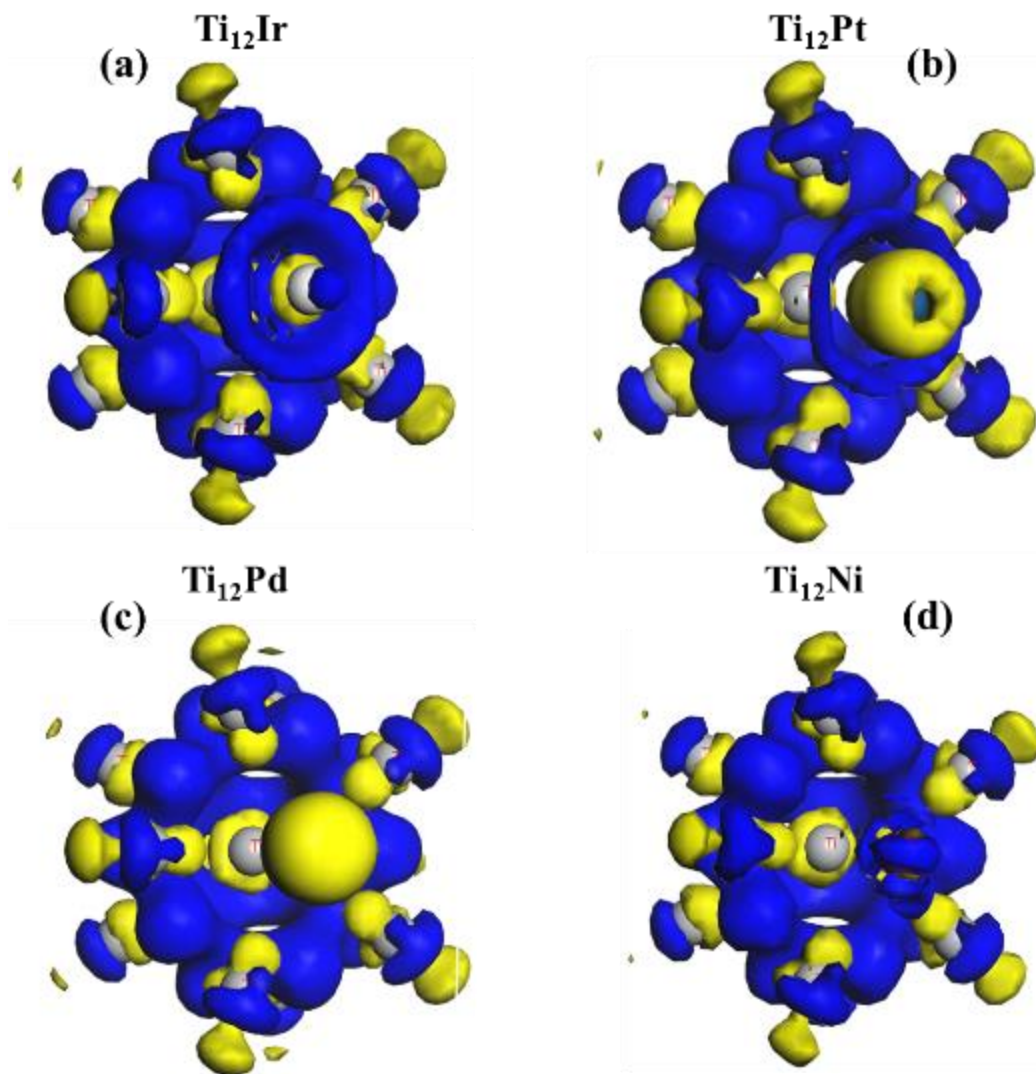


Figure 7.16: Charge density difference for (a) $Ti_{12}Ir$, (b) $Ti_{12}Pt$, (c) $Ti_{12}Pd$ and (d) $Ti_{12}Ni$. The blue region represents accumulation while the yellow region represents electron depletion.

The magnitude of the charge is displayed by different colours where the blue colour indicates the electron-rich region which is subject to electrophilic attack and the yellow colour indicates electron

depletion or electron-poor region which is subject to nucleophilic attack. The stability of the metal finite-sized clusters can be derived by calculating the electron density distribution [296].

The Pt impurity shows a more negative region surrounding its atom which is indicative of the electron depletion. It displayed a single state which is associated with the highest electron depleted state. However, we observe an electron-rich cloud surrounding the electron-poor Pt atom. This observation reveals that there might be deformed electron density along the Ti-Pt bond that signifies higher ionic character and lesser covalent [296]. Thus, larger deformed electron density along the bonds is ascribed to higher stability due to its higher ionic character. Moreover, the Ir atom displays an electron-rich region and an electron-poor region.

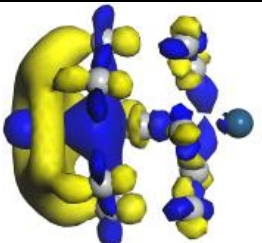
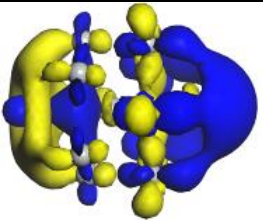
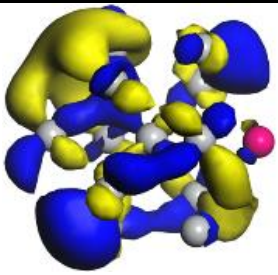
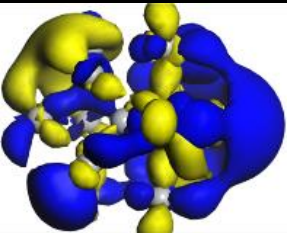
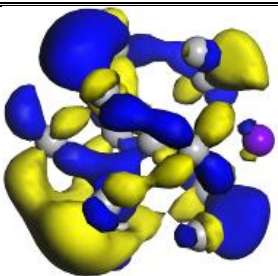
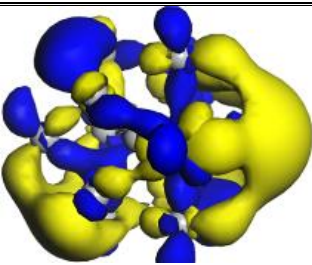
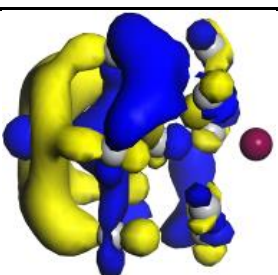
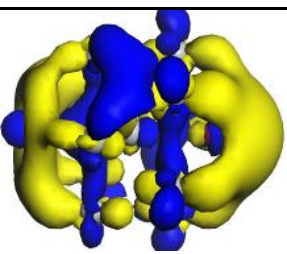
The electron accumulation is observed to be higher on the Ir atom which may be associated with the highest states. This phenomenon might be attributed to the depletion of an electron from the Ti atom into the Ir atoms. The isosurface diagram of $Ti_{12}Ir$ charge density difference reveals an electron-rich cloud surrounding the Ir atom. It also reveals the overlapping of d and p orbitals. The Ti atoms surrounding the Ir atom are observed to have higher electron density, whose p and d orbitals overlaps. Furthermore, the Pd impurity shows a more negative region surrounds its atom which is also associated with a more electron depletion. There is no electron-rich cloud observed for Pd impurity. This observation suggests that electrons are redistributed from the Pd atom into the Ti atom. The electron densities are more deformed in Pd doped than Pt, Ir and Ni-doped titanium clusters. The Ni atom displays a particularly more positive region surrounding the atom which corresponds to electron-rich areas. All the central atoms of Ti are electron depleted. Thus, the Pd interaction with Ti is subject to nucleophilic attack due to its more ionic character, whereas Ni and Ir reactions are subject to electrophilic attack. We observed that the degree of electronic depletion around the impurities is as follows; Pd > Pt > Ir > Ni.

7.9. HOMO-HOMO orbital analysis for Ti_{12}M (M = Pt, Ni, Pd, Ir)

This section intends to compare the computed HOMO-LUMO pictorial diagram of the most stable isomers, Ti_{12}M (M = Ir, Pt, Pd and Ni). This approach was previously used on doped stable rhodium clusters [296] and doped titanium and vanadium clusters [297]. Dutta and Mondal [296] found that the electronic redistribution occurs from HOMO (Rh) to LUMO (non-metal). The isosurface diagram of HOMO and LUMO orbitals are shown in table 7.7. It is observed from the table that the electronic cloud of HOMO is at the titanium atoms for all doped clusters. In Ti_{12}Ir , Ti_{12}Pt , Ti_{12}Pd and Ti_{12}Ni , higher orbital densities are observed around titanium atoms which reveals that the d-orbitals of titanium atoms are involved in bond formation. There is a little contribution of electron density for the formation of Pt, Pd and Ir doped titanium clusters, whereas, no contribution of electron density is observed in the formation of Ni-doped titanium clusters.

Amongst all the cluster HOMO orbital densities, they are mainly observed to be localised around the titanium atoms. In the case of the LUMO orbital, Ti_{12}Ir and Ti_{12}Pt are observed to have higher electronic cloud at the iridium and platinum atom. This observation suggests electronic redistribution or migration amongst Ti, Ir and Pt atoms. These clusters are observed to have overlapping of d-orbitals and p-orbitals of titanium. Electrons are observed moved from the p – orbitals into the d-orbitals. This can clearly be seen from the electron-deficient p-orbitals. Similar observations were found in section 7.8. The electronic isosurface diagram of the Ti_{12}M (M = Pd, Ni) reveals that all cluster HOMO electronic densities are seen to be situated at titanium atoms, whereas, LUMO displays electron-deficient cloud around Ni and Pd atoms. The p-orbital displays the movement of electrons from Pd and Ni into the titanium atoms.

Table 7.7 The computed iso-surfaces of the HOMO-LUMO for $Ti_{12}M$ ($M = Pt, Pd, Ir, Ni$)

Cluster	HOMO	LUMO
$Ti_{12}Ir$		
$Ti_{12}Pt$		
$Ti_{12}Pd$		
$Ti_{12}Ni$		

CHAPTER 8

Summary and conclusion

The transition metal clusters with a diameter of 1 – 100 nm have received great attention due to their efficacy in catalysis, sensory and antimicrobial agents [298]. These nanoclusters are distinct by a limited number of atoms and their geometries have different chemical species, forming diverse phases and morphologies [299]. They possess exceptional physicochemical properties that vary according to their cluster size, geometries and compositions. In this study, simulations for Ti_N ($N = 2 - 32, 57, 80$ and 89) were carried out using the Knowledge-Led Master Code (KLMC) software suite and its recently improved genetic algorithm (GA) module, which has proved to locate efficiently local (LM) and global (GM) minima on potential energy surface (PES). Alternative global optimisation techniques, typically based on either GA or a Monte Carlo Basin Hopping scheme, have been applied to predicting the structure of metallic Ti clusters or their alloys or generic atomistic energy landscapes.

The PES of Ti_N nanoclusters was evaluated using a many-body embedded atom method (EAM), which includes a combination of a many-body attractive term and a repulsive two-body Born–Mayer IP. Parameters for the EAM IP were obtained from a mathematically equivalent parameterisation of the tight-binding potentials. After completing the search on the IP PES, we have selected for refinement a subset of the lowest energy LM within approximately 1.0 eV energy range above the corresponding tentative GM. Using this criterion, for example, the Ti_{32} subset included 250 LM.

The selected clusters were re-optimised at the quantum mechanical, DFT level using the all-electron, full potential electronic structure code FHI-aims. The MD calculations were performed employing DL_POLY to investigate the effect of temperature on the most stable titanium nanocluster. Amongst the three canonical (NVT) ensembles (Hoover, Berendsen and Andersen) employed on the Ti_{13} cluster, the Hoover thermostat was found to generate results that are in agreement with the literature. Two sets of calculations were considered for $N = 7, 13, 17$ and 32 ; firstly the nanoclusters were calculated in a vacuum and secondly in the presents of Argon gas. For bigger clusters ($N = 57, 80$ and 89), only one set of calculations was successfully evaluated. The equation of motion in the Argon environment was derived on the basis of the extended Lennard – Jones as the effective pair potential. These parameters were chosen to monitor the inert gas effect on the Ti nanoclusters. To simulate properly the thermodynamics properties of the nanoclusters, the EAM and the Born-Mayer interatomic potentials were successfully incorporated together to express the total internal energy of pure metals in terms of Gupta potentials.

The effect of impurity substitution on Ti_N ($N = 2 - 16$) atoms with Pt, Pd, Ir and Ni were performed by employing density functional theory code (FHI-aims) with PBE functional revised for solids (PBEsol). Two sets of calculations were performed; firstly Pt dopant was successfully used as a benchmark to locate the most energetic position during the substitution and secondly the same position was used to evaluate the effect of other impurities on the Ti clusters. Their binding energy, dissociation energy, relative stability and Homo-Lumo energies were successfully calculated.

Chapter 4

The results for $N = 2$ to 20 show good agreement with those reported by Sun *et al.* [33]. It was revealed that clusters with $N = 7, 13$ and 15 atoms are magic clusters. Here, a higher level of theory is employed, a more detailed exploration of LM and larger clusters ($N = 21-32$) were

systematically studied for the first time. Our results show that the GM are formed of interpenetrating icosahedra and Frank–Kasper polyhedral. Early reports of small Ti clusters have found that the magnetic moments tend to decrease with the system size and disappear by $N = 17$. In contrast, we found non-zero spin moments persist to larger sized clusters: we report that magnetic moments of the lowest energy structures for $N = 18, 25, 26,$ and 27 have an overall spin moment of $1 \hbar$.

Analysis of the cluster energetics and structural features allowed us to identify new sizes of greater stability, which might be observed in a greater abundance. In particular, both PBEsol and PBEsol0 calculations agree with previous suggestions that $N = 7$ and 13 are “magic”. Furthermore, a match was found for additional seven sizes of enhanced stability using both levels of theory. Key to rationalising our results has been the development of a new analytical toolkit including the measurement of surface area for a cluster and the identification of centres of coordination, which act as centres of bulk nucleation in medium-sized clusters. The increase in the number of the latter is found to relate to the changes in the morphological features of GM.

Chapter 5

To understand the thermodynamic behaviour of these clusters we further investigated the thermal agitation of the nanoclusters. The molecular dynamics (MD) simulation was carried out to investigate the characteristics of the ground state configuration predicted for the Ti_N ($N = 7, 13, 17, 32, 57, 80$ and 89) nanoclusters. Analysis of the thermal agitation on nanoclusters allowed us to identify new phases, which form part of the building block. Three thermostats (Andersen, Hoover and Berendsen), showed transitions for $N = 13$ cluster at different temperatures both in a vacuum and inert gas conditions. In vacuum condition, Hoover thermostat displayed structural transition at 2100 K and regained its equilibrium structure at 2200 K, however, it was transitioned

again at 2300 – 2400 K. At 1700 K, Andersen thermostat showed structural transition and regained its equilibrium cluster at 2000 K and the cluster was also transitioned after being relaxed to its original form. Meanwhile, Berendsen thermostat displayed structural transition at 2100 K and regained its equilibrium cluster at 2200 – 2400 K. In particular, all the thermostats are observed to have pentagonal bi-pyramid and triangular bi-pyramid as the most dominant geometries.

The hysteresis loop was found for all the thermostats. However, this melting identifier showed that the melting behaviour of the nanocluster occurs beyond the melting point of bulk Ti for Hoover and Berendsen. The phase transition was identified by a single jump in the total energy. The radial distribution function decrease with increasing temperature. This observation reveals the structural and phase transitions as cluster approaches melting. The structural thermal transitions for $N = 17$ are observed to occur at 300 – 2400 K. This transitional range was observed to be dominated by icosahedral geometry interpenetrating with triangular bi-pyramidal. The potential energy revealed a loop at 1100 K which is ascribed to the formation of a new unstable geometry as the cluster is cooled.

The structural transitions for Ti_7 were observed to occur at a lower temperature (1100 K). However, the nanocluster was observed to regain its equilibrium morphology at $T > 1200$ K. The potential energy for $N = 7$ also reveals two loops at 1900 K and 2100 K. These loops are attributed to the formation of new phases which are as well unstable. Ti_{32} cluster also showed structural transformation at 300 – 2400 K. The structural transition for this cluster was observed to be dominated by icosahedral ($N = 13$) and interpenetrating icosahedral ($N = 19$). The potential energy for $N = 32$ reveals a small hysteresis loop at 2000 K. The RDFs for $N = 7, 17$ and 32 clusters are observed to decrease with increasing temperature.

In argon gas conditions, smaller nanoclusters ($N = 7, 13, 17$ and 32) were inserted into inert gas to reduce their melting point. The argon gas is capable of allowing arc melting to be carried at lower pressures or temperatures. Ti_7 and Ti_{13} clusters are observed to be compact and thermodynamically unfavourable as we observed in a vacuum. The calculations allowed the nanocluster to show melting features below the bulk Ti melting point for $N = 7$ and 13 clusters. The Hoover, Andersen and Berendsen thermostats showed melting features at $T < 1500$ K, $T < 1300$ K and $T < 1400$ K for Ti_{13} nanocluster. The Ti_7 showed melting features at $T < 800$ K with the Ti_{17} nanocluster at $T < 1300$ K.

The effect of inert gas was found to reduce the structural distortions and melting point for $N = 7$ and 13 clusters to temperatures below the bulk Ti melting as compared to vacuum. However, the Ti_{32} is observed to have structural distortions at 600 K compared to 300 K in a vacuum. The inert gas enhances the stability of the $N = 32$ nanocluster. These observations are also revealed by the elongated surface and interlayer distance. The potential energy for all the clusters is observed to be enhanced when these clusters are in an inert gas condition.

Chapter 6

The bigger clusters ($N = 32, 57, 80$ and 89) are observed to transition at temperatures below the bulk Ti melting point. At 1300 K, $N = 57$ atoms are observed to segregate to clusters surface and become more uniformly distributed in the surface and interior at higher temperatures. However, $N = 80$ and 89 atoms are observed to segregate to their cluster surfaces at 1600 K and 1800 K.

These changes are revealed by the surface melting at lower temperatures ($300 - 1400$ K). However, the interlayer melting is observed at 1500 K where the interlayer distance is elongated as compared to clusters at lower temperatures. As the outermost surface exhibits melting features, the core

atoms are found to migrate to the layers closer to the surface of the clusters. The thermal agitated transitions of the bigger nanoclusters are dominated by two interpenetrating pentagonal icosahedra, icosahedron at $T < 1700$ K. However, at $T > 1800$ K the pentagonal bi-pyramid and triangular bi-pyramidal are observed to be dominant. The potential energies reveal the melting behaviour occurring at 2000 K and 1941.15 K for Ti_{32} , Ti_{57} and Ti_{80} , and it is enhanced with increasing cluster size. The RDFs are observed to decrease with increasing temperature. Moreover, the magnitude of their values decreases with increasing cluster size. This phenomenon was ascribed to the change of phases of the clusters.

Chapter 7

In the case of doped Ti_N ($N = 2 - 16$) with Pt, Pd, Ni and Ir impurity, it was observed that the impurities enhance the binding energy of the Ti clusters. The relative stability and dissociation energy for Pt dopant is also found to be energetically favoured compared to other impurities. The substitution of Pt impurity at almost all the positions of Ti_{13} atoms is found to linearly enhance the total energy as the number of Pt atoms is increased. Iridium was found to enhance the binding energy of the clusters more compared to other impurities. However, all the impurities displayed $N = 13$ as the most stable isomer or magic cluster.

The total DOS of $N = 6, 7, 8, 13$ and 15 were calculated for comparison which shows that Pd electronically stabilises $N = 7$ clusters, whereas, it is the least stabilising impurity for $N = 13$ cluster. Iridium dopant was found to stabilise the $N = 15$ cluster more compared to Ni and Pt dopants. The iso-surface of the charge density and H-L revealed higher electronic charge transfer from the inner core of the Ti atoms towards the surface of the cluster where there is Ti-Pt and Ti-Ir are bonding. These results showed a charge depletion from Ti atoms and accumulated by the impurities (Ir and Pt).

Future work

In future, investigation of larger Ti clusters ($N > 100$) and doped Ti clusters with transition metal impurities such as Ru, Rh, Co and Os will be conducted using the Knowledge Led Master Code (KMLC) [34] and Fritz Haber Institute ab initio molecular simulation package (FHI-aims) [148]. The KLMC code will be used to search the tentative local and global minima of pure Ti clusters and M (M = Rh, Ru, Os and Co) doped Ti clusters. These clusters will be re-optimised using FHI-aims to investigate the structures and electronic properties of Ti-doped clusters from a theoretical perspective. Their geometrical structures, relative stabilities, and electronic properties will be computed. The relative stable geometries will be given for every size. The average binding energy, second-order energy, dissociation energy will be compared with pure Ti clusters. The average bond lengths and coordination numbers will be analysed to investigate how the clusters are bonded and coordinated as they evolve towards the bulk.

Furthermore, we will apply the molecular dynamics (MD) method using DL_POLY to simulate the melting crystallisation process for pure Ti and Ti-doped nanoclusters. We aim to extend the molecular dynamics simulations to investigate the dynamics and thermodynamic properties of Ti-doped clusters. In particular, we will examine how the melting temperature is dependent on cluster size, including premelting before the transition. Then we will as well examine the cluster formed upon solidification and the melting temperature during reheating of newly formed clusters.

The co-doping of titanium clusters with Pt, Pd, Rh, Ru, Os and Co will be investigated to assess their effect and influence on the geometry and thermodynamic stability.

APPENDIX A.

Publications and Presentations at the Conferences

A. Presentations at Conferences

1. Phaahla T.M., G.M. Mashaba and P.E. Ngoepe “Effect of pressure on the nanostructured TiO_2 during recrystallization” 4-8 July 2016, South African Institute of Physics Conference, University of Cape Town, South Africa.
2. Phaahla T.M, H.R. Chauke, C.R.A. Catlow and P.E. Ngoepe “Modelling studies of the evolution of Tin ($n = 2-32$) clusters” Post Graduate Research day, 29-30 September 2016, Bolivia Lodge, Polokwane, South Africa.
3. H.R. Chauke, T.M. Phaahla and P.E. Ngoepe “Modelling of Ti metal clusters” Characterization of Metal Particle Workshop, 6-7 October 2016, Glenshiel Hotel, Haenertsburg, Polokwane, South Africa.
4. T.M. Phaahla, H.R. Chauke, C.R.A. Catlow and P.E. Ngoepe “Computational modelling studies of the evolution and growth of titanium nanoclusters” Centre for High Performance Computing National Meeting, 4-9 December 2016, ICC, East London, South Africa.
5. H.R. Chauke, T.M. Phaahla, C.R.A. Catlow and P.E. Ngoepe “Structural evolution, growth and stability of metal titanium clusters” American Physical Society March Meeting 2017, March 13–17, 2017, New Orleans, Louisiana, USA.
6. T.M. Phaahla, H.R. Chauke, P.E. Ngoepe and C.R.A. Catlow “Density functional theory study of Tin ($n = 2-32$) clusters: Lowest energy configurations and electronic properties” South African Institute of Physics Conference, 3-7 July 2017, Stellenbosch University, Western Cape, South Africa.
7. T.M. Phaahla, H.R. Chauke, C.R.A. Catlow and P.E. Ngoepe “Density functional theory study of Ti_N ($N = 2-32$) clusters: Lowest energy configuration and electronics properties” CCP5, DL_Software Training, 19-22 February 2018, Daresbury Laboratory, Liverpool, United Kingdom.
8. T.M. Phaahla, H.R. Chauke, C.R.A. Catlow and P.E. Ngoepe “Structure and dynamics of noble gas temperature control on Ti metal clusters” 25-29 June 2018, South African Institute of Physics Conference, University of Free State, South Africa.
9. T.M. Phaahla, H.R. Chauke, C.R.A. Catlow and P.E. Ngoepe “A molecular dynamics study of noble gas effect on the structure and shape of titanium metal clusters” Faculty of Science and Agriculture Research Day, 20-21 September 2018, Fusion Boutique Hotel, Polokwane, South Africa.
10. T.M. Phaahla, H.R. Chauke, C.R.A. Catlow and P.E. Ngoepe “Temperature effect on Ti_{13} metal cluster: A molecular dynamics study” Centre for High Performance Computing National Meeting, 2-6 December 2018, Century City Convention Centre, Cape Town, South Africa.

11. T.M. Phaahla, H.R. Chauke, C.R.A Catlow and P.E. Ngoepe “Temperature effect on Ti₁₇ metal cluster: A molecular dynamics study” South African Institute of Physics Conference, 8-12 June 2019, Venda University, The Ranch Hotel, Polokwane, South Africa.
12. T.M. Phaahla, H.R. Chauke, C.R.A. Catlow and P.E. Ngoepe “Molecular dynamics comparison study on the stable Ti₁₃ & meta stable Ti₁₇ nanoclusters” 19th - 20th September 2019, 10th Faculty of Science and Agriculture Postgraduate Research Day, University of Limpopo, The Ranch Hotel, Polokwane, South Africa.
13. T.M. Phaahla, P.E. Ngoepe, C.R.A. Catlow and H.R. Chauke “ A molecular dynamic study of Ti₃₂ nanocluster” 22 – 25 October 2019, Riverside Sun, Vanderbijlpark, South Africa.
14. T.M. Phaahla, P.E. Ngoepe, C.R.A. Catlow and H.R. Chauke “The thermodynamic phase transitions in Ti₁₇ metal nanocluster: A molecular dynamics study” 01 – 05 December 2019, Birchwood, Johannesburg, South Africa.
15. T.M. Phaahla, C.R.A. Catlow, A.A. Sokol, S.W. Woodely, P.E. Ngoepe and H.R. Chauke “Molecular dynamics study of structural properties of Ti₅₇ nanocluster” 22 – 30 July 2021, South African Institute of Physics Conference, North West University, South Africa.
16. T.M. Phaahla, P.E. Ngoepe, C.R.A. Catlow and H.R. Chauke “The role of transition metal doping in Ti nanoclusters: Synergistic or Counteractive?” 06 - 08 October 2021, 11th Faculty of Science and Agriculture Postgraduate Research Day, University of Limpopo, Bolivia Lodge, Polokwane, South Africa.
17. T.M. Phaahla, P.E. Ngoepe, C.R.A. Catlow and H.R. Chauke “Structures and stability of palladium and nickel doped Ti_N (N = 1 – 15) nanoparticle” 07 - 08 October 2021, 10 th SANI-NYRS SYMPOSIUM: NATIONAL, University of the Witwatersrand, Johannesburg, South Africa.
18. T.M. Phaahla, P.E. Ngoepe, C.R.A. Catlow and H.R. Chauke “The effect of doping with Pt impurity on Ti clusters: A density functional theory study” 18 - 22 October 2021, Conference of the South African Advanced Materials Initiative, The Council for Scientific and Industrial Research (CSIR), Council for Mineral Technology (Mintek) and South African Nuclear Energy Corporation (Necsa), South Africa.

B. Publications

- **Papers in preparation**

1. Phaahla, T.M., Catlow, C.R.A., Ngoepe, P.E., Chauke, H.R “Density functional investigation on the impact of M atom (M = Ni, Pd, Ir) on the structure and energetics of Ti_N (N = 1 – 15) nanoparticles”

- **Papers published**

1. Tomas Lazauskas, Alexey A. Sokol, John Buckeridge, C. Richard A. Catlow, Susanne G. E. T. Escher, Matthew R. Farrow David Mora-Fonz, Volker W. Blum, Tshegofatso M. Phaahla, Hasani R. Chauke, Phuti E. Ngoepe and Scott M. Woodley “Thermodynamically accessible titanium clusters Ti_N , $N = 2-32$ ” *J. Phys. Chem. Chem. Phys.*, 2018, 20, 13962-13973.
2. Tshegofatso M Phaahla., Alexey A. Sokol., Charles R. A. Catlow., Scott M. Woodley., Phuti E. Ngoepe and Hasani R. Chauke “The Thermal Agitated Phase Transitions on the Ti_{32} Nanocluster: a Molecular Dynamics Simulation Study” *S. Afr. J. Chem.*, 2021, 74 (Special Edition), 17–22.
3. T. M Phaahla, P.E Ngoepe, R. A Catlow and H. R Catlow “The effect of doping with Pt impurity on Ti clusters: A density functional theory study” *S. Afr. J. Sci.*, 2022, 40, 75-78.

References

- [1] Nalwa, H. S, “Encyclopedia of nanoscience and nanotechnology,” American scientific, New York, 2004.
- [2] Baletto, F.; Ferrado, R, “Structural properties of nanoclusters: Energetic, thermodynamic and kinetic effects,” *Rev. Mod. Phys.*, vol. 77, pp. 385-392, 2005.
- [3] Wales, D. J, “Energy landscape with applications to clusters, biomolecules and glasses,” Cambridge University, Cambridge, England, 2003.
- [4] Johnston, R. L, “Atomic and molecular clusters,” Taylor & Francis, Londo, 2002.
- [5] Henry, C. R, “Surface studies of supported model catalysts,” *J. Surf. Sci. Rep.*, vol. 31, p. 235, 1998.
- [6] Lee, S.-T.; Apai, G.; Mason, M. G.; Benbow, R.; Hurych, Z, “Evolution of band structure in gold clusters as studied by photoemission,” *Phys. Rev B.*, vol. 23, p. 505, 1981.
- [7] Jennifer A. Nekuda Malik, “CSIR to launch titanium pilot plant,” Cambridge University Press, Cambridge, 2013.
- [8] Farrow, M. R.; Chow, Y.; Woodley, S. M, “Structure prediction of nanoclusters; a direct or a direct or a pre-screened search on the DFT energy landscapes?,” *Phys. Chem. Chem. Phys.*, vol. 16, pp. 21119-21134, 2014.

- [9] Noda, T, "Titanium from Slag in Japan," *J. Met.*, vol. 17, pp. 25-32, 1965.
- [10] Sakurai, M.; Watanabe, K.; Sumiyama, K.; Suzuki, K, "Magic numbers in transition metal (Fe, Ti, Nb, and Ta) clusters observed by Time-of-flight Mass Spectroscopy," *J. Chem. Phys.*, vol. 111, pp. 235-238, 1999.
- [11] Sun, H.; Ren, Y.; Wu, Z.; Xu, N. . , "s, "Density functional theory of the growth and bonding properties of titanium cluster," *J. Comp: TheoChem.*, vol. 1062, pp. 74-83, 2015.
- [12] Wei.; S. H.; Zeng, Z.; You, J. Q.; Yan, X. H.; Gong, X. G, "A Density-Functional Study of Small Titanium Clusters," *J. Chem. Phys.*, vol. 113, pp. 11127-1113, 2000.
- [13] Doverstål, M.; Karlsson, L.; Lindgren, B.; Sassenberg, U, "The $3\Delta_u-X3\Delta_g$ Band System of Jet-Cooled Ti_2 ," *Chem. Phys. Lett.*, vol. 270, p. 273-277, 1997.
- [14] Alonso, J. A, "Electronic and Atomic Structure, and Magnetism of Transition-Metal Clusters," *Chem. Rev.*, vol. 100, no. 2, pp. 637-678, 2000.
- [15] Fernando, A.; Weerawardene, K. L. D. M.; Karimova, N. V.; Aikens, C. M, "Quantum mechanical studies of large metal, metal oxide, and metal chalcogenide nanoparticles and clusters," *Chem. Rev.*, vol. 115, p. 6112-6216, 2015.
- [16] Woodley, S. M.; Catlow, R. ., "Crystal structure prediction from first principles," *Nat. Mater.*, vol. 7, p. 937-946, 2008.
- [17] Farrow, M. R.; Buckeridge, J.; Lazauskas, T.; Mora-Fonz, D.; Scanlon, D. O.; Catlow, C. R. A.; Woodley, S. M.; and Sokol, A. A, "Heterostructures of GaN with SiC and ZnO

- enhance carrier stability and separation in framework semiconductors,” *J. Phys. Status Solidi A*, vol. 214, p. 1600440, 2017.
- [18] Froes, F. H. S, “In Titanium Powder Metallurgy, ed. M. Qian and F. H. S. Froes,” *Elsevier, Boston*, p. 1–19, 2015.
- [19] Froes, F. H. S, “Titanium Powder Metallurgy,” *Elsevier*, p. 95–99, 2015.
- [20] Van Vuuren, D. S, “In Titanium Powder Metallurgy, ed. Qian, Q and Froes, F. H. S,” *Elsevier, Boston.*, p. 69–93, 2015.
- [21] Grigoryan, V. G; Springborg, M, “Structure and energetics of Ni clusters with up to 150 atoms,” *Chem. Phys. Lett.*, vol. 375, p. 219–226, 2003.
- [22] Rata, I, Shvartsburg, A. A.; Horoi, M.; Frauenheim, T.; Siu, K. W. M.; Jackson, K. A, “Single-Parent Evolution Algorithm and the Optimization of Si Clusters,” *Phys. Rev. Lett.*, vol. 85, p. 546, 2000.
- [23] Zhang, W.; Lu, W. -C.; Sun, J.; Wang, C. Z.; Ho, K. M, “Structures of Al_n (n = 27, 28, 29 and 30) clusters with double-tetrahedron structures.,” *Phys. Lett.*, vol. 455, p. 232, 2008.
- [24] Desai, S. R.; Wu, H.; Wang, L. S, “Evolution of the electronic structure of small vanadium clusters from molecular to bulklike,” *Phys. Rev. Lett.*, p. 2436–2439, 1996.
- [25] Gronbeck, H.; Rosen, A, “Geometric and electronic properties of small vanadium clusters: A density functional study,” *J. Chem. Phys.*, vol. 107, p. 10620–10625., 1997.

- [26] Estiu, G. L.; Zener, M. C., "Interplay between geometric and electronic structure and the magnetism of small Pd clusters," *J. Phys. Chem.*, vol. 98, p. 4793, 1994.
- [27] Lian, C.-X. Su and P. B. Armentrout, "Collision-induced dissociation of Ti+n (n=2–22) with Xe: Bond energies, geometric structures, and dissociation pathways," *J. Chem. Phys.*, vol. 97, p. 4084–4093, 1992.
- [28] Liu, H. B.; Ascencio, J. A.; Perez-Alvarez, M, Jose-Yacaman, "Melting behaviour of nanometer sized gold isomers," *J. Surf. Sci.*, vol. 491, p. 88, 2001.
- [29] Du, J, "Structures of the Small Tin Clusters: A DFT Study.," *J. Mol. Struct. TheoChem.*, vol. 817, pp. 47-53, 2007.
- [30] Doverstål, M.; Lindgren, B.; Sassenberg, U.; Arrington, C. A.; Morse, M. D, "The $3\Pi0_u \leftarrow X3\Delta1_g$ Band System of Jet-Cooled Ti₂," *J. Chem. Phys.*, vol. 97, p. 7087–7092, 1992.
- [31] Zhao, J.; Qiu, Q.; Wang, B.; J.; Wang, G, "Geometric and Electronic Properties of Titanium Clusters Studied by Ultrasoft Pseudopotential," *Solid State Commun.*, vol. 118, pp. 157-161, 2001.
- [32] Rodríguez-Kessler, P. L.; Rodríguez-Domínguez, A. R, "Structures and Electronic Properties of TinV Clusters: First-Principles Calculations," *J. Phys. Chem.*, vol. 120, pp. 2401-2407, 2016.
- [33] Sun, H.; Ren, Y.; Wu, Z.; Xu, N. ., "Density Functional Theory of the Growth and Bonding Properties of Titanium Clusters," *J. Comp: TheoChem.*, vol. 1062, pp. 74-83, 2015.

- [34] Woodley, S. M, “Knowledge Led Master Code search for atomic and electronic structures of LaF₃ nanoclusters on hybrid rigid ion-shed model-DFT landscape,” *J. Phys. Chem.*, vol. 117, pp. 24003-24014, 2013.
- [35] Smith, S.; Todorov, I. T, The DL-Poly4 User Manual version 4.07, Daresbury, Warrington, U.K, 2015.
- [36] Hünenberger, P. H, “Thermostat Algorithms for Molecular Dynamics Simulations,” *Adv. Polymer.Sci.*, vol. 173, pp. 105-149, 2005.
- [37] Andersen, H. C, “Molecular Dynamics Simulations at Constant Pressure and/or Temperature,” *J. Chem. Phys.*, vol. 72, p. 2384, 1980.
- [38] Berendsen, H. J. C.; Postma, J. P. M.; van Gunsteren, W. F.; Dinola, A.; Haak, J. R, “Molecular Dynamics with Coupling to an External Bath,” *J. Chem. Phys.*, vol. 81, p. 3684–3690., 1984.
- [39] Hohenberg, P.; Kohn, W, “Inhomogeneous Electron Gas,” *Phys. Rev B.*, vol. 136, p. B864–B871, 1964.
- [40] Kohn, W.; Sham, L. J, “Self-consistent equations including exchange and correlation effects,” *Phys. Rev A.*, vol. 140, p. A1133, 1965.
- [41] Haynes, W. M, CRC Handbook of Chemistry and Physics, 95th Edition, Boca Raton, FL: CRC Press/Taylor and Francis, 2014.

- [42] J. Hafner, "Ab-initio simulations of materials using VASP: Density functional theory and beyond.," *J. Comput. Chem.*, vol. 29, pp. 2044-2078, 2008.
- [43] Schmidt, M.; Kusche, R.; Kronmuller, W.; Von Issendorff, B.; Haberland, H, "Experimental Determination of the Melting Point and Heat Capacity for a Free Cluster of 139 Sodium Atoms," *Phys. Rev. Lett.*, vol. 79, p. 99, 1997.
- [44] Ercolessi, F.; Andreoni, W.; Tosatti, E, "Melting of Small Gold Particles: Mechanism and Size Effects," *Phys. Rev. Lett.*, vol. 66, p. 911, 1991.
- [45] Lai, S. L.; Guo, J. Y.; Petrova, V.; Ramanath., G, Allen, L. H, "Size-Dependent Melting Properties of Small Tin Particles: Nanocalorimetric Measurements," *Phys. Rev. Lett.*, vol. 77, p. 99, 1996.
- [46] Peters, K. P.; Cohen, J. B.; Chung, Y. –W. Melting of Pb nanocrystals .*J. Phys. Rev. B* 57, 13430, 1998., "Peters, K. P.; Cohen, J. B.; Chung, Y. –W. Melting of Pb nanocrystals," *Phys. Rev B.*, vol. B 57, p. 13430, 1998.
- [47] Couchman, R. R, "The Lindemann hypothesis and the size dependence of melting temperatures," *Philos. Mag.*, vol. A40, p. 637, 1979.
- [48] Borel, J. P, "Thermodynamical size effect and the structure of metallic clusters," *J. Surf. Sci.*, vol. 106, p. 1, 1981.
- [49] Longo, R. C.; Rey, C.; Gallego, L. J, "Molecular dynamics study of the melting behaviour of seven-atom clusters of fcc transition and noble metals on the (111) surface of the same metal using the embedded atom model," *J. Surf. Sci.*, vol. 459, p. L441, 2000.

- [50] Li, T. X.; Ji, Y. L.; Yu, S. W.; Wang, G.H, “Melting properties of noble metal clusters,” *J. Solid State Commun.*, vol. 116, p. 547, 2000.
- [51] Yasushi S.; Kensuke S. I.; Shin-ichi S, “Spontaneous alloying in binary metal microclusters: A molecular dynamics study,” *Phys. Rev B.*, vol. B 64, p. 075412, 2001.
- [52] Huang, S. P.; Balbuena, P. B, “Melting of Bimetallic Cu–Ni Nanoclusters.,” *J. Phys. Chem.*, vol. B106, p. 7225, 2002.
- [53] Pawar, R.R.; Deshpande, V.T, “The anisotropy of the thermal expansion of alpha-titanium,” *Acta Crystallogr A.*, vol. 24, pp. 316-317, 1968.
- [54] Burgers, W.G.; Jacobs, F.M, “Crystal Structure of β -Titanium,” *Z. Kristallog.*, vol. 94, pp. 299-300, 1936.
- [55] Leyens, C.; Peters, M, Titanium and Titanium alloys, 4, Cologne, 2014.
- [56] ANDREW, D, “Fabrication of micro-scale features on titanium alloys through micromilling,” *Mres.*, p. 20, 2017.
- [57] Estiu, G. L.; Zerner, M. C, “Interplay between Geometric and Electronic Structure and the Magnetism of Small Pd Clusters,” *J. Phys. Chem.*, vol. 98, pp. 4793-4799, 1994.
- [58] Du, J.; Sun, X.; Chen, J.; Jiang, G., “The Changes in the Geometrical, Electronic and Magnetic Properties of Titanium Clusters as one Titanium atom is Substituted by Boron,” *J. Phys. B: At. Mol. Opt. Phys.*, vol. 43, p. 205103, 2010.

- [59] Chibisov, A.N, "Oxygen Adsorption on Small Ti Clusters: A first-Principles Study," *Comput. Mater. Sci.*, vol. 82, pp. 131-133, 2014.
- [60] Chibisov, A.N, "Ab Initio Calculations of Elastic Properties of Titanium Nanoclusters," *Nanotechnology in Russia.*, vol. 9, pp. 189-193, 2014.
- [61] Wu, H.; Desai, S. R.; Wang, S. L., "Electronic structures of small titanium clusters: emergence and evolution of the 3d band," *Phys. Rev. Lett.*, vol. 76, p. 2, 1996.
- [62] Salazar-Villanueva, M. S.; Tejada, P. H. H.; Pal, U.; Rivas-Silva, J. F.; Mora, J. I. R.; Ascencio, J. A, "Stable Titanium Clusters and Their Geometries: DFT Calculations," *J. Phys. Chem.*, vol. 110, pp. 10274-10278, 2006.
- [63] Kant, A.; Lin, S, "Dissociation energy of Ti₂ and V₂," *J. Chem. Phys*, vol. 51, pp. 1644-1647, 1969.
- [64] Haslett, T. L.; Moskovits, M.; Weitzman, A. L, "Dissociation Energies of Transition Metal Diatomics," *J. Mol. Spectrosc.*, vol. 135, p. 259, 1989.
- [65] Russon, L. M.; Heidecke, S. A.; Birke, M. K.; Conceicao, J.; Morse, M. D.; Armentrout, P. B, " Photodissociation Measurements of Bond Dissociation Energies: Ti⁺², V⁺², Co⁺², and Co⁺³," *J. Chem. Phys*, vol. 100, pp. 4747-4755, 1994.
- [66] Liu, S.R.; Zhai, H.J.; Castro, M.; Wang, L.S., "Photoelectronic Spectroscopy of Ti_n⁺-Clusters," *J. Chem. Phys.*, vol. 118, pp. 2108-2115, 2003.

- [67] Venkataramanan, N. S.; Sahara, R.; Mizuseki, H.; Kawazoe, Y., "Titanium-Doped Nickel Clusters TiN_n . Geometry, Electronic, Magnetic, and Hydrogen Adsorption Properties," *J. Phys. Chem.*, vol. 114, p. 5049–5057, 2010.
- [68] Tzeli, D.; Mavridis, A, "Electronic Structure and Bonding of the 3d Transition Metal Borides, MB , $M = Sc, Ti, V, Cr, Mn, Fe, Co, Ni,$ and Cu through all Electron Ab initio Calculations," *J. Chem. Phys.*, vol. 128, p. 034309, 2008.
- [69] Wang, S. -Y.; Duan, W.; Zhao, D. -L.; Wang, C. -Y, "First-principles study of the stability of the icosahedral Ti_{13} , Ti^{-13} , and Ti^{+13} clusters," *Phys. Rev B.*, vol. 65, p. 165424, 2002.
- [70] Wang. S. -Y.; Yu, J. Z.; Misuzeki, H.; Yan, J. -A.; Kawazoe, Y.; Wang, C. -Y, "First-principles study of the electronic structures of icosahedral $TiN(N=13,19,43,55)$ clusters," *J. Chem. Phys.*, vol. 120, p. 8463, 2004.
- [71] Lee, B.; Lee, G. W, "Comparative study of Ti and Ni clusters from first principles," *J. Chem. Phys.*, vol. 127, p. 164316, 2007.
- [72] Medina, J.; deCoss, R.; Tapia, A.; Canto, G, "Structural, energetic and magnetic properties of small Tin ($n = 2-13$) clusters: a density functional study," *J. Eur. Phys.*, vol. 76, p. 427, 2010.
- [73] Wang, H.; Hu, N.; Tao, D. -J.; Lu, Z. -H.; Nie, J.; Chen, X. -S, "The geometric, electronic, and magnetic properties of phosphorous - doped Ti clusters, Ti_nP ($n = 1-12$)," *J. Comput. Theor. Chem.*, vol. 50, p. 977, 2011.

- [74] Reddy, B. V.; Khanna, S. N, "Giant Magnetic Moments in 4d Clusters," *Phys. Rev. Lett.*, vol. 70, p. 3323, 1993.
- [75] Nava, P.; Sierka, M.; Ahlrichs, R, "Density functional study of palladium clusters," *Phys. Chem. Chem. Phys.*, vol. 5, pp. 3372-3381, 2003.
- [76] Kumar, V.; Kawazoe, Y, "Icosahedral growth, magnetic behavior, and adsorbate-induced metal-nonmetal transition in palladium clusters," *Phys. Rev B.*, vol. 66, p. 144413, 2002.
- [77] Chang, Y. -C.; Wang, C. Z.; Ho, K. H, "Structure of neutral aluminum clusters Al_n $2 \leq n \leq 23$: Genetic algorithm tight-binding calculations," *Phys. Rev B.*, vol. 73, p. 125431, 2006.
- [78] Montiel, E.; Cruz, J.; Gonzales, J.Z.; Jayanthi, N.; Pandiyan, T, "Fen Clusters (n = 2-7) Interaction with Furan Ring: DFT Studies over Iron Surface Suitability for Furan Adsorption," *J. clust. Sci.*, vol. 22, pp. 459-471, 2011.
- [79] Dunlap, B. I. Z, "Symmetry and Ferromagnetic Clusters," *J. Phys. D: At., Mol. Clusters.*, vol. 19, p. 255, 1991.
- [80] Diequez, O.; Alemany, M. M. G.; Rey, C.; Ordejon, P.; Gallego, L, "Density-functional calculations of the structures, binding energies, and magnetic moments of Fe clusters with 2 to 17 atoms.," *Phys. Rev.*, vol. 63, p. 205407, 2001.
- [81] Duan, H. M.; Zheng, Q. Q, "Symmetry and magnetic properties of transition metal clusters," *Phys. Lett.*, vol. 280, p. 333, 2001.

- [82] Kumar, V.; Kawazoe, Y, "Evolution of the atomic and electronic structure of Pt clusters: Planar, layered, pyranidal, cage, cubic, and octahedral growth," *Phys. Rev B.*, vol. 77, p. 205418, 2008.
- [83] Xu, W, -X.; Schierbaum, K. D.; Goepel, W, "Ab initio study of electronic structures of Ptn clusters (n = 2–12)," *J. Int. Quantum Chem.*, vol. 62, p. 427, 1997.
- [84] Watari, N.; Ohnishi, S, "Electronic structure of H adsorbed on Pt13 clusters," *J. Chem. Phys.*, vol. 106, p. 7531, 1997.
- [85] Sun, Y.; Zhang, M.; Fournier, R, "Periodic trends in the geometric structures of 13-atom metal clusters," *Phys. Rev B.*, vol. 77, p. 075435, 2008.
- [86] Watari, N.; Ohnishi, S, "Atomic and electronic structures of Pd13 and Pt13 clusters," *Phys. Rev.*, vol. 58, p. 1665, 1998.
- [87] Bachels, T.; Schafer, R, "Binding energies of neutral silicon clusters," *Chem. Phys. Lett.*, vol. 324, p. 365, 2000.
- [88] Raghavachari, K.; Logovinsky, V, "Structure and bonding in small silicon clusters," *Phys. Rev. Lett.*, vol. 55, p. 2853, 1985.
- [89] Raghavachari, K.; McMichael-Rohlfing, C, "Bonding and stabilities of small silicon clusters: A theoretical study of Si7–Si10," *Chem. Phys.*, vol. 89, p. 2219, 1988.
- [90] Yu, D. K.; Zhang, R. Q.; Lee, S. T, "Structural transition in nanosized silicon clusters," *Phys. Rev B.*, vol. B 65, p. 245417, 2002.

- [91] Mitas, L. J. C. Gressman.; Stich, I.; Tobik, J., "Silicon Clusters of Intermediate Size: Energetics, Dynamics, and Thermal Effects," *Phys. Rev. Lett.*, vol. 84, p. 1479, 2000.
- [92] Kaxiras, E.; Jackson, K, "Shape of small silicon clusters," *Phys. Rev. Lett.*, vol. 71, p. 727, 1993.
- [93] Kaxiras, E.; Jackson, K, "Structural Models for Intermediate-Sized Si Clusters," *Z. Phys. D: At., Mol. Clusters.*, vol. 26, p. 346, 1993.
- [94] Hudgins, R .R.; Imai, M.; Jarrold, M. F.; Dugourd, P, "High-resolution ion mobility measurements for silicon cluster anions and cations," *J. Chem. Phys.*, vol. 111, p. 7865, 1999.
- [95] Ehbrecht, M.; Huisken, F, "Gas-phase characterization of silicon nanoclusters produced by laser pyrolysis of silane," *Phys. Rev B.*, vol. B 59, p. 2975, 1999.
- [96] Ho, K. M.; Shvartsburg, A. A.; Pan, B. G.; Lu, Z. Y.; Wang, C. Z.; Wacker, J. G .; Fye, J. L .; Jarrold, M. F, "Structures of medium-sized silicon clusters," *Nature London.*, vol. 392, p. 582, 1998.
- [97] Bonacic-koutecky, V.; Fantucci, P.; Fuchs, C.; Gatti, C.; Pittner, J.; Polezzo, S, "Ab initio predictions of optically allowed transitions in Na₂₀. Nature of excitations and influence of geometry," *Chem. Phys. Lett.*, vol. 213, p. 522, 1993.
- [98] Bonacic-koutecky, V.; Cespiva, L.; Fantucci, P.; Koutecky, J, "Effective core potential-configuration interaction study of electronic structure and geometry of small anionic Ag_n

- clusters: Predictions and interpretation of photodetachment spectra,” *J. Chem. Phys.*, vol. 100, p. 490, 1994.
- [99] Gantefor, G.; Gauss, M.; Meiwes-Broer, K. H.; Lutz, H, “Photoelectron spectroscopy of silver and palladium cluster anions. Electron delocalization versus, localization,” *J. Chem. Soc., Faraday Trans.*, vol. 86, p. 2483, 1990.
- [100] Jackschath, C.; Rabin, I.; Schulze, W, “Electron impact ionization of silver clusters Ag_n , $n \leq 36$,” *Z. Phys. D: At., Mol. Clusters.*, vol. 22, p. 517, 1992.
- [101] Matulis, V. E.; Ivashkevich, O. A.; Gurin, V. S, “DFT study of electronic structure and geometry of neutral and anionic silver clusters,” *J. Mol. Struct.: THEOCHEM*, Vols. 664-665, p. 291, 2003.
- [102] Santamaria, R.; Kaplan, I. G.; Novaro, O, A, “A comparative theoretical study of stable geometries and energetic properties of small silver clusters,” *Chem. Phys. Lett.*, vol. 218, p. 395, 1994.
- [103] Fournier, R, “Theoretical study of the structure of silver clusters,” *J. Chem. Phys.*, vol. 115, p. 2165, 2001.
- [104] Oviedo, J.; Palmer, R. E, “Amorphous structures of Cu, Ag, and Au nanoclusters from first principles calculations,” *J. Chem. Phys.*, vol. 117, p. 9548, 2002.
- [105] Jennison, D. R., Schultz, P. A., Sears, M. P, “Ab initio calculations of Ru, Pd, and Ag cluster structure with 55, 135, and 140 atoms,” *J. Chem. Phys.*, vol. 106, p. 1856, 1997.

- [106] Doye, J. P.; Wales, D. J., "Global minima for transition metal clusters described by Sutton–Chen potentials," *New J. Chem.*, vol. 22, p. 733, 1998.
- [107] Erkoç, S.; Yılmaz, T., "Molecular-dynamics simulations of silver clusters," *Physica E (Amsterdam)*, vol. 5, p. 1, 1999.
- [108] Sutton, A. P.; Chen, J., "Long-range finnis–sinclair potentials," *Philos. Mag. Lett.*, vol. 61, p. 139, 1990.
- [109] Mottet, C.; Treglia, G.; Legrand, B., "New magic numbers in metallic clusters: an unexpected metal dependence," *Surf. Sci.*, vol. 383, p. 719, 1997.
- [110] Reuse, F. A.; Khanna, S. N., "Geometry, electronic structure, and magnetism of small Ni_n (n= 2–6, 8, 13) clusters," *Chem. Phys. Lett.*, vol. 234, p. 77, 1995.
- [111] Reuse, F. A.; Khanna, S. N.; Bernel, S., "Electronic structure and magnetic behavior of Ni₁₃ Clusters," *Phys. Rev B.*, vol. B52, p. 11650, 1995.
- [112] Nygren, M. A.; Siegbahn, P. E. M.; Wahlgren, U.; Akeby, H., "Theoretical ionization energies and geometries for nickel (Ni_n 4. Itoreq. n. Itoreq. 9)," *J. Phys. Chem.*, vol. 96, p. 3633, 1992.
- [113] Parks, E. K.; Zhu, L.; Ho, J.; Riley, S. J., "The structure of small nickel clusters. I. Ni₃–Ni₁₅," *J. Chem. Phys.*, vol. 100, p. 7206, 1994.
- [114] Nayak, S. K.; Reddy, B.; Rao B. K.; Khanna, S. N.; Jena, P., "Structure and properties of Ni₇ cluster isomers," *Chem. Phys. Lett.*, vol. 253, p. 390, 1996.

- [115] Finnis, M. W.; Sinclair, J. E., "A Simple Empirical N-body Potential for Transition Metals," *Philos. Mag. A.*, vol. 50, pp. 45-55, 1984.
- [116] Parks, E. K., Kerns, K. P., Riley, S. J., "The structure of Ni₃₉, 1998 109, 10207," *J. Chem. Phys.*, vol. 109, p. 10207, 1998.
- [117] Parks, E. K.; Kerns, K. P.; Nieman, G. C.; Riley, S. J., "The thermodynamics of nitrogen adsorption on nickel clusters: Ni₁₉–Ni₇₁," *J. Chem. Phys.*, vol. 107, p. 1861, 1997.
- [118] Lathiotakis, N. N.; Andriotis, A. N.; Menon, M.; Connolly, J., "Tight binding molecular dynamics study of Ni clusters," *J. Chem. Phys.*, vol. 104, p. 992, 1992.
- [119] Andriotis, A. N.; Menon, M., "Degradation of inter-atomic bonds during structural phase change in intermediate Ni-clusters (N₃₉ – N₄₉)," *J. Chem. Phys.*, vol. 120, p. 230, 2004.
- [120] Mottet, C.; Goniakowski, J.; Baletto, F.; Ferrando, R.; Treglia, G., "Modeling free and supported metallic nanoclusters: structure and dynamics," *Phase Transitions.*, vol. 77, p. 101, 2004.
- [121] Jug, K.; Zimmermann, B.; Koster, A. M.; Calaminici, P., "Structure and stability of small copper clusters," *J. Chem. Phys.*, vol. 116, p. 4497, 2002.
- [122] Jug, K.; Zimmermann, B.; Köster, A. M., "Growth pattern and bonding of copper clusters," *Int. J. Quantum Chem.*, vol. 90, p. 594, 2002.
- [123] Fujima, N.; Yamaguchi, T., "Shell Structure of Electronic State of Icosahedral Al and Cu Clusters," *J. Phys. Soc.*, vol. Jpn 58, p. 1334, 1989.

- [124] Darby, S.; Mortimer-Jones, T. V.; Johnson, R. L.; Robbets, C, “Theoretical study of Cu–Au nanoalloy clusters using a genetic algorithm,” *J. Chem. Phys.*, vol. 116, p. 1536, 2002.
- [125] Gupta, R. P, “Lattice Relaxation At a Metal Surface,” *Phys. Rev. B: Condens. Matter Mater. Phys.*, vol. 23, p. 6265–6270, 1981.
- [126] Reinhard, D.; Hall, B. D.; Berthoud, P.; Valkealahti, S.; Monot, R, “Unsupported nanometer-sized copper clusters studied by electron diffraction and molecular dynamics,” *Phys. Rev B.*, vol. B58, p. 4917, 1998.
- [127] Akbarzadeh, H.; Yaghoubi, H.; Shamkhali, A. M.; Taherkhani, F, “Effects of Gas Adsorption on the Graphite-Supported Ag Nanoclusters: A Molecular Dynamics Study,” *J. Phys. Chem.*, vol. 117, p. 26287–26294, 2013.
- [128] Akbarzadeh, H.; Parsafar, G. A, “A molecular-dynamics study of thermal and physical properties of platinum nanoclusters,” *Fluid phase equilibria.*, vol. 280, pp. 16-21, 2009.
- [129] Büyükata, M.; Belchior, J. C, “Molecular Dynamics Study of Palladium Clusters: Size Dependent Analysis of structural Stabilities and Energetics of Pd_n (n ≤ 40) via a Lennard-Jones Type Potential,” *Croat. Chem.*, vol. Acta 81, pp. 289-297, 2008.
- [130] Smith, S.; Forester, T. R, *The DL-Poly2 User Manual version 2.20*, Daresbury, Warrington, U.K, 2001.
- [131] Frenkel, D.; Smit, B, “Understanding molecular simulations,” Academic Press, San Diego, 1996.

- [132] Allen, M. P.; Tildesley, D. J, "Computer simulation of liquids," Oxford University Press, Oxford, 1990.
- [133] Gubbins, K. E.; Quirke, N, "Molecular simulation and industrial applications," Amsterdam: Gordon and Breach, Amsterdam , 1996.
- [134] Frenkel, D.; Smit, B, "Understanding molecular simulation: From Algorithm to Applications," London: Academic Press, London, 1996.
- [135] Shvartsburg, A. A.; Jarrold, M. F, "Solid clusters above the bulk melting," *Phys. Rev. Lett.*, vol. 85, p. 2530, 2000.
- [136] Joshi, K.; Kanhere, D. G.; Blundell, S. A, "Abnormally high melting temperature of Sn₁₀ cluster," *Phys. Rev B.*, vol. B 66, p. 155329, 2002.
- [137] Joshi, K.; Kanhere, D. G.; Blundell, S. A, "Thermodynamics of tin clusters," *Phys. Rev B.*, vol. B 67, p. 235413, 2003.
- [138] Chuang, F. -C.; Wang, S.; Ogut, S.; Chelikowsky, J. R.; Ho, K. M, "Melting of small Sn clusters by ab initio molecular dynamics simulation," *Phys. Rev B.*, vol. B 69, p. 165408, 2004.
- [139] Liu, H. B.; Perez, R.; Canizal, G.; Ascencio, J. A, "Stability and phase transition of sodium nanoclusters," *Surf. Sci.*, vol. 14, p. 518, 2002.
- [140] Calvo, F.; Spiegelman, F, "Mechanism of phase transitions in sodium clusters: From molecular to bulk behavior," *J. Chem. Phys.*, vol. 112, p. 2888, 2000.

- [141] Westergren J.; Nordholm, S, “Melting of paladium clusters-density of states determination by Monte Carlo simulation,” *J. Chem. Phys.*, vol. 290, p. 196, 2003.
- [142] Clevaland, C. L.; Luedtke, W. D.; Landman, U, “Melting of gold clusters,” *Phys. Rev B.*, vol. B 60, p. 5065, 1999.
- [143] Lee, Y. J.; Nieminen, R. M.; Lee, E. -K.; Kim, S, “Universal melting behaviour of clusters,” *Comput. Phys. Commun.*, vol. 142, p. 201, 2001.
- [144] Li, T. X.; Lee, S. M.; Han, S. J.; Wang, G. H, “Structural transitions of Au₅₅ isomers,” *Phys. Lett.*, vol. A 300, p. 86, 2002.
- [145] Lou, J.; Landman, U.; Jortner, J, *Physics and Chemical of small clusters*, edited by Jena, P.; Rao, B. K.; Khanna, S. N, New York: Plenum, New York, 1987.
- [146] Wang, J. L.; Wang, G. H.; Ding, F.; Lee, H.; Shen, W. F, Zhao, J. J, “Structural transition of Si clusters and their thermodynamics,” *Chem. Phys. Lett.*, vol. 341, p. 529, 2001.
- [147] Koga, K.; Ikeshoji, T.; Sugawara, K, “Size -and temperature dependent structural transition in gold nanoparticles,” *Phys. Rev. Lett.*, vol. 92, p. 115507, 2004.
- [148] Blum, V.; Gehrke, R.; Hanke, F.; Havu, P.; Havu, V.; Ren, X. G.; Reuter, K.; and Scheffler, M, “Ab initio molecular simulations with numeric atom-centered orbitals,” *Comput. Phys. Commun.*, vol. 180, p. 2175–2196, 2009.

- [149] Milman, V.; Winkler, B.; White, J. A.; Pickard, C. J.; Payne, M. C.; Akhmatkaya, E. V.; Nobes, R. H, "Electronic structure of materials," *Int. J. Quantum Chem.*, vol. 77, pp. 799-926, 2000.
- [150] Segall, M. D.; Lindan, P. L. D.; Probert, Pickard, C. J.; Hasnip, P. J.; Clark, S. J.; Payne, M. C, "First-principles simulation: ideas, illustrations and the CASTEP code," *Phys. Cond. Matt.*, vol. 14, pp. 2717-2744, 2002.
- [151] Delley, B, "An all-electron numerical method for solving the local density functional for polyatomic molecules," *J. chem. phys.*, vol. 92, pp. 508-517, 1999.
- [152] Delley, B, "From molecules to solids with the DMol3 approach," *J. chem. phys.*, vol. 113, pp. 7756-7764, 2000.
- [153] Dirac P. A. M, "Quantum mechanics of many-electron systems," *Proc. R. Soc. Lond. Ser. A.*, vol. 123, p. 714, 1929.
- [154] Mattsson A. E, "In pursuit of the 'Divine' functional," *Science.*, vol. 298, p. 759, 2002.
- [155] Martin, R. M, "Electronic structure: basic theory and practical methods," Cambridge university press, Cambridge, 2004.
- [156] Koch, W.; Holthausen, M. C, "A chemist's guide to density functional theory.," John Wiley & Sons,, New Jersey , 2015.
- [157] Sholl, D.; Steckel, J. A, "Density functional theory: a practical introduction," John Wiley & Sons, New Jersey, 2011.

- [158] Slater, J. C., "A simplification of the Hartree-Fock method," *Phys. Rev.*, vol. 81, p. 385, 1951.
- [159] Thomas, L.H., "The calculation of atomic fields," *J. Proc. Camb. Phil. Soc.*, vol. 23, pp. 542-548, 1926.
- [160] Fermi, E., "Statistical method to determine some properties of atoms," *Rend. Lincei.*, vol. 6, pp. 602-607, 1927.
- [161] Vosko, S. H.; Wilk, L.; Nusair, M., "Accurate spin-dependent electron liquid correlation energies for local spin density calculations: a critical analysis," *Can. J. Phys.*, vol. 58, pp. 80-159, 1980.
- [162] Ceperley, D. M.; Alder, B. J., "Ground state of the electron gas by a stochastic method," *Phys. Rev. Lett.*, vol. 45, p. 566, 1980.
- [163] Perdew, P.; Wang, Y., "Accurate and simple analytic representation of the electron-gas correlation energy," *Phys. Rev B.*, vol. 45, p. 13244, 1992.
- [164] Perdew, J. P.; Burke, K.; Ernzerhof, M., "Generalised gradient approximation made simple," *Phys. Rev. Lett.*, vol. 77, pp. 3865-3868, 1996.
- [165] Perdew, J. P.; Chevary, J. A.; SVosko, S. H.; Jackson, K. A.; Pederson, M. R.; Singh, D. J.; Fiolhais, C., "Atoms, molecules, solids, and surfaces: Applications of the generalized gradient approximation for exchange and correlation," *Phys. Rev B.*, vol. 46, p. 6671, 1992.

- [166] Becke, A. D, "Density-functional thermochemistry. I. The effect of the exchange-only gradient correction," *J. Chem. Phys.*, vol. 96, p. 2155, 1992.
- [167] Hammer B.; Scheffler, M, "Local chemical reactivity of a metal alloy surface," *Phys. Rev. Lett.*, vol. 74, p. 3487, 1995.
- [168] Proynov, E. I.; Ruiz, E.; Vela, A.; D. R. Salahub, D. R, "Determining and extending the domain of exchange and correlation functionals," *Int. J. Quantum Chem.* , vol. 29, p. 61, 1995.
- [169] Ozolins, V.; Körling, M, "Full-potential calculations using the generalized gradient approximation: Structural properties of transition metals," *Phys. Rev B.*, vol. 48, p. 18304, 1993.
- [170] Filippi, C.; Singh, D. J.; Umrigar, C, "All-electron local-density and generalized-gradient calculations of the structural properties of semiconductors," *Phys. Rev B.* , vol. 50, p. 14 947 , 1994.
- [171] Perdew, J. P.; Ruzsinszky, A.; Csonka, G. I.; Vydrov, O. A.; Scuseria, G. E.; Constantin, L. A.; Zhou, X.; Burke, K, "Restoring the density-gradient expansion for exchange in solids and surfaces," *Phys. Rev. Lett.*, vol. 100, p. 136406, 2008.
- [172] Hammer, B.; Hansen L. B.; Nørskov, J. K, "Improved adsorption energetics within density-functionaltheory using revised Perdew-Burke-Ernzerhof functionals," *Phys. Rev. B.*, vol. 59, p. 7413, 1999.

- [173] Gill, P.M. W.; Johnson, B. G.; Pople, J. A.; Frisch, M. J, “The performance of the Becke-Lee-Yang-Parr (B-LYP) density functional theory with various ba-sis sets,” *Chem. Phys. Lett.*, vol. 197, p. 499, 1992.
- [174] Armiento, R.; Mattsson, A. E, “Functional designed to include surface effects in self-consistent density functional theory,” *Phys. Rev B.*, vol. 72, p. 085108, 2005.
- [175] Engel, E.; Vosko, S. H, “Exact exchange-only potentials and the virial relation as microscopic criteria for generalized gradient approximations,” *Phys. Rev B.*, vol. 47, p. 13164, 1993.
- [176] Mattson, A. E.; Schultz, P. A.; Desjarlais, M. P.; Mattsson, T. R.; Leung, K , “Designing meaningful density functional theory calculations in materials science,” *J. Mod. and Simul. Mater. Sci. and Eng*, vol. 13, pp. 1-32, 2005.
- [177] Tao, J.; Perdew, J. P.; Staroverov, V. N.; Scuseria, G. E , “Climbing the density functional ladder: nonempirical meta-generalized gradient approximation designed for molecules and solids,” *Phys. Rev. Lett.*, vol. 91, p. 146401, 2003.
- [178] Combes, J. M.; Duclos, P.; Seiler, R. (1981), “The Born-Oppenheimer Approximation,” in *In: Velo, G.; Wightman, A.S. (eds) Rigorous Atomic and Molecular Physics. NATO Advanced Study Institutes Series.*, Boston, Springer, 1981.
- [179] Payne, M. C.; Teter, M. P.; Allan, D. C.; Arias, T. A.; Joannopoulos, J.D, “Iterative Minimization Techniques for ab initio Total-Energy Calculations: Molecular Dynamic and Conjugate Gradients,” *Rev. Mod. Phys.*, vol. 64, pp. 1045-1097, 1992.

- [180] Blöch, P, “Projector augmented-wave method,” *Phys. Rev. B.*, vol. 50, p. 17953–17979, 1994.
- [181] Ashcroft, N. W.; Mermin, N.D, “On Introductory Concepts,” Saunders College Publishing, Philadelphia, 1976.
- [182] Blakemore, J. S , Solid State Physics, Cambridge: Cambridge University Press, 1985.
- [183] Hans, H. A, “New Approximation Method in the Problem of Many Electrons,” *J. Chem. Phys.*, vol. 3, p. 61, 1935.
- [184] Martin R. M, “Norm-conserving pseudopotentials,” in *Electronic structure: Basic theory and practical methods*, New York, Cambridge University Press, 2004, pp. 212-213.
- [185] Kresse, G.; Joubert, D, “From ultrasoft pseudopotentials to the projector augmented-wave method,” *Phys. Rev B.*, vol. 59, pp. 1758-1775, 1999.
- [186] Kresse, G.; Joubert, D, “From ultrasoft pseudopotentials to the projector augmented-wave method,” *Phys. Rev B.*, vol. 59, pp. 1758-1775, 1999.
- [187] Rapaport, D. C, The art of molecular dynamics simulation, New York: Cambridge University Press, 2009.
- [188] Birdsall, C. K.; Langdon, A. B, Plasma physics via computer simulation, New York: McGraw, 1985.
- [189] Hockney, R. W.; Eastwood, J. W, Computer simulation using particles, New York: McGraw, 1981.

- [190] Abramowitz, M.; Stegun, I, Handbook of mathematical functions, New York: Dover, 1970.
- [191] Spreiter, Q.; Walter, M, “Classical molecular dynamics simulation with the Velocity Verlet algorithm at strong external magnetic fields,” *J. Comput.*, vol. 152, p. 102–119, 1999.
- [192] Alder, B. J.; Wainwright, T. E, “Phase Transition for a hard sphere system,” *J. Chem. Phys.*, vol. 27, pp. 1208-1209, 1957.
- [193] Nose, S, “A molecular dynamics method for simulations in the canonical ensemble,” *Mol. Phys.*, vol. 52, pp. 255-268, 1984.
- [194] Nosé, S, “Constant temperature molecular dynamics methods,” *Prog. Theor. Phys.*, vol. 103, pp. 1-46, 1991.
- [195] R. Clausius , “X. On a modified form of the second fundamental theorem in the mechanical theory of heat,” *Phil. Mag.*, vol. 12, pp. 1-102, 1856.
- [196] Ju Li, “Basic molecular dynamics,” in *Handbook of materials modeling* , Springer, 2005, pp. 565-588.
- [197] Erpenbek, J. J; Wood, W. W, “Molecular dynamics calculation of the hard-sphere equation of state,” *J. Stat. Phys.*, vol. 35, pp. 321-340, 1984.
- [198] Fraternali, F, “Restrained and unrestrained molecular dynamics simulations in the NVT ensemble of alamethicin,” *Biopolymers.*, vol. 30, pp. 1083-1099, 1990.
- [199] Gert, A.; Erhard, S.; Ion-Olimpiu, S, “Complex Langevin method: When can it be trusted?,” *Phys. Rev D.*, vol. 81, p. 054508, 2010.

- [200] Onsage, L, "Crystal statistics, A two dimensional model with an order-disorder transition," *Phys. Rev.*, vol. 65, pp. 3-4, 1994.
- [201] Metropolis, N.; Rosenbluth, A. W.; Rosenbluth, M. N.; Teller, A. H.; Teller, E , "Equation of state calculations by fast computing machines," *J. Chem. Phys.*, vol. 21, pp. 1087-1092, 1953.
- [202] Gabrielli, A.; Mastrandrea, R.; Caldarelli, G.; Cimini, G, "Grand canonical ensemble of weighted networks," *Phys. Rev E.* , vol. 99, p. 030301, 2019.
- [203] Allen, M. P.; Tildesley, D. J. , *Computational Simulation of Liquids*, Oxford, England: Oxford University Press, 1989.
- [204] Daw, M.S.; Foiles, S.M.; Baskes, M.I, "The embedded-atom method: a review of theory and applications," *J. Mat. Sci. Rep.*, vol. 9, p. 251, 1999.
- [205] Foiles, S.M.; Baskes, M.I.; Daw, M.S, "Embedded-atom-method functions for the fcc metals Cu, Ag, Au, Ni, Pd, Pt, and their alloys," *Phys. Rev.*, vol. B33, p. 7983, 1986.
- [206] Asta, M.; Morgan, D.; Hoyt, J. j; Sadigh, B.; Althoff, J. D.; de Fontaine, D.; Foiles, S. M, "Embedded-atom-method study of structural, thermodynamic, and atomic-transport properties of liquid Ni-Al alloys," *Phys. Rev B.*, vol. B59, p. 14271, 1999.
- [207] Hohenberg, C.; Martin, P. C, "Superfluid Hydrodynamics in the Hydrodynamic and Collisionless Domains," *Phys. Rev. Lett.*, vol. 12, p. 69, 1964.

- [208] Fabrizio, C.; Rosato, V, “Tight-Binding Potentials for transition metals and Alloys,” *Phys. Rev.*, vol. 48, pp. 25-26, 1993.
- [209] Buckingham, R. A, “The classical equation of state of gaseous helium, neon and argon,” *A. Series A, Mathematical and Physical Sciences.*, vol. 168, pp. 264-283, 1938.
- [210] Carlsson, A, “Beyond pair potentials in elemental transition metals and semiconductors,” *Solid State Phys.*, vol. 43, p. 1–91, 1990.
- [211] Ackland, G.; Wooding, S.; Bacon, D, “Defect, surface and displacement of α -zirconium simulated with a many-body potential,” *Philos. Mag.*, vol. A 71, p. 553–565, 1995.
- [212] Ackland, G. J, “Theoretical study of titanium surfaces and defects with a new many-body potential,” *Philos. Mag.*, vol. A 66, pp. 917-932, 1992.
- [213] Johnson, R, “Many-body effects on calculated defect properties in hcp metals,” *Philos. Mag.*, vol. A 63, pp. 865-872, 1991.
- [214] Cleri, F.; Rosato, V, “Tight-binding Potentials for Transition Metals and Alloys,” *Phys. Rev. B: Condens. Matter Mater. Phys.*, vol. 48, pp. 22-23, 1993.
- [215] Ercolessi, F.; Tosatti, E.; Parrinello, M, “Au (100) surface reconstruction,” *Phys. Rev. Lett.*, vol. 57, p. 719–722, 1986.
- [216] Tománek, D.; Aligia, A. A.; Balseiro, C. A, “Calculation of elastic strain and electronic effects on surface segregation,” *Phys. Rev B.*, vol. B 32, p. 5051–5056, 1985.

- [217] Guevara, J.; Llois, A. M.; Weissmann, M, “Model potential based on tight-binding total energy calculations for transition-metal systems,” *Phys. Rev B.*, vol. B 52, p. 11509–11516, 1995.
- [218] Gómez, L.; Dobry, A.; Diep, H. T, “Melting properties of fcc metals using a tight-binding potential,” *Phys. Rev B.*, vol. B 55, p. 6265–6271, 1997.
- [219] Alemany, M. M. G.; Diéguez, O.; Rey, C.; Gallego, L. J, “Molecular-dynamics study of the dynamic properties of fcc transition and simple metals in the liquid phase using the second-moment approximation to the tight binding method,” *Phys. Rev B.*, vol. B 60, pp. 9208-9211, 1999.
- [220] Gale, J. D.; Rohl, A. L, “The General Utility Lattice Program (GULP),” *Mol. Simul.*, vol. 29, p. 291–341, 2003.
- [221] Gale, J. D, “GULP: A computational program for the symmetry-adapted simulation of solids. Faraday Trans,” *J. Chem. Soc.*, vol. 93, pp. 629-637, 1997.
- [222] Woodley, S. M, “Knowledge Led Master Code,” <http://www.ucl.ac.uk/klmc/Software>, accessed 2012.
- [223] Holland J.H, “Genetic Algorithm,” *J. Sci. Amer.*, pp. 66-72, 1992.
- [224] Zheng-Jun P, “Evolutionary Algorithm,” Tsinghua University Press, Beijing, 1998.

- [225] Frangini, S , “Corrosion Behaviour of AISI 316L Stainless Steel and ODS FeAl Aluminide in Eutectic Li₂CO₃–K₂CO₃ Molten Carbonates under Flowing CO₂–O₂ Gas Mixture,” *J. Oxid. Met.*, vol. 53, pp. 139-156, 2000.
- [226] Leach, A. R , “principles and applications,” in *Molecular Modelling*, New Jersey, Prentice-Hall, 2001.
- [227] Yip, S.; Gilmer, G , “Basic Monte Carlo models: Equilibrium and kinetics,” in *Handbook of Materials Modeling*, New York, Springer , 2005, pp. 613-628.
- [228] Lazauskas, T.; Sokol, A. A.; Buckeridge, J.; Catlow, C. R. A.; Escher, S. G. E. T.; Farrow, M. R.; Mora-Fonz, D.; Blum, V. W.; Phaahla, T. M.; Chauke, H. R.; Ngoepe, P. E.; Woodley, S. M, “Thermodynamically accessible titanium clusters TiN, N = 2–32,” *Phys.Chem.Chem.Phys.*, vol. 20, pp. 13962 -13973, 2018.
- [229] Ernzerhof, M.; Scuseria, G. E, “Assessment of the Perdew–Burke–Ernzerhof exchange–correlation Functional,” *J. Chem. Phys.*, vol. 110, p. 5029–5036, 1999.
- [230] Allen, M. P.; Tildesley, D. J, “Computer Simulation of Liquids; Oxford University Press: Oxford, U.K., 1987th Coupling to an External Bath,” *J. Chem. Phys.*, vol. 81, p. 3684–3690, 1984.
- [231] Lazauskas, T.; Sokol, A. A .; Woodley, S. M, “An Efficient Genetic Algorithm For Structure Prediction At The Nanoscale. Nanoscale,” *Nanoscale.*, vol. 9, p. 3850–3864, 2017.

- [232] Escher, S. G.; Lazauskas, T.; Zwijnenburg, M. A.; Woodley, S. M, “Structure Prediction Of (BaO)_n Nanoclusters for $n \leq 24$ Using An Evolutionary Algorithm,” *Comput. Theor. Chem.*, vol. 1107, pp. 74-81, 2017.
- [233] Mora-Fonz, D.; Lazauskas, T.; Farrow, M. R.; Catlow, C. R. A.; S. M. Woodley, S. M and Sokol, A. A, “Why Are Polar Surfaces Of ZnO Stable?,” *Chem. Mater.*, vol. 29, p. 5306–5320, 2017.
- [234] Mora-Fonz, D.; Lazauskas, T.; Woodley, S. M.; Bromley, S. T.; Catlow, C. R. A.; Sokol, A. A, “Development Of Interatomic Potentials For Supported Nanoparticles: The Cu/ZnO Case,” *J. Phys. Chem.*, vol. 121, p. 16831–16844, 2017.
- [235] Li, R.; Odunlami, M.; Carbonnie`re, P, “Low-lying Ptn Cluster Structures (n= 6–10) From Global Optimizations Based On DFT Potential Energy Surfaces: Sensitivity Of The Chemical Ordering With The Functional,” *Comput. Theor. Chem.*, Vols. 1107,, p. 136–141., 2017.
- [236] Dittner, M.; Hartke, B, “Conquering The Hard Cases Of Lennard-Jones Clusters With Simple Recipes,” *Comput. Theor. Chem.*, vol. 1107, pp. 7 - 13, 2017.
- [237] Cuko, A.; Macia´, A.; Calatayud, M.; Bromley, S. T, “Global Optimisation Of Hydroxylated Silica Clusters: A Cascade Monte Carlo Basin Hopping Approach,” *Comput. Theor. Chem.*, vol. 1102, pp. 38-43, 2017.

- [238] Mora-Fonz, D.; Buckeridge, J.; Logsdail, A. J.; Scanlon, D. O.; Sokol, A. A.; Woodley, S. M.; Catlow, C. R. A, “Morphological Features and Band Bending at Nonpolar Surfaces of ZnO,” *J. Phys. Chem C.*, vol. 119, p. 11598–11611, 2015.
- [239] Deacon-Smith, D. E. E.; Scanlon, D. O.; Catlow, C. R. A.; Sokol, A. A.; Woodley, S. M, “Interlayer Cation Exchange Stabilizes Polar Perovskite Surfaces,” *Adv. Mater.*, vol. 26, p. 7252–7256, 2014.
- [240] Jensen, S. R.; Saha, S.; Flores-Livas, J. A.; Huhn, W.; Blum, V.; Goedecker, S.; Frediani, L, “The Elephant in the Room of Density Functional Theory Calculations,” *Phys. Lett.*, vol. 8, p. 1449–1457, 2017.
- [241] Catlow, C. R. A.; Bromley, S. T.; Hamad, S.; Mora-Fonz, D.; Sokol, A. A.; Woodley, S. M, “Modelling Nano-clusters and Nucleation.,” *Phys. Chem. Chem. Phys.*, vol. 12, p. 786–811, 2010.
- [242] Schroeder, W.; Martin, K.; Lorensen, B, *The Visualization Toolkit: An Object-oriented Approach to 3D Graphics*, New York: Kitware, Inc, 4th edn, 2006.
- [243] Lazauskas, T, “Simulating Radiation Effects in Iron With Embedded Oxide Nanoparticles, PhD thesis,” Loughborough University,, Loughborough, 2014.
- [244] Le Grand, S. M.; Merz, K. M, “Rapid Approximation to Molecular Surface Area via The Use of Boolean Logic and Look up Tables,” *J. Comput. Chem.*, vol. 14, p. 349–352, 1993.

- [245] Pascual-ahuir, J. L.; Silla, E.; Tuñon, I, “An improved Description of Molecular Surfaces. III. A new algorithm for the computation of a solvent excluding surface,” *J. Comput. Chem.*, vol. 15, p. 1127–1138, 1994.
- [246] WASP@N , – Web Assisted Structure Prediction at the Nanoscale., London: hive.chem.ucl.ac.uk..
- [247] Sun, H.; Ren, Y.; Hao, Y.; Wu, Z.; Xu, N, “The stability mechanism of titanium cluster,” *J. Phys. Chem. Sol.*, vol. 80, pp. 105-111, 2005.
- [248] Kittel, C, Introduction to Solid State Physics, 6th edn, John Wiley & Sons, Inc, 1986, p. 23.
- [249] Datta, S.; Kabir, M.; Ganguly, S.; Sanyal, B.; Saha-Dasgupta, T.; Mookerjee, A, “Structure, bonding, and magnetism of cobalt clusters from first-principles calculations,” *Phys. Rev B.*, vol. 76, p. 014429, 2007.
- [250] Reddy, B. V.; Nayak, S. K.; Khanna, S. N.; Rao, B. K.; Jena, P, “Electronic structure and magnetism of Rhn (n = 2-3) clusters,” *Phys. Rev B.*, vol. 59, p. 7, 1999.
- [251] Bobadova-Parvanova, P.; Jackson, K. A.; Horoi, M, “Structure, bonding, and magnetism in manganese clusters,” *J. Chem .Phys.*, vol. 122, p. 014310, 2005.
- [252] Boyukata, M., “Molecular-dynamics study of possible packing sequence of medium size gold clusters: Au₂-Au₄₃,” *J. Physica.*, vol. E 33, pp. 182-190, 2006.
- [253] Scoles, G, The Chemical Physics of Atomic and Molecular Clusters, North Holland, Amsterdam, 1990.

- [254] Sun, Houqian.; Ren, Yun.; Wang, Guanghou, “Structural, Electronic, and Magnetic Properties of Mixed V_{13-x}Rh_x (x = 0 to 13) Clusters,” *J. Phys. stat. sol b.*, vol. 225, pp. 301-310, 2001.
- [255] Walsh, A.; Catlow, C. R. A.; Galvelis, R.; Scanlon, D. O.; Schiffmann, F.; Sokol, A. A.; Woodley, S. M, “Prediction on the Existence and Chemical Stability of Cuprous Fluoride,” *Chem. Sci.*, vol. 3, p. 2565, 2012.
- [256] Buckeridge, J.; Jevdokimovs, D.; Catlow, C. R. A and Sokol, A. A, “Nonstoichiometry and Weyl fermionic Behavior in TaAs,” *Phys. Rev. B: Condens. Matter Mater. Phys.*, vol. 94, p. 180101, 2016.
- [257] Taneda, k.; Kawazoe, Y, “Ground state structures of neutral and charged Ti clusters containing 2 to 16 atoms,” *Materials Transitions, JIM.*, vol. 41, pp. 635-638, 2000.
- [258] Chauhan, V; Singh, A; Majumder, C; Sen, P, “Structural, electronic and magnetic properties of binary transition metal aluminum clusters: absence of electronic shell structure,” *J. Phys. Condens. Matter*, vol. 26, pp. 015006-015007, 2014.
- [259] Graoui, H.; Giorgio, S.; Henry, C. R, “Shape Variations Of Pd Particles Under Oxygen Adsorption,” *J. Surf. Sci.*, vol. 417, pp. 350-360, 1998.
- [260] Verlet L, “Computer "Experiments" on Classical Fluids. I. Thermodynamical Properties of Lennard-Jones Molecules,” *Phys. Rev.*, vol. 159, p. 98, 1967.
- [261] Luo, W. H.; Hu, W. Y.; Xiao, S. F, “Size effect on thermodynamic properties of silver nanoparticles,” *J. Phys. Chem C.*, vol. 112, p. 2359, 2008.

- [262] Feng, D.; Feng, Y.; Yuan, S.; Zhang, X.; Wang, G, “Melting behaviour of Ag nanoparticles and their clusters,” *J. Appl. Thermal. Phys.*, vol. 11, pp. 1457-1463, 2017.
- [263] Chacko, S.; Joshi, K.; Kanhere, D. G.; Blundell, S. A, “Why do gallium clusters have a higher melting point than the bulk?,” *Phys. Rev. Lett.*, vol. 92, p. 135506, 2004.
- [264] Lewis, L. J.; Jensen, P.; Barrat, J. L, “Melting, freezing, and coalescence of gold nanoclusters,” *Phys. Rev B.*, vol. B56, p. 2248, 1997.
- [265] Kofman, R.; Cheyssac, P.; Aouaj, A.; Lereah, Y.; Deutscher, D.; Ben-David, T.; Penisson, J. M.; and Bourret, A, “Surface melting enhanced by curvature effects,” *Surf. Sci.*, vol. 303, p. 231, 1994.
- [266] Schmidt, M.; Kusche, R.; Kronmuller, W.; Von Issendorff, B.; Haberland, H, “Irregular variations in the melting point of size-selected atomic clusters,” *Phys. Rev. Lett.*, vol. 79, p. 99, 1997.
- [267] Chushak, Y. G.; Bartell, L. S, “Freezing of Ni–Al Bimetallic Nanoclusters in Computer Simulations,” *J. Phys. Chem*, vol. B107, p. 3747, 2003.
- [268] Qi, Y.; Cagin, K.; Samwer, W. L.; Johnson, W. A.; Goddard III, “Melting and crystallization in Ni nanoclusters: The mesoscale regime,” *J. Chem. Phys.*, vol. 115, pp. 385-394, 2001.
- [269] Lamas, E. J.; Balbuena, P. B, “Adsorbate Effects On Structure And Shape Of Supported Nanoclusters: A Molecular Dynamics Study,” *J. Phys. Chem.*, vol. 107, pp. 11682-11689, 2003.

- [270] Zinelis, S, “Effect of pressure of helium, argon, krypton, and xenon on the porosity, microstructure, and mechanical properties of commercially pure titanium casting,” *J. Prosthet. Dent.*, vol. 84, no. 5, pp. 575-582, 2000.
- [271] Hansen, P. L.; Wagner, J. B.; Helveg, S.; Rostrup-Nielsen, J. R.; Clausen, B. S.; Topsøe, H, “Atom-Resolved Imaging Of Dynamic Shape Changes In Supported Copper Nanocrystals,” *Science.*, vol. 295, p. 2053–2055, 2002.
- [272] Wu, G.-W.; Chan, K.-Y, “Molecular Simulation Of Oxygen On Supported Platinum Clusters,” *J. Electroanal. Chem.*, vol. 450, p. 25–231, 1998.
- [273] Mettela, G.; Boya, R.; Singh, D.; Pavan Kumar, G. V.; Kulkarni, G. U, “Highly tapered pentagonal bipyramidal Au microcrystals with high index faceted corrugation: Synthesis and optical properties,” *J. Sci. Rep.*, vol. 3, pp. 4-5, 2013.
- [274] Tatsuichiro Nakamoto.; Ken-ichi Motomiya, Shun Yokoyama.; Hideyuki Takahashi, “Precursor-templated synthesis of thermodynamically unfavored platinum nanoplates for the oxygen reduction reaction,” *Dalton Trans.*, vol. 49, p. 15837, 2020.
- [275] Steele, M. C.; Hein, R. A, “Superconductivity Of Titanium,” *Phys. Rev.*, vol. 92, p. 243–247, 1953.
- [276] Majumder, C.; Kumar, V.; Mizuseki H.; Kawazoe, Y, “Small clusters of tin: Atomic structures, energetics, and fragmentation behaviour,” *Phys. Rev.*, vol. B 64, p. 233405, 2001.

- [277] Joshi, K.; Kanhere, D. G.; Blundell, S. A., "Abnormally high melting temperature of the Sn₁₀ cluster," *Phys. Rev B.*, vol. B 66, p. 155329, 2002.
- [278] Subramanian K. R. S. Sankaranarayanan.; Venkat R. Bhethanabotla.; Babu, J, "Molecular dynamics simulation study of the melting of Pd-Pt nanoclusters," *J. Phys. Rev B.*, vol. B 71, p. 195415, 2005.
- [279] Lee, Y. J.; Lee, E. -K.; Kim, S.; Nieminen, R. M, "Effect of potential energy distribution on the melting of clusters," *Phys. Rev. Lett.*, vol. 86, p. 999, 2001.
- [280] Calvo, F.; Spiegelman, F, "Mechanisms of phase transitions in sodium clusters: From molecular to bulk behaviour," *J. Chem. Phys.*, vol. 112, p. 2888, 2000.
- [281] Shvartsburg, A. A.; Jarrold, M. M, "Solid clusters above bulk melting point," *Phys. Rev. Lett.*, vol. 85, p. 2530, 2000.
- [282] Petroski, J. M.; Wang, Z. L.; Green, T. C, EI-Sayed, M. A, "Kinetically Controlled Growth and Shape Formation Mechanism of Platinum Nanoparticles," *J. Phys. Chem.*, vol. B102, p. 3316, 1998.
- [283] Kart, S, O.; Erbay, A.; Kilic, H.; Cagin, T.; Tomak, M, "Molecular dynamics study of Cu-Pd ordered alloys," *J. Achiev. Mater. Manuf. Eng.*, vol. 31, no. 1, pp. 44-45, 2008.
- [284] Cleveland, C. L.; Luedtke, W. D.; Landman, U, "Melting of gold clusters," *Phys. Rev. Lett.*, vol. 81, p. 2036, 1998.

- [285] Bonnemann, H.; Richards, R. M, “Nanoscopic metal particless Synthetic methods and potential applications,” *Eur. J. Inorg. Chem.*, p. 2455, 2001.
- [286] Amendra, Fernando.; Dimuthu M, Weerawardene K. L.; Natalia V, Karimova.; Aikens, Christine M, “Quantum Mechanical Studies of Large Metal, Metal Oxide, and Metal Chalcogenide Nanoparticles and Clusters,” *Chem. Rev.*, vol. 115, no. 12, pp. 6112-6216, 2015.
- [287] Toshima, N.; Yonezawa, T, “Bimetallic nanoparticlessnovel materi-als for chemical and physical applications,” *New J. Chem.*, p. 1179, 1998.
- [288] Rabouw, Freddy T.; Donega, Celso de Mello, “Excited-State Dynamics in Colloidal Semiconductor Nanocrystals,” *J. Top. Curr .Chem (Z)*, vol. 58, pp. 3-5, 2016.
- [289] Groeneveld, E.; Delerue, C.; Allan, G.; Niquet, Y.; de Mello Donega, C, “Size Dependence of the Exciton Transitions in Colloidal CdTe Quantum Dots,” *J. Phys. Chem C.*, vol. 116, p. 23160–23167, 2012.
- [290] Rodríguez-Kessler, P. L.; Rodríguez-Domínguez, “Size and structure effects of PtN (N = 12 – 13) clusters for the oxygen reduction reaction: First-principles calculations,” *J. Chem. Phys.*, vol. 143, p. 184312, 2015.
- [291] Mahlangu, R.; Phasha, M. J.; Chauke, H. R.; Ngoepe, P. E, “Structural, elastic and electronic properties of equiatomic PtTi as potential high-temperature shape memory alloy,” *Intermetallics.*, vol. 33, pp. 27-32, 2013.

- [292] Chauke, H. R.; Minisini, B.; Drautz, R.; Nguyen-Manh, D.; Ngoepe, P. E.; Pettifor, D. G., “Theoretical investigation of the Pt₃Al ground state,” *Intermetallics.*, vol. 18, pp. 417-421, 2010.
- [293] Tshwane, D. M.; Modiba, R.; Govender, G.; Ngoepe, P. E.; Chauke, H. R., “The adsorption of halogen molecules on Ti (110) surface,” *J. Mater. Res.*, vol. 36, no. 3, pp. 592-601, 2020.
- [294] Corneliu, I. O.; Mihai, A. G., “Structure and electronic properties of TiO₂ nanoclusters and dye-nanocluster systems appropriate to model hybrid photovoltaic or photocatalytic applications,” *J. nanomater.*, vol. 357, no. 9, pp. 7-10, 2019.
- [295] Bader, R. F. W.; Henneker, W. H., “Molecular charge distributions and chemical binding,” *J. Chem. Phys.*, vol. 46, p. 3361, 1967.
- [296] Dutta, A.; Mondal, P., “Density functional theory study of structure, electronic and magnetic properties of non-metal (Group 13) doped stable Rh_n (n = 2-8) clusters and catalytic activities towards methanol activities,” *J. Chem. Sci.*, vol. 130, pp. 1-22, 2018.
- [297] Bautista Hernandez, A.; Cortes-Arriagada, D.; Camacho Garcia, H.; Chigo Anota, E.; Salaza Villanueva, M., “Quantum molecular study on doping effect in titanium and vanadium clusters: their application to remove some chemical species,” *Appl. Nanosci.*, vol. 10, pp. 37-49, 2020.
- [298] Vajda, S.; Pellin, M. J.; Greeley, J. P.; Marshall, C. L.; Curtiss, L. A.; Ballentine, G. A.; Elam, J. W.; Catillon-Mucherie, S.; Redfern, P. C.; Mehmood, F.; Zapol, P., “Subnanometre

platinum clusters as highly active and selective catalysts for the oxidative dehydrogenation of propane,” *Nat. Mater.*, vol. 8, p. 213, 2009.

- [299] Fernando, A.; Dimuthu, K. L.; Weerawardene, M.; Karimova, N. V.; Aikens, C. M., “Quantum Mechanical Studies of Large Metal, Metal Oxide, and Metal Chalcogenide Nanoparticles and Clusters,” *Chem. Rev.*, vol. 115, pp. 6112-6216, 2015.